UNIVERSITY OF BIRMINGHAM

Fabrication and Characterisation of Vegetable Chitosan Derived Microcapsules

by

Daniele Baiocco

School of Chemical Engineering

University of Birmingham

A Thesis submitted to the
University of Birmingham
for the degree of

Doctor of Philosophy

October 2021

Dedication

To Carlotta, Fernanda, and Pierluigi

Declaration

I hereby declare that the contents of this dissertation are original and have not been submitted in whole or in part for consideration for any other degree or qualification in this or any other University. This dissertation is the result of my own work and includes nothing which is the outcome of work done in collaboration, except where specifically indicated in the text. In submitting the present thesis to the University of Birmingham for the degree of Doctor of Philosophy, I agree that it will be deposited and made freely available to the public for genuine inspection. Legally, permission to wholly/partly reproduce any extracts, including images, figures, and schematic diagrams may be granted, for scholarly purposes only, by Professor Zhibing Zhang who supervised this project, or, in his absence, by the Head of the School of Chemical Engineering at the University of Birmingham. It is well understood that any copying/reproduction of the pieces of information contained in this thesis for financial profit shall not be granted without a written permission letter to be obtained from the educational institution, the relevant supervisory and sponsoring board, and the author.

Daniele Baiocco

October 2021

Acknowledgement

I would like to express my sincerest and heartfelt appreciation towards my primary supervisor Prof. Zhibing Zhang for his excellent hands-on supervision, constant encouragement, and superb guidance. His outstanding experience, promptness, insightful advices and inputs have helped me to progress on schedule throughout my PhD project journey.

A sincere ‘thank-you’ to my second supervisor Prof. Jon A. Preece for the valuable discussions, help, and feedback.

I would like to acknowledge the *Engineering and Physical Sciences Research Council* (EPSRC) National Productivity Investment Fund (NPIF), UK Research & Innovation (UKRI), and the School of Chemical Engineering at the University of Birmingham for funding the project, along with the financial support and collaboration provided by Lambson Ltd, UK at the early stage of my PhD project.

I would like to express my grateful appreciation to the colleagues, research fellows, and staff in the School of Chemical Engineering. Moreover, I cannot stop thanking the past and present members in the Micromanipulation and Microencapsulation Group, particularly Dr Iryna Mikheenko and Mr Zhihua Zhang for their assistance, support, and encouragement. Furthermore, a massive ‘thank-you’ to Dr Alejandro Avila-Sierra, whose friendship I do truly cherish.

Last but not least, I truthfully mean to express my deepest thankfulness to my family overseas, which have been apart in geographical terms only, for their lofty love and understanding. Besides, a special ‘thank-you’ to my partner and friends who have patiently companied and proactively stimulated me all over this journey – especially during the Covid-19 pandemic.

Abstract

Microencapsulation is a highly effective technology to deliver value-added actives at end-use applications, such as in food, personal care, and detergent products. The goal of the present research was to develop a novel microencapsulation system to encapsulate perfume/flavour oils by complex coacervation using plant-based biopolymers. Complex coacervation entails the electrostatic interplay between pairs of polymers carrying opposite charges. Specifically, this research was aimed towards: (i) investigating the feasibility and the experimental conditions required to induce complex coacervation between fungal chitosan (fCh) and gum Arabic (GA); (ii) determining the optimum fabrication conditions of fCh-GA complexes including pH and the weight ratio of GA-to-fCh based on their electrokinetic charge and turbidimetric analysis; (iii) developing methodologies for encapsulating perfumes (*i.e.* hexylsalicylate) and food flavour (*i.e.* L-carvone) oils within a safe fCh-GA shell *via* complex coacervation; (iv) understanding the physico-chemical, structural, surface topographic, mechanical, and barrier properties of the resulting plant-based microcapsules using several analytical techniques, such as scanning (SEM) and transmission electron microscopy (TEM), micromanipulation, UV-Visible spectrometer, and Fourier-transform infrared spectroscopy (FT-IR). The electrokinetic analysis of fCh and GA revealed that complex coacervation was optimised at a GA-to-fCh weight ratio approximately equal to 7:1. The interactions of the biopolymer pair was examined as a function of pH (1.0~8.0), which enabled to identify their complex coacervation comfort zone (CCCZ) as well as critical turbidity zone (CTZ). The optimised pH was 3.4, which triggered the strongest electrostatic attraction between fCh and GA. The stability of oil-in-water emulsions was investigated *via* interfacial tension analysis, which included the use of sorbitan esters (Spans), polysorbates (Tweens), and their combined adducts as the stabilising agents. Under the above conditions, microcapsules with a plant-based shell and a core of value-added oil were produced. Elongated as well as spherically shaped microcapsules could be fabricated conditionally upon the stirring rate during coacervation. Surface topography by SEM revealed well sealed microcapsules with a core of oil. The mechanical properties of microcapsules were determined *via* a micromanipulation technique.

The rupture force and nominal rupture stress of perfume oil microcapsules were 2.0±0.1 mN and 3.6±0.3 MPa, respectively, which are comparable to those of commercially available melamine formaldehyde (MF) based microcapsules. In-depth shell thickness analysis on the resulting microcapsules was performed by TEM. The results were used to validate the predicted shell thickness of microcapsules using experimental micromanipulation data combined with the simulation results of finite element analysis (FEA), which also enabled to quantify the intrinsic material property parameter (*i.e.* Young's modulus of the shell material). The oil leakage tests were carried out to assess the barrier properties of the microcapsules. Furthermore, the oil leakage data were fitted to a solute-diffusion model, which allowed to estimate the shell permeability.

As a further step towards developing highly versatile cutting-edge microencapsulation systems with a potential application in food industry as well, several formulation modifications were made to encapsulate L-carvone. The introduction of a two-stage microencapsulation process (*i.e.* complex coacervation followed by spray drying) allowed to achieve food grade free-flowing powders with a load of L-carvone, which proved stable for over a month.

Overall, the results evidenced that perfume/flavour oil microcapsules within a safe plant-based shell could be fabricated *via* complex coacervation. Moreover, the fCh-GA system has shown to be a promising carrier for the encapsulation of fragrance/flavour ingredients, which presents a new opportunity to globally overcome cultural and religious concerns associated with animal sourced products.

Table of Contents

List of Figures

List of Tables

Nomenclature

a_i	First log-normal/Gaussian distribution performance parameter
$\hat{a}$	Area ratio of microcapsules on one image (%)
A	Absorbance of specimen
A_k	Area covered by an individual microcapsule on one image (m^2)
A_c	Cumulative area covered by all microcapsules on one image (m^2)
A_b	Area of a blank PET film image (m^2)
A_d	Area covered by the microcapsules on a PET film upon deposition (m^2)
b	Second log-normal/Gaussian distribution performance parameter
$\mathbb{C}_k$	Force transducer compliance ($m \cdot N^{-1}$)
C_i	Concentration of the specimen ($g \cdot mL^{-1}$)
C_s	Oil solubility in the receptor medium ($g \cdot mL^{-1}$)
C_{in}	Oil concentration inside the microcapsule ($g \cdot mL^{-1}$)

C_{out} Oil concentration outside the microcapsule ($g \cdot mL^{-1}$)

d_{90} Diameter under which the cumulative volume of microcapsules is 90% (m)

d_{50} Diameter under which the cumulative volume of microcapsules is 50% (m)

d_{10} Diameter under which the cumulative volume of microcapsules is 10% (m)

D_h Hydraulic diameter (m)

$D_{[4,3]}$ Brouckere mean diameter (m)

$D_{[3,2]}$ Sauter mean diameter (m)

d_i Diameter of individual droplets/microcapsules (m)

$D_{n\text{-}b}$ Number-based mean diameter by micromanipulation (m)

E Young's modulus of microcapsules/beads (GPa)

$EE_{\%}$ Encapsulation Efficiency (% w/w)

F Compression force of microcapsules (mN)

F_b Force at microcapsule's bursting point (mN)

g Acceleration of gravity ($m \cdot s^{-2}$)

h Shell thickness (m)

h_m Imaged shell thickness (m)

h_i Inner height of a flow chamber (m)

I_i Intensity of laser light ($W \cdot m^{-2}$)

I_T Intensity of transmitted light ($W \cdot m^{-2}$)

I_{in} Intensity of incident light ($W \cdot m^{-2}$)

J Oil flux through the microcapsule shell ($mol \cdot s^{-1} \cdot m^{-2}$)

k_B Boltzmann's constant ($m^2 \cdot kg \cdot s^{-2} \cdot K^{-1}$)

K_p Two-phase partition coefficient

L Optical length of the cuvette (0.01 m)

m Parameter (exponent) of the rotational speed equation

N Number of microcapsules

P Permeability of microcapsules shell ($m^2 \cdot s^{-1}$)

r Radius of microcapsules (m)

R^2 Coefficient of determination

$R(t)$ Cumulative weight oil release (%)

Re Reynolds number

$\mathrm{d}R/\mathrm{d}t$ Release rate for thin-shell microcapsules (s^{-1})

s_0 Proportionality parameter of the rotational speed equation

t_r Microcapsule release time (s)

T Absolute Temperature (K)

T_T Transmittance

v_0 Volumetric flowrate ($m^3 \cdot s^{-1}$)

V_s Volume of the receptor medium (m^3)

w Inner width of a flow chamber (m)

w_{oil} Waste oil in slurry (%)

x_0 third performance parameter of log-normal/Gaussian distribution

Greek Symbols

α Spherical shape parameter of microcapsules

β Transcendental equation: first coefficient of non-linear regression (s^{-1})

γ Interfacial tension of the two phases ($N \cdot m^{-1}$)

δ Axial displacement (m)

ε Extinction coefficient of the UV-Vis standard calibration curve ($cm^{-1}(mol/l)^{-1}$)

ζ Zeta Potential (mV)

ϑ Volume factor for spherically shaped microcapsules

$\Lambda_{H \cdot FEA}$ Dimensionless factor of proportionality between E_H and E_{FEA}

λ Absorbance wavelength (nm)

μ Dynamic viscosity of fluid (Pa·s)

ν Poisson's ratio

ξ Transcendental equation: second coefficient of non-linear regression (%)

π Mathematical constant

ρ_{bi} Weighted bulk density of the generic phase i ($kg \cdot m^{-3}$)

ρ_i Density of the generic phase i ($kg \cdot m^{-3}$)

σ Microcapsule nominal rupture stress (MPa)

ς Dynamic EDS constant (s^{-1})

τ_w Wall shear stress (MPa)

τ_{max} Maximum shear stress at the flow chamber wall (MPa)

φ Critical complex coacervation parameter

ϕ Diameter of the impeller (m)

χ Microfluidic shape factor of a flow chamber device

ψ Surface factor for spherically shaped microcapsules

ω Stirring speed of the stirred impeller (rpm)

Abbreviations

Abs Absorbance of specimen

AFM Atomic Force Microscopy

ATR Attenuated Total Reflection

CC Complex Coacervation

CCCZ Complex Coacervation Comfort Zone

Ch Animal derived Chitosan

CL Crosslinking

CSS Combined Stock Solution

CSSDU Continuously Stirred Sample Dispersing Unit

CTS Core-to-Shell (ratio)

CTZ Critical Turbidity Zone

DDA Degree of deacetylation of chitosan

DI-w Deionised water

EDX Energy dispersive X-ray spectroscopy

EDS Emulsion dynamic stability

fCh Fungal Chitosan

fGl Fish gelatine

F_r Threshold rupture force

FM Fluorescence microscopy

FT-IR Fourier Transform Infrared Spectroscopy

FTU Formazine Turbidity Units

GA Gum Arabic

Gl Gelatine

Glu Glutaric aldehyde

HLB Hydrophilic Lipophilic Balance

HS Hexyl Salicylate

IFT Static interfacial tension at the two-liquid interface ($N \cdot m^{-1}$)

LC L-Carvone

MWCO Molecular Weight Cut-Off

MD Maltodextrin

MF Melamine-Formaldehyde

o/w Oil-in-water

NEC Net electrokinetic charge

NOD Normalised optical density

OM Optical microscopy

PET Polyethylene terephthalate

pH Potential of hydrogen

pH_{CC} Optimum Complex Coacervation pH

pI Isoelectric point

PMCs Perfume microcapsules

PrOH Propan-1-ol

QC Quartz Crystal

RI Refractive Index

RP Retention Performance

SC Simple Coacervation

SEI Strength of Electrostatic Interaction

SDS Safety Data Sheet

SEM Scanning Electron Microscopy

SPI Soy Protein Isolate

SFi Silk Fibroin

TEA Tri-Ethanol-Amine

TEM Transmission Electron Microscopy

TV Television

UV-Vis Ultraviolet-Visible spectroscopy

VOC Volatile Organic Compounds

vCh Vegan Chitosan

WPI Whey Protein Isolate

ζ-CCCZ NEC/Zeta potential based Complex Coacervation Comfort Zone

List of Publications and Awards [§]

Journal publications:

Baiocco, D., J.A. Preece, and Z. Zhang, Microcapsules with a Fungal Chitosan-gum Arabic-maltodextrin Shell to Encapsulate Health-Beneficial Peppermint Oil. Food Hydrocolloids for Health, 2021: Article no. 100016.

Baiocco, D., J.A. Preece, and Z. Zhang, Encapsulation of Hexylsalicylate in an Animal-Free Chitosan-Gum Arabic Shell by Complex Coacervation. Colloids and Surfaces A: Physicochemical and Engineering Aspects, 2021: Article no. 126861.

Zhang, Y., **D. Baiocco**, A.N. Mustapha, X. Zhang, Q. Yu, G. Wellio, Z. Zhang, and Y. Li, Hydrocolloids: Nova materials assisting encapsulation of volatile phase change materials for cryogenic energy transport and storage. Chemical Engineering Journal, 2020. 382: Article no. 123028.

Zhang, Y., A.N. Mustapha, X. Zhang, **D. Baiocco**, G. Wellio, T. Davies, Z. Zhang, and Y. Li, Improved volatile cargo retention and mechanical properties of capsules via sediment-free in situ polymerization with cross-linked poly(vinyl alcohol) as an emulsifier. Journal of Colloid and Interface Science, 2020. 568: 155-164.

[§] *PhD*-related publications (2017-2021)

Conference presentations:

Baiocco, D., Liu, S. and Zhang, Z. (2019) Determination of optimum conditions to encapsulate fragrance oils based on understanding pH-dependant complex coacervation comfort zone and critical turbidity zone, 26th International Conference on Bioencapsulation, Strasbourg, France - August 27-29, 2019.

Baiocco, D., Liu, S. and Zhang, Z. (2019) Animal-free oil-retaining microcapsules *via* complex coacervation, 22nd International Symposium on Microencapsulation, Salvador, Brazil - September 25-27, 2019

Baiocco, D., Preece, J.A. and Zhang, Z. (2021) Vegan microcapsules to encapsulate health-beneficial peppermint oil, International Conference on Formulations in Food and Healthcare (ICFFH), Gujurat, India & Birmingham, UK (organised virtually) - March 8-11, 2021

Baiocco, D., Preece, J.A. and Zhang, Z. (2021) Plant-based microcapsules to encapsulate peppermint oil, 9th European Young Engineers Conference (EYEC), Warsaw, Poland (organised virtually) - April 19-21, 2021

Baiocco, D., Preece, J.A. and Zhang, Z. (2021) Adhesion properties of plant-based perfume microcapsules for laundry applications, 9th European Young Engineers Conference (EYEC), Warsaw, Poland (organised virtually) - April 19-21, 2021

Awards:

1st Place Award for Oral Presentation

Baiocco, D., Preece, J.A. and Zhang, Z. (2021) Plant-based microcapsules to encapsulate peppermint oil, 9th European Young Engineers Conference (EYEC), Warsaw, Poland - April 19-21, 2021

2nd Place Award for Poster Presentation

Baiocco, D., Preece, J.A. and Zhang, Z. (2021) Adhesion properties of plant-based perfume microcapsules for laundry applications, 9th European Young Engineers Conference (EYEC), Warsaw, Poland - April 19-21, 2021

Chapter 1 Introduction

With rising consumer awareness, market trends are shifting towards functionalised fast-moving consumer goods (FMCG), such as health-promoting bioactives in foods and long-lasting fragrances in detergent products [1, 2]. In recent years, there has been a growing need to deliver functional actives onto solid surfaces [3]. Therefore, these actives are being incorporated into many FMCG [4]. Among all, a broad range of readily available products from personal and health care, household and cleaning products [5] to nutraceuticals and pharmaceuticals have been targeted [4, 6]. Specifically, the sustained release of functional actives at end-use applications has drawn more and more attention over the years, with particular emphasis on perfume molecules onto fabrics to aid the consumer perception of cleanliness and freshness, as well as encouraging consumer to repeat purchase [4, 7]. Similarly, flavours have become popular in food products as well, which has enhanced consumers' food experience [3]. However, fragrances are volatile organic compounds (VOCs) which may be thermally sensitive and/or chemically reactive [8]. Thus, they are prone to evaporating during storage and/or react with other formulated ingredients, if incorporated into a formulated product as such [9]. Moreover, fragrances may be highly susceptible to variations in the pH and temperature, as well as external factors including light, oxygen, and airborne pollutants [10, 11]. Therefore, strategies to inhibit fragrance evaporation and chemical degradation in formulated products are desirable, leading to a reduced amount of costly fragrances required in the product. Therefore, this would reduce the overall cost of manufacture, as well as enhancing the consumer experience, thereby generating an increasing revenue. To this end, microencapsulation, first pioneered by Bungenberg de Jong [12], has been used to encapsulate value-added actives, including VOCs. Interestingly, microencapsulation can suppress the volatility of VOCs in formulated products, as well as partitioning VOCs from the rest of the formulation, hence reducing cross-reactivity with other formulated ingredients [3].

Ghosh [13] has outlined the rationale behind microencapsulation, which consists in the process of entrapping micro-scaled solid materials or liquid droplets or gas within an inert wall which segregates the active load from the external environment. Therefore, microencapsulation has enabled a dramatic reduction of the active required in product formulation, with particular emphasis on perfume and flavour oils at laundry [14] and food [15] end-use applications, respectively. In addition, this has also enhanced the shelf-life of the resulting detergent/food products [16]. At laundry applications, the microcapsules entrapping the perfume oil act as delivery vehicles, by physically attaching themselves to fabrics during a wash cycle [17]. Such microcapsules in a dry state are designed not to release the perfume until external mechanical action breaks them, *e.g.* caressing clothing, wearing of a garment or running fingers through fabrics, which thus results in a much enhanced customer experience of long-lasting cleanliness and freshness up to days post-wash [18].

Similarly, food microcapsules can rupture upon chewing, thereby leading to consumers' enhanced taste experience [3]. Alternatively, they can provide food products with higher stability when exposed to adverse conditions. Food and nutraceutical microcapsules can preserve temperature and pH-sensitive compounds [19], such as probiotics, enzymes and essential oils, to reach the lower gastrointestinal tract undamaged, which is crucial to exert their health-promoting effects [20]. Notably, microcapsules' effectiveness is conditional upon the nature of the shell, as well as its physical and mechanical properties to inhibit undesired active leakage [17]. Accordingly, the selection of the shell precursor materials is strictly related to the desired end-use applications of the microcapsules [21].

Academic as well as industrial research has evidenced that many polymers have been employed as shell materials depending on their physico-chemical properties to form engineered microcapsules with an active load [22]. Reported shell materials have included urea formaldehyde [23, 24], melamine formaldehyde [25-28], polyurea [5, 29], polyamide [30], poly(methyl methacrylate) [31], and polyvinyl-polyacrylate [32]. The aforementioned

materials are fairly inexpensive and have proven effective in a significant number of detergent products [6, 33-35]. However, environmental, health & safety (EHS) regulations against the use of synthetic polymers as the microcapsule shells have arisen recently, which contribute to the accumulation of persistent microplastics in the environment. Moreover, formaldehyde has become an important object of concern due to its multiple drawbacks including carcinogenic effects [36, 37], poor indoor air quality [38], and negative environmental impact once released, although still within the legal limit [39].

Alternative coating materials, such as polysulfone [40], polyurethanes-urea [5], and polyesters [41] have proven thermally stable, as well as promising mechanical properties [42], which may thus have a potential for detergent/textile industry [40]. However, outstanding concerns around their safety and suitability at a large-scale have recently arisen [43]. Specifically, the high cost of raw materials and their processing [44], their non-biodegradability, as well as the content of respiratory-toxic and/or asthma-inducing isocyanates have drastically reduced their potential [45]. For this reason, innovative hazard-free materials as potential shell materials for the encapsulation of perfumes/fragrances are eagerly being sought.

When dealing with the food industry, gelatine as a shell material has largely dominated the scene over the last decades owing to its unique physico-mechanical properties [46-48]. Although gelatine has been recognised as one of the best performing encapsulating materials in food industry, hence leading to pretty strong microcapsules [15, 49, 50], serious consumer alerts around the safety of animal-sourced products, dietary habits, religious restrictions, and personal beliefs have emerged worldwide [51]. These shortcomings dramatically limit the portion of individuals to potentially benefit from these products due to the animal-derived ingredients. Therefore, great efforts have been launched to cut out animal derivatives (*e.g.* chitosan from the hard outer skeleton of shellfish, including crab, lobster, and shrimp) [52-54] in favour of plant-based alternatives as encapsulating materials [9]. To date, very little has been

reported on this topic, and no plant-based ingredients for microencapsulation have exhibited desirable properties and performance comparable to animal-sourced materials [9, 55].

As a step towards all-in-one tackling the EHS and the non-biodegradability issues associated with formaldehyde and other microplastic-releasing synthetic polymers, as well as complying with the recently enforced regulations on food safety against animal-based ingredients (e.g. pathogenesis of prion disease) [56], and fulfilling personal and religious beliefs (*e.g.* vegetarianism and veganism), pioneering attempts have been undertaken in order to develop safe and animal-free microcapsules with desirable properties at least comparable to those of their animal-based competitors [9]. Among all the microencapsulation techniques, complex coacervation has proven relatively time effective and suitable for emulsified fragrance oil droplets to get encapsulated into a biopolymeric shell [15, 57]. In addition, complex coacervation may produce microcapsules with promisingly high payloads, and remarkable mechanical properties [58].

Coacervation is one of the most preferred methodologies for microencapsulation of hydrophobic ingredients such as inks, flavour and perfume oils [6]. This dates back to the fifties following the introduction of ink-loaded microcapsules *via* coacervation for carbonless copy paper. Interestingly, this method was first proven suitable for laboratory production, and feasible for a systematic industrial scale-up [59]. However, scale-up of complex coacervation driven systems is typically not trivial as both microcapsules morphology and size are greatly affected by the processing conditions. The turbulence level is often referred to as the key scale-up criterium to affect the level of production scale, and its control is imperative to avoid aggregation or clustering among microcapsules [60]. Additionally, industrial manufacturing criteria face high capital and production costs, which makes industrial scale-up extremely challenging. Therefore, a technoeconomic process analyses of industrial scale microencapsulation should be conducted carefully [61].

1.1 Aims and Objectives of the Research Project

Based on the above, the primary focus of this research was on the feasibility of encapsulating key fragrance ingredients with a potential for detergent (*e.g.* hexylsalicylate) and food industry (*e.g.* L-carvone) *via* complex coacervation, utilising safe plant-based biopolymers as the shell precursors (*i.e.* fungal chitosan and gum Arabic). Formulation and microcapsule fabrication conditions (*e.g.* weight ratio between the biopolymers and pH) were investigated by electrokinetic and turbidimetric analyses of the biopolymers. Accordingly, a comprehensive characterisation of the resulting plant-based microcapsules was performed for an in-depth understanding of their structural, surface topographic, mechanical, barrier, and adhesion properties.

More specifically, the goal of this work was to assess whether plant-based microcapsules could be fabricated with desirable mechanical, barrier and surface properties, possibly comparable to those of commercially available ones (*e.g.* melamine-formaldehyde). To this end, characterisation of the mechanistic properties (*i.e.* rupture force, nominal rupture stress, displacement at rupture, and Young's modulus) of plant-based microcapsules with a potential for detergent industry is vital. Microcapsules for such applications need to be sufficiently strong to withstand washing and drying cycles, and capable of fracture to release the fragrance on-demand [6]. Similarly, food microcapsules should either rupture on chewing or stay intact to reach the inner gut, conditionally upon their end-use applications. However, no report on the mechanical properties of plant-based microcapsules has been made available in the public domain so far, where only synthetic polymer systems [25, 31, 62], or food formulation of an animal origin [63] have been addressed. In addition, understanding of the surface topographic and shell thickness of fungal chitosan derived microcapsules or quantification of their barrier properties is completely lacking.

Therefore, an important aspect of research presented in the present thesis aims to determinate the mechanical property parameters (*i.e.* rupture force and the displacement at rupture) of the resulting plant-based microcapsules, which were determined *via* a micromanipulation technique [64, 65]. In addition, the intrinsic material parameter (*i.e.* Young's modulus) and the shell-to-radius ratio of microcapsules were determined *via* the implementation of a model resulting from finite element analysis (FEA) by Mercadé-Prieto *et al.* [17a, 66], which had never been utilised on plant-based microcapsules before [18].

Furthermore, an experimental methodology combined with mathematical modelling [16b] has enabled to quantify the barrier properties of the resulting microcapsules. The shell permeability of model oils (*e.g.* hexylsalicylate and L-carvone) into specific receptor media from plant-based microcapsules was thus estimated, which had not been hitherto reported in literature. Overall, versatile plant-based microcapsules may contribute to a step change towards the next generation of microcapsules, which have an innovation potential at end-use applications of multiple bespoke industrial sectors [67].

1.2 Thesis Overview

A summary of this thesis is outlined as follows:

Chapter 2 provides a fundamental literature review on microcapsules and their applications. An overview on the main microencapsulation processes is included. Several characterisation techniques are also reviewed. Readily available models for the quantification of the intrinsic material property parameters of microcapsules, such as the elasticity modulus, are presented. A brief survey on the mechanism of deposition, adhesion, and retention of microcapsules onto model fabric surfaces at potential end-use applications is also conducted.

Chapter 3 introduces the materials, equipment tools, and devices used for the synthesis and characterisation of microcapsules. The experimental protocols including the relevant technical background, and processing conditions are also described.

Chapter 4 focuses on investigating complex coacervation under different experimental conditions. The feasibility of fabricating fungal chitosan – gum Arabic complexes is defined based on pH, zeta potential, turbidity, and electrokinetic considerations. Data analysis has helped to determine the key process conditions, which has led to a comprehensive understanding of the process. Novel concepts of pH-dependent Complex Coacervation Comfort zone (CCCZ) and Critical Turbidity zone (CTZ) are herein introduced, and utilised. Besides, interfacial tension and optical density studies towards producing stable emulsions suitable for the coacervation process are presented.

Chapter 5 describes the fabrication of animal-free perfume oil (hexylsalicylate) microcapsules with a potential for detergent industry using a safe biopolymeric pair (*i.e.* fungal chitosan and gum Arabic). Both experimental procedures and conditions are detailed. The physico-chemical, structural, surface topographic, barrier, and mechanical properties characterised from the resulting microcapsules were characterised and are extensively discussed. This chapter also gives an insight into the adhesion properties between plant-based perfume microcapsules and model fabric films using a microfluidic flow chamber technique.

Chapter 6 investigates the feasibility of adapting the encapsulation process previously developed to food-grade systems. Since such technology initially failed to produce acceptable microcapsules with a content of peppermint oil (L-carvone), the formulation was modified, and a two-stage procedure (*i.e.* complex coacervation followed by spray drying) was adopted. An extensive characterisation of two-stage microcapsules made from safe ingredients (*i.e.* fungal

chitosan, gum Arabic, and maltodextrin) is presented, with particular emphasis on the morphology of the microcapsules and their barrier properties. A micromanipulation technique was employed to determine their mechanical properties. Moreover, a fluorescence-sensing method was utilised to assess the effective presence of peppermint oil within the microcapsule shell.

Chapter 7 goes further by determining the intrinsic material properties of fungal chitosan and gum Arabic based microcapsules. The compression data of individual microcapsules were fitted to models in order to evaluate their Young's modulus. Specifically, the Hertz model and a Finite Element Analysis were employed independently. Interestingly, the results highlighted a strong relationship between the two Young's moduli which led to a new correlation. Moreover, these results led far beyond to establish a theoretical relationship between the two models, which is reported herein. Moreover, additional investigation on the barrier properties, such as shell permeability, was conducted *via* an experimental methodology combined with mathematical modelling.

Chapter 8 outlines the key findings and the overall conclusions of this project, followed by recommendations towards new horizons and potential future explorations.

Chapter 2 Literature Review

2.1 Introduction

In this chapter, literature on microencapsulation technologies, their experimental methodologies, and related theoretical frameworks and modelling are presented herein. The end-use applications of microcapsules in industry are also outlined. The overall literature survey consists of six main sections. In the first area, an introductory overview on microcapsules and their typical structural configurations are provided. The second section deals with the most relevant industrial applications of microcapsules with potential connections with this project. In the third section, a concise up-to-date summary on the available microencapsulation technologies for flavour microcapsules is given, with particular emphasis on complex coacervation. The fourth section provides a quick-take overview of emulsion and emulsification, with attention to homogenisation. In the fifth section, a brief introduction to the shell materials preferred in industry is provided, with great focus on safe animal-free alternatives, such as fungal chitosan. The last section pertains to the experimental methods and analytical techniques to characterise microcapsules. Several theoretical models to determine barrier, intrinsic material, and adhesion properties of the microcapsules are reviewed.

2.2 Microencapsulation

2.2.1 Overview

Microencapsulation is the technology to entrap micron-sized solid materials [68] or liquid droplets [69] or gas [70] within an inert shell consisting of natural [3, 71] or synthetic materials [72], which is apt to segregate as well as preserve the active load from adverse conditions [3, 13]. Although microencapsulation was originally developed to produce carbonless copying paper (CCP) systems during the first half of the twentieth century [59], it has been applied to several industrial areas over the years [73]. Different microencapsulation technologies have been employed for the encapsulation of living mammalian cells [74] and enzymatic formulations [75], with particular focus on their pharmaceutical/biomedical use [76]. Similarly, microencapsulation has played a proactive role to preserve value-added flavours in food products [77], including essential oils [78] and vitamins [79]. Alternatively, microencapsulation has helped masking undesirable off-flavours in nutraceutical/dietary supplements [80], which are frequently due to bitter-tasting flavonoids, such as quercetin [81]. Furthermore, microcapsules may act as protective and delivery vehicles of liquid bioactives within solid shells [82], which can be handled more safely and functionally than using the liquid ingredients as such [83]. This also facilitates the deposition of functional actives onto the required site-specific solid surface, such as fabrics [84], plants [85], biomedical substrates [86], and edible films [87]. Overall, when compared to their liquid form, multiple benefits associated with encapsulated actives have been evidenced [3]. These advantages include chemical inertness [13] *via* segregation of chemically reactive compounds [3, 88], enhanced storage stability [31] and protection of the encapsulated active ingredient against adverse environmental conditions [83], sustained release at end-use applications [21], masking unpleasant tastes/odours [89], as well as facilitation in handling [33], dispensability [90], dispersibility [91], free flowability [92], and suspensibility [13].

2.2.2 Microcapsules

Intense endeavours towards developing suitable microencapsulation systems have been undertaken over the past years. Several techniques have been developed to assure that valued-added actives can be effectively preserved during all stages of manufacturing products [40]. One methodology is to entrap active substances firmly within a shell, hence forming a microcapsule. Microcapsules can occur with different structures and mechanical properties, conditionally upon their intended end use [93]. The active substance is the core material, whereas the encapsulating material is the shell, which is the backbone of the microcapsule [94]. The material to be encapsulated is often referred to as the core, load, fill, active, kernel or internal phase, while the shell is the wall, encapsulant, carrier, membrane, coating or shield. The shell can be single-layered or an arrangement of multiple layers, where each layer may have a different composition [95]. Shell materials determine the structural scaffolding of the microcapsules, hence are responsible for the storage stability and chemical inertness of the core. The formation of a microcapsule strictly depends on the amount of both core and shell materials, which is referred to as core-to-shell ratio [96]. The appropriate core-to-shell ratio is crucial to determining the shell thickness, which in turn affects the sustained release of the microcapsule and its end-use performance [97]. High core-to-shell ratios may result in undesirable active leakage from the microcapsules, thus a reduced shelf life. In contrast, excessively low core-to-shell ratios may involve excess encapsulating materials, hence extra costs, which is commercially not appealing [98]. Therefore, an optimum core-to-shell ratio is desirable in order to fabricate microcapsules with specific structural, barrier, and mechanical properties [99]. Microcapsules can be categorised based on their size and/or configuration. Generally, microcapsules range between a few micrometres ($\geq$ 1 μm) and one millimetre ($\leq$ 1000 μm) [100]. In a simplistic approach, they can be divided into four classes: (i) core-shell (also reservoir/single-core), (ii) multiple-core, (iii) matrix-type, and (iv) multiple-shell. Accordingly, core-shell structures (Figure 2.1A) possess a lone reservoir chamber within the shell whose thickness depends on the methodology and processing conditions [101]. Multiple-core microcapsules exhibit several cores possibly with variable size [93]. Matrix-type microcapsules (Figure 2.1B) have infinitesimal hearts of active integrated within the

microcapsule network/shell [102]. Multiple-shell microcapsules exhibit a combination of concentric shells usually made up of different ingredients [21]. Figure 2.2 displays the most common microcapsule configurations.

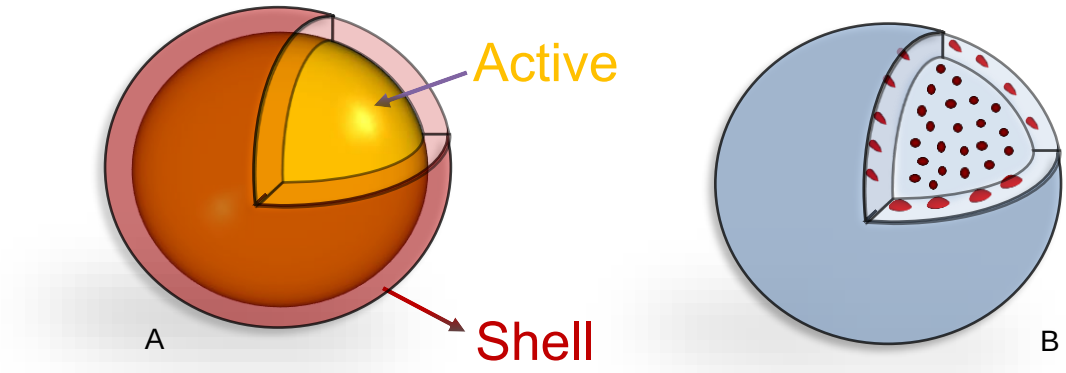

Figure 2.1– 3D-Configuration of a core-shell (A) and active matrix-integrated microcapsule (B).

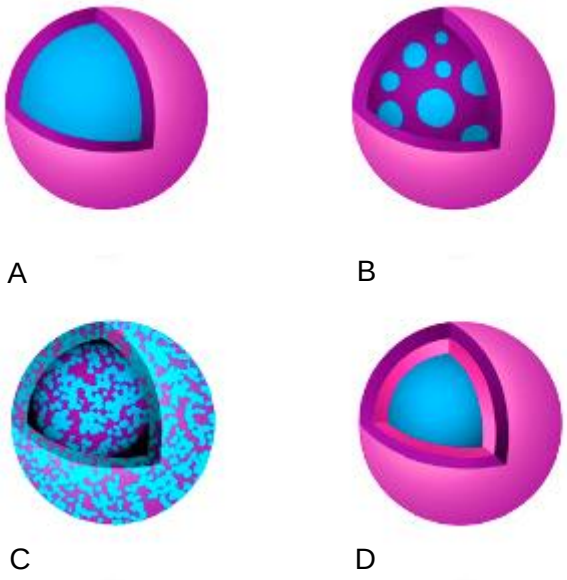

Figure 2.2– Different types of microcapsules: reservoir-type (A), multiple core (B), matrix-type (C), and multiple-shell microcapsule (D). Adapted from Trojanowska *et al.* [103], Jurkowska and Szczygieł [104] and Shishir *et al.* [105].

2.2.3 End-use Applications of Microcapsules

Microcapsules with a core of chromogenic material were first employed in pressure-activated carbonless copying paper in early 1950s. Specifically, dye microcapsules were designed to fracture, as well as triggering a chromogenic reaction with the paper substrate below when pressure upon writing/typing was exerted onto, resulting in a permanent coloured mark [106]. From that time onwards, noteworthy efforts have been undertaken towards developing medical and non-medical microcapsules with potential end-use applications. Over the years, industries have shown strong interests in microcapsules owing to their unique characteristics, which have

led to extended storage stability of many products, thereby facilitating their marketability. Specifically, microcapsules have found extensive applications in pharmaceuticals [107] with antimicrobial activities [108] or for diabetes treatment [109]. Biotechnology industry has employed microcapsules for controlled delivery of specific proteins and DNA-targeting vaccines to enhance the immunogenicity of certain individuals [110]. When dealing with agrochemical applications, pesticide-loaded microcapsules have been formulated to minimise the quantity of insecticide required [111]. In addition, pesticides have also been encapsulated within biodegradable carriers to develop environmentally safer products [112]. Pertaining to food industry, many flavours, essential oils, vitamins, and probiotic agents have been encapsulated to formulate fortified edibles [113], and controlled-release agents for cooking or baking [7]. Microcapsules have also gained interest in cosmetics and personal care products [8]. They have enabled many chemo/thermo-sensitive bioactives from a natural source to stay stable for an extended timeframe [114]. Other uses of microcapsules have included functional coating and spray-painting with the encapsulation of inorganic substances acting as pigments [115]. Furthermore, self-healing systems in construction industry, such as surface varnishing and corrosion-protection materials have relied on microencapsulation techniques [116, 117].

2.2.4 Fragrance Ingredients in Industry

Nowadays, many key ingredients in detergent as well as food industry are being delivered by microencapsulation [118]. Fabric detergents and conditioners are enriched with perfume oils, which consist of a complex blend of functional chemicals, such as aldehydes, ketones, ethers, and aliphatic hydrocarbons [119]. Similarly, fortified nutraceuticals and edibles enriched with essential oils are manufactured to include dietary supplements and delightful aromas, respectively. Essential oils are chemically constituted by esters, alcohols, terpenes, amines, ketones and aldehydes [120]. Therefore, these chemicals are responsible for the occurring fragrance, which is commercially attractive, thereby encouraging end-use consumers to repeat purchase [7]. However, perfumes, scents, aromas, and flavours are typically the costliest materials in laundry detergents [121], and food formulations [122] respectively. Therefore,

there is a growing need to minimise any waste/loss of fragrances, while promoting their delivery. Generally, massive losses of volatile fragrances are experienced during manufacturing, storage, freight, and handling prior to being purchased [123]. Fragrance losses may be due to natural evaporation and oxidative reactions, side interactions with exogenous ingredients contained in the formulation, as well as adverse environmental conditions (*i.e.* oxygen, UV light exposure, humidity, and sudden pH variations) [2, 11]. The key fragrance loss factors are summarised in Figure 2.3.

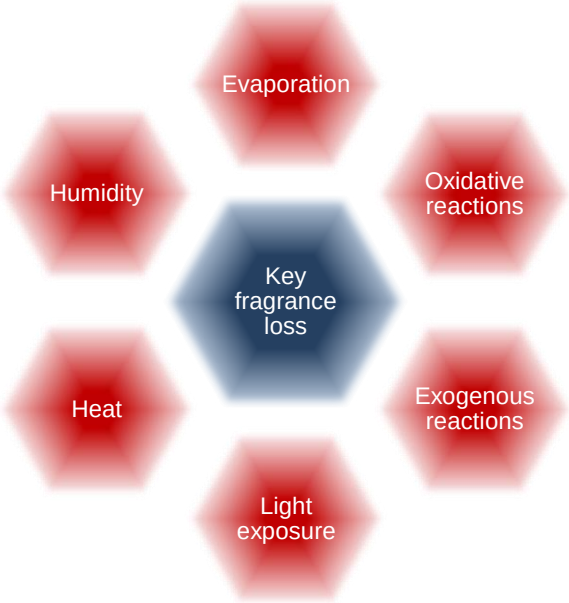

Figure 2.3– Independent factors likely to provoke depletion/loss of the fragrance during the production chain.

2.2.5 Perfume Molecules

Liquid perfumes may be washed off promptly upon contacting aqueous surfactant-rich media during a washing cycle [87]. Besides, they may quickly evaporate during cloth drying, leading to no perfume impregnation onto the fabric fibres [88]. Therefore, hydrophobic perfume oils

are typically retained by microcapsules, which are added to functional laundry garments, detergents, and conditioners [31, 89-92]. Microcapsules for such applications typically possess a core-shell structure [93, 94], as displayed in Figure 2.1A and Figure 2.4A-B. They can be fabricated by dispersing and then emulsifying perfume oils to generate small droplets to be coated by a shell (Figure 2.4C). The shell provides the scaffolding of the whole microcapsule and is responsible for its structure, integrity, and mechanical properties [95].

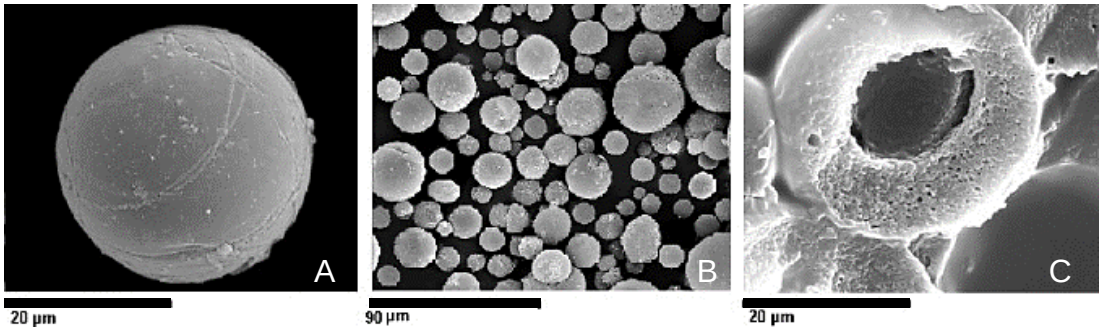

Figure 2.4– SEM micrographs of core-shell perfume microcapsules. Foreground image of a self-isolated microcapsule (A); poly-dispersed formation of microcapsules (B); cross-sectional image of the shell thickness [40].

Melamine-formaldehyde (MF) has long been a preferred shell precursor to produce perfume microcapsules [26]. Oil-in-water (o/w) emulsion droplets need to be followed by *in-situ* polymerisation of MF pre-condensate, which occurs at the oil droplet interface, hence forming the microcapsules [124]. It is imperative to achieve stable (non-coalescing) oil droplets, whose size distribution will roughly reflect that of the resulting microcapsules. Stable emulsions can be produced using a surfactant *via* vigorous agitation [125], homogenisation [126], and membrane emulsification [46]. Former literature has reported quality microcapsules with remarkable mechanical properties, great stability and durability, leading to a longer lasting

impregnation on fabrics [6, 27, 28, 35, 84]. Accordingly, such microcapsules are engineered for a gradual or burst perfume release, which can be triggered by mechanical action, such as rubbing [16].

2.2.6 Microcapsules with Food-Grade Actives

With enhanced consumer self-awareness, food industry markets have shifted towards edibles with extra health-promoting nutrients, referred to as functional foods [127]. Specifically, everyday functional foods may not only boost health, but also reduce or even prevent the risk of chronic diseases [128]. These functional ingredients can target and improve human physiological processes, and include natural extracts, nutraceuticals, and flavours [94]. Among them, essential oils are extracted naturally from different plant/shrub, such as rosemary, eucalyptus, and peppermint (leaves), roses (flowers), clove (seeds and stem), ginger (roots), orange (peels), lime (zest), and cinnamons (barks) [11]. In recent years, these extracts have gained more and more attention owing to their important biological, antimicrobial, and antibiotic activities [129]. Interestingly, peppermint oil has been of high interest due to its multiple beneficial effects against different conditions, such as irritable bowel syndrome (IBS), nausea, gastrointestinal disease and other digestive complications, as well as treating the common cold, headaches, and muscle pain [130]. However, essential oils are volatile, prone to oxidisation and degradation, which is analogous with perfume oils. To circumvent these shortcomings, essential oils have been encapsulated. Accordingly, former contributions have evidenced that microcapsules with monoterpene-rich essential oils, such as oregano [78], rosemary [131], ginger [132], lemon [133], orange [71], cinnamon [123], and peppermint [134-136] can be fabricated (Figure 2.5). Methodologies to fabricate food microcapsules have been reviewed by Madene *et al.* [3] . Among all, spray drying has been reported as the preferred technique to achieve free-flowing powders of microcapsules from food emulsions at a reduced cost [11]. Alternatively, coacervation has proven effective for the microencapsulation of food flavour oils leading to high payloads and promising mechanical properties of the resulting

microcapsules [9, 58]. Over the last few decades, gelatine has been the preferred shell ingredient to encapsulate food flavour oils [47, 50]. Although gelatine has been a cornerstone to food industry, noteworthy efforts towards developing non-animal alternatives have been undertaken, with particular heed to gum Arabic, soybean protein isolate, pectin, and xanthan gum [137]. Overall, health-beneficial actives together with safe and plant-based shell materials may help to develop globally accepted products. However, they are still at their very early stages [3]. Therefore, more research is required in order to develop new microcapsules and understand their various properties and performance at their end-use applications.

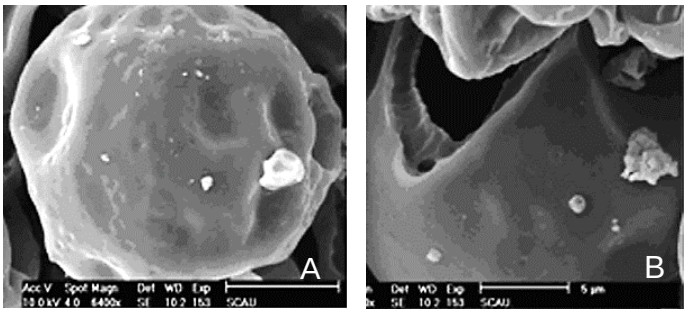

Figure 2.5– SEM micrographs of core-shell microcapsules encapsulating essential oil. Foreground image of a self-isolated (A) and an incomplete microcapsule with its shell thickness (B) [9].

2.3 Up-to-date Encapsulation Technologies

2.3.1 Overview

Encapsulation refers to the process enabling actives to be caught into a polymeric matrix (coating), which can be subsequently dried to achieve a free-flowing powder [138]. Capsules fall into three size categories: (i) macro-capsules when their size is of the order of millimetres,

(ii) micro-capsules when their size is in the order of microns, and (iii) nano-capsules when dealing with submicron sizes [139]. Their morphology could be spherical, elliptical or irregular. [3]. Morphology and mechanical properties of capsules depend on the choice of the materials, the encapsulation method, and the process conditions [60]. According to Finch and Bodmeier [140], encapsulation technologies can be also grouped based on the nature/phase of the reaction/suspending medium. When dealing with microencapsulation, liquid systems are typically preferred. Specifically, emulsification of two or more non-miscible phases is often performed to break the active into droplets, which are the core of microcapsules. Alternatively, vapour-suspended media involve the atomisation/nebulisation of a liquid formulation to fabricate microcapsules. Generally, microencapsulation methodologies can be classed into mechanical, physico-chemical, and chemical processes [141], which are outlined in Table 2.1.

Table 2.1 – Mechanical, physico-chemical, and chemical microencapsulation methods cross-checked with the nature of the suspending medium.

Type	Overview	Technique (particle size)	Process Summary	Suspending medium phase	Applications	Reference
Mechanical processes	Polymer-based constituents are generally employed in physical processes involving no chemical reaction.	Fluidised bed coating	Core particles are suspended by an air stream, moved around in the fluidised bed, and simultaneously sprayed with the film-forming coating liquid.	Vapour	Probiotics	[142]
		Spray-drying/	A core-shell emulsion is atomised to allow wall constituents to harden.	Vapour	Lipids/ Flavours	[134, 143]

	Spray-chilling (5-5000 µm)				
	Spinning disk (5-1500 µm)	A core-shell emulsion is laden onto a rotary disk. The suspension separation mechanism drives the wall materials onto the core ingredient.	Liquid	Flavours/ Fragrances	[58]
	Vibrating jet nozzle/ Prilling	Microencapsulation is accomplished by extruding the liquid through a jet nozzle vibrating at specific frequencies, and thus causing break-ups *i.e.* spherical droplets.	Liquid	Cells/ Microbes	[144]
	Centrifugal Extrusion/ Dripping (0.25-2.5 mm)	Liquid active and shell constituents are forced through the centre orifice and the external annulus concentric to the orifice, respectively.	Liquid	Flavours/ Fragrances	[13, 145]

Physico-chemical processes	The generation of the shell is driven by pH and temperature variations, or by the addition of electrolytes.	Solvent evaporation (<1-1000 μm)	A polymeric material is dissolved in an appropriate immiscible aqueous solvent in which and the active is dispersed. As solvent evaporation progresses, microspheres harden up. Free flowing powder may be obtained upon filtration and drying.	Liquid	Drugs	[73, 146]
		Supercritical fluid (SC-F) precipitation	The SC-F technology uses the solute effect of supercritical carbon dioxide (SC-CO_2) to trigger the precipitation of the substrate which had been initially dissolved in a polymer.	Supercritical	Drugs/ Proteins	[147]
		Ionotropic gelation/	Involves the electrostatic interaction of a cation/anion with an ionic polymer under specific	Liquid / Vapour	Core drug/	[99, 148, 149]

		Polyelectrolyte complexation	conditions to generate highly crosslinked structures. At least one of the species needs to be a polymer.		Antibodies (Ig) / Plant bioactives	
		Simple/Complex Coacervation (2-1200 μm)	Wall is formed by adding hydrophilic salts leading to salting-out of the biopolymer (simple); Electrostatic interactions between a pair of oppositely charged biopolymers.	Liquid	Perfumes/ Fragrances/Dyes	[53, 150]
Chemical processes	The shell is formed from chemical precursors to typically react at the interface of emulsions, suspensions, and dispersions.	Molecular inclusion (5-50 μm)	Entrapment of non-polar molecules by means of cyclodextrins having a lipophilic centre.	Liquid	Flavours/ Fragrance	[151]
		Interfacial cross-linking	A membrane is formed upon contacting a polymer-rich aqueous phase with an organic phase containing a highly crosslinking agent.	Liquid	Plant derivatives	[152]
		Interfacial polymerisation/	Apolar polymerisable monomers together with the core ingredient are suspended in a polar phase, and polymerise at the interface	Liquid	Lipids	[111]

	polycondensation (<1-1000 µm)	of the emulsion droplets. Polymerisation may be catalyst driven.			
	In-situ polymerisation	Based on the polymerisation reaction of precondensate with acrylic copolymers precipitating onto the core particles. May be heat/catalyst assisted.	Liquid	Perfumes/ Fragrances	[34]

2.3.2 Microencapsulation by Coacervation

Among all microencapsulation techniques detailed in Table 2.1, coacervation has been long adopted to encapsulate volatile organic compounds (VOCs), such as fragrances and flavours [153]. Coacervation has proven effective, leading to microcapsules with high payloads and mechanically tuneable [3, 58]. Microencapsulation *via* coacervation refers to the self-assembly of macromolecules at an oil-aqueous interface to give colloidal systems (colloidosomes) [154]. More specifically, suspended biopolymer-based solids combine into a concentrated colloidal phase, the coacervate (biopolymer-rich phase), which is separated out of a very diluted colloidal system (biopolymer-poor phase) [53]. Non-soluble biopolymer-derived complexes naturally settle down within the medium, thereby resulting in a phase-separated mixture [52].

Following Bungenberg De Jong's [12] pioneering studies, it was proven that a biopolymer-abundant phase can act as an encapsulating agent around a non-miscible core (oil), thereby leading to the formation of the capsule walls. This phenomenon relies on the free interfacial energy balance among the three phases (oil/solvent/polymer-rich phase). The interrelationship of the three-phase interfacial energy balance must be such that the polymer-rich phase can rearrange towards its lowest possible energy level (thermodynamically spontaneous process), which is likely at the oil-water interface. This phenomenon enables the polymer-rich phase to wet and then assemble around the oil droplets (exergonic coating process) resulting in a suspension of oil cores contained within larger networks of phase-separated polymer [155].

The phase separation, as well as the ensuing dynamic deposition of the colloidosomes layering up around a non-miscible core, can be triggered either by a single colloidal species or multiple biopolyelectrolytes consisting in simple or complex coacervation, respectively [156]. Conditionally upon the hydration level of the reacting medium, simple coacervation (SC) can be physically developed when a single-colloid solution is enriched with a very hydrophilic ingredient [154, 157]. This results in two separated phases, which are the colloidal-abundant

and colloidal-depleted ones [12]. Alternatively, complex coacervation (CC) refers to systems including more than one colloidal ingredient [158]. Specifically, CC consists in a naturally occurring phase conversion into two immiscible phases being the biopolymer-rich phase and biopolymer-poor (solvent) phase with precipitated biopolymer. As reported by Bruyninckx and Dusselier [6], CC has long proven effective to entrap many value-added actives, thereby leading to microcapsules, whose shell is formed by the coacervated biopolymers indeed [154]. Therefore, CC may be employed to pair biopolymers around the desired actives safely, resulting in novel and more consumer-friendly microcapsules [6]. To this end, CC is the key methodology adopted in this project, hence only a concise discussion on SC is provided herein.

2.3.2.1 Simple Coacervation

SC requires the use of a single biopolymer, which can form as the shell around an immiscible core. Phase separation is typically triggered by pH/temperature adjustments [157] or by the addition of a salt [159]. The separation of the polymer from its solvent can be also promoted by the addition of a highly hydrophilic coacervating agent [160]. Specifically, sodium sulphates and hydro-alcoholic solutions [161] have proven effective to induce biopolymer salting-out phenomena [162]. Over the years, SC has proven beneficial for the encapsulation of fish [163] and tea tree oils [164], and antipyretic drugs within a gelatine matrix [165]. To date, the research on SC has been limited which has mainly addressed animal-derived biopolymers [162]. No extensive contribution has arisen around the encapsulation of hydrophobic cores using plant-based derivatives except for soy glycinin [166] and gliadin [167]. Key steps of microencapsulation by SC are displayed in Figure 2.6.

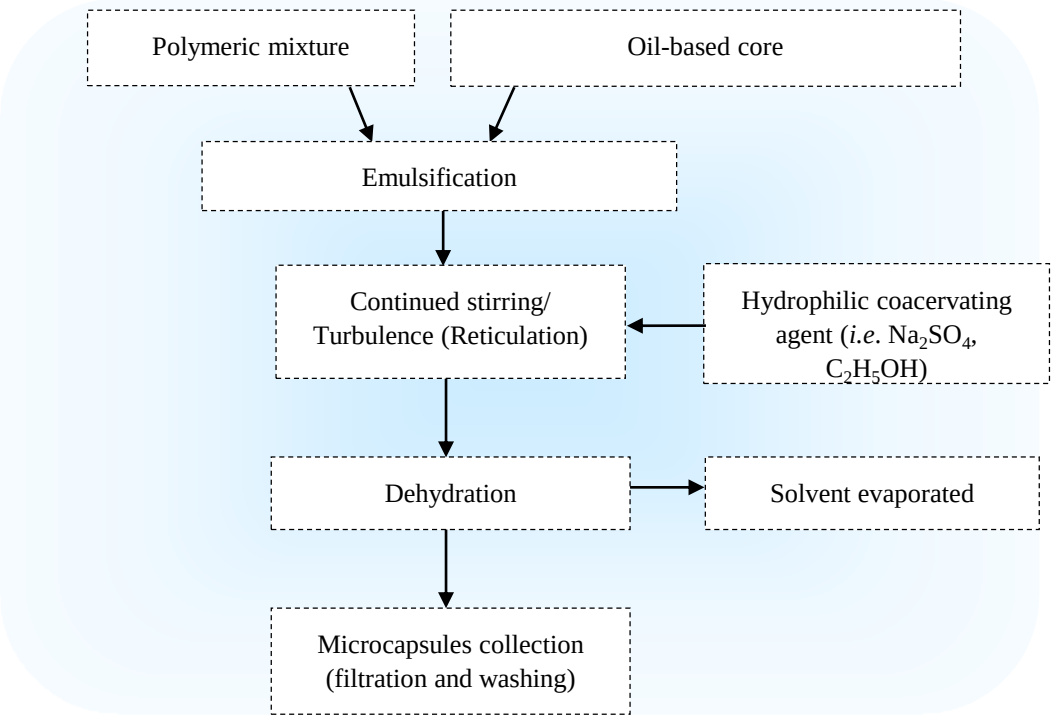

Figure 2.6– Simplistic quick-take of microencapsulation by SC.

2.3.2.2 Complex Coacervation

CC occurs when two suitable biopolyelectrolytes (*e.g.* proteins and polysaccharides) carrying opposite charges combine together into complexes. Accordingly, complexes forming around non-miscible oil droplets could result in the shell of the ensuing microcapsules [168]. Successful microencapsulation *via* CC has been formerly reported employing gelatine-gum Arabic for peppermint oil [15] and chitosan-gum Arabic for a blend of triglycerides [169]. Furthermore, novel CC systems pairing chitosan with xanthan gum [170], soybean protein isolate [171], and silk fibroin [172] have arisen in recent years. Generally, microencapsulation *via* CC consists of three crucial steps:

(i) development of complexes, which relies on the attractive electrostatic interaction between the two oppositely charged biopolyelectrolytes;

(ii) dynamic deposition of a layer around a lipophilic core ingredient under specific processing conditions (temperature and pH) [173];

(iii) hardening (also solidification/reticulation) of the mobile coating material into a firm shell, which is obtained by chemical crosslinking, heat, and/or spray drying [174].

Importantly, it is critical to ensure complex coacervation to occur spontaneously at non-cold temperatures to avoid gelling, which thus requires the use of thermostated baths. Moreover, the viscosity of the whole system is crucial to stabilise the formulations; accordingly, drag reducing agents such as gum Arabic have been extensively used [175]. Overall, high payload and cost-effectiveness are the main advantage of CC, yet processes may be highly system-specific [7].

2.3.2.2.1 Development of Complex Coacervates

Complex coacervation deals with the two-phase separation of a polymer-rich phase forming complexes, and a polymer-poor phase being the solvent [161]. Complexes develop due to the mutual (attractive) interaction between a pair of biopolyelectrolytes bearing opposite charges [53]. Biopolyelectrolytes can be polysaccharides and proteinaceous compounds, which naturally occur in living organisms [176, 177]. Interestingly, polysaccharide-protein interactions have often resulted in complexes with enhanced functional properties, which have been of significant interest in industry over the last decades [178]. Conditionally upon solvent, biopolymer, as well as processing conditions, there may be different CC-related scenarios, as displayed in Figure 2.7. Highly to infinitely dilute solutions may result in solvent-suspended co-soluble biopolymers, which exhibit little or negligible interaction (Figure 2.7A). Non-compatible pairs of polysaccharides/proteins bearing similar charges would electrostatically

repel each other, resulting in a thermodynamic phase separation, referred to as depleted interactivity or segregation. Therefore, a suspension consisting of two separated-out phases with similar charges would occur, one being protein-rich, whereas the other polysaccharide-rich only (Figure 2.7B). Alternatively, when biopolyelectrolytes with oppositely charged moieties occur, the electrostatic attraction may result in the interaction between the protein-polysaccharide pair. This phenomenon would thus lead to the formation of nil net surface charge structures, namely complex coacervates. The formation of coacervates is also evident macroscopically with the phase separation into biopolymer-abundant and solvent-rich phases, being the coacervates and the supernatant, respectively (Figure 2.7C). Both phases remain in equilibrium with each other [159]. Besides, the formation of coacervates (liquid-liquid phase separation) is followed by their precipitation (liquid-solid phase separation), which is referred to as associative phase separation [161]. The electrostatic status of a biopolymer pair can be 'perturbed' following the increase of their total biopolymer concentration (c_{tot}). This modifies the overall balance of charged ions in solution, which can then lead to enhanced attraction between the biopolyelectrolytes. This phenomenon is also conducive to the configurational entropy of the biopolymeric system, transitioning from a low entropy (segregated molecules) to a high entropy state due to the coacervate formation [159]. Accordingly, the gain in the entropy of the system is associated with the increased charge density of polyions which bind to their counter-polyions, thereby reaching the electro-neutrality [172]. Despite multiple attempts towards understanding the rationale behind complex coacervation, the biopolymer-to-biopolymer interaction is still poorly understood, nor has an electrostatic interpretation of the associative/segregative mechanism been provided yet [179]. Bungenberg de Jong (1929) first advocated that CC is likely ascribable to the achievement of a zero-surface charge of the biopolymers within a continuous medium. Subsequently, the ensuing electroneutral complexes separate out from the solvent [12, 161, 180, 181]. Overbeek and Voorn [182] have stated that CC is a spontaneous process under certain conditions. Specifically, the researchers first proposed a model on the total surface charge density (σ_x) of a biopolymer system, which has proved important to drive CC effectively. The model focuses on the charge density in relation with the critical number of sites activated by the biopolymers (r_c) which basically corresponds to their molecular mass [162]. Specifically, the empirical condition $\sigma_x^3 r_c \geq \varphi$ (where φ is a

critical CC parameter) should be met to facilitate coacervation, with the proviso that $\varphi \geq \varphi_{cc}$ (φ_{cc}=0.53) [182]. More recently, the applicability of the model was investigated by Dubin *et al.* [183] and Bohidar [159]. It was found that high molecular mass and large charge density of biopolyelectrolytes with opposite charges actively promote coacervation. Additional investigations around CC were conducted by Veis *et al.* [184-188]. Particular emphasis was placed on the two-phase transitioning, as well as the development of complexes, prior to the critical threshold (φ_c). It was inferred that attractive interaction between the biopolyelectrolytes gradually begins at $\varphi < \varphi_c$, which becomes more evident at $\varphi \geq \varphi_c$. Similarly, extra endeavours were undertaken by Nakajima and Sato [189] to identify the induction point of CC on a theoretical basis. According to Tainaka [190], CC between two compatible biopolymers can be induced within a specific charge density zone, outside of which the biopolymers are co-soluble, resulting in no/hindered coacervation. Although noteworthy efforts towards understanding CC have been developed over the years, the theoretical models still cannot address all parameters playing a role for CC. CC develops under a strongly attractive interaction between biopolyelectrolytes bearing opposite charges, which leads to new chemical bonds between the biopolymers, as well as their electro-neutralisation. When binding to each other, the overall polarity of polysaccharide-protein based complexes drops. Therefore, the solubility of complexes is dramatically depleted as nil surface charge is attained, hence phase separation is triggered.

Once complex coacervates have formed, the whole system reaches a new equilibrium towards the state with the minimum energy. If a lipophilic (water insoluble) active is emulsified into the system, the resulting oil-in-water droplets may get coated with a thin film of coacervate under specific conditions. However, the dynamic deposition of the coacervates onto the surface of the oil droplets may not be spontaneous (*i.e.* pH-driven coacervation) which is conditional upon the nature and affinity of coacervates to adsorb onto the oil-water interface [191].

To date, the mechanism by which complex coacervates move to the oil-water surface is still not fully understood. When coacervation is triggered, the two biopolymers likely begin bonding to each other in bulk to possibly form nanoscaled coacervates. Tentatively, the mechanism of interfacial coacervation seems to be similar to that of Pickering emulsion [192]. Accordingly, the oil-water interfaces may be stabilised by adsorption of the preformed nanocoacervates from the continuous aqueous phase onto the surface of the oil droplets. This eventually strengthens the oil-water interface by lowering the interfacial energy of the system. Subsequently, the coacervates (with a higher molecular weight than that of the individual precursors) continue to accrete around the oil droplets, hence generating a more and more stable system, and eventually the microcapsule walls.

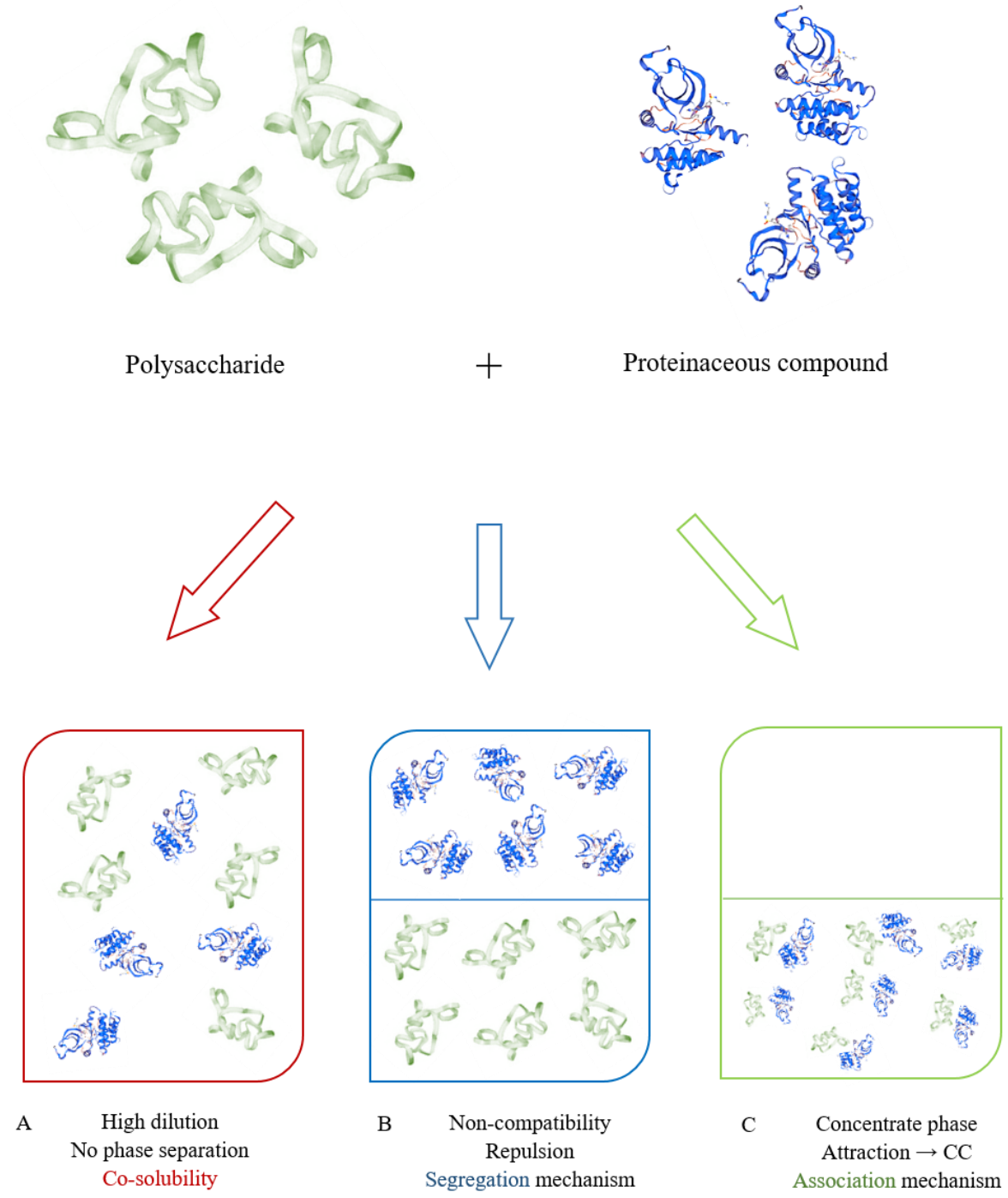

Figure 2.7– Schematic diagram on the possible outcomes resulting from the combination of proteins and polysaccharides. Adapted from Weinbreck [176].

2.3.2.2.2 Parameters Involved in Complex Coacervation

As reported in literature, several parameters affect the development of coacervates [176]. CC is likely to progress when two biopolymers with opposite charges bind to each other. When dealing with polysaccharide-protein systems, their functional branches can get ionised depending on their own dissociation constants, proteins' isoelectric point, and the pH of their medium. Therefore, amine ($-NH_2$) and carboxylate groups (-COOH) along the backbone of proteins and polysaccharides, respectively, can extend into cations and anions, which enables their electrostatic interaction. Accordingly, their net charge can be adjusted by varying the biopolymer-to-biopolymer ratio, which has proven crucial to form coacervates. Besides, the presence of dissolved salts also affects the attractive/repulsive interaction between the biopolymers, hence the development of coacervates.

2.3.2.2.3 pH

Charged polymers of natural/synthetic origin are referred to as polyelectrolytes or polyions [176]. Attractive interaction between two polyelectrolytes is an essential requirement for complexes to form. Polyelectrolytes carrying positive and negative charges are referred to as polycations and polyanions, respectively. Moreover, proteinaceous compounds may bear both negative and positive branches, which are termed as polyampholytes. The ionisation yield of biopolymers' functional moieties is strictly related to the pH of the medium. When no ionisation of amines occurs, proteins' minimum solubility is reached [193]. In other words, if protein–protein interplays are favoured over protein–water interplays, no reactive conformation of proteins can be made available, hence no coacervates will form. This condition is referred to as protein's isoelectricity point (pH_i) [194]. Accordingly, both biopolymers need to operate at a pH enabling them to exhibit opposite charges. It is therefore vital to identify the precise value of the dissociation constants (pK_a) of the biopolymers' functional groups (*e.g.* carboxylates). Previous contributions have shown that CC phenomena are typically confined into a narrow pH region [150, 195]. As an example, biopolymer systems consisting of gelatine

(Gl) and gum Arabic (GA) have been intensively explored over the years. Specifically, it was made clear that swine-derived gelatine exhibited an electrostatic switchover from a positive to negative charge at pH~9, which represents its pH_I [60]. In contrast, GA is negatively charged within solutions with a pH≥2, which is its $pK_{a,GA}$. Thus, optimal CC occurs within a narrow pH range (Figure 2.8A). Similarly, Deveci and Basal [172] have investigated the feasibility of CC on another biopolymeric system (*i.e.* silk fibroin (sFi) and crustacean-derived chitosan (Ch)). sFi was found to bear negative (non-protonated) charges above its own pH_I~4.2, whereas Ch exhibited positive (protonated) charges at pH<6.5, which is its $pK_{a,Ch}$ (Figure 2.8B). Similar work was conducted on hyaluronic acid (HA) with sFi [196], Ch with soybean protein isolate (SPI) [171] and GA [197], which are depicted in Figure 2.8C, Figure 2.8D, and Figure 2.8E, respectively. Additional studies on plant-based proteins were carried out by Ducel *et al.* [198], with emphasis on cereal (α-gliadin) and leguminous protein (pea globulin). According to Veis and Arany [184], benchmark pH-values around CC can be identified for specific biopolymeric systems. Specifically, soluble complexes are induced at pH_c, whereas the phase separation and the subsequent dissociation phenomena of complexes occur at $pH_{\varphi 1}$ and $pH_{\varphi 2}$, respectively. GA and whey protein isolate (WPI) were investigated by Weinbreck *et al.* [52]. Considering the pK_a of the carboxylate groups of GA ($pK_{a,COOH}$~2.2) and WPI's $pH_{i,WPI}$~4.8, it was inferred that CC phenomena could develop only at $pH_{\varphi 2} \geq pK_{a,COOH}$ and $pH_{\varphi 1} \leq pH_{i,WPI}$. GA's carboxylates can be protonated at $pH<pK_{a,COOH}$, where WPI also exhibits positive charges, hence only repulsive interaction is possible. Alternatively, no positive charge is borne by WPI at $pH>pH_{i,WPI}$, where GA is negatively charged as well. Therefore, CC may potentially occur at $2.2 \leq pH \leq 4.8$ only, where oppositely charged GA and WPI occur (Figure 2.8F).

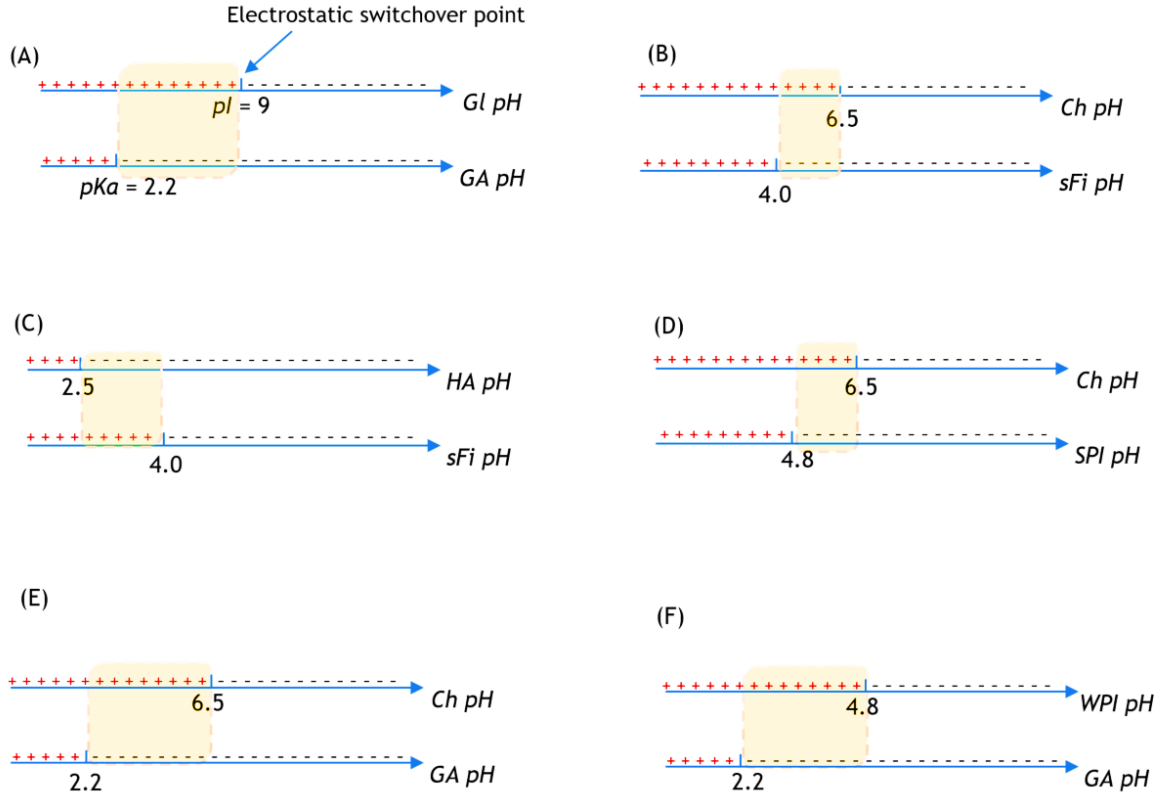

Figure 2.8– Electrostatic comparison of several biopolymeric systems: Gl-GA (A), Ch-sFi (B), HA-sFi (C), Ch-SPI (D), Ch-GA (E), WPI-GA (F); pH_i (proteins), pK_a (polysaccharides), and $pH_{\varphi 2} \leq pH \leq pH_{\varphi 1}$ windows are displayed along with their charge switchover.

2.3.2.2.4 Ionic Strength

Former literature has investigated the effect of the ionic strength on the CC phases, including $pH_{\varphi 2}$, $pH_{\varphi 1}$, and pH_c [199]. Generally, high ionic strength (electrolyte/salt concentrations in the order of tenths of mM) may result in a depletion of CC [176]. This phenomenon is likely due to the salt dissociating into its own ions, which may generate a screen around the biopolyelectrolytes which are thus inhibited to attractively interact [199]. The screening effect associated with high ionic strength was also reported by Jun-xia *et al.* [9] and Kayitmazer *et al.* [200] for SPI-GA and HA-Ch systems, respectively.

In contrast, low ionic strength may pair up with the protainceous scaffolding, modifying its conformation into an extended structure, thereby exposing additional charged moieties to react *via* CC [199].

2.3.2.2.5 Biopolymer-to-Biopolymer Ratio

When there is an attractive interaction between biopolymers carrying opposite charges, CC occurs. However, whether high CC yields can be achieved depends on the biopolymer-to-biopolymer ratio, which needs to be optimised. This is possible when opposite charged biopolymers combine into perfectly electroneutral complexes. Proteinaceous compounds and polysaccharides possess net opposite charges at a given pH, which determines an electrostatic gap [201]. Therefore, it is essential to neutralise this electrostatic gap by identifying the optimum biopolymer-to-biopolymer ratio to balance the net opposite charges, thereby resulting in electroneutral complexes.

2.3.2.2.6 Functional Analysis of Coacervates

The development of protein-polysaccharide complexes is influenced by the spatial conformation of the proteinaceous structure. An extended conformation will better expose the protein's charged moieties, hence their reactivity towards the counter-polyions. CC between proteins and polysaccharides not only leads to the re-arrangement of the reacting structures, but also to a new chemical species being the complex [202]. Although the physico-chemical properties of the new species may differ from those of the simple protein, some multiple protein-related functionalities, such as foamability can even be enhanced by the complexes. When contacting a given solvent, protein's solubility is conditional upon the stability of its conformational state (folded/aggregated/extended) [203]. Spatial conformation, surface charge, and hydrophobicity of a protein at a given pH and temperature determine the solvent-protein equilibrium [204]. High temperatures trigger the irreversible denaturation of proteins

and their reactive sites, which should be avoided [205]. When dealing with the pH, the further away a protein is from its pH_i, the higher its resulting net charge. Therefore, the solubility of a charged protein is enhanced due to its non-folded conformation. This generates an increased protein-water interaction, which better exposes the protonated branches of the protein towards the counter-polyions of the polysaccharide [206]. Following CC, some specific properties of the protein, such as its conformational extensibility, are likely reflected onto the coacervate scaffolding too. This may provide the coacervates with extra functional properties, such as foamability, which is defined as the capacity of particles to produce and stabilise foams [207]. Overall, this structure-functional interrelationship among proteins, polysaccharides, and their ensuing complexes may be of interest in many industrial processes, such as emulsification and emulsion stabilisation, which are discussed as follows.

2.4 Emulsification

2.4.1 Emulsion Stability

An emulsion typically consists of a fine dispersion of tiny droplets of a liquid which is not soluble/miscible in another, which is the 'hosting' liquid (continuous phase). Emulsions are formed by supplying energy to at least two non-miscible liquids in order to get the dispersed phase broken down into small droplets. Particularly, emulsions can be generated mechanically, by inducing high turbulence *via* specific emulsification techniques, such as energy-intensive homogenisation [208]. Alternatively, other techniques including micro-fluidics devices [209] and pressure-driven membranes can generate emulsions of highly monodisperse droplets without significant turbulence [210].

Conditionally upon the selected liquids, simple emulsions can be divided into categories *i.e.* oil-in-water (o/w) and water-in-oil (w/o) [211]. In addition, it is important to appreciate that spontaneous liquid-liquid phase separation may also trigger water-in-water (w/w) emulsion droplets provided that two immiscible water phases are contacted, which may occur when the

relative viscosities of two aqueous phases are significantly different [212]. However, the droplets formed following emulsification are thermodynamically unstable and prone to regressing into two split phases [213].

When new interfaces of one phase form into another phase, a greater surface area is achieved. Consequently, the corresponding free surface energy (droplets) is greater, which requires a considerable energy input to disperse one phase (disperse phase) into the other one (continuous phase) effectively [214]. This can be accomplished *via* homogenisation where external energy can be provided chemically (*i.e.* chemical potential of the system) or more often mechanically (*e.g.* rotor-stator homogeniser). Since emulsions are unstable, the energy input is also related to the 'over-processing' of emulsions, which refers to the re-coalescence of new droplets, and their subsequent re-homogenisation during high-energy emulsification [215].

Figure 2.9 shows the phenomena possibly occurring within non-stable emulsions, encompassing creaming, sedimentation, coalescence, flocculation, Ostwald ripening [216]. As a step towards enhancing the stability of emulsions, surfactants (also emulsifying agents or emulsifiers) and co-polymers are included prior to emulsification [217]. Emulsifiers consist of amphipathic protein-based segments, which direct towards the biphasic interface, thereby reducing the interfacial tension. Specifically, they are substances with a hydrophilic head (ionic or strongly polar groups *e.g.* polyglycols) and a hydrophobic tail (a linear/branched hydrocarbon). Interestingly, the balance between the head and tail groups determines the configuration of the surfactant, namely a positive or negative curvature. This is associated with its amphiphilic structure, and its corresponding capability for micellisation, which is described by the Hydrophilic Lipophilic Balance (HLB).

In o/w emulsions, a protein should unfold and be promptly adsorbable at the biphasic interface in order to generate a cohesive film around the oil droplets [218]. However, the effectiveness

of an emulsifier is very system specific. For this reason, emulsifiers may provide short-, mid- or long-term stability of an emulsion depending on their diffusion rate towards the interface and the strength of the viscoelastic film formed around the oil droplets [219]. Under given circumstances, emulsion stability is improved employing non-soluble lipophilic/amphiphilic colloidal particles, namely Pickering nanostructures (*e.g.* nanoparticles and nanocomposites) [220]. Pertaining to protein-polysaccharide dispersions as the precursors to CC, emulsion stability can be enhanced by the biopolymers themselves, which naturally reduced the interfacial tension [158]. As an example, GA has long been known for its superb emulsifying properties, and reduced viscosity at moderate concentration. Biopolymers are usually added to the continuous/disperse phase prior to emulsification. Specifically, emulsions for microencapsulation *via* CC can be stabilised to a specific HLB using a combination of hydrophilic polysorbates (Tweens) and hydrophobic sorbitan esters (Spans) as the surfactants (steric stabilisation) [7]. The technique used to input energy to a system with a specific pH and temperature has a key role in determining the stability of the emulsion.

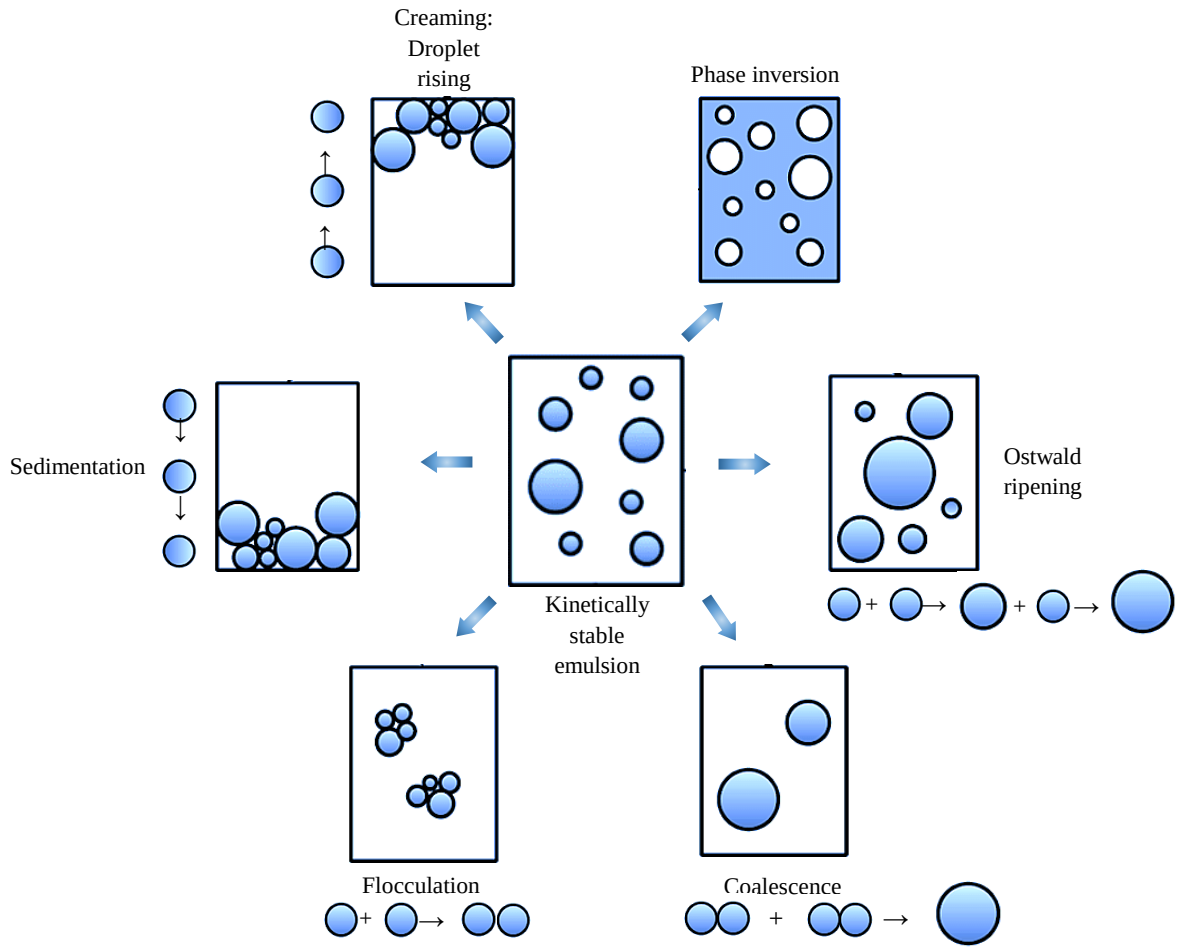

Figure 2.9– Mechanisms triggering emulsion instability.

2.4.2 Homogenisation

One of the most popular approach to produce emulsions in industry is homogenisation. There are two types of homogenisation, namely primary and secondary. The former refers to emulsions directly generated from separate liquids, whereas the latter occurs when existing droplets are broken down into smaller ones [221]. Homogenisation is mechanically performed by a high pressure homogeniser (HPH) or high shear rotor-stator homogeniser (HSRSH), which is typically employed to produce nano-scaled [222] and micro-scaled emulsions [223], respectively. HSRSH is equipped with a metal-based membrane (stator) around the impeller

blades (rotor), (Figure 2.10). The high stirring rate of the blade first generates a coarse emulsion that is, in turn, homogenised through a fine emulsion screen (emulsor). Specifically, the liquids are forcibly passed through the membrane stator under the action of continuous centrifugal forces, which break down the immiscible phase into small droplets. At increasingly high stirring rates, the droplets are deformed into ellipsoids and then into smaller droplets due to the interfacial tension. Conditionally on the turbulence and dissipation rate of the energy in the system, the mean droplet size can be controlled. The relationship between the Sauter/surface-based diameter ($d_{[3,2]}$) of the droplets produced by emulsification and the rotational speed (Equation (2.1)) was proposed by Calabrese *et al.* [224]

$$D_{[3,2]} = s_0 \omega^m \tag{2.1}$$

where s_0 and m are proportionality parameters and ω is the rotational speed (rpm). Recently, this heuristic relation has been adapted to investigate the influence of the agitation rate on thin-shelled microcapsules by homogenisation [62].

Since homogenisation is a key technique in microencapsulation, it is therefore crucial to understand its implications. The droplet size of the disperse phase strictly depends on the amount of energy absorbed by the system during emulsification. Accordingly, the higher the stirring rate, the higher the energy inputted, the lower the size of the droplets [214]. Interestingly, the size distribution of the encapsulates is likely similar to that of the oil droplets since the shell forming around the oil droplets are typically very thin.

Homogenisation is relatively cost-effective and can be scaled up, since the droplets mean size is correlated to the energy dissipation rate (energy input per volume/weight) to determine the agitation speed required.

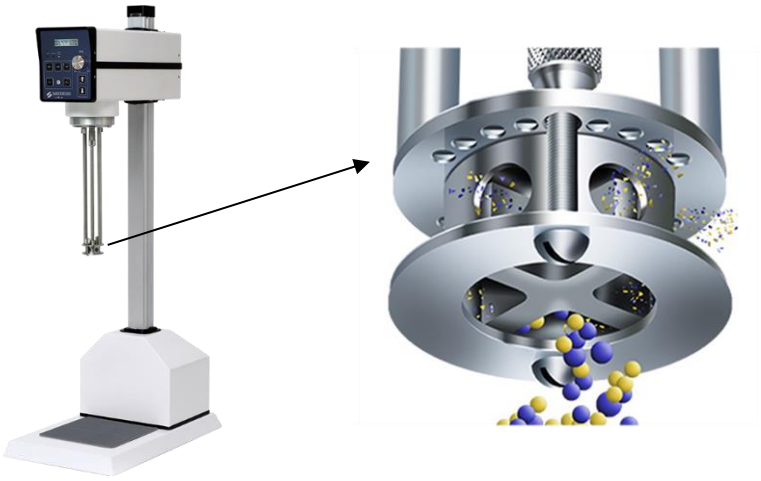

Figure 2.10– High shear rotor-stator homogeniser equipped with a mid-positioned 4-blade impeller (90°blade angle, ⌀ 1.2″) encircled by a metal membrane-like cylinder (⌀ 1.4″) possessing homogeneous meshes (Model L4RT, Silverson Ltd, UK) 2.0.

2.4.3 Extra Emulsification Techniques

Several novel methodologies to form homogeneous emulsions have recently arisen within the scientific community. Homogeneous emulsions of very narrow droplet size distributions can be achieved by cross-flow membrane systems [225], system-specific gauges including microchannels [226] and one-step microfluidic [227], flow-focusing [228] and microchipped devices [229].

2.5 Selection of the Ingredients for Encapsulation

2.5.1 Overview

The fabrication of microcapsules is performed following emulsification of a lipophilic phase, namely the active ingredient, within an aqueous polymeric phase, which is the shell precursor. Two oppositely charged biopolymers are required for CC. Thus, biopolymeric complexes dynamically layer up at the o/w interface around the oil droplets to form the shell. Since the freshly formed shell is still mobile, spray/freeze drying techniques are exploited to reticulate the cohesive film, and also to attain free-flowing powder of microcapsules. The amount of oil retained, namely payload or loading efficiency, (*i.e.* the ratio between retained active to the microcapsules) is affected by the shell/core materials, and their total concentration.

2.5.2 Core-to-Shell Ratio

The core-to-shell (CTS) ratio is a critical parameter, which helps to maximise the encapsulation efficiency (EE) of the core within the shell. Moreover, an optimal CTS ratio is conducive to the physico-mechanical stability of the shell, hence the whole microcapsule. Madene *et al.* [3] have reported that the stability of microcapsules *via* spray drying is influenced by the nature of the shell precursors, and the CTS ratio. Hogan *et al.* [230] have shown that the stability of microcapsules *via* spray drying was depleted at high CTS ratios. When dealing with CC, a high EE (~90%) of vanilla oil microcapsules with a Ch-GA shell was attained with a CTS weight ratio of 2:1 approximately [7]. Alternatively, Junyaprasert *et al.* [231] have reported the highest EE of vitamin-A-palmitate within a Gl-GA-based shell by CC at a CTS weight ratio of 1:2. Besides, the EE of peppermint oil microcapsules with a Gl-based shell by CC was much improved when the CTS weight ratio was increased from 1:2 to 4:1 [232]. However, it was also proven that both size and shell thickness of microcapsules depend on the CTS ratio [15]. For this reason, it is not possible to determine a generally valid CTS ratio, which is system-

specific, and should be determined experimentally based on the end-use applications of microcapsules.

2.5.3 Total Biopolymer Concentration

Total biopolymer concentration (c_{TOT}) represents the amount of biopolymeric materials potentially available as the shell precursor, which therefore influences the viscosity of the biopolymer-rich phase. Weinbreck *et al.* [150] have advised that extremely high c_{TOT} should be avoided since high viscosity may hinder well mixed conditions, possibly inducing the separation of oil-free coacervates. Therefore, c_{TOT} should strike the right balance to enable the separation of the phases appropriately during microencapsulation, which can lead to coacervates forming around oil droplets, hence microcapsules. Conditionally upon c_{TOT} and CTS ratio, thin/thick shell microcapsules may be fabricated, which has great influence on the microcapsule barrier properties towards a quicker/slower oil release. Orange oil microcapsules *via* CC were synthesised by Jun-xia *et al.* [9] at a c_{TOT} of 7.5% (w/v) with a high EE (~93%), which was different from that reported by Weinbreck *et al.* [233]. Surprisingly, the latter researchers evidenced that only ~5% oil was encapsulated at an optimal c_{TOT} of 0.5–1.0% (w/w). Yang *et al.* [7] encapsulated vanilla oil within Ch-GA shell, which resulted in an EE of 62.4% at a CTS ratio of 4:1. Alternatively, Huang et al. [171] suggested that the maximum CC yield for a SPI-Ch system may be independent of c_{TOT}. Overall, there appears to be controversial information on c_{TOT} and EE, which seems to suggest that an optimal c_{TOT} (only based on the amounts of polymers required for CC) might not directly result in a maximised EE.

2.5.4 Shell Ingredients

Microcapsules fabricated *via* CC consist of protein-polysaccharide pairs. Under given conditions, both biopolymers possess gel/film-inducing properties enabling them as suitable shell-forming materials. Proteins are large biomolecules which are built upon their structural sub-units (aminoacids). Owing to their amphipathic nature, proteins may also exhibit

emulsifying properties conducive to emulsion stability [234]. In contrast, polysaccharides comprise of long linear and/or branched chains of carbohydrates. A broad variety of collagen-rich materials have been used to obtain gelatine, such as porcine skin [15], bovine hide [235], and fish flesh [46]. Gelatine has long been paired with other polysaccharides including crustacean chitosan and gum Arabic to fabricate food and textile microcapsules [7, 169]. However, outstanding health & safety concerns against animal-sourced products have arisen worldwide, with emphasis on the potential transmission of the prion disease [9, 51]. Therefore, these shortcomings together with the recently enforced regulations on food products have shifted industrial markets towards new animal-free horizons. Importantly, non-animal products would be beneficial to more and more communities, including individuals with special dietary requirements (*e.g.* vegan and allergic/intolerant individuals), as well as overcoming religious beliefs. In this scenario, plant-based biopolymers with an industrial potential may thus play a vital role.

In this research, fungal Chitosan (fCh) and GA were therefore selected as the encapsulating ingredients. Preliminary studies by Mint *et al.* [236] have suggested that fCh have promising physico-chemical properties (*e.g.* degree of deacetylation (78%-86%) and molecular weight (50-190 kDa)), similar to animal chitosan [237]. To the best of the author's knowledge, there has been no published report on fCh as a potential encapsulating ingredient together with GA. GA carboxylates have not only proven excellent emulsifying properties but may also bind to the amines of fCh. For this reason, this novel, safe, and animal-free opportunity to form complexes using plant-based biopolymers should be extensively investigated [238].

2.5.5 Well Established Ingredients in Detergent Industry: a Need for Change

Melamine-formaldehyde microcapsules have been actively employed in textile/detergent industry [35] owing to their remarkable properties [6]. Notwithstanding, formaldehyde is linked to health & safety hazards due to its carcinogenic effects [36, 37], poor indoor air quality

[38], and negative environmental disadvantages once released although its residue in products is within the legal limit [39]. As a step towards complying with the enforced regulations against cancer-causing materials, new coating materials being polysulfone [40], polyurethanes-urea [5], poly(methyl-methacrylate) [31], and polyesters [41] have been recently attempted for textile applications. They provide several desirable features, such as thermal stability [42, 239, 240] and mechanical stability [40]. However, their poor biodegradability, high cost of processing [44], and suspected asthma-inducing effects [45, 241] make them industrially unappealing [43]. Therefore, there has been a growing interest towards safe, non-toxic, biocompatible, and environment-friendly biomaterials for microcapsules to fulfil the needs of modern fast-growing industries.

2.5.6 Suitable Biopolymers for Complex Coacervation

2.5.6.1 Gelatine

Gelatin (Gl) is a water-dissolvable protein obtainable by an incomplete hydrolysis of animal-based collagenous tissues such as skin, bones, and ligaments under specific processing conditions [187]. Specifically, the terms type-A and type-B connote swine-derived Gl and bovine bone/hide-based Gl, respectively [46]. After drying, Gl is whitish, and tasteless. It has played a primary role as a thickening agent for processed food, pharmaceuticals and cosmetics products [7, 195]. Other than mammalian sourced Gl, fish gelatine (fGl) has attracted more and more attention [242]. fGl can be derived from marine residues (*e.g.* fishbone, scales, and fins). Interestingly, fGl has proven many microencapsulation-friendly features, such as jellification, emulsification, foaming and film-forming properties [243]. Although fGl has partially overcome some pending safety concerns associated with mammalian derivatives, it is still ineffective to meet all people's dietary requirements globally. To date, no gelatine is vegan. Thus, its inclusion in products may be a drawback to vegans. Several seaweed- and vegetable-extracted ingredients including agar-agar, carrageenan, pectin, and cellulose gum have lately arisen [244], as potential replacement to Gl. As a further step to fulfilling worldwide demands,

the present research focuses on non-animal derivatives (*e.g.* fCh and GA) to use for encapsulating flavour/perfume oils by CC.

2.5.6.2 Gum Arabic

Owing to its desirable physico-chemical properties (*e.g.* superb emulsifying activity, high solubility, and moderate viscosity at high concentrations), Gum Arabic (GA) has gained attention in recent decades [245]. GA is naturally secreted as a gummy glue-like exudate from *Acacia Senegal* and other plants native to the *Leguminosas* family. Raw GA is then dried to use in foods, nutraceuticals, and pharmaceuticals. GA is a biopolysaccharide with excellent emulsifying properties, which has found broad applications in microencapsulation [245]. GA is a branched anionic arabinogalactan, which is arranged into different segments [53]. Specifically, its galactose, rhamnose, arabinose, and glucuronic acids provide important features for the encapsulation of hydrophobic ingredients [6]. Furthermore, the polypeptide backbone naturally occurring in GA contributes to providing good viscoelastic and film-creating properties [154], as well as potential antioxidant activity [246]. Zeta-potentiometry has proven that GA carries negative charges when dissolved from powder into aqueous environments at pH≥1.8~2.2 [154, 197], which corresponds to the $pK_{a,GA}$ of its carboxylates [60].

2.5.6.3 Chitosan

Chitosan (Ch) can be obtained by partial/complete alkaline [247] as well as enzymatic [248] deacetylation of chitin, which is largely available from the exoskeletons of arthropods *e.g.* crustaceans, molluscs, and insects [249]. Chitin is a fibrous material consisting of polysaccharide chains. After cellulose, it is the second mostly bioavailable polymeric material on earth [250]. Ch can be classified according to its degree of deacetylation (DDA). When dealing with Ch as a biomaterial for encapsulation, Ch with a DDA<70% is rarely employed

[250]. Several microencapsulation research teams have used Ch with DDA of 75-85% [169, 172], 79% [197], 90% [7], 92.2% [154], 93.3% [171], and 95.2% [251]. DDA greater than 95% may require complex and costly biological procedures [252]. Owing to its glucosamine segments rich in protonable amines ($–NH_2$), Ch has proven effective to electrostatically interact *via* CC with other polyelectrolytes carrying opposite charges [253]. Espinosa-Andrews *et al.* [154] have reported that the pK_a of Ch's amines is 6.3-7. Therefore, positive charges likely occur in slightly/highly acidic admixtures ($pH<pK_{a,Ch}$) [254]. Owing to its versatility, Ch has gained importance, over the years, in multiple industrial applications encompassing cosmetics, pharmaceuticals, nutraceuticals, and food [255, 256]. Although animal chitosan is still commercially valid, intense efforts have been made towards novel animal-free chitosan. Interestingly, the cell walls of filamentous fungi (e.g. *Aspergillus niger*) are chitin-based [257]. Thus, deacetylation can be performed *via* solid-state fermentation to achieve vegan Ch for industrial applications [236]. Fungal Ch (fCh) possesses a chemical structure with glucosamine and N-acetylglucosamines (Figure 2.11), which is similar to that of animal Ch. In addition, fCh is non-allergenic, non-GMO, gluten-free, non-toxic, and fully biodegradable. To the best of the author's knowledge, no microencapsulation work has been conducted with fCh. Therefore, fCh has been selected as the key ingredient of this project.

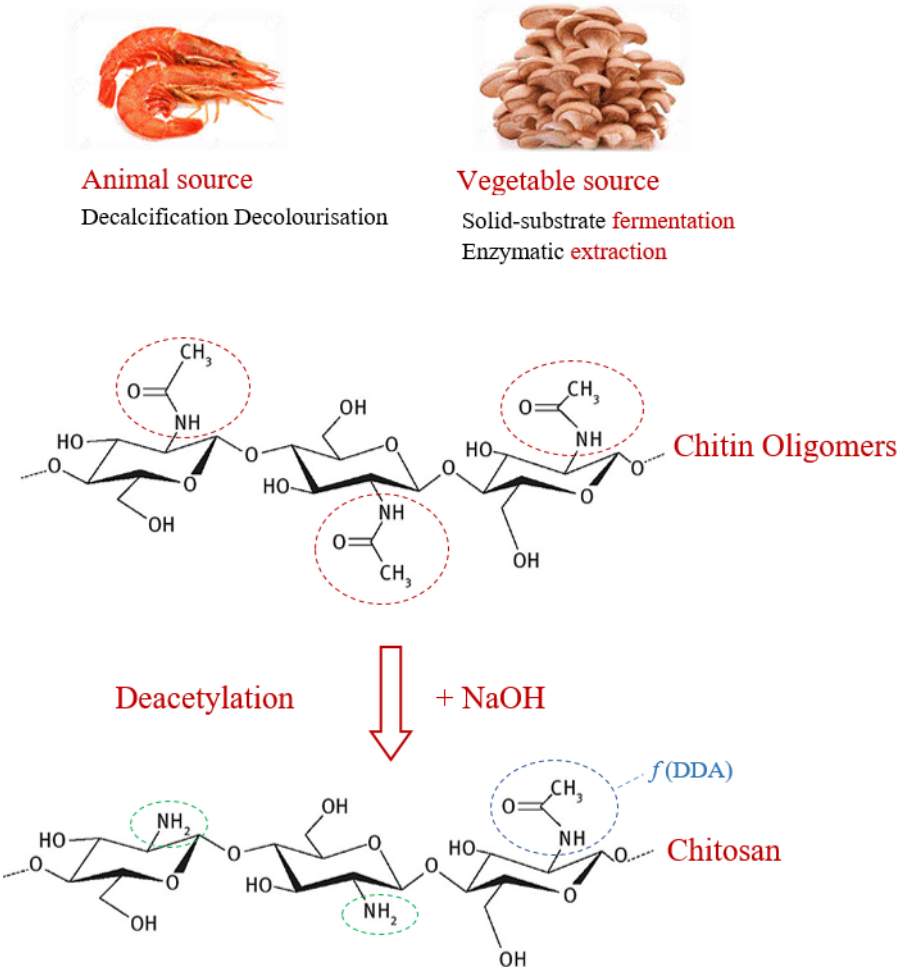

Figure 2.11– Deacetylation of animal/fungal chitin into chitosan *via* alkaline hydrolysis/enzymatic extraction and solid-state fermentation.

2.5.6.4 Maltodextrin

Maltodextrin (MD) is a polysaccharide consisting of carbohydrates combined into a chain. MD is a food-grade tasteless whitish powder, largely used in industry. Owing to its unique physico-chemical properties and high water dissolvability, MD is used as a food additive to enhance the texture of many edibles [258]. It can be obtained from many botanical starchy sources, such

as wheat, corn, potato, rice, and tapioca. MD is industrially produced by partial enzymatic/acidic hydrolysis of vegetable starch yielding small sugar molecules. Hydrolysis is followed by purification and spray drying to achieve a hygroscopic free-flowing powder [259]. MD comprises of D-glucose segments arranged into chains of variable length (between 3 and 17 glucose subunits), connected through α(1→4) glycosidic bonds. Therefore, MD is referred to in terms of dextrose equivalent (DE 3-20), which represents the degree of hydrolysis of the starch. High DE index indicates highly hydrolysed starches [260]. The greater the DE, the shorter the glucose chains, resulting in higher sweetness and solubility. Other than food industry, MD has proven effective in many other industrial fields, including textiles and plastics to enhance the stiffness of materials. In addition, MD has been used effectively in microencapsulation to enhance performance and quality of microcapsules [9, 63]. MD as well as sucrose has been employed in flavour microencapsulation *via* spray drying as a strengthening agent [6]. Specifically, such ingredients are successfully used as drying aids to facilitate drying, hence fabricating more robust microcapsules apt to resist the shear stress [261]. MD-assisted processes were proven effective to build up a secondary layer around coacervate shells. Interestingly, gelatine-gum Arabic microcapsules with a double shell made of maltodextrin were achieved by Yu *et al.* [63], which had proven a greater average rupture force (0.58±0.10 mN) than that of the primary microcapsules (1.73±0.27 mN).

2.5.7 Industrially Relevant Oils as Core Ingredients

Biopolymers (*e.g.* Gl, GA, Ch, SPI, etc.) exhibiting oppositely charges have extensively been employed to encapsulate fragrances *via* CC [7, 15]. Flavours and perfumes are typically oil-based, which form the core of microcapsules. Being hydrophobic and volatile, they are emulsified and then caught into polymeric shells, which prevents their degradation [262]. Generally, real perfumes are blends of ingredients. Since it is hard to quantify multiple ingredients, thus, a single-molecule fragrance oil was selected as the model active for this project.

2.5.7.1 Hexyl-Salicylate

Hexylsalicylate (HS) is a fragrance ingredient employed in decorative cosmetics, personal care products, and other toiletries, as well as household cleansing agents [238]. It has been estimated that roughly 10^6-10^7 kg/annum are globally used in industry [263]. HS is a single-molecule organic compound ($C_{13}H_{18}O_3$) belonging to the benzoic acid esters family (Figure 2.12A). HS was previously used with MF-microcapsules by Mercade-Prieto *et al.* [16]. HS is fairly inexpensive and can provide hazard-free floral scents, which is attractive at end-use applications [119]. HS is easy to handle due to its moderate volatility [264]. At ambient temperature it has a very low water solubility (~$6 \cdot 10^{-6}$ g·mL^{-1}) and specific density greater than water (~1.04 g·mL^{-1}) [16, 263]. Previous literature has evidenced that HS can be effectively encapsulated in a melamine-formaldehyde shell [18, 265, 266], hence has been herein utilised.

2.5.7.2 Carvone

Carvone is an EO belonging to the family of terpenoids. It is extracted from the seeds of spearmint and caraway [267]. Two enantiomers of carvone are known: L-carvone (LC) has a sweetish minty aroma (Figure 2.12B), whereas its mirror image, D-carvone, has a strong spicy smell [268]. Although both are employed in industry, LC is used in many sectors including not only food but also hygiene products, sunscreens, and depilatory formulations [269]. However, the LC's high volatility negatively affects the shelf-life of its resulting products. Thus, microencapsulation technologies have been exploited to prolong its shelf-life in products. However, mainly animal-based encapsulation solutions have arisen so far [15, 50, 232, 270]. Therefore, a novel food-grade animal-free microencapsulation system for LC has been attempted in this thesis.

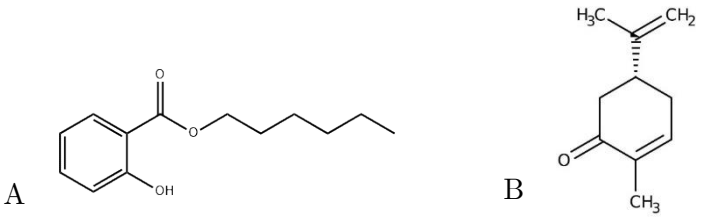

Figure 2.12– Chemical structure of hexylsalicylate (A) and L-carvone (B).

2.5.8 Cross-linking Agents

2.5.8.1 Industrially Relevant Cross-linking Agents

Freshly formed shells via CC are mobile, hence further processing is required to harden them [271]. Crosslinking (CL; also hardening/curing stage) enables the reticulation of the shell in order to achieve microcapsules with better structural and mechanical properties [272]. CL is performed using chemicals or enzymatic preparations [53]. Although chemicals such as formaldehyde can crosslink microcapsules for detergent effectively, there is a rising need for safer and consumer-friendly CL agents [238]. When dealing with food industry, stringent rules on the selection of the ingredients are imposed by the governments and the joint panel of Food and Agriculture Organisation (FAO) of the United Nations and the World Health Organisation (WHO) [273, 274]. Food control must assure: (*i*) safety (toxicological/microbiological hazards); (*ii*) nutrition (formulations with healthy nutritional profiles); (*iii*) quality (high-profile sensory and organoleptic properties); (*iv*) prolonged shelf-life of food products, especially those containing flavour microcapsules. To this end, CL is essential to prevent taste/aroma depletion. However, very few CL agents as food additives have been declared safe by the Food and Drug Administration (FDA).

2.5.8.1.1 Cross-linking Agents for Detergent Industry

As such, microcapsules fabricated *via* CC are mechanically weak due to the ionic nature of the electrostatic interaction which binds oppositely charged biopolymers [275]. Therefore, crosslinking is an important step to attain stronger shells [276]. Microcapsules used in detergent should be stable throughout the shelf life and the washing cycle, hence resisting challenging conditions, such as high shear stress and elevated temperatures (~65 ^{o}C) inside the washing machine and/or tumble dryer [6]. Such microcapsules have long been crosslinked using aldehydes, with particular attention to formaldehyde (HCHO) which has proven highly effective [26]. Although its residue in detergent products is within the legal limit, formaldehyde should best be avoided due to environmental and human health issues.

Alternatively, the biological acceptance of glutaraldehyde (GLT) is greater, which is used as a cold sterilising agent for heat-sensitive medical, surgical and dental equipment. Although large amounts may result in respiratory sensitisation, it is considered safer than formaldehyde [277]. GLT is a larger molecule than HCHO, hence its diffusion through the tissues is depleted [278]. As for formaldehyde, GLT reacts with proteins' free amines forming irreversible covalent bonds [279]. For this reason, GLT has been used in textile industry as a finishing agent for cotton fabric [280], and as a CL agent for microcapsules used in detergent [6]. Following crosslinking, microcapsules' shells are thus stronger against adverse conditions of pH/temperature [271]. In addition, GLT is unlikely to bioaccumulate in fatty tissues of aquatic organisms, resulting in more eco-friendly wastewater [281].

2.5.8.1.2 Cross-linking Agents for Food and Healthcare Industry

Although the GLT toxicity is dose-related, human exposure to GLT must never be direct [271], which precludes its employment in food products [282]. Therefore, endeavours have been undertaken by researchers to identify safe and cost-effective CL alternatives for food microencapsulation [169]. Among all, sodium tripolyphosphate (NaTPP) [283], glyceraldehyde [282], tannic acid (TA) [275], oxidised TA [279] and polyphenols [284],

genipin [285], transglutaminase enzyme (TG) [279, 286] have been used as CL agents. Specifically, TG is an enzyme naturally occurring in humans, animals and plants, which has been intensively adopted in food processing. TG promotes proteins to bind covalently. Thus, protein binding leads to the formation of intra- and intermolecular ε-(γ-glutamyl) lysine bonds [287]. Interestingly, TG has also been exploited as a CL agent. More specifically, Dong *et al.* [15] have proven TG effective to achieve thermal resistant microcapsules with reduced active leakage. In contrast, Grosso *et al.* [288] and [289] have reported that the barrier properties of TG-crosslinked microcapsules can be much worse when compared to GLT-crosslinked ones. To date, the above mentioned CL agents have been applied to Gl-GA systems, which are animal-sourced. In this research, TG has been applied to a non-animal system (fCh-GA) to encapsulate peppermint oil, for which no study in literature has been reported.

2.6 Characterisation of Microcapsules

The performance of microcapsules for a given application can be assessed *via* rigorous characterisation of their relevant properties. Many parameters should be then investigated to understand microcapsules' performance, with attention to size, sphericity, mechanical resistance, and shell permeability. Due to the commercial interest of many microcapsules, information on their characterisation is not available in the public domain. As an example, sensory analysis techniques used by companies for quantifying the effectiveness of an encapsulated fragrance are kept confidential. Therefore, the present section describes non-confidential techniques to characterise microcapsules.

2.6.1 Size and Size Distribution

Size and size distribution of emulsified droplets and then microcapsules are important. Several techniques are reported in literature, with emphasis on microscopy image analysis (MIA) [290],

size sieving [291], and static light scattering (SLS) or laser diffraction [17, 21]. MIA *via* bright-field or scanning electron microscopy (SEM) is helpful to investigate the morphology and surface topography of microcapsules. Although precise, this technique is time-consuming if a significant number of microcapsules are required to be measured. Similarly, sieving has been used for the separation and sizing of wet/dry particles; however, it is not suitable for emulsified droplets. In contrast, SLS is relatively fast for measuring the size and size distribution of droplets and microcapsules [292]. The majority of SLS devices are capable of measuring many thousands of droplets/microcapsules within a few seconds, covering a broad size range (20nm–2mm), with high resolution, reliability, and repeatability [293]. SLS has been utilised in research and industry to measure the size of droplets [294], hydrocolloids [126], and microcapsules fabricated with plant-based biopolymers [238] . The working principles are detailed in Chapter III.

2.6.2 Mechanical Strength of a Microcapsule Population

Several characterisation techniques to investigate the mechanical properties of a microcapsule population are reported in literature. Among all, three methodologies have drawn attention: (i) 'sandwich' compression of a given amount of microcapsule slurry between two plates [295] or onto a non-movable balance [296], (ii) shear breakage of a microcapsule slurry within a turbine reactor [297], and (iii) osmotic pressure shocks against a microcapsule population [298]. However, these techniques cannot provide any information on single microcapsules, which is a limitation to understanding their variations with a sample.

2.6.3 Mechanical Strength of Single Microstructures

Information on the mechanical properties of individual microcapsules is crucial. Over the years, several techniques for the mechanical characterisation of microstructures have arisen around the scientific community, such as strip and ring extensiometry for hydrogels [299], microinjection technique for biological cells [300], optical tweezers for human red blood cells and cell lipid membranes [301], microfluidic channels for artificial liquid-loaded capsules

[302], and microelectromechanical systems (MEMS) for investigating the biophysical properties of human breast cancer cells [303]. Notwithstanding, the above mentioned techniques are bespoke, which makes setups and calibration difficult. Another technique is micropipette aspiration, which was initially developed to quantify the elasticity of cells [304], and then adapted to measure the deformability of single microcapsules [305]. However, the drawback of micropipette aspiration is the stress concentration at the micropipette edges, which results in extra friction against the testing samples. Besides, texture analysers have validly emerged for compressing/stretching samples by operating a mobile piston [306]. Unfortunately, this technique can be applied only to microcapsules with a diameter between several hundred microns and a few millimetres [307]. The microcapsules fabricated for this research project are much smaller, hence different approaches were sought for.

2.6.3.1 Atomic Force Microscopy

Atomic Force Microscopy (AFM) is a scanning probe microscopy technique, where a colloidal probe/tip is capable of mapping the contours of the sample [266]. The colloidal probe was originally used to measure the adhesive force of self-isolated colloidal particles on a planar surface [308]. As a further development, particles with a large radius of curvature (*e.g.* glass spheres) were employed to compress smaller particles onto a flat surface [309]. This variant allows measurements of small and large deformations, in the size range of shell thickness and microcapsule, respectively. The tip is coupled with a cantilever and scanned over the surface of the testing sample, thereby generating a weak repulsive force between the testing sample and the tip [310]. The deformation of polyelectrolyte microcapsules under compression has been previously investigated by Lulevich *et al.* [311]. Similarly, the loading/unloading force applied to other types of microcapsules was studied *via* the deflection of cantilever [309]. Depending on the sensitivity of the cantilever and the nature of microcapsules, the forces resulting from the shell deformation can range from tens of pN to several tens of μN [312]. However, AFM is cumbersome, and time-consuming especially for highly deformable microcapsules [313]. Moreover, it is difficult to maintain the alignment between the AFM

colloid probe and spherical capsules following the initial contact point, thus the microcapsules can easily slip away [266].

2.6.3.2 Micromanipulation

Some limitations associated with the above mentioned techniques were overcome by a novel micromanipulation technique [314]. This technique was first attempted to characterise individual MF microcapsules. These microcapsules were successfully compressed between two small parallel surfaces (a flat-tip glass probe against a flat glass substrate). The thin glass probe was connected to a force transducer to record compression forces at given times. Time was converted into displacement basing on compression speed and transducer compliance [64]. Many types of microparticles/microcapsules have been tested over the years in order to characterise their mechanical properties, such as urea-formaldehyde [29] and coacervates [238], micro-beads [99], pollen grains [315], hydrogels [316], pharmaceutical powder excipients [317], and yeast cells [318]. Parallel compression *via* micromanipulation has proven effective for characterising microparticles mechanically owing to its high adaptability, system-versatility, and the wide range of applicable loads [101, 266]. When compared to AFM, micromanipulation covers a broader force range (100 nN-1.0 N). Micromanipulation allows displacements greater than the object of study (*e.g.* microparticle size) following compression between parallel plates at a pre-set speed [29, 265, 319]. Moreover, micromanipulation datasets can be processed by modelling to quantify the intrinsic material properties, such as elasticity modulus To this end, Hertz's [320] and finite element analysis (FEA) models [18, 66] were introduced for solid particles and core-shell microcapsules, respectively. The disadvantages associated with micromanipulation include slow testing process and incapability of measuring submicron particles.

2.6.3.3 Nanomanipulation

Since micromanipulation allows to measure microparticles no smaller than 1-2 μm [64, 314], a nanomanipulation technique was later developed by Liu *et al.* [321] for measuring the mechanical properties of single nanoparticles (~0.5-0.9 μm) *via* ultra-high vacuum SEM. Interestingly, the research team have validated this technique using benchmark microparticles between 1 and 3 μm. Negligible differences were observed from the comparison between micro- and nanomanipulation techniques. Thus, nanomanipulation has proven effective for characterising the mechanical properties of submicron particles.

2.6.4 Mechanical Strength of Microcapsules

Consistent performance of microcapsules is essential. Microcapsules are required with specific size and mechanical properties at end-use applications. It is important that microcapsules remain intact throughout manufacturing, processing, and storage; however, they should get ruptured to release their load on-demand [16]. Specifically, perfume microcapsules (PMCs) should resist through several steps (*i.e.* manufacturing, formulation with detergents/softeners, washing as well as tumble drying cycles) before they are deposited onto fabrics [35]. Later, PMCs should rupture by mechanical rubbing/caressing of dry fabrics for an improved customer experience. In order to achieve this goal, the size distribution of PMCs has to be narrow. Hu *et al.* [62] have evidenced that a narrow size distribution of MF PMCs led to a narrow rupture strength distribution. Thus, understanding the correlation between microcapsule size and their rupture strength is vital to formulate PMCs with the desired properties.

2.6.5 Elastic Properties of Microcapsules by Modelling

Several researchers have exploited the compression data related to the elastic deformation of microparticles/capsules to implement suitable mathematical models [66]. The most relevant models are presented.

2.6.5.1 Hertz Model

Hertz's elastic theory has been extensively utilised to investigate the elastic behaviour of solid particles. As reported by Dintwa *et al.* [322], the assumptions underlying the Hertz model are herein summarised, namely:

(i) The contacting surfaces are continuous and smooth (no friction effects included);

(ii) The material of the contacting bodies is isotropic and homogeneous;

(iii) The deformations are minute (infinitesimal strains with geometric non-linearity due to large deformations neglected);

(iv) The material is linearly elastic, which behaviour is described by Hooke's law;

(v) The radii of curvature of the contacting bodies are much larger than the contact radius (elastic half-space or semi-infinite sphere);

(vi) The dimension of the contacting surface is much lower than that of the bodies.

The apparent Young's modulus of a solid sphere is classically described by the following equation (Equation (2.2)) [323]:

$$E_H = \frac{F}{\alpha}(1-\nu^2)r^{-1/2}\left(\frac{\delta}{2}\right)^{-3/2} \quad (2.2)$$

where F is the compression force, $\alpha=4/3$ is the spherical shape coefficient, ν is the Poisson ratio (ν=0.5 for non-compressible polymeric rubber-like materials), r is the initial radius, δ is the compressive axial displacement. Previous literature has suggested that micromanipulation data of microparticles can be fitted to the Hertz model. Specifically, the elastic deformation of pollen [315], gelatine-based [324], and pharmaceutical microparticles [317] was investigated up to a nominal deformation of 10%. Accordingly, this assumption will apply to the microcapsules fabricated for this project.

2.6.5.2 Tatara Model

The Hertz model is restricted to minute nominal deformation (up to 10%), linear, and elastic deformations only. As a step forward to describe larger elastic deformation of particles, Tatara's model has arisen as an extension to the Hertz model [325]. This model has been demonstrated to show consistent fittings to the experimental compression data of elastomeric particles at deformations higher than 10% [326, 327]. However, complex numerical methods were required to solve the constitutive equations, which is the main disadvantage of the model.

2.6.5.3 Finite Element Analysis (FEA)

Over the years, efforts have been made to produce accurate information on the intrinsic material properties of microcapsules by processing the experimental micromanipulation data. The deformation of spherical gas-inflated membranes between two twin rigid plates was investigated by Feng and Yang [328], which was proven nonlinear elastic. It was described by Mooney-Rivlin's model for rubber-like materials. Subsequently, extra endeavours were undertaken by Lardner and Pujara [329] to adapt Feng-Yang's model to biological cells laden with non-compressible liquid. More recently, the least squares method was utilised to fit the experimental compression data of microparticles to specific constitutive equations [330]. A novel finite element analysis (FEA) approach to quantify the viscoelastic properties of alginate microspheres was used by Nguyen *et al.* [331]. FEA can takes into account geometric irregularities of the sample (*e.g.* non-sphericity), which was not possible before [17]. Later, a novel FEA method was developed by Mercadé-Prieto *et al.* [66] to characterise the elastic properties of core-shell microcapsules. This model was validated on MF PMCs [18], and their Young's modulus was evaluated. A similar approach has been used in this thesis.

2.6.6 Morphological Properties and Shell Thickness of Microcapsules

Efforts have been made by researchers to evaluate the intrinsic material properties of microcapsules *via* numerical simulations. As a step forward to better understand the structure of microcapsules, Mercadé-Prieto *et al.* (2011b) have developed a novel model to estimate not only the Young's modulus of microcapsules but also their shell thickness directly from the micromanipulation compression data. This model was validated using the conventional image-analysis techniques for the shell thickness, which are described as follows.

2.6.6.1 Optical Microscopy

Reported in literature, a technique to study the shell thickness of microcapsules is optical microscopy (OM). Yuan *et al.* [332] utilised OM to investigate urea-formaldehyde microcapsules. A rigorous procedure was followed to prepare the sample of microcapsules, which were embedded in a resin-based matrix, cured, and razor-sectioned prior to observation. Although the shell thickness imaging was successful, microcapsule shadowing and overlapping effects were inevitable. This noise leads to imprecise measurements since the edges of the shell may not focalise properly. Moreover, any shell thickness thinner than 1 μm cannot be measured.

2.6.6.2 Scanning Electron Microscopy (SEM)

Depending on the nature of microcapsules, the shell thickness can also be investigated by SEM imaging following cryogenic rupture. Interestingly, chitosan based microcapsules were frozen by liquid nitrogen, and ground in an agate pestle and mortar to mechanically cause structural damage [238]. Similarly, Zhang *et al.* [125] successfully characterised the shell thickness of urea-gelatine capsules by crushing them with liquid nitrogen prior to SEM imaging. At least ten different shell locations from each randomly selected capsule were measured for characterisation, hence their average was used. Although cryogenically driven shell investigation is the straightforward, expensive cryogenic equipment and commodities are required [333]. Moreover, the results achievable from this technique may not perfectly reflect the shell thickness of microcapsules due to the breakage effects, random slicing, and orientation of the object imaged by SEM.

2.6.6.3 Transmission Electron Microscopy (TEM)

A technique capable of accurately quantifying the shell thickness of cells/microcapsules at a nanoscale is TEM. Former literature suggested that microcapsules should be embedded into resin, trimmed, and ultra-cut prior to TEM observation [126]. Multiple essential steps are applied in TEM sample preparation, which makes the whole procedure costly and time-consuming. The resin brick can take five days to form. Subsequently, trimming, sectioning, and ultra-cutting is required. Artefacts due to random slicing during sample preparation cannot be excluded but can be corrected according to Mercadé-Prieto *et al.* [18]. The protocol for preparing a TEM sample is detailed in Chapter III.

2.6.7 Adhesion of Microcapsules

Over the last decades, there has been a growing need to deliver perfume molecules to solid surfaces, especially to fabrics. Since perfumes are typically costly and volatile, microencapsulation techniques are used to entrap perfumes within a shell, thereby minimising the amount of perfume required in formulation [6]. Perfume microcapsules (PMCs) in detergent should stay intact throughout the whole wash-and-dry process in order then to adhere to fabrics firmly. For this reason, understanding the adhesion properties between PMCs and fabric surfaces under different environmental conditions is fundamentally important.

2.6.7.1 Adhesion of PMCs to Solid Surfaces

In recent years, PMCs have gained more and more interest, which have been included in many detergent products [16]. Specifically, PMCs are designed to get caught onto fabrics during washing. Their deposition onto fabrics allows delightful scents to release for several weeks [238]. Thus, understanding the rationale behind the mechanisms of deposition (impregnation) and adhesion (retention) of PMCs onto fabric is crucial. Adhesion between two items relies on

their mutual molecular interaction [334]. Adhesion plays a key role in biological phenomena, such as cell-to-cell and cell-to-tissue interaction [335]. Similarly, PMC-to-fabric interaction is originated in liquid suspensions based on the nature of PMCs and the substrate of interest. For this reason, it is vital to understand the nature of the interaction to enhance the delivery of PMCs to fabrics. Although natural cotton-based and synthetic fabrics are popular in industry, they are coarse with ridges/wrinkles, hence may not be ideal for conducting adhesion tests. Therefore, a smooth model fibre substrate is essential to exclusively mimic the adhesion of PMCs in order to disregard any possible physical entrapment of PMCs due to steric effects. Interestingly, polyethylene terephthalate (PET) films are transparent, amorphous and isotropic, which makes them an ideal candidate to exclusively investigate the adhesion and retention properties of PMCs onto such PET films. Thus, they have been used along with HS PMCs fabricated for this research.

2.6.7.2 Principles of Contact and Adhesion: Modelling

Laundry PMCs should rupture on-demand at end-use applications. When depositing onto fabrics, PMCs burst to release their perfume when exposed to external forces, such as caressing and rubbing of fabrics themselves. Available theories and modelling describe the principles and mechanics of adhesive contact between particles and flat surfaces. Specifically:

(i) Bradley's rigid-body theory deals with Van-der-Waals forces in solid beads [336];

(ii) Hertz's purely elastic deformation model (no adhesion effect) was modified by Johnson-Kendall-Roberts (JKR) [337] to describe the effect of the adhesion on the elastic deformation of spherical particles adhering to a flat surface, with attention to the forces around the particle-surface area (Figure 2.13A);

(iii) Derjaguin-Muller-Toporov (DMT) theory focused on the adhesion forces of elastically deformable spheres onto elastic surfaces [338], with attention to the VdW forces outside the particle-surface contact area (Figure 2.13B);

(iv) Tabor [339] theory claimed that the pull-off adhesion force of a particle could be described by a parameter μ_T, which should return to Bradley rigid-body & DMT model at $\mu_T = 0$ (lower bound), and to JKR model at $\mu_T \rightarrow \infty$ (upper bound);

(v) Maugis proposed an advanced application to the model by Dugdale [340], in which plastic deformations of particles are considered as well (JKR and DMT only focused on elastic deformation).

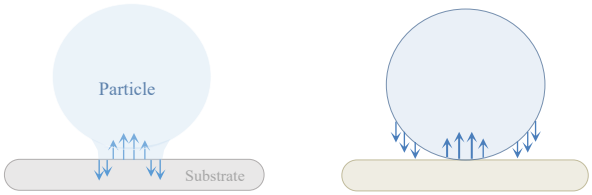

(A) (B)

Figure 2.13– Traction force distribution in JKR/DMT models. (A) JKR: adhesion surface traction forces (compressive/tensile) are confined within the particle-surface contact area; (B) DMT: adhesion surface traction forces are confined outside the particle-surface contact area.

2.6.7.3 Operative Method of Adhesion

Previous literature has proven that direct measurement of the adhesion properties between particles and solid surfaces is feasible. Therefore, investigation at a microscale can help to quantify the local adhesion force/energy between single microcapsules (*e.g.* PMCs) and a specific substrate (*e.g.* PET film). Several system-specific techniques, such as flow chamber, surface force apparatus (SFA), and atomic force microscopy (AFM) have arisen recently. Flow chamber devices are powerful platforms to investigate the adhesion properties of microcapsules onto a surface in a liquid environment under given hydrodynamic conditions. Parallel-plate flow chambers were employed to measure the adhesion of yeast cells [341], and particles onto different substrates [342]. Moreover, the degree of microcapsule removal (pull-off) from a solid substrate is conditional upon the system hydrodynamics and its flow velocity, hence the shear stress generated [28]. Particles/PMCs facing shear stress and torque may experience lifting, sliding, dragging, and rolling phenomena due to which adhesion is impaired. In addition, a flow chamber technique offers statistically significant data on a population of particles/PMCs within a reasonably brief timeframe.

2.7 Conclusions

Chapter II highlights the compositions and manufacturing methods of microcapsules which have been reported in literature, as well as their end-use in industry, such as in detergent and food products. Key encapsulation methodologies are detailed, with attention to the aspect of emulsification and processing. The main analytical techniques to characterise microcapsules are also introduced, with emphasis on their principles, merits, and drawbacks. Specifically, the micromanipulation technique has proven effective to determine the mechanical properties of particles based on parallel plate compression.

Nowadays, microcapsules used in detergent are being fabricated using formaldehyde-based ingredients. Similarly, food industry has long adopted gelatine-based microcapsules in edibles

and nutraceutical products, which are animal-sourced. Although these capsules can be produced effectively, the industrial market urges for hazard-free microcapsules relying on safe, naturally derived, and plant-based ingredients to meet both regulatory standards and consumers' needs. For this reason, plant-based ingredients with a potential for microencapsulation *via* coacervation are detailed.

To the best of author's knowledge, fungal chitosan-gum Arabic oil-entrapping microcapsules fabricated *via* complex coacervation have not been reported in literature, which is one important goal of this project. Moreover, in-depth understanding of the effect of formulation and processing conditions on the mechanical strength of plant-based microcapsules is completely lacking. Thus, mechanistic studies on plant-based microcapsules have been conducted in this research. Overall, such PMCs should release their actives on-demand following mechanical action, such as rubbing and crushing, thereby delivering the perfume for an improved consumer experience. Moreover, cost-effective fragrance delivery at end-use applications is also essential, especially in detergent industry. For this reason, adhesion/deposition mechanisms of PMCs onto fabrics have also been investigated.

Similarly, food microcapsules embedded in edible matrices should be ruptured upon chewing or crunching to release their flavour for an enhanced consumer experience. However, understanding towards the performance in relation to their relevant properties of microcapsules is still in its infancy. To this end, systematic characterisation of their mechanical properties is thus vital in order to achieve consumer-friendly microcapsules suitable for the intended use. Therefore, another goal of this work is to investigate the mechanical properties and intrinsic material properties of plant-based microcapsules, which has been accomplished using bespoke modelling.

2.7.1 Key Objectives of this Research

Overall, the key objectives of this research can be summarised as follows:

(i) Assessing the feasibility of driving complex coacervation on a novel plant-based biopolymeric (fCh-GA) system;

(ii) Developing a safe and robust microencapsulation process to fabricate core-shell microcapsules;

(iii) Investigating the feasibility of entrapping a model perfume oil (HS), and providing a comprehensive characterisation of the resulting microcapsules with a potential use in detergent, with emphasis on their morphological, structural, mechanical, and barrier/leakage properties;

(iv) Mimicking the adhesion of plant-based microcapsules with a core of perfume oil onto model fabrics in real washing by using a flow chamber technique, and processing data *via* ImageJ;

(v) Extending the novel microencapsulation process *via* coacervation to encapsulate food-grade peppermint oil (LC), and investigating the physical, mechanical and barrier properties of the resulting microcapsules with a potential application in food industry;

(vi) Utilising the Hertz model and FEA simulation results to: (a) quantify the intrinsic material property parameters (*e.g.* Young's modulus) of whole microcapsules and their shell materials respectively, (b) establish a relationship between the aforementioned two the Young's modulus values, (c) evaluate the shell thickness of microcapsules to be validated experimentally by TEM-imaging, and (d) determine the shell permeability of microcapsules in given liquid environments.

Chapter 3 Materials & Experimental Methods

3.1 Introduction

This chapter focuses on the materials, techniques, and experimental methods utilised in this research project. It is divided into three main sections. The first section deals with all materials and formulations developed for this work. Specifically, all the ingredients adopted for the development of coacervates and the encapsulation of model perfume and food oils (*i.e.* HS and LC, respectively) are herein detailed. The second section concerns the experimental methods and setups to identify the optimal conditions to form microcapsules *via* complex coacervation. This section particularly emphasises on the conditions adapted for the fabrication of microcapsules in suspension, as well as the further processing required to achieve microcapsules in their powdered form. The third section encompasses all analytical techniques used to characterise the physio-chemical, morphological, structural, surface topographical, barrier, mechanical properties of the resulting microcapsules conditionally upon their end-use applications. Therefore, particular emphasis is also laid upon the adhesion properties of perfume oil (HS) microcapsules onto solid surfaces (*e.g.* fabrics), whose analysis is not essential for food oil (LC) microcapsules.

3.2 Materials

The key materials employed in this project include the chemicals to synthesise and characterise the different types of microcapsules, and the model fabric films for the adhesion studies.

3.2.1 Perfume Microcapsules

Plant-based microcapsules with a core of perfume oil were synthesised *via* coacervation, and the experimental details are provided later. Gum Arabic (InstantGum Acacia AA) and fungal Chitosan, fCh, (molecular weight <190 kDa, degree of deacetylation (DDA) 80%, KiOsmetine-Cs®) were provided by Nexira Food (Rouen, France, EU) and Kitozyme S.A. (Herstal, Belgium, EU), respectively. All other analytical grade chemicals including hexylsalicylate (HS; specific gravity at 25ºC ~ 1.04 $g \cdot mL^{-1}$, CAS number: 6259-76-3), sorbitan triolate (SPAN85, CAS number:26266-58-0), triethanolamine (TEA; CAS number:121-44-8), 50% (w/w) aqueous glutaraldehyde (GLT; CAS number:111-30-8), 36% (w/v) fuming hydrochloric acid (HCl; CAS number:7647-01-0), and potassium bromide (KBr; CAS number: 7758-02-3), were purchased from Sigma-Aldrich (Dorset, UK), stored in agreement with the Safety Data Sheet (SDS) guidelines, and utilised without additional purification. All the solutions/suspensions were prepared employing demineralised water (MilliQ, 18.2 MΩ·cm at 25ºC). Liquid Nitrogen (ℓ-N_2) was generously donated by the Birmingham Centre for Energy Storage (BCES, Birmingham, UK).

3.2.2 Food-grade Microcapsules

In addition to fCh and GA mentioned above, vegan Activa® TI microbial Transglutaminase (TGase) as the crosslinking agent was obtained from ModernistPantry (ME, USA). Food-grade Kosher Tween®80 (Polysorbate80) as the emulsifier (0.1% w/w) was bought from Fluka, UK. All food-grade reagents including L-Carvone (LC; ρ_{LC}=0.96 $g \cdot mL^{-1}$) as the core ingredient, maltodextrin (MD; dextrose equivalent 16.5-19.5), glacial acetic acid ($\rho_{CH3COOH}$=1.05 $g \cdot mL^{-1}$), diluted hydrochloric acid (HCl; 5% w/w), absolute ethanol (EtOH), and sodium hydroxide were purchased from Sigma-Aldrich (Darmstadt, Germany, EU), stored as per Safety Data Sheets (SDS), and used without further purification. Nile red (NR) dye for fluorescence microscopy (purity ≥ 99%) was bought from Acros Organics (Geel, Belgium, EU). White

acrylic London Resin (LR) was obtained from Agar Scientific Ltd (Essex, UK). All the solutions were prepared using MilliQ water.

3.2.3 Adhesion Substrates

The Polyethylene Terephtalate (PET) films employed for investigating the adhesion properties of perfume microcapsules were obtained from Goodfellow Cambridge Limited (Huntingdon, England, UK). The selected PET film as a model was transparent, amorphous, and isotropic with a thickness of ~0.25 mm, which was cut into the required size (17±0.4 cm × 3.5±0.2 cm) and used without any surface modification.

3.3 Experimental Procedures to Fabricate Microcapsules

3.3.1 Dispensing and Dissolvability of fCh and GA

Chitosan is a weak base with glucosamine units along its backbone. It is non-soluble in water/organic solvents. However, it can turn soluble in acidic solutions at pH<5.5-6.0, which converts its glucosamine units into their extended soluble form [343]. Therefore, the pH of chitosan-based media is important. Gum Arabic is fully soluble in hot and cold water, yielding a viscous solution, independently of the pH. GA as well as fCh powders should be dispensed slowly into the required medium because aggregate grains are likely to form at the air-water (a-w) interface if added rapidly. Overall, dispensing conditions and dissolvability of biopolymers play a crucial role in the process.

3.3.2 Preparation of Stock Solutions

Aqueous fCh-based stock solutions (100 mL, 2.0 % w/w) were prepared by adding fCh (2g) into water under stirring (400 rpm) with a Rushton turbine (ϕ~38 mm) mounted on an overhead stirrer (IKA, Germany) at 400 rpm. Addition of aqueous HCl (0.1 N, ~3 drops) was followed to adjust the pH from 6.0 to 4.0 (pH probe in solution). Stirring was continued for 30 min to afford a slightly turbid dispersion. Aqueous GA stock solutions (100 mL, 1.0 % w/w) were prepared over 20 min by adding the GA (1g) into deionised water, with stirring as for fCh, to afford a clear solution (pH~6). Solutions were thermostated at 25±0.3°C using double-glazed jacketed reactors (250 mL) each equipped with 4 baffles and connected to a circulating water bath (Grant R-1, Grant Instruments, UK).

3.3.3 Preparation of Coacervate Beads

Oil-free coacervate beads (CBs) were synthesised as a proof of concept to investigate the feasibility of coacervation between fCh and GA. CBs were fabricated according to the following protocol developed for microencapsulation *via* CC (§3.3.4.3), provided that neither oil-in-water emulsification nor any surfactant required. Benchmark CBs were used to compare their structural and mechanical properties with those of fCh-GA microcapsules by CC.

3.3.4 Perfume Microcapsules *via* Coacervation

3.3.4.1 Dispensing

fCh (2.25 g) was added into water (130 mL) under stirring (400 rpm). Stirring was continued for 25 min, after which a turbid dispersion resulted. GA (15.0 g) was added under stirring (ω_{RD}=400 rpm), which was continued for 45 min. The resulting dispersion (RD) with a GA-to-fCh weight ratio of 6.7 was turbid, and acidified down to pH 1.95 (Figure 3.1– Step1) by

adding HCl_{aq} (36% w/v, (~0.6mL)). Acidification resulted in a reduction in turbidity leading to a clear solution. The solution was stirred (400 rpm) for 30 min, at which point a foam at the air-water interface was obvious. Stirring was stopped. Subsequently, ~0.4mL of 1-octanol (defoaming agent) was added to deplete the foam. The resulting solution (RS*) was left to rest for 15 min.

3.3.4.2 One-Step Emulsification

HS (40g) was added to the RS* (Figure 3.1– Step2) forming two phases. Sorbitan triolate (Span85, 0.8g) as the emulsifying agent was added *via* a 5-mL disposable syringe (Emerald, Becton Dickinson, Spain, EU) in order to achieve a kinetically stable oil-in-water (o/w) emulsion (Span85-to-oil weight ratio 0.02(g-Span85)·(g-oil)$^{-1}$). The mixture was homogenised ($\omega_{o/w}$=1000 rpm; 30 min) with an overhead stirrer (Microstar7.5, IKA, Germany, EU) equipped with a six-blade Rushton turbine (ϕ~38 mm) to generate an o/w emulsion (Figure 3.1– Step3) within a pilot plant cylindrical jacketed vessel (liquid Height (H)/Tank diameter (T) = 1; Clearance (C)/Impeller Diameter (D) ~3/4) with four baffles (baffle width (b)/Tank diameter ~0.1) and thermostated at 25±0.1°C (Model F33-HL, Julabo GmbH, Germany, EU). The size of the resulting emulsified droplets, which is directly related to the stirring rate [62, 224], was measured with a particle sizer (Mastersizer2000, Malvern, UK). Oil droplets with a volume-based mean size of ~30 μm were formed under stirring (1000 rpm). They were allowed to stabilise (30 min) to lower the interfacial tension and the resulting interfacial energy, hence increasing the stability of emulsion [344]. No variation in the droplet mean size (~30 μm) was detected by particle sizer after 30 min [345]. The stirring speed was progressively reduced to 0 rpm over 5 min. The o/w emulsified mixture was found to form a whitish froth at the air-water interface, due to pockets of air naturally entrapped into the liquid phase during emulsification. 1-octanol (~0.2 mL) as a defoaming agent was spread onto the air-water interface using the tip of a transfer pipette to reduce/eliminate the froth.

3.3.4.3 Fabrication of Microcapsules *via* Complex Coacervation

The emulsified RS* was transferred into a double-glazed jacketed 2L-reactor (equipped with 4 baffles and connected to a temperature-controlled water circulator thermostated at 25±0.3°C (Model F33-HL, Julabo GmbH, Germany, EU) containing water (600 mL) at pH 1.95, which had been pre-acidified *via* dropwise addition of HCl_{aq} (36% w/v). At this point, CC phenomena between fCh and GA were induced under stirring (ω_{CC}~400 rpm/1000 rpm) by addition of TEA_{aq} (2% w/w, 160 mL) using a motorised syringe pump (Harvard Apparatus, US) at a controlled flowrate (2mL·min^{-1}). The infusion TEA_{aq} was carried out slowly (80 min) because clusters of coarcevates would occur if the pH was increased rapidly. Therefore, the pH was increased gradually (Figure 3.1– Step4). The progression of CC (*i.e.* the formation of the walls *via* CC around the oil droplets) was monitored using an optical microscope (Leica DM500, USA) by taking out samples at every 0.1 pH-unit increase of the medium (probe-in-solution pH meter resolution of ±0.01, FP20, Mettler Toledo, UK)). The infusion of TEA_{aq} was stopped once the CC wall encircling each oil droplet had become visible by optical microscopy. The stirring rate was gradually reduced (300 rpm), which was then maintained for further 20 minutes. At this point, the resulting microcapsules were inspected again by optical microscopy to check for the successful formation of the shell around the oil droplets.

3.3.4.4 Microcapsule Shell Hardening: Cross-linking

GLT_{aq} (5.0 g) was added to allow the freshly formed microcapsules to crosslink for ~20 hours at 40±0.3ºC under continuous stirring (ω_{CL}=300 rpm) (Figure 3.1– Step5). GLU_{aq} can be used at 40-45ºC to crosslink the shell materials of the microcapsules obtained by CC [346]. This temperature range seemed to trigger a more irreversible polymer bonding, thereby promoting the hardening stage (crosslinking (CL)). However, GLU_{aq} seems to lose efficacy above 50°C from a thermal stability standpoint [347]). The whole microencapsulation process is displayed in Figure 3.1. Subsequently, the microcapsules were washed off thoroughly using deionised water on filter paper (mesh size 2 µm, Whatmann, diameter 80mm) and separated by vacuum drying (KNF Laboport N938, Germany, EU).

3.3 Experimental Procedures to Fabricate Microcapsules

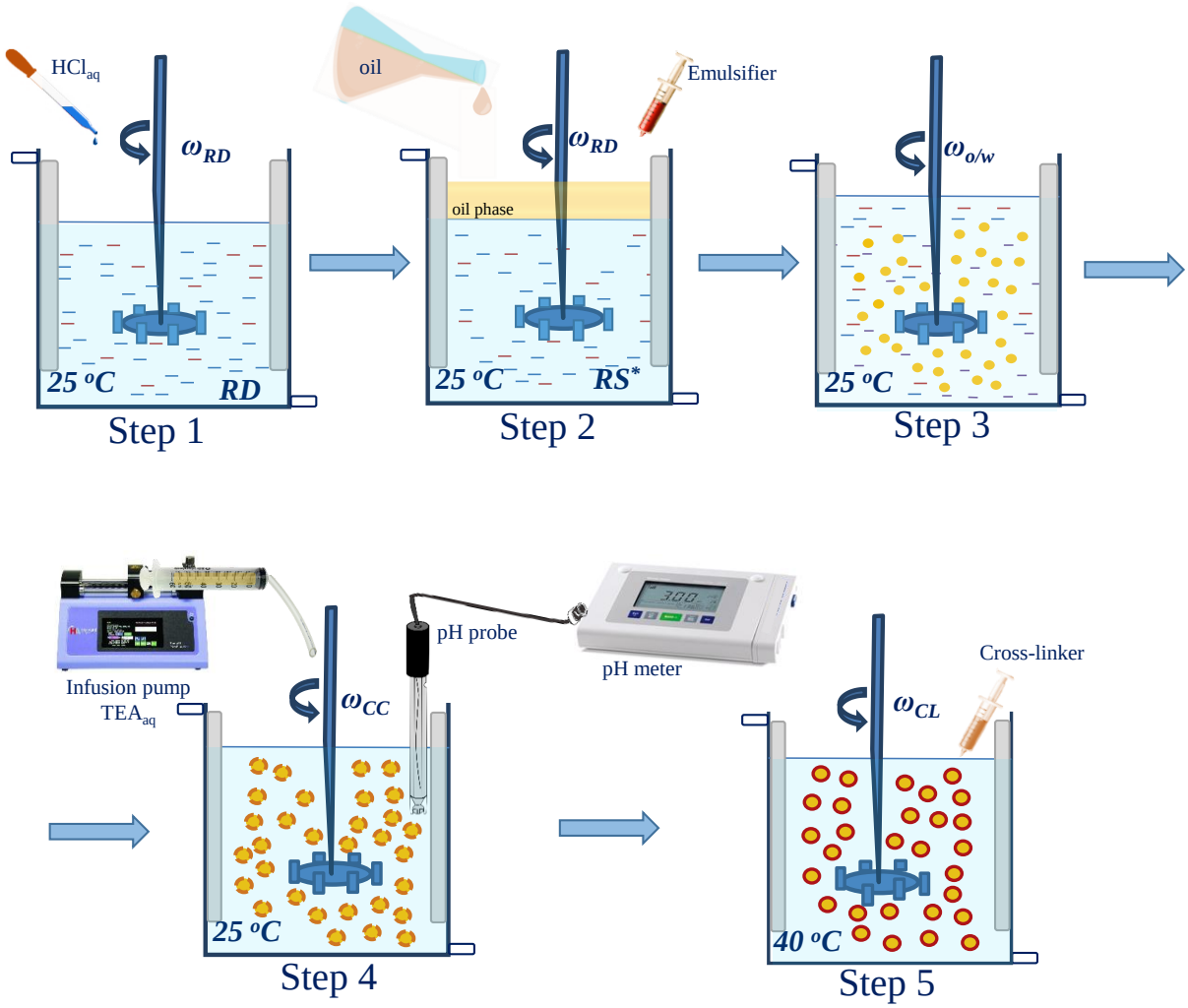

Figure 3.1– Schematic diagram of the encapsulation process of HS *via* CC within a fCh-GA based shell: biopolymeric dispersion (GA-to-fCh weight ratio of 6.7 and pH 1.95) (Step 1); gradual addition of HS with the emulsifier (Span85) (Step 2); emulsification step (1000 rpm; 30 min) to form o/w droplets (Step 3); gradual infusion TEA_{aq} 2%(w/w) into the emulsified RS* at 25±0.3°C to induce CC phenomena (Step 4); crosslinking *via* addition of GLT_{aq} at 40±0.3°C (Step 5). Top/Bottom rectangles (▭) represent the inlet/outlet of the jacketed reactor. Vertical grey bars represent the baffles. Red and blue dashes represent fCh and GA in solution, respectively (Step 1-2-3); yellow spheres represent the emulsified oil droplets (Step 3); dashed orange and solid red annuli represent the freshly formed and crosslinked shells, respectively (Step 4-5).

3.3.5 Food-Grade Microcapsules

3.3.5.1 Preparation of Biopolymer Solutions

All biopolymer solutions were prepared by dispensing fCh (0.5% w/w), GA (2.0% w/w), and MD (1.25% w/w) into an aqueous solution (720 mL) acidified to pH 2 by dropwise addition of HCl_{aq}. The solution was contained within a double-glazed jacketed 2ℓ-reactor equipped with four baffles and connected to a programmable temperature-controlled water circulator (Model F33-HL, Julabo GmbH, Germany, EU). The solution was homogenised (5000 rpm; 20 min) using a high shear mixer equipped with a 4-blade impeller (rotor) and a fine emulsor screen (stator; mesh ~800 μm) with a diameter of 25.4 and 28.2 mm, respectively (Model L4RT, Silverson, UK) (Figure 3.2A). Following homogenisation, the temperature of the solution increased (~50°C) due to energy dissipation, thus the solution was left to cool to the thermostated temperature (25±0.3 °C). Also, any supernatant froth formed following homogenisation was removed manually with a lab scoop.

3.3.5.2 Emulsification with Fluorescent Dye

A fluorescence sensing method may help to assess the effective entrapment of volatile substances (*e.g.* LC) within a shell. Nile red (~10mg) as the fluorescent dye was dissolved into LC (40g) *via* ultrasonication (Kerry KC3, Guyson Ltd, UK) for ~20 min which afforded a clear red solution. Polysorbate 80 as the emulsifier (0.8g) was added together with the NR-dyed LC into the 2ℓ-reactor containing the biopolymeric solution (720 mL), affording two phases (Figure 3.2B). Subsequently, homogenisation (8000 rpm, 30 min) was used to achieve oil-in-water (o/w) emulsified droplets of approximately 30 μm (Figure 3.2C) measured *via* laser diffraction (Mastersizer 2000, Malvern, UK) coupled with a continuously stirred (2000 rpm) sample dispersing unit (Hydro2000SM, Malvern, UK). Following the emulsification, a pink emulsion was obtained. The emulsified solution was left to cool to 25±0.3°C.

3.3.5.3 Two-Stage Microencapsulation

Complex coacervation was induced under stirring (350 rpm) using a Rushton turbine (ϕ~38 mm) fitted to an overhead stirrer (IKA Eurostar20, Germany, EU) by increasing the pH gradually up from 2.0 to 3.4 using an infusion pump loaded with $NaOH_{aq}$ (0.1M) at a flowrate of 0.06 ℓ/h (Figure 3.2D) with the pH monitored by a bench-top pH meter (FP20, Mettler Toledo, UK). Subsequently, coacervate layers were crosslinked enzymatically (Figure 3.2E), through the addition of TGase (80mg TGase/g·biopolymer) to catalyse the cross-linking between fCh-GA which forms the shells of microcapsules [348]. The temperature of the suspension of microcapsules was raised (40±0.3 ºC) to initiate the enzymatic cross-linking reaction [349] under stirring (350 rpm, ~15h). As reported by Shi *et al.* [350], both cross-linking and immobilisation activity of transglutaminase was found to enhanced at such temperature.

3.3.5.4 Free-Flowing Powders

The maltodextrin-rich suspension of LC-microcapsules was naturally cooled for 40 min, and fed (0.25 L/h) to a spray-dryer (Mini B290, Büchi, Switzerland) operating at 0.6 MPa (Stage Two; Step 6), with an inlet temperature of 160 ºC (Figure 3.2F). The outlet temperature was 70 ºC with an air feeder pump flowrate of 35 m^3/h. Suspended LC-microcapsules were sprayed into the cylindrical chamber through a 1.5-mm nozzle (atomiser), where they were dried. Free-flowing powders of microcapsules were collected from the bottom collector and stored within an airtight glass container until further analysis.

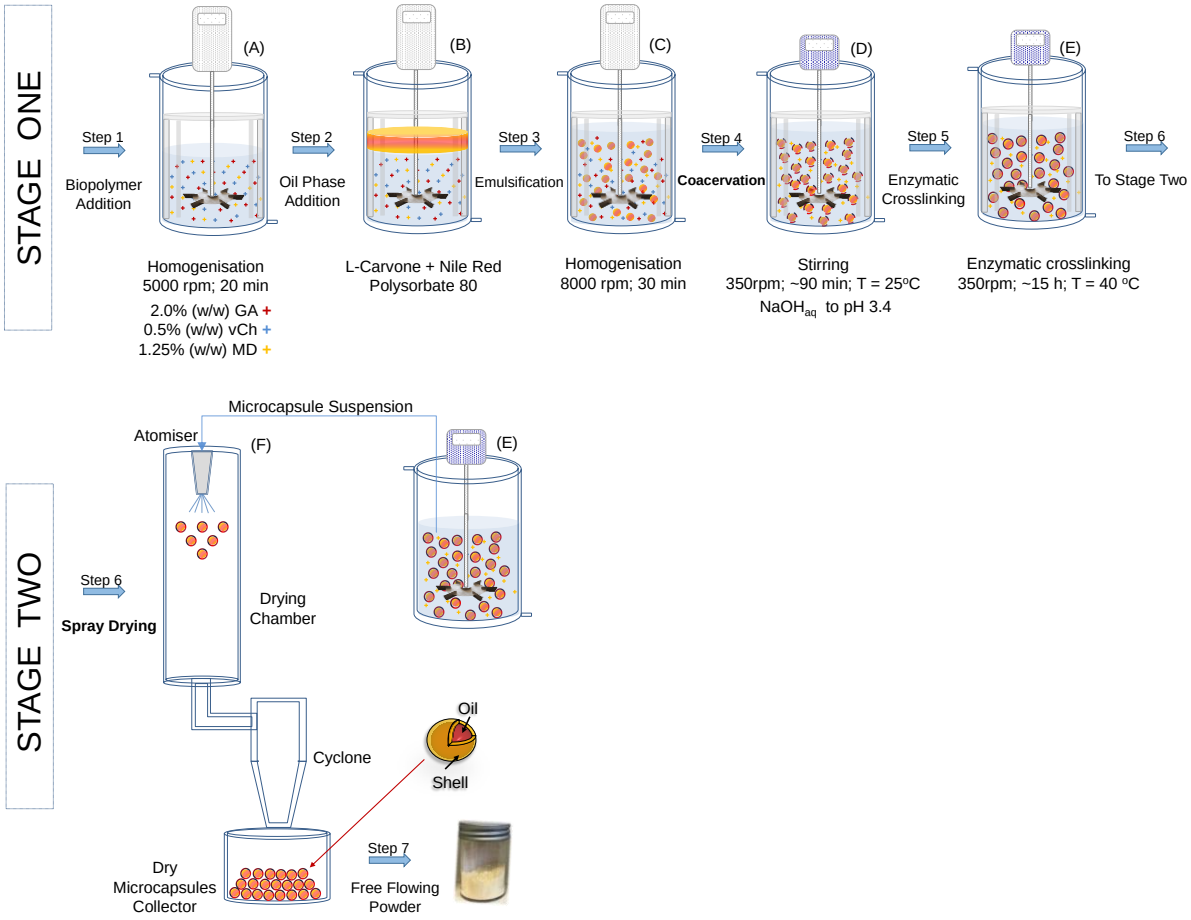

Figure 3.2– Schematic diagram of the two-stage encapsulation process of LC *via* complex coacervation (Stage One) followed by spray drying (Stage Two) within a fCh-GA based shell. Stage two enables to achieve free-flowing powders of microcapsules.

3.4 Characterisation Techniques

3.4.1 Laser Diffraction Particle Size Analyser (LDPSA)

Laser diffraction enables to determine the volume-weighted mean size and size distribution of emulsified droplets and suspended microcapsules. It relies on Mie theory, which deals with the angular intensity and absorption of laser light scattered by moving particles. Light scattering patterns are originated from the interaction between particles and a laser beam. Specifically, incident light can be refracted/diffracted or pass through without any interaction. Information on the particle nature is required, such as its refractive index. A Malvern Mastersizer LDPSA (M2000, Malvern Instruments Ltd., UK) is capable of detecting particles from 20 nm to 2mm, with high resolution and repeatability. It is equipped with a continuously stirred (2000rpm) sample dispersing unit (CSSDU) (Hydro2000SM, Malvern Instruments Ltd., UK) in which a microparticle suspension (~5 mL) is added to deionised water (~120 mL) inside the CSSDU. Once the measurement has started, the sample suspension is circulated throughout the system, where the light sensor detects the scattered light due to particles at a fixed wavelength (633 nm). The results are the average of five consecutive measurements, with two-minute intervals.

In this research, the instrument was aligned using an effective refractive index ($\widetilde{RI}$=1.482) resulting from the weighted average (Equation (3.1)) of the individual *RI* of GA (RI_{GA}~1.476) and fCh (RI_{fCh}~1.521). The refractive indices of oils (HS and LC) were 1.505 and 1.481, respectively. RI of water was 1.332. $D_{[3,2]}$ is the Sauter mean diameter (Equation (3.2)), whereas a size distribution is characterised by the SPAN value (Equation (3.3)) [31, 62]:

$$\widetilde{RI} = \beta \cdot RI_{Ch} + (1 - \beta) \cdot RI_{GA} \tag{3.1}$$

$$D_{[3,2]} = \frac{\sum_{i=1}^{N} d_i^3}{\sum_{i=1}^{N} d_i^2} \tag{3.2}$$

$$SPAN = \frac{d_{90\%} - d_{10\%}}{d_{50\%}} \tag{3.3}$$

where β represents the biopolymer weight fraction (fCh-to-GA); d_i represents the diameter of individual microcapsules, N refers to the total number of microcapsules being measured; $d_{10\%}$, $d_{50\%}$, $d_{90\%}$ are the diameter of particles when the cumulative volume fraction is caught at 10%, 50% and 90%, respectively.

3.4.2 Zeta-Potential

3.4.2.1 Principle

Particles dispersed in aqueous environments are surrounded by a double layer, which consists of an inner (Stern layer) and outer (diffuse-dynamic layer) region. The former is related to the presence of counterions firmly bound to the particle surface, whereas the latter has only loosely attached ions/counterions. A boundary layer (slipping plane) where ions, counterions, and particles are in pseudo-equilibrium also occurs within the diffuse-dynamic layer. Beyond the boundary layer, the ions are comfortable in the liquid bulk. The surface charge at this boundary is the zeta potential (ζ-P), which represents the charge difference between the double layer and the dispersant [351]. It is conditional upon the nature of particle and conditions of dispersant, such as ionic strength and pH. ζ-P is also referred to as the remote surface charge effect;

however, other techniques are required for measuring the actual surface charge. A schematic of ζ-P is depicted in Figure 3.3.

3.4.2.2 Operational Method

Zeta-potentiometry was employed to measure the net electrokinetic charge (NEC) of a polymer solution or the Zeta potential of a suspension of particles (NanoZS90, Malvern, UK) at ambient temperature. The equipment is capable of detecting the Zeta potential of particles ranging 4nm-0.1mm The equipment's software benefitting from Smoluchowsky's mathematical theory is enabled to convert electrophoresis-based measurements into NEC (soluble polymers) or ζ-values (colloidal dispersions) [352]. Specifically, the light beam travelling throughout each sample detects orientation and velocity of the electrically oriented polyelectrolyte dispersions when an electrostatic field is being applied.

3.4.2.3 Measurement

GA (1.0% w/w) and fCh (2.0% w/w) stock solutions were stored into two separate airtight vials covered with aluminium foil. Subsequently, ten aliquots (3.5 mL each) were prepared from each stock solution. The pH of each aliquot was manually adjusted *via* acidic/alkaline titration (0.1N HCl_{aq} and 0.1N $NaOH_{aq}$) to cover the pH range 1.0-8.0, which must include both pK_{afCh} and pK_{aGA}. When dealing with fCh, the pH values as measured by a pH meter were 1.12, 1.96, 2.78, 3.01, 4.02, 4.29, 4.67, 5.67, 6.50, and 7.98. The pH 6.50 aliquot was prepared to monitor the behaviour of NEC of fCh around its own pK_{afCh} (~6.0-6.5). In addition, the pH 3.01 aliquot was utilised 5 times, initially, as such, at pH 3.01, whose pH was then raised to 3.25, 3.42, 3.73, 3.92 by addition of NaOH to achieve four additional NEC measurements between pH 3-4, where Espinosa-Andrews *et al.* [197] had shown the highest NEC for Ch. As for fCh, the pH values for GA, as measured by a pH meter, were 1.10, 1.80, 2.05, 2.23, 3.10, 4.10, 5.14, 6.32,

7.03, and 7.95. The pH 1.80 and 2.23 aliquots were prepared to monitor the behaviour of the zeta potential of GA around its own pK_{aGA} (~1.8-2.2).

3.4.2.4 Dilution

0.5 mL from each aliquot was diluted into 4.5mL of HCl_{aq}/$NaOH_{aq}$ with the same pH as each aliquot. The folded capillary zeta measurement cell (plastic cuvette, capacity~0.8mL), DTS1070, Malvern, UK) was thoroughly rinsed three times with deionised water (18.2 MΩ·cm), prior to being inoculated with any fCh/GA aliquot to be measured.

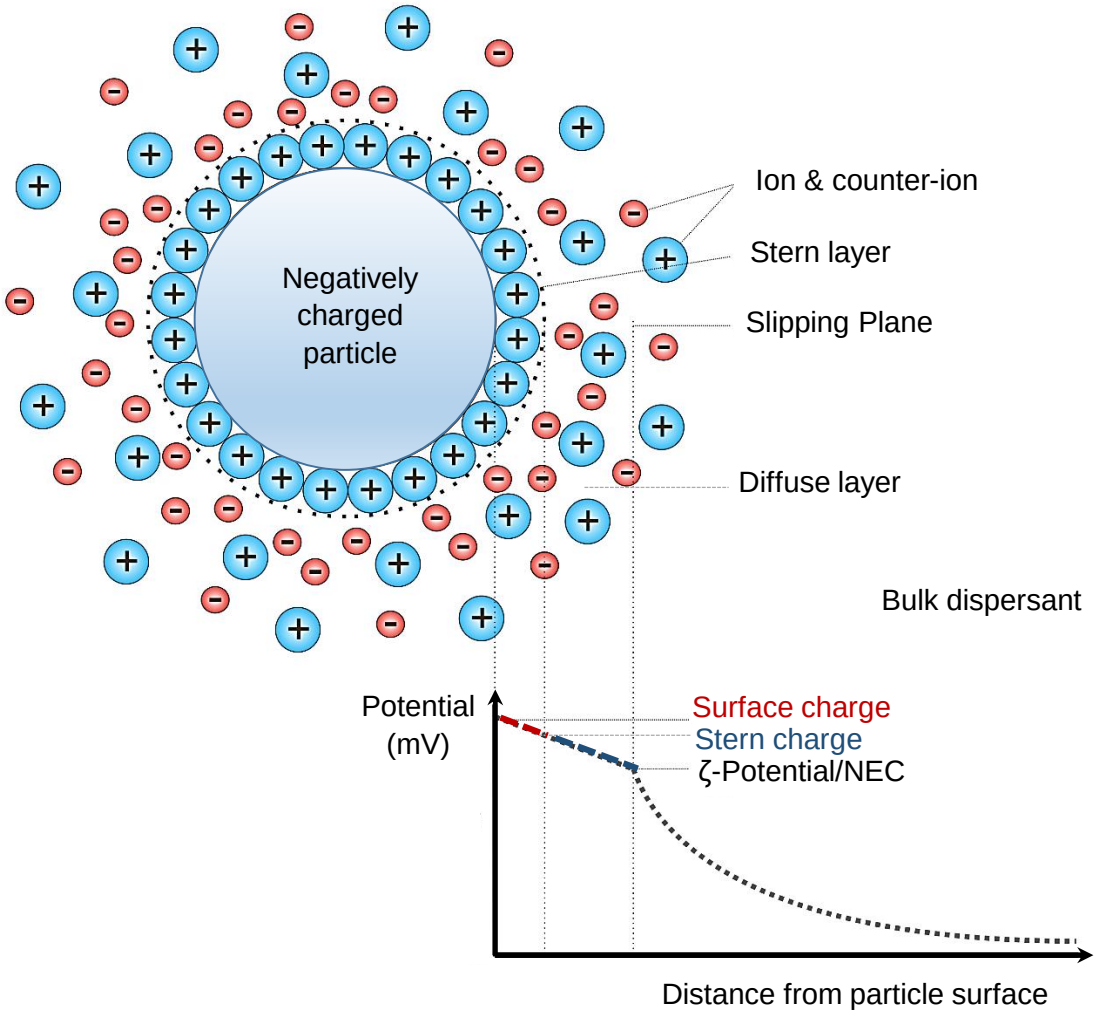

Figure 3.3– Schematics to elucidate the zeta potential and net electrokinetic charge (NEC).

3.4.3 Turbidity

The aliquots which had been previously prepared for the NEC/ζ-P analysis (1:10 dilution) were utilised for the turbidity measurements of fCh and GA to cover the same pH range (1.0-8.0). The turbidity of fCh and GA samples at different pH values was measured to investigate how the turbidity of fCh/GA dispersion occurs at different pHs. A benchtop turbidity meter (HI-93703, Hanna Instruments, UK) specially designed for maintaining the required wavelength

(peaking at 890 nm) and passing a beam of infrared (IR) light through 25-mm round glass vials was calibrated with the aid of three reference standards and employed to measure each aliquot. The 90°-scattered light was detected by a built-in light sensor, quantified by a microprocessor displaying the readings in Formazine Turbidity Units (FTU), which can be converted into mg $SiO_2 \cdot L^{-1}$ (FTU/ $mg \cdot L^{-1} \simeq 0.13$) or into ppm ($\rho_{sol} \simeq 1\ g \cdot mL^{-1}$). The data collected from the turbidity studies were then associated with that from the ζ-potential measurements, in order to investigate any potential interrelationship between turbidity and the electrostatic charge of the biopolymers at different pHs.

3.4.4 Ultraviolet-Visible (UV-Vis) Spectrophotometry

UV-Vis spectrophotometry is a well-established technique to investigate and quantify the presence of chemicals in solution, both organic and inorganic. Basic requirements of this technique include an appropriate wavelength range, a known optical geometry, a specimen holder, and a light detector. The technique relies on Lambert-Beer's law (Equation (3.4)), which focuses on the intensity of the transmittable light (i_τ) over the incident light (i_i):

$$Abs = -\log(T_\tau) = \mathcal{E}\, \ell\, \mathbb{C} \tag{3.4}$$

where *Abs* is the specimen's absorbance, $T_\tau = i_\tau / i_i$ is the transmittance, $\mathcal{E}$ [$cm^{-1}(mol/l)^{-1}$] is the molar absorptivity (extinction coefficient), which is constant for a given chemical at a fixed wavelength; ℓ [cm] is optical path (1 cm), and $\mathbb{C}$ [mol/l] is the concentration of the sample. Prior to any measurement, a standard calibration curve (*Abs* corresponding to known concentrations of the solute of interest) is needed. Therefore, the full UV-Vis pattern of the species of interest is scanned to identify the wavelength λ* [nm] at which the signal (Abs*) is

maximised. Absolute solvent (*i.e.* no solute) is utilised as the baseline (blank) to zero the instrument at λ*. In this project, ten reference samples with increasing concentrations of the solute of interest were prepared, hence their absorbance at λ* was measured. Abs *vs* concentration was plotted for both HS and LC (Figure 3.4A-B). A linear regression along with its coefficient of determination (R^2) was generated, whose slope is proportional to $\mathscr{E}$.

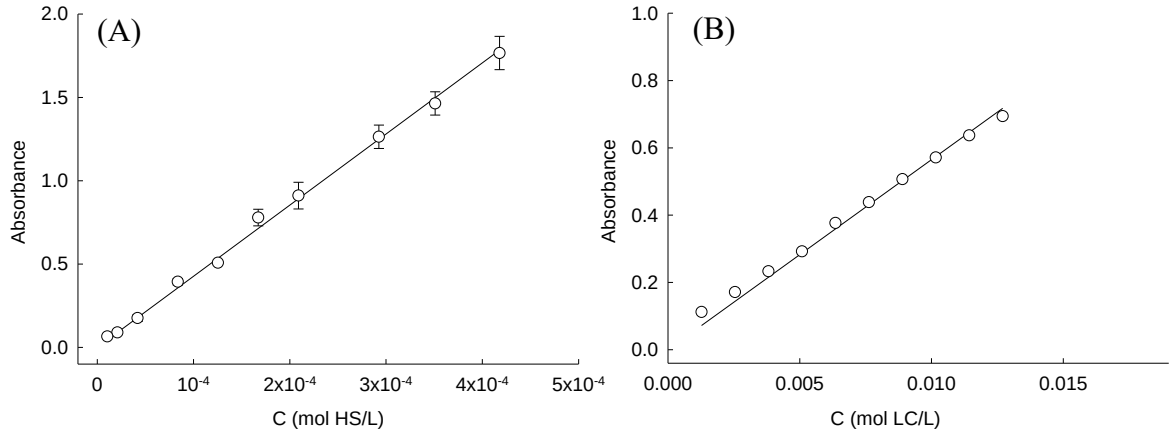

Figure 3.4– Standard calibration curves of HS and LC. Data points display the absorbance of the solute at λ* at its corresponding concentrations. Best linear fittings provided $\mathscr{E}_{HS}\simeq42981\pm284$ $(mol/l)^{-1}cm^{-1}$ and $\mathscr{E}_{LC}\simeq565\pm1$ $(mol/l)^{-1}$ cm^{-1} for HS (A) and LC (B), in 36% (w/w) 1-propanol and absolute ethanol, at λ^*_{HS}=306nm and λ^*_{LC}=320nm, respectively (Average ± St. Err); R^2>0.98. Error bars may be smaller than the size of symbols.

3.4.4.1 Encapsulation Efficiency and Payload

UV-Vis measurements were performed to evaluate both encapsulation efficiency (EE) and payload of microcapsules *via* a standard calibration curve. EE deals with the amount of active that has been successfully entrapped/absorbed into the shell, whereas the payload refers the

actual active content inside the microcapsule following separation from the medium. Three specimens (50 mg each) of HS spray-dried microcapsules were first loaded into three different screw capped bottles, and then dispersed into aqueous propanol (50 mL; 36% w/w) as the receptor medium according to Mercade-Prieto *et al.* [16]. The bottles were placed in an ultrasonic water bath (VWR Ultrasonicator, USC100TH, UK) for 30 min at ambient temperature to extract the core material (HS) from microcapsules. Following the ultrasonication, damaged microcapsules/shell residues occurring in the aqueous medium were separated out by centrifugation (1900 g-force, 5 min; Hermle Labortechnik Z-180, Labnet, Germany, EU) to afford a clear HS-containing supernatant. The absorbance of the supernatant was measured by a UV-Vis spectrophotometer (CE 2021, Cecil Instruments Ltd., UK) zeroed with aqueous propanol (36% (w/w) as the blank. UV-Vis measurements of HS were recorded at λ^*_{HS}=306 nm [16]. The supernatant was diluted in a quartz cuvette 10 times using the blank sample prior to measurement. Thus, the amount of HS was calculated using the relevant calibration curve (*i.e. Abs*(HS) *vs* 36%(w/w) aqueous propanol). As for HS microcapsules, the same procedure was followed for LC microcapsules using absolute ethanol (EtOH) as the receptor medium at λ^*_{LC}=320 nm. All measurements were performed in triplicate. Both $EE_{\%}$ (Equation (3.5)) and $Payload_{\%}$ (Equation (3.6)) were evaluated with the following formulae:

$$EE_{\%} = \frac{m_a}{m_{TL}} \cdot 100 = \frac{\frac{m_{core}}{m_{sample}}}{1 + \frac{m_{s,EN}}{m_{c,EN}}} \cdot 100 \tag{3.5}$$

$$Payload_{\%} = \frac{m_{core}}{m_{sample}} \cdot 100 \tag{3.6}$$

where m_{core} represents the mass of core material in microcapsules; m_{sample} is the mass of the sample; $m_{s,EN}$/ $m_{c,EN}$ is the weight ratio of the amount of shell to core materials used for encapsulation; m_a and m_{TL} are the actual and theoretical loadings, respectively.

3.4.4.2 Release Profile of Actives

Active release was investigated at ambient temperature by exposing microcapsules to different aqueous environments. When dealing with HS-microcapsules, absolute water and aqueous propanol (36%w/w) as an accelerated test were employed according to the solubility tests by Mercade-Prieto *et* al., (2012). Spray-dried microcapsules (2.5 mg) placed inside a dialysis tube (length~5 cm, internal diameter~14.3 mm, molecular weight cut-off (MWCO) 12-14 kDa, visking code DTV12000, Medicell Membranes Ltd, UK), which had been immersed into deionised water (60 ºC; 3 hours), and then thoroughly rinsed with deionised water (25 ºC) to remove the glycerol coating. The edges of each tube were folded twice, and secured by applying lab pegs at either end. Each tube containing HS-microcapsules was immersed in the selected receptor medium (50mL) being deionised water (DI-w) and 36% (w/w) aqueous propanol (aq-PropOH)) inside an airtight vial, and continuously stirred with a magnetic flea. Aliquots (3mL) were sampled every 10 minutes within the first hour; every 30 minutes within the second and third hour; every 60 minutes until the sixth hour. Afterwards, the release of HS was monitored on the daily basis within the first week, and then observed on the weekly basis until release plateaued. Following each withdrawn aliquot, the same volume (3mL) of fresh DI-w/aq-PropOH solution was promptly added to the appropriate receptor medium in order to assure the sink condition. UV-Vis spectra of each sample were recorded, with attention to the typical absorption band of HS at 306 nm. Each dataset was processed using the appropriate calibration curve obtained between HS and DI-w/aq-PropOH. Similarly, LC-microcapsules were exposed to several hydro-alcoholic environments (*i.e.* 0, 5, 10, 15, 20% $EtOH_{aq}$ w/w) as an accelerated test. As for HS, LC release was monitored at regular time intervals. Co-solvent concentrations were determined according to the solubility studies of LC in $EtOH_{aq}$ [353]. All experiments were carried out in triplicate.

3.4.4.3 Solubility Studies

HS/LC (0.25g) were added to $EtOH_{aq}$ (10mL) at several concentrations (0-100% w/w), and energetically shaken by hand at ambient temperature. The concentration of the dissolved oil in the hydro-propanolic/hydro-alcoholic solvent was obtained by the UV-Vis spectrophotometer at regular time intervals until no variation of the absorbance signal was detected. Such plateau was the solubility concentration of the oil (c_s) in the given solvent.

3.4.4.4 Optical Density of Emulsion

UV-Vis measurements were also performed to assess the kinetic stability (KS) of oil-in-water emulsion droplets (§2.3.1.2) *via* a turbidity method adapted from Song *et al.* [354]. Specifically, two wavelengths, namely λ^* and λ_{Ref} (λ_{Ref} = 650nm is a typical reference for turbidity and microbiological studies in wines and bacterial cultures [355]), were used to measure the increase in turbidity over time of fresh emulsions (*i.e.* HS, LC) with or without emulsifiers. Sorbitan oleate (Tween 20, 60, 65, 80, 85) and sorbitan esters (Span 20, 60, 65, 80, 85) and their combined matches (Span20-Tween20, Span60-Tween60, Span65-Tween65, Span80-Tween80, Span85-Tween85) with a total concentration of 0.05%(w/w) were added to each oil, and tested *via* UV-Vis in a quartz cuvette at ambient temperature. Subsequently, the absorbance values obtained from each oil-emulsifier combination were plotted as a function of time to investigate the KS of emulsions for microencapsulation. Since emulsified droplets naturally undergo coalescence and flocculation, it is crucial to understand how rapidly these phenomena may occur, which might hinder encapsulation. The KS of emulsions was evaluated from the resulting slope of the turbidity-time curve *via* linear regression. Accordingly, high slopes are associated with great absorbances, which are due to reduced scattered light caused by increased droplets size following coalescence. All measurements were performed at pH 2, which is suitable for the microencapsulation process by CC (§3.3.4). Overall, KS experiments were designed to identify: (i) the timeframe within which the stabilised emulsion droplets with

the desired size can stay stable for prior to inducing CC; and (ii) what surfactant could better stabilise the emulsion.

3.4.5 Scanning Electron Microscopy (SEM)

A Scanning Electron Microscope (SEM, JEOL 6060, USA) operating in dry mode and paired with an Electron Dispersive X-ray (EDX) spectroscopy detector (EDX-System, INCA-Oxford, High Wycombe, UK) was utilised to examine the morphology and surface topography of coacervate beads (CBs) and microcapsules. Spray-dried microcapsules/CBs (~0.1 mg) per sample were gently tapped onto a stainless steel stub fitted with a conductive two-side adhesive carbon tab as the substrate. Subsequently, the specimen was covered through gold sputtering (Polaron Sputter Coater SC7640 equipped with a valve-controlled argon cylinder, Quorum Technology Ltd, UK) to create an electrically conductive coating of gold onto the specimen (~8 nm). This inhibits charging effects at the specimen surface, and enables to exploit the high resolution features of a high-vacuum (10-270 Pa) SEM under accelerating voltages (15-30 kV). The thickness of the Au-coating was monitored by means of a thickness monitor coupled with a quartz crystal (QC) microbalance. Previous literature has suggested that melamine-formaldehyde microcapsules stay intact when exposed to an accelerating voltage of ~20kV within the first sixty seconds [356]. Therefore, any structural damage associated with fCh-GA microcapsules by CC due to SEM-exposure should be verified in this study. For this reason, no more than five SEM images were acquired for each microcapsules/CB. Moreover, the shell thickness of microcapsules was preliminarily evaluated by SEM imaging on them which had been frozen by liquid N_2, and ground in an agate pestle and mortar to mechanically cause their structural damage.

3.4.6 Transmission Electron Microscopy (TEM)

Transmission electron microscopy (TEM) was utilised to image the cross-sectional areas of microcapsules, thereby measuring their shell thickness. TEM specimen preparation consists of three main steps. Spray-dried microcapsules (dehydrated) were mixed with an equimolar

admixture of ethanol and hard-grade white acrylic resin (London Resin LR Ltd., UK) in a rotator at 5 rpm (Agar Scientific, UK). The specimen was left to set overnight in oven at 60° C to evaporate the supernatant (embedment). Subsequently, the polymerised specimen was sliced off (ultracutting) by a diamond knife ultramicrotome (UltracutE, Reichert-Jung, Austria) to achieve ultrathin sections (~100nm) [266, 357]. TEM micrographs of randomly selected ultrathin sections were acquired by JEM-2100 TEM (JEOL Ltd., Japan) at an accelerating voltage (200 kV). TEM artefacts during specimen preparation may occur. If any, thicker regions of ultrathin sections are shown darker than the thinner ones, since fewer electrons can pass through. Captured images were analysed *via* ImageJ (1.53c, National Institute of Health, USA). If the ultrathin cross-sectional areas (CSAs) are spherical, the resulting shell thickness (annulus) can be evaluated as follows (Equation (3.7)):

$$h = r_{out} - r_{in} = \left(A_{out}^{1/2} - A_{in}^{1/2}\right)\pi^{-1/2} \tag{3.7}$$

where r_{out} and r_{in} are the on-screen measured outer and inner radii of the annulus, and A_{out} and A_{in} are the outer and inner CSAs, respectively. However, CSAs of microcapsules *via* CC were often found to be elliptically shaped. Therefore, a variant to Equation (3.7) was introduced:

$$h = \left(A_{eq,out}^{1/2} - A_{eq,in}^{1/2}\right)\pi^{-1/2} = (a \cdot b)_{out}^{1/2}\pi^{-1/2} - (a \cdot b)_{in}^{1/2}\pi^{-1/2} \tag{3.8}$$

where $a_{in/out}$ and $b_{in/out}$ are the major and minor axis (inner and outer) of the elliptical ring, given that the area of an ellipse is $A_e = \pi ab$; for simplicity, A_e was considered equivalent to a circular area $A_e \sim A_{eq}$, when the ellipticity factor b/a is $0.75 \leq b/a \leq 1$. Ultrathin TEM sections were sliced off at random distance from the equatorial plane of the microcapsule, which affected both apparent radius and shell thickness. This shortcoming was overcome via applying

the model by Mercadé-Prieto *et al.* [18]. This correlates the apparent (on-screen) thickness of microcapsules' shells with the actual one using a correction factor of 0.86.

3.4.7 Fourier Transform Infrared Spectroscopy (FT-IR)

Fourier Transform Infrared Spectroscopy (FT-IR) spectra of all solid samples were obtained employing a FT-IR GX System (Perkin-Elmer, US) paired with an attenuated total reflection (ATR) sampling accessory (DuraSampleIR device, US). All spectra were given as an average of 200 scans from 4000 to 400 cm^{-1} (wavenumber) at a resolution of 4.0 cm^{-1}. Solid powders (7.5 mg) were gently mixed and contained within an IR-transparent anhydrous KBr (0.5 g) based matrix acting as a window material, and then compressed (force applied 80 kN for 2 min) into pellets using a semi-automatic rotary tablet press equipment with a pellet-forming die (LFA Tablet Presses, UK). The sample-to-KBr weight ratio equal to 0.015 was selected to prevent the formation of opaque pellets, which may undesirably result in little IR beam passing throughout the pellets, hence generating poor IR response.

3.4.8 Micromanipulation

A well-established micromanipulation technique based on parallel plate compression of single particles [25, 99, 266] was employed to determine the mechanical properties of microcapsules/CBs. The schematic of the micromanipulation rig is displayed in Figure 3.5. Specifically, one plate travels downwards towards another parallel plate at a constant speed (2 $\mu m \cdot s^{-1}$), whilst a voltage signal due to the ongoing compression is generated and filed.

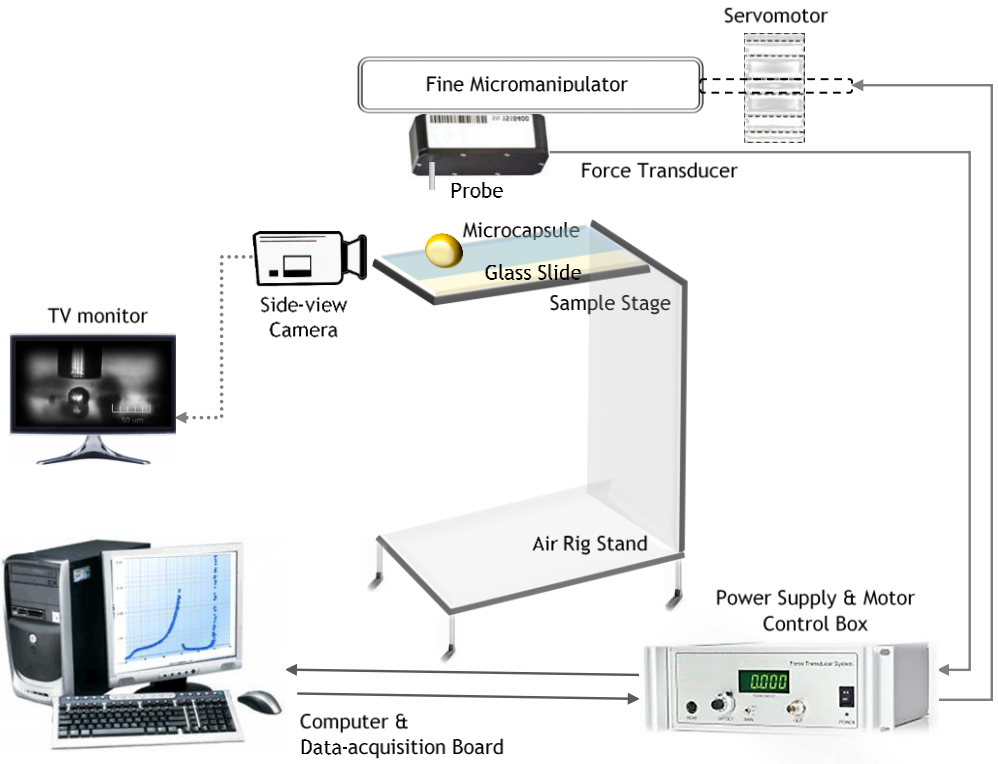

Figure 3.5– Schematic of the micromanipulation rig. Both computer screen and TV monitor depict what is being displayed during compression of a single microparticle/microcapsule.

3.4.8.1 Micromanipulation of Dry Microparticles

Two drops of microcapsule slurry were left drying naturally in air on a thin pre-cut glass slide (~2.5 cm^2) tightly secured on the sample stage (Figure 3.6A). The glass probe (original diameter~1 mm) with a tapered tip of ~70µm (total length~0.8 cm) was polished against a fine lapping film (1 µm) mounted on a high-speed rotary polisher (Model EG-40, Narishige, MicroInstruments Ltd., Long Hanborough, UK). Subsequently, the resulting probe was longitudinally glued (Loctite Cyanoacrylate Superglue, Henkel, Germany, EU) to the borosilicate output glass tube (outer diameter~1 mm, inner diameter~0.58 mm; Harvard

Apparatus Ltd, Kent, UK) of a selected force transducer. A force transducer (Model 400A, 403A, 405A with operating force scale of 50 mN, 5 mN, and 10mN respectively; Aurora Scientific Inc., Canada) coupled with an electrically driven control box was enabled to move downwards by a fine micromanipulator. The force transducer was attached to a three-dimensional micromanipulator controlled by a servomotor (Parker Compumotor, USA) responsible for both moving distance and speed. The system is capable of measuring forces with a superb resolution of ±0.1 μN and a probe displacement precision of ±0.2 μm. Former literature has evidenced that rupture force and displacement at rupture of MF-microcapsules were not influenced by the variation of compression speed between 1.0 and 6.0 $\mu m \cdot s^{-1}$ [99]. This finding suggested that the viscous effect of MF-microcapsules was not significant. Having said that, the descending speed for polymeric microcapsules is typically set to be 2 $\mu m \cdot s^{-1}$ to allow contact, and progressive rupture of a microcapsule [126]. Both position and focus of the side-view camera were adjusted to align the compressing probe with the testing microcapsule correctly. A self-isolated microcapsule was selected on the slide, and its size was preliminarily measured on-screen (LWD MPlan 40X/0.50 210; Ultramacro, UK) using a digital calliper (0-150mm, Draper Expert, Hampshire, UK). Further image analysis was performed on side-view images/videos of microcapsules to determine their size accurately prior to compression. Thirty microcapsules/CBs from each sample were randomly selected and compressed to generate statistically representative results. Micromanipulation experiments were carried out at ambient temperature. Data was recorded as voltage *versus* sampling time generated from the ongoing compression of microcapsules. The voltage signal was then converted into force through the sensitivity ($mN \cdot V^{-1}$) of the transducer. Sensitivity and compliance were calculated according to Zhang *et al.* [319] and [64]. Compliance of the system was run three times prior to each test, and their average was used to calculate the real displacement of the force probe. Data were processed using the novel Micro-particle Strength Analysis software (μCAP, version 2.0.3, Micromanipulation and Microencapsulation Group, School of Chemical Engineering, University of Birmingham, 2020) developed in our group by Mr Zhihua Zhang.

When dry micromanipulation is operated, the external temperature is not controlled. Ambient temperature may be a source of error, as well as the seasonal relative humidity which can be absorbed by the microcapsules, thereby affecting their mechanical property. Another potential

source of error may be associated with the number/selection of microcapsules, and what side of their shell is exposed for compression.

3.4.8.2 Micromanipulation of Wet Microparticles

Three drops of suspended microcapsules at the required pH were transferred into a sample chamber (L x w x h = 14.90 x 4.05 x 6.90 mm; thickness of quartz glass = 1.0 mm; Comar Optics Ltd, UK), which was secured with blue tack (BostikGlobal, France, EU) onto the sample stage beneath a flat-end glass probe (Figure 3.6B). As for micromanipulation of dry microparticles, the glass probe was connected to the selected transducer, and enabled to move downwards towards the air-water interface of the liquid suspension (meniscus). Once the probe had entered the liquid, it appeared blurred on the monitor due to the refractive index of water. Thus, the focus of the side-view camera onto the probe was adjusted carefully. The probe was slowly driven towards the bottom of the sample chamber, where the microcapsules/CBs were expected to settle down. Importantly, only microcapsules with a specific gravity higher than that of water could be tested. The compression procedure and data processing were similar to what described earlier.

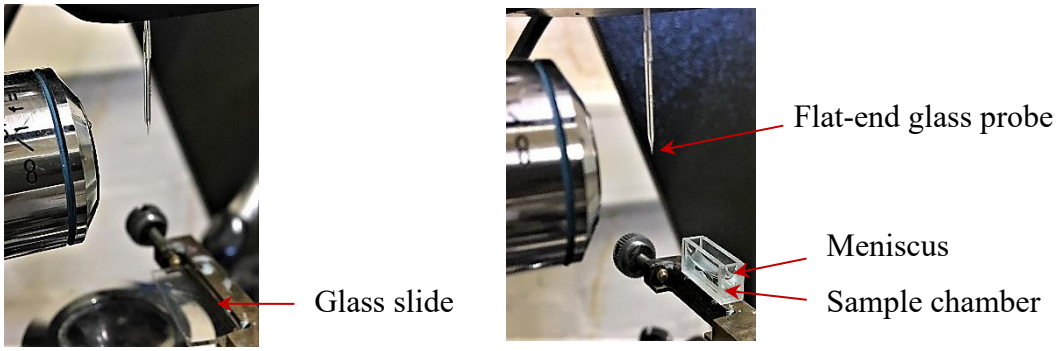

Figure 3.6– Dry (A) and wet (B) configuration of the micromanipulation rig.

3.4.8.3 Statistically Representative Number of Microcapsules

Thirty microcapsules from a given sample are typically compressed. Previous studies conducted by the undersigned author of this thesis on other reference samples, including gelatine, xanthan gum, and methycellulose microcapsules, showed no significant difference in the average values of mechanical property parameters obtained between 30 and 60 tested microcapsules [126]. As expected, the standard errors were lower when the number of measured capsules was doubled.

Table 3.1 –Mean values of the mechanical property parameters based on 30 and 60 microcapsules from reference batches (gelatine, methylcellulose, and xanthan gum). The values are expressed as Mean ± St.Err. Δϵ (%) represents the percentage difference of mechanical property parameters between 30 and 60 microcapsules [126].

	Number of capsules compressed	**Diameter**	**Displacement At rupture**	**Rupture Force**	**Deformation at rupture**	**Nominal Rupture Stress**
	(#)	(μm)	(μm)	(mN)	(%)	(MPa)
Gelatine	30	45.4±2.2	17.2±1.6	3.07±0.26	37.3±2.7	1.92±0.14
	60	44.7±1.4	16.3±1.0	2.98±0.17	36.2±1.8	1.97±0.11
	Δϵ (%)	1.6	4.9	2.9	2.9	2.5
Methyl cellulose	30	39.7±2.0	19.1±1.6	3.07±0.23	48.2±3.3	2.66±0.19
	60	40.0±1.2	19.6±1.0	3.11±0.16	48.5±2.1	2.58±0.13
	Δϵ (%)	0.9	2.4	1.5	0.7	3.1
Xanthan Gum	30	49.7±1.5	18.3±1.2	3.20±0.17	37.2±2.5	1.77±0.14
	60	50.4±1.1	17.0±0.9	3.23±0.14	33.6±1.6	1.71±0.09
	Δϵ (%)	1.5	7.0	0.9	9.5	3.5

3.4.8.4 Calibration of Force Transducers

3.4.8.4.1 Sensitivity

The applied load and the recorded voltage output are conditional upon the sensitivity of the selected transducer, for which appropriate calibration is required. As an example, 403A is a model of force transducer that can measure up to 0.5g-force. Its calibration is conducted applying minute paper flaps (~0.5 cm^2) with increasing weights (5mg-0.5±0.0001g; Sartorius Secura, Model 124-1S, Germany, EU). Therefore, the heavier the weight, the larger the voltage output. Ten different measurements were carried out. The gravitational forces (mN) are calculated ($g \simeq 9.81\ m \cdot s^{-2}$), which are plotted with the corresponding voltage (V). A linear regression model is applied, whose slope provides the sensitivity κ_S ($mN \cdot V^{-1}$) of the force transducer.

3.4.8.4.2 Compliance

It is important to identify correctly the effective distance travelled by the probe downwards through the microparticle. Accordingly, the distance travelled in air (before contacting the microparticle) should be discarded. Compliance ($\mathbb{C}_k$) is obtained by compressing the flat-end probe against an empty, hard, smooth, and fully flat surface on the glass slide or at the bottom of the sample chamber. The procedure is repeated three times. A typical compliance curve (voltage *versus* sampling points) is displayed in Figure 3.7 .

The segments A-B and B-C correspond to the probe before and after contacting the hard surface, respectively. The slope B-C ($\widetilde{m}_{B\text{-}C}$ average of five measurements) is inversely proportional to $\mathbb{C}_k$:

$$\mathbb{C}_k = \frac{v_{tr} t_a}{\kappa_S \widetilde{m_{BC}}} \tag{3.9}$$

where v_{tr} is the compression speed (2.0 μm·s^{-1}) and t_a is the acquisition time (0.3s).

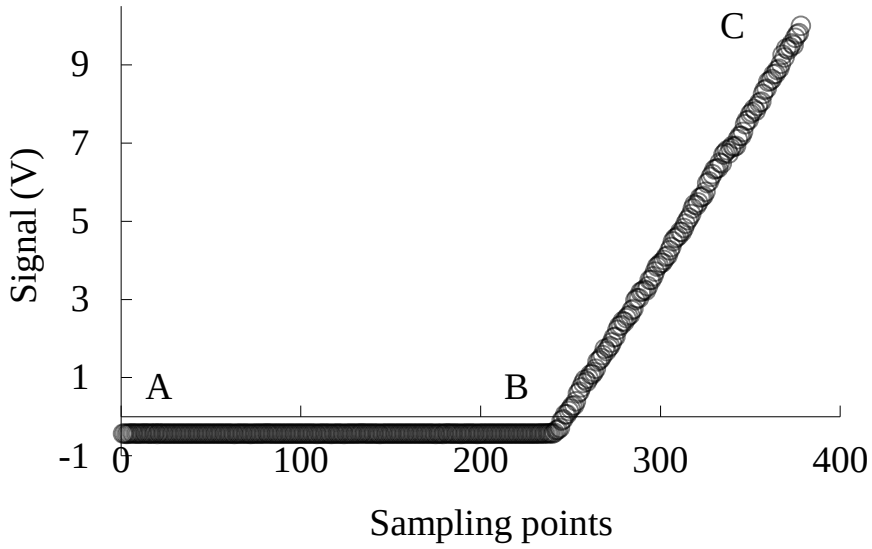

Figure 3.7– Typical compliance curve (voltage *versus* sampling points).

3.4.8.5 Preparation of Compression Probe Tips

Borosilicate glass tubes with an initial diameter of 1.0 mm were used to produce compression probes. They were coil heated and stretched away using a glass puller (MicroForge, MF900, Japan). During compression, microcapsules may deform to a diameter around three-fold larger than their initial one. Therefore, the size of the glass probe needs to be at least three-fold larger than that of microcapsules. Freshly pulled glass probes were fitted onto a high-speed rotary

polisher to grind the tip to the desired size, which was monitored by optical microscopy prior to being glued to the force transducer.

3.4.8.6 Approach to Image Analysis

During micromanipulation, the size of a self-isolated microcapsule can be measured using a digital calliper on-screen, which has been calibrated with an eyepiece graticule. However, image analysis (IA) can provide this information more accurately *via* an on-screen tool specially designed for micromanipulation in our group. Good lighting for a clear and sharp side-view image of the microcapsule is crucial. IA first requires to draw a segment along the probe end from left to right at different travelling heights (baseline) for measuring its compliance (Figure 3.8A). The baselined probe is divided into vertical 'slices' to convert pixels into microns (Figure 3.8B). Subsequently, the boundaries of a microparticle are drawn freehand into a circular outline (Figure 3.8C). For a spherical microcapsule, the circular outline is obtained by clicking three points around its edges; for irregular microcapsules, the outline is drawn along their deformities; for ellipsoidal microcapsules (often obtained by CC), two line segments, namely a (major axis) and b (minor axis), are drawn ($a \neq b$) across the microcapsule.

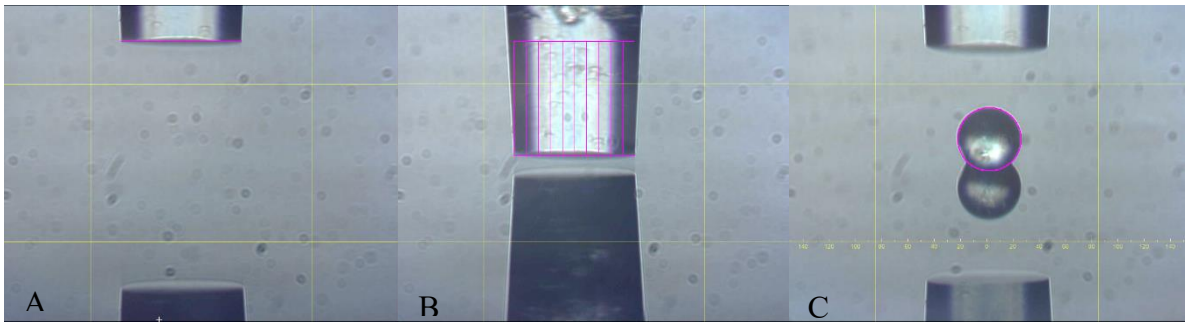

Figure 3.8– Main steps of image analysis of microcapsules for micromanipulation: probe for measuring its compliance (A); baselined probe for converting pixels into microns (B); microcapsule outline drawn (C).

3.4.9 Flow Chamber Technique

3.4.9.1 Methodology

A rectangular-shaped flow chamber consists of two parallel plates. Inlet/Outlet and inner passageways enable fluids to enter/exit and flow through the chamber, respectively. The wall shear stress (τ_w) represents the force per unit area exerted by a solid boundary (wall) against a fluid moving in a longitudinal direction to the wall. For a rectangular-shaped flow chamber:

$$\tau_w = \frac{\mu \cdot v_v}{\chi \cdot \delta \cdot h^2} \tag{3.10}$$

where μ [kg·m^{-1}s^{-1}] is the dynamic viscosity of the fluid, v_v is the flow rate set on the syringe pump [m^3·s^{-1}], χ = 1/6 is the shape factor, δ [m] and h [m] are the inner width and height of the flow chamber, respectively [341, 358]. As reported in literature, the flow is expected to be laminar. The flow regime can be determined *via* Reynolds number (laminar regime: Re<2.1·10^3) for non-circular ducts:

$$Re = \frac{\rho_w}{\mu} \frac{v_v}{\delta \cdot h} D_h \tag{3.11}$$

where ρ_w [kg·m^{-3}] is the density of the fluid, and D_h is the hydraulic diameter [m]:

$$D_h = \frac{2}{\frac{1}{\delta} + \frac{1}{h}} \tag{3.12}$$

which is derived as the ratio of cross-sectional area to the wetted perimeter of the duct.

3.4.9.2 Assembly of a Flow Chamber System

The flow chamber utilised in this study was based on a previous report by Lane *et al.* [358]. Its design consisted of two parallel-fitting metal plates (top and bottom plate), which had been manufactured with precipitation-hardened 6061-aluminium alloy (Poynting Physics Workshop, University of Birmingham, UK). A chamber window was built on each plate at the same position. Each window was fitted with pre-cut tempered glass (7.2±0.1cm × 2.1±0.1cm; thickness~0.2cm), applying cyanoacrylate glass glue (Loctite SuperBonder, Henkel Loctite, USA) to each edge. Silicon O-rings (BS044/046, Polymax, Bordon, UK) were mounted inside to seal the chamber. As detailed by Lane *et al.* [358], the flow chamber had length and width of 10.5 cm and 1.7 cm, respectively, and a flow height of 0.25-0.35 mm. A fully flat, transparent, smooth, and amorphous PET film (thickness 0.25 mm; Goodfellow Cambridge Limited, Huntingdon, England, UK) was selected as the model fabric. The PET film was cut out into the required rectangular shape (17±0.4cm × 3.5±0.2cm) in order to fit in between the top and bottom plates of the chamber, thereby covering the inner passageways completely. The plates were secured onto each other using ten stainless steel screws (cordless electric screwdriver, AS6NG, Black&Decker, USA) to assure a liquid-tight assembly. Inlet/Outlet soft silicone tubing (inner ⌀~3 mm) was fitted with one-/three-way stopcocks as well as female/male lock-ring luer connectors (Cole Parmer Instruments, England, UK). A luer lock-tip syringe (Fisher Scientific, Loughborough, UK) was employed for sample inoculation, the tip of which was connected to one side of a split-end silicone tubing. The other tubing end was connected to a syringe (60mL; Becton Dickinson, Spain, EU) loaded with the test solution at the required pH. The syringe was fixed to a syringe pump (Ultra 70-3007, Harvard Apparatus, USA). The full schematics of a flow chamber system is shown in Figure 3.9.

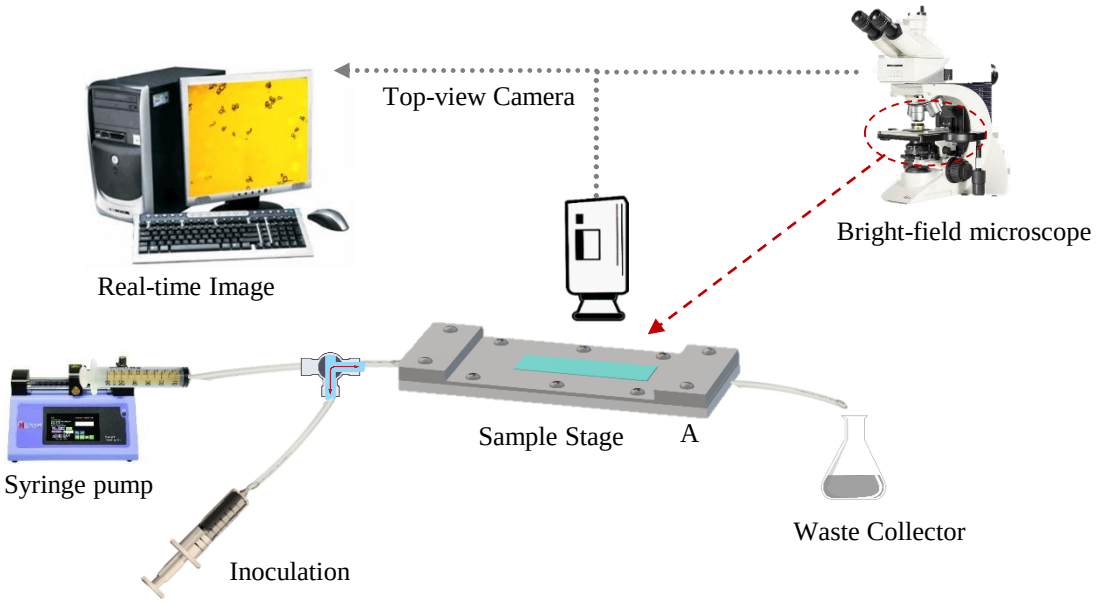

Figure 3.9– Schematics of a flow chamber system with a fully integrated bright-field optical microscope and computer workstation.

3.4.9.3 Test Solution

Test solutions at different pH (3.2; 4.2; 5.1; 6.1; 7.2) were prepared for each experiment to investigate the effect of pH on the retention performance of perfume microcapsules by CC onto PET films. Each test solution was prepared with deionised water by dropwise addition of aqueous 0.1N HCl_{aq} and 0.1N $NaOH_{aq}$ to the required pH.

3.4.9.4 Specimen

Specimens (*i.e.* diluted suspension of microcapsules to inoculate into the flow chamber) were obtained from microcapsule slurries. Each slurry (~0.05g) was weighed and added to the

required test solution (20 mL) with the desired pH in order to achieve a 0.25% (w/w) suspension of perfume microcapsules. The resulting specimens were left to rest to equilibrium (30 min), which is similar to the detergent dissolution at the beginning of a real washing cycle. Each specimen was gently shaken prior to its inoculation into the chamber. The size distribution of microcapsules was also measured to prove their size suitable for the height of the passageway (microcapsule-to-height ≤0.3) so that no aggregates formed.

3.4.9.5 Investigation of Microcapsule Adhesion onto PET films

One of the most relevant parameters is the relative density (ρ_r) of microcapsules in aqueous media (ρ_w). It is essential to know whether the microcapsules naturally float ($\rho_r<\rho_w$) or settle down ($\rho_r>\rho_w$) in order to configure the flow chamber correctly. For HS-microcapsules ($\rho_{r,HS}>\rho_w$), the flow chamber was positioned standardly, with the top plate upwards and facing the microscope lens (Figure 3.9A). Alternatively, if the relative density of the core oil is lower than water ($\rho_{r,oil}<\rho_w$), the flow chamber should positioned reversed, with the top plate downwards and facing the microscope light. The main steps of the process are summarised herein:

i. **Loading** - The test solution at the required pH was infused into the chamber with a syringe pump (5 mL·min^{-1}; 3 min). The outlet of the flow chamber was slightly tilted upwards to achieve no air bubbles within the system. The chamber was then secured onto the flat microscope stage, and configured according to microcapsules' ρ_r (upwards/downwards);

ii. **Image focusing** - The PET film was adjusted into focus on either the lower or the upper surface of the PET film, depending on microcapsules' ρ_r. Specifically, the focus was onto the upper layer of the PET film for HS ($\rho_{r,HS}>\rho_w$)

microcapsules, respectively. The focus (11-14 mm) included the cross-sectional area of the chamber;

iii. **Deposition –** A specimen aliquot (4 mL) containing suspended microcapsules was inoculated into the flower chamber. Microcapsules were left to rest to equilibrium (30 min), which was monitored *via* digitalised optical microscopy;

iv. **Cleaning -** The test solution at the required pH and flowrate (15 $\mu L \cdot min^{-1}$) was fed into the system (5 min). This step helped to remove free oil droplets, which may be due to microcapsules ruptured when inoculated;

v. **Flushing -** Increasing flowrates were selected, leading to a gradual increase of the shear stress. Each flowrate (0.065, 0.125, 0.3, 0.6, 1.2, 3.0, 4.5, 6.0, 9.0, 12.0 $mL \cdot min^{-1}$) was held for 3 min to afford the equilibrium between microcapsules and the PET film. Accordingly, images of microcapsules adhering to the PET film were captured every 3 minutes from a fixed position.

3.4.9.6 Image Analysis

Images taken during flushing were analysed using open source image analysis (IA) software being ImageJ (1.53c, National Institute of Health, USA). *Ad-hoc* coding was developed to automatically analyse the images (Appendix A), which enabled to evaluate the specific area ($\hat{a}$) occupied by HS microcapsules as compared to their background. Images were first fully desaturated to grey scale, and then converted into black & white to minimise any shading effect. Any hollow hole was automatically filled up for HS microcapsules to appear as black spots on a white background. The area covered by each microcapsule (A_k) was quantified by detecting the diameter of its corresponding black spot. The total number of spots allowed to determine the cumulative area (A_c) actively covered by all microcapsules on each image, hence $\hat{a}$:

$$\hat{a} = \frac{A_c - A_b}{A_d - A_b} = \frac{1 - \frac{\sum_{k=1}^{n} A_k}{A_b}}{1 - \frac{A_d}{A_b}} \tag{3.13}$$

where A_d and A_b are the maximised area occupied by microcapsules at nil shear stress and the baseline area of commercially available model films (where defects might occur), respectively.

When IA is performed, the potential sources of error should be considered. Specifically, the surface of the PET film may not be fully homogeneous. Consequently, this may affect the hydrophobic interaction between the film and microcapsules, thereby impairing their retention performance quantified *via* IA.

3.4.10 Dynamic Interfacial Tension

Interfacial tension (IFT) plays an important role in multiple chemical engineering applications involving multiphase systems. Quantifying IFT *via* a pendant drop analysis (PDA) technique has proven effective and accurate [359]. PDA enables to measure IFT of liquid-liquid phases. In this study, an oil drop was obtained from a needle (capillary tube) into an aqueous bulk phase inside a quartz glass cell (20 × 20 × 24 mm). Since the shape of the oil drop is conditional upon its specific gravity and interfacial tension, it was crucial to identify a convenient experimental setup. Oils heavier than the bulk aqueous phase (*e.g.* HS) required a standard capillary needle (Figure 3.10A), whereas oils lighter than the aqueous bulk phase (*e.g.* LC) required a hook (J-shaped) capillary needle (Figure 3.10B) [126]. The stainless steel needle (capillary width ~0.5 mm) was mounted onto a 500µL dosing glass syringe (ILS, Germany, EU). The drop was generated at 1.0 $\mu L \cdot s^{-1}$ to a standardised volume (~5µL) to let air bubbles off. The IFT was calculated (±0.05 $mN \cdot m^{-1}$) from the digitalised shade of the oil drop captured by an integrated camera (DSA25, KRÜSS GmbH, Hamburg, Germany). The drop shape was analysed every 60s for 6 h, resulting in 360 readings. IFT was automatically calculated by an

integrated software package (Advanced Kruss, Germany, EU) relying on the Young-Laplace equation reported elsewhere [360].

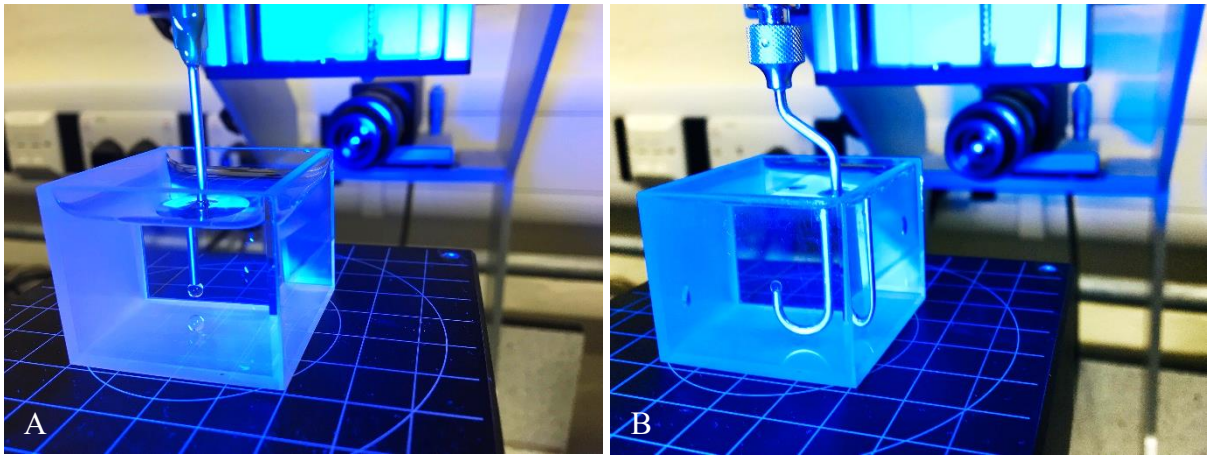

Figure 3.10– Different configurations of the IFT analyser: standard (A) and hook (J-shaped) needle (B) depending on the specific gravity of the two phases.

Chapter 4 Investigation of zeta potential, turbidity, and interfacial tension to enhance emulsion stability and drive effective complex coacervation †

4.1 Introduction

4.1.1 Overview

In this chapter, the feasibility of inducing complex coacervation (CC) on a fully animal-free biopolymeric system was investigated. CC was accomplished by interacting two oppositely charged biopolyelectrolytes, namely fungal Chitosan (fCh) and Gum Arabic (GA), following the procedures detailed in Section 3.2. The experimental parameters associated with CC were investigated, with particular emphasis on the formulation conditions, such as zeta-potential, turbidity, and formulation pH. The effectiveness of coacervation was evidenced by fabricating pure coacervate beads based on the electrostatic, turbidimetric, and pH-related studies. The examination of the results contributed to understanding the key process conditions of pH-driven CC between fCh and GA. Moreover, such results led far beyond all expectations to also establish novel concepts *i.e.* Complex Coacervation Comfort zone (CCCZ) and Critical Turbidity zone (CTZ), which were determined to be intimately interrelated with each other. As a further step towards microencapsulation *via* CC, oil-in-water emulsions of oil-based active ingredients (HS and LC) were generated with a broad range of emulsifying agents *via* homogenisation in order to investigate the kinetic stability of emulsions. The effect of the

† Part published at Baiocco, D., Preece, J. A., & Zhang, Z. (2021), *Colloids and Surfaces A: Physicochemical and Engineering Aspects*, 126861.

emulsifying agent on the stability of emulsions was assessed *via* optical density and interfacial tension measurements, which are comprehensively discussed in this chapter.

4.1.2 pH and Electrostatic Interpretation of Biopolymers

Nowadays, biopolymer-biopolymer interplays have drawn more and more attention in multiple sectors, such as textile and food technologies [197]. They have proven responsible for influencing the microstructure of many biopolymer-based products and, in turn, their own appearance, texture, and mechanical properties [361]. Therefore, an extensive understanding of the parameters influencing the interplays among biopolymers is essential, with particular attention to their electrostatic nature. Conditionally upon the strength of attractive interplays between two different biopolymers, the formation of soluble complexes/hydrogels and precipitates may occur. The former are likely to occur when the electrostatic interplays are weak, whereas the latter are associated with strong interactions [362]. Such interplays may result into segregative/associative biopolymer-biopolymer interaction phenomena depending upon the physico-chemical characteristics of biopolymers (*e.g.* charge density, nature or distribution of reactive branches along the biopolymer backbone), and the processing conditions (pH, temperature, ionic strength). CC refers to the self-assembly of macromolecules to afford a two-phase liquid separation, consisting of solvent-abundant and solvent-depleted phase. The latter is made up of co-precipitates of both biopolymers, which are the coacervates [154]. The optimum conditions for CC have been associated with those oppositely charged biopolymers approaching their isoelectric point (pI). This phenomenon results in the highest level of oppositely charged polyions electrostatically interacting with each other, thereby maximising their binding *via* salt bridges [363]. Espinosa-Andrews *et al.* (2013) have suggested that an accurate zeta-potential analysis of the biopolymer formulations provide crucial information on the stability of biopolymers, as well as the pH maximising the electrostatic interactions between the selected biopolymers. To date, the associative/segregative biopolymer-biopolymer interaction mechanism is still not fully understood [179].

4.1.3 pKa of Biopolymers

Relying on pH control, bi-polymeric systems consisting of gelatin (Gl) and gum Arabic (GA) are reported in literature. The results have revealed that an effective neutralisation of the charge density between Gl and GA triggered the formation of strong and stable ion-counterion bonds [47]. Moreover, attention has recently been drawn to protein-polysaccharide systems including soybean/pea-protein isolate-chitosan (Ch) [171], silk fibroin-Ch, *beta*-lactoglobulin-Ch [364], whey protein-GA [156, 195], elucidating the process conditions leading to CC [53]. Moreover, polysaccharide-polysaccharide systems including Gl-GA and GA-Ch have been investigated [169]. Specifically, the former is popular and effective to fabricate coacervates with particular properties, whereas the latter has not been studied much [197]. GA and Ch may result in attractive interplays when CC is driven under specific pH conditions. Ch is a potential candidate for CC since it carries positive charges at acidic pH below its pK_{aCh} (~6.2-7), which is associated with the deprotonation of the glucosamines along its backbone [154, 171]. GA has proven suitable for matching to Ch at pH values above its pK_{aGA} (~2.2) where negative charges are borne by the carboxylate groups [251, 365]. Furthermore, both biopolymers are biodegradable and biocompatible. However, the main drawback associated with Ch, as well as Gl, is that it is animal sourced, at a time when consumers are demanding for solely plant-based ingredients [169, 250]. Animal-sourced ingredients may contain allergen proteins, heavy metal, and health-compromising pollutants, which are coming under regulatory control [9, 51]. Therefore, ambitious efforts have been recently launched to formulate animal-free alternatives *via* CC, which may pave the way to novel structures and carriers for active ingredients. In this chapter, the first objective was to investigate the conditions triggering the formation of the coacervates from a fully vegetable chitosan-GA system. For this reason, the interrelationship between the zeta potential and turbidity of the biopolymeric solutions (*i.e.* coacervate precursors) was examined. As a further step towards microencapsulation, the storage stability of two oil-in-water emulsions was also studied.

4.2 Materials & Methods

In-depth description of the materials, procedure, and all experimental methodologies, including process schematics, can be referred to in Chapter 3, Section §3.2, §3.3.2, §3.3.3.

4.3 Results & Discussion

4.3.1 Net Electrokinetic Charge (NEC) of Biopolymers

The trend of NEC as a function of the pH is displayed in Figure 4.1A, for both fCh and GA solutions. All aqueous fCh solutions/dispersions showed non-negative NEC/Zeta potential values over the selected pH range (1.0-8.0). The most positive value of fCh approximately equal to +65 mV was obtained at pH 3.4. The typical positive charge is ascribable to the protonation of glucosamine segments ($NH_2 + H^+ \rightleftarrows NH_3^+$) occurring at pH<5.5-6.0, which corresponds to its $pK_{a,fCh}$ [343]. Interestingly, the positive charge of fCh was found to drop dramatically at any pH above ~5.5-6.0 since protonation of fCh's glucosamine segments is severely impaired at near-neutral pHs [366]. Particularly, this behaviour has been associated with the deprotonation of the ammonium groups $NH_3^+ \rightleftarrows NH_2 + H^+$ resulting in loss of positive charge [343]. Also, this phenomenon has been tentatively related with the coil conformation of chitosan, which is extended only at low acidic pHs due to strong segment-segment repulsion phenomena [367]. Moreover, the rotational flexibility of chitosan's carbon rings is reduced, especially at pH ≥ pKa_{Ch}, resulting in a much stiffer conformation [197].

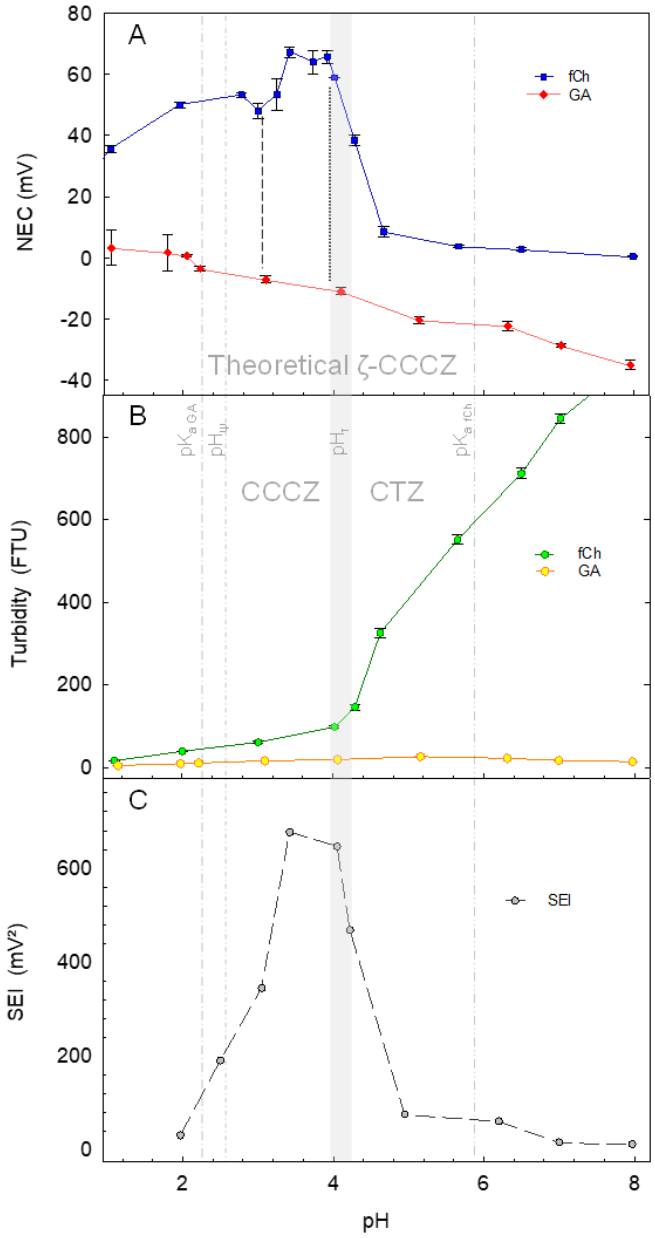

Figure 4.1– Net electrokinetic charge (NEC) of soluble biopolymers or ζ-potential of biopolymer dispersion (A) and turbidity (B) of fCh/GA solutions/dispersions with the strength of electrostatic interaction (SEI) (C) at different pH values. The resulting theoretical NEC/zeta-potential Complex Coacervation Comfort Zone (ζ-CCCZ) solely based on NEC measurements is displayed between $pK_{a,GA}$ (· — ·) and $pK_{a,fCh}$ (·· — ··); the operative CCCZ is displayed between pH_{ψ} (· - ·) and the left edge of pH_{τ} (grey bar) since the critical turbidity zone (CTZ) occurs at $pH \geq pH_{\tau}$; pH_{τ} represents the solubility-to-insolubility transition area of fCh. Error bars may be smaller than the size of the symbols.

Moderately acidic fCh-based dispersions (pH 4.3) were found to develop a slightly turbid appearance (Figure 4.2B), whereas highly acidic fCh dispersions (pH 1.1) turned completely clear (Figure 4.2A). Previous literature has suggested that chitosan solubility is conditional upon the distribution of N-acetyl and free amino functional groups (NH_2) in the glucosamine units [368]. Protonation of amino groups into NH_3^+ was observed at pH below 6.0 (~pK_{aCh}) due to which Ch/fCh had become partly soluble [343]. Clear fCh solutions were generated, at highly acidic pH, by the distribution of active NH_3^+ units naturally available below its own pKa_{fCh}, which are thus responsible for the degree of solubility of fCh in aqueous media. Therefore, turbid dispersions of fCh observed at pH values above its $pKa_{,fCh}$ (Figure 4.2C) would contain a large distribution of non-protonated amines leading to fCh insolubility. As for animal-derived Ch, no fCh is expected to electrostatically interact with any oppositely charged species (*e.g.* GA) above its $pKa_{,fCh}$ [369].

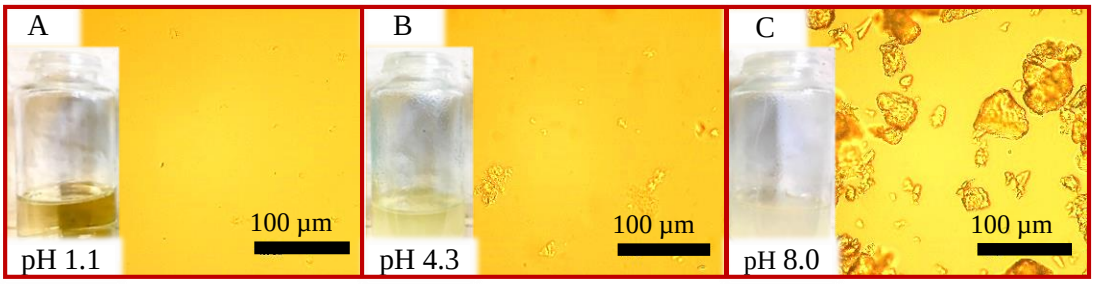

Figure 4.2– Bright-field microscopy imaging of fCh-based aqueous solution/dispersion at different pH values: clear and translucent at pH 1.1 with fully dissolved fCh (A), slightly turbid with non-fully dissolved fCh at pH 4.3 (B), and highly turbid and non-translucent due to non-dissolved fCh at pH 8.0 (>pK_{afCh}) (C). The vials show the appearance of the fCh-based aqueous solution/dispersion at the pH values displayed.

When dealing with GA, non-positive NEC values were exhibited by GA solutions between pH 2 and 8, whereas cautiously weak cationic charges were detected for GA at pH 1.0-2.0 (Figure 4.1A). Previous literature confirmed that GA is always negatively charged in solution having pH above 2.0 [60]. The interrelationship between the charge nature of GA and the pH is governed by the deprotonation mechanism of GA's carboxylic moieties ($COOH \rightleftarrows COO^- + H^+$), which is associated with its pKa_{GA} occurring at pH 1.8-2.2 [370]. Accordingly, a charge switchover point for GA was clearly identified at pH 2.1-2.2 where its electrostatic charge was found to be transitioning from a weakly positive value to increasingly negative value, as also reported by Dong and Hua [371]. The overall zeta charge distribution of GA progressively became more and more negative as the pH was increased, with a zeta value equal to –35.1 mV following alkalinisation to pH~8.0. The results were found to be in good agreement with the data previously presented for GA by Weinbreck *et al.* [156], Espinosa-Andrews *et al.* [197], and Dong and Hua (2016). However, several values measured for GA were determined to be slightly different from those provided by Jiménez-Alvarado [372]. Most likely, such discrepancies might result from differences in the nature, purity, ageing, chemical composition, and dispensing stage of the raw ingredient supplied.

4.3.2 Strength of Electrostatic Interaction (SEI) of Biopolymers

Strength of Electrostatic Interaction (SEI) is displayed in Figure 4.1C. SEI is a parameter derived as the absolute value of product between the zeta potential values of both oppositely charged polyelectrolytes taken at a specific pH (Weinbreck *et al.*, 2004, Espinosa-Andrews *et al.*, 2013). As such, SEI values are pH-dependent and meaningful over the pH range where biopolymer pairs only exhibit opposite charges, and hence attractively interplay with each other [156]. As shown in Figure 4.1C, this range was found to occur between pH ~2.2 and ~6.0 for the investigated GA-fCh system. More particularly, the greatest SEI value (677 mV^2) for the GA-fCh system was determined between pH 3.0 and 4.0. Overall, SEI should be considered as a theoretical electrostatic indicator to tentatively suggest the pH region where the interactions

between GA and fCh are maximised, thereby promoting their mutual charge neutralisation. Therefore, a net pH-triggered charge cancellation between two biopolymers carrying opposite charges would result in CC phenomena [176]. Besides, CC occurring at the maximised attractive interaction point of two biopolymers bearing opposite charges may not only lead to the separation of coacervates, but also to robust structures as benefitting from the strongest possible interplays. When all involved ion *vs* counter-ion charges (carried by fCh and GA) actively interact with each other at the most favourable pH, the fCh-GA system becomes more strongly bound, thereby triggering more compact complexes. This behaviour has also been reported for chitosan-GA systems by Vuillemin *et al.* [373]. Moreover, the same authors have suggested that the effectiveness of strong Ch-GA pairs is influenced by the steric hindrance of Ch itself, which is beneficially reduced at specific temperature-pH conditions.

4.3.3 Establishment of Theoretical Zeta Potential Complex Coacervation Comfort Zone (ζ-CCCZ)

Following the above, a theoretical NEC/zeta-potential Complex Coacervation Comfort Zone (ζ-CCCZ) based on the electrostatic interactions between GA and fCh can be introduced. This indicator is shown in Figure 4.1 between pK_{aGA} and pK_{afCh}, thereby encompassing the whole pH region within which only opposite charges are borne by the biopolymers. ζ-CCCZ is aimed at identifying all theoretical pH matches which may induce coacervation between two oppositely charged biopolymers, such as fCh and GA. As displayed in Figure 4.1B, the lower bound pH value of ζ-CCCZ referred to the GA-fCh system was determined to be pH_{ψ} 2.5. pH_{ψ} value has been experimentally validated as the starting point of phase separation phenomena of GA and fCh by CC, at which independent GA-fCh based coacervates were first observed to begin separating out (Figure 4.3). As can be seen, this phenomenon was clearly discernible in the case of coacervate beads, which becomes more obvious with coacervates forming around oil droplets, as detailed in Chapter 5. Alternatively, the upper bound pH value was associated with pKa_{fCh} (~6.0) since no formation of the intact coacervates is expected at $pH \geq pKa_{fCh}$ due to impaired protonation of fCh's amine branches [154]. Hindered CC phenomena were

probably due to the cationic charge drop of fCh at pH ~ pKa_{fCh}. Moreover, no significant CC at pH~pKa_{fCh} appeared consistent with the extremely low SEI values exhibited by the fCh-GA system at pH≥pKa_{fCh}. As previously mentioned, poor/no solubility of fCh in aqueous media with near-neutral (~6.0-6.5) as well as alkaline pH (>7) leads to no CC because no protonation of fCh's amine moieties occurs above pKa_{fCh} [343]. As expected, non-protonated fCh resulted in highly turbid fCh dispersions, which were observed at slightly basic pH~8.0 (Figure 4.2C). In addition, slightly turbid dispersions observed at pH~4.0-4.3 (Figure 4.2B) suggest the incipiently impaired solubility of fCh in water (due to partially protonated glucosamine units), which may tentatively identify the solubility-to-insolubility transition area of fCh (Figure 4.1), *i.e.* pH_{τ} [366].

Notwithstanding, the establishment of an *a-priori* ζ-CCCZ relying on the mere electrostatic analysis may only be utilised as a guideline to preliminarily choose CC-suitable matches between pairs of biopolymers bearing opposite charges within a specific pH range. Overall, ζ-CCCZ does not directly involve any turbidity implications, hence extra endeavours were undertaken to interrelate the NEC/zeta-potential analysis with the turbidity related studies.

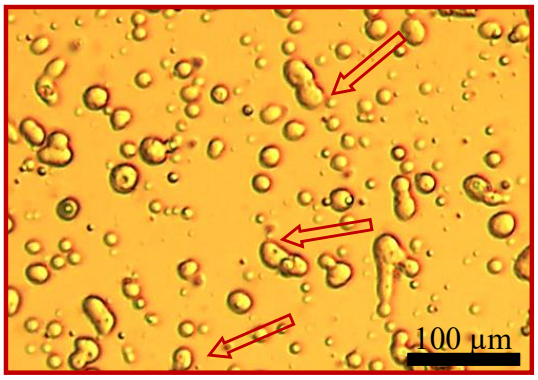

Figure 4.3– Incipient formation of coacervate beads (pH 2.5, T= 25.0 ºC) observed by optical microscopy.

4.3.4 Measurement of Turbidity of Biopolymers

Turbidity is defined as the cloudiness of a dispersion due to non-dissolved colloidal matter [374]. As explained by Davies-Colley and Smith [375], this phenomenon directly results from solid particles likely scattering a light beam passing through the dispersing medium. Information relating to the turbidity of the fCh-GA system was collected, and interrelated with the ζ-potential analysis (Figure 4.1A-B). The turbidity *versus* pH of GA and fCh is shown in Figure 4.1B.

4.3.4.1 Turbimetric Analysis of fCh

As can be seen in Figure 4.1B, fCh exhibited a moderate rise in turbidity from 15 to 150 FTU when the pH was increased from 1.1 to 4.3 (*i.e.* right edge of pH_{τ}), which is consistent with what is shown in Figure 4.2A-B. Moreover, similar results have been reported by Geng *et al.* [376] suggesting that chitosan may be from partly to completely dissolvable when exposed to slightly and highly acidic media, respectively. As the pH was increased above pH_{τ}, a surge in the turbidity level of fCh solutions was observed. Interestingly, the turbidity level of fCh at pH 5.5 was determined to be around 4-fold higher than that observed within pH_{τ}. The appearance of fCh dispersions became more and more turbid when the pH was adjusted from slightly acidic to neutral/alkaline, which is reflected in the exponential-like boost in fCh's turbidity curve presented in Figure 4.1B. These findings are in agreement with what was previously observed from the ζ-analysis since no highly positive ζ-values had been found for fCh at and above pH~5. As formerly mentioned, this phenomenon could be ascribable to fCh adopting a non-extended conformation at weakly acidic pHs and above (≥5.5-6.0) probably due to the depleted glucosamine segment-segment repulsion, resulting in a lower intrinsic viscosity of fCh itself [154, 367]. The net increase in turbidity of fCh dispersions under non-optimal dissolution conditions is attributed to the cationic charge loss of the glucosamine units along fCh's chains [377]. Thus, limited/no occurrence of free positive charges around fCh's glucosamine units

would lead to limited/no electrostatic phenomena [343]. Moreover, the increase in turbidity could be taken as a physical evidence of fCh possessing a non-extended conformation at weakly acidic pH and above [343]. As reported for animal chitosan, non-extended conformations of Ch, at weakly acidic pHs and above, have also been associated with its semicrystalline nature due to inter- and intra-molecular hydrogen bonds, which trigger insolubility [378]. In addition, previous literature suggests that the flexibility of chitosan's reactive moieties along its chains may be enhanced at pH ~ 3, thereby maximising the protonation of its own available glucosamine units [379].

4.3.4.2 Turbidimetric Analysis of GA

Turbidity analysis suggested that GA (~1.5-8.0) was fully soluble at all pH values investigated. This finding was anticipated since GA is known to be water soluble [380]. When compared to fCh, the turbidity of GA solutions exhibited minor variations over the investigated pH range with typical values ranging between 5 and 30 FTU (Figure 4.1B). More specifically, the turbidity exhibited a quadratic trend. A gradual increase of the turbidity values was obtained by alkalising the medium to a maximum at pH ~5 (30 FTU). pHs higher than ~5 led to a progressive decline of turbidity to 15 FTU at pH 8.

4.3.4.3 Effect of pH on fCh-GA Turbidity Levels

Overall, the turbidity data suggests that well-dissolved fCh-GA-based mixtures should be achieved exclusively at highly acidic pH values ($<pH_{\tau}$) where very low turbidity levels of both biopolymers had been observed. Besides, the vertical gap between the turbidity curves of both GA and fCh increased mildly below pH_{τ}, whereas a much higher gap was observed above pH_{τ}. When comparing GA/fCh turbidity curves with each other, it could be inferred that fCh has a

leading role in terms of turbidity and dissolvability in water, whereas GA only plays a supplementary role.

4.3.4.4 Development of a Critical Turbidity Zone (CTZ)

As shown in Figure 4.1C, any pH higher than pH_{τ} and below pK_{afCh} hits the increasingly high turbidity zone of fCh. Based on above discussion, no reactivity of fCh may be expected within its high turbidity zone. Therefore, a critical turbidity zone (CTZ) can be individuated. CTZ is aimed at spotlighting the high turbidity zone generated by the investigated fCh-GA system. Alternatively, CTZ suggests the pH region in which a polymeric pair are highly unlikely to react *via* CC due to the impaired solubility of one or both polymers in the reacting medium. CTZ of the fCh-GA system is displayed between pH_{τ} and pK_{afCh}.

4.3.5 Interrelationship between Turbidity and Zeta Potential

The interrelationship between pH-dependent turbidity and ζ-potential plots requires further interpretations. As shown in Figure 4.1C, the greatest biopolymer-biopolymer electrostatic interaction for the fCh-GA system was determined *via* SEI to fall between pH 3.0 and ~4.3 (Figure 4.1C). SEI was then found to collapse as the turbidity of the system (led by fCh) surged above pH_{τ}. Basing on a mere electrostatic analysis, fCh and GA bear positive and negative charges at pHs lower and higher than their own pKa values (pK_{afCh}~5.5-6.0; pK_{aGA}~1.8-2.2), respectively. Notwithstanding, increasing turbidity levels of fCh at $pH \geq pH_{\tau}$ are the evidence of fCh's insolubility due to its non-extended conformation on which no reactive glucosamine groups can occur. For this reason, the previously identified theoretical ζ-CCCZ should be accordingly reduced in width due to the turbidity of fCh occurring at and above pH_{τ}. More specifically, the former ζ-CCCZ should be narrowed down between pH_{ψ} and the left edge of pH_{τ} (~4.0) to hit a turbidity-free zone, which is CCCZ (Figure 4.1B). Thus, CCCZ also includes the turbidity effects on the solubility/reactivity of the biopolymers. In addition, the derivative of SEI was determined to be positive and steep between pH 2.2 and 3.5 ($\partial SEI/\partial pH > 0$), evidencing the increase in the strength of the electrostatic interaction between GA and fCh.

Basing on the highest SEI value obtained, the most convenient theoretical pH for CC (pH_{CC}) between fCh and GA should be around 3.4-3.5, at which the most effective neutralisation of their opposite charges is anticipated. Overall, the establishment of CCCZ paired with CTZ may be considered as a useful approach for predicting suitable biopolymer pairs to chemically react *via* CC within their most convenient turbidity-free pH range. A compact representation of Figure 4.1 is presented below (Figure 4.4).

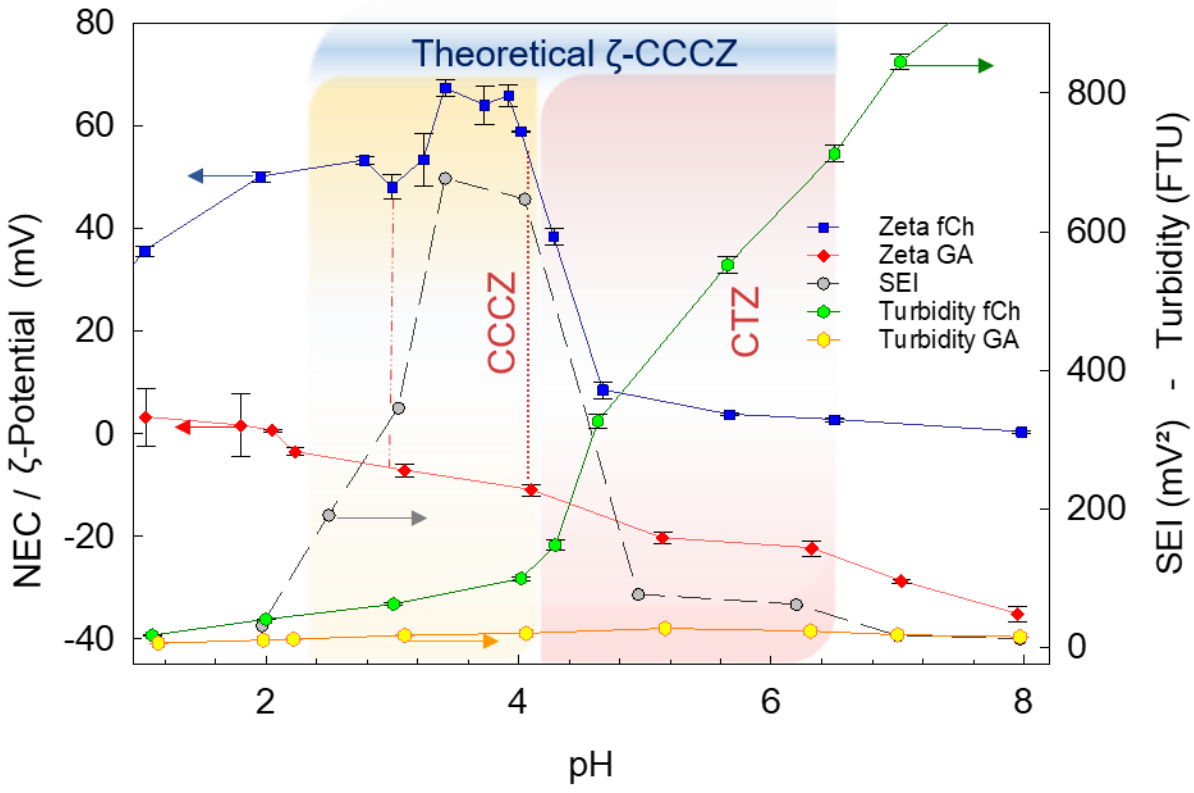

Figure 4.4– All-in-one representation from Figure 4.1A-B-C. Interrelationship between NEC/ζ-potential and turbidity curves of fCh/GA dispersions at different pH values. ζ-potential (together with the resulting SEI curve) and turbidity trends of fCh and GA dispersions at different pH values are displayed. The resulting theoretical zeta-potential based Complex Coacervation Comfort Zone (ζ-CCCZ) solely based on the electrostatic charge analysis is shown as the top-sitting blue strip; the critical turbidity zone (CTZ) is shown as the red band, whereas the operative CCCZ is displayed as the yellow strip. ζ-potential values can be read on the principal vertical axis, whereas turbidity values as well as SEI can be read on the secondary vertical axis. Error bars may be smaller than the size of the symbols.

4.3.6 Determination of the Optimum CC Ratio

The optimisation of the processing conditions is crucial to achieve microcapsules successfully. More particularly, the biopolymer-biopolymer ratio can be determined by comparing the NEC trends of each biopolymer occurring in the turbidity-free CCCZ [47]. Specifically, several straight lines being perpendicular to the pH axis are contained within CCCZ. The vertical dashed line originating through pH 3 hit the NEC curves of fCh and GA exhibiting charges of around +54.2 mV and -7.3 mV, respectively (Figure 4.1A and Figure 4.4). Similarly, the dotted line through pH 4 shows the NEC of fCh and GA solutions to be +59.1 mV and -9.3 mV, respectively. As presented, in both cases (pH 3 and pH 4), the absolute NEC of fCh were found to be very different when compared to GA, and vice versa. Therefore, the vertical lines originating from the NEC values of each biopolymer through a given pH were quantified in order to identify a biopolymer-biopolymer weight ratio suitable for CC between GA and fCh. It appeared that non-equal amounts of each biopolymer were required to compensate the electrostatic gap between GA and fCh and to enable their mutual charge cancellation effectively [47]. Accordingly, a greater amount of GA would be needed to promote full neutralisation of all counter-ions carried by fCh. Basing on the concentrations adopted, the vertical gaps taken at pH 3 and 4 suggest that the amount of GA to employ should be stoichiometrically within six to seven-fold higher than fCh. Particularly, the highest NEC value between GA and fCh was detected at pH 3.4 ($\zeta_{fCh,max}$= +67.9 mV; $\zeta_{GA,max}$= –9.9 mV) with a globally maximised SEI of 677 mV^2. The corresponding GA-to-fCh weight ratio at pH 3.4 was 6.7 (m_{GA}/m_{fCh}=15g-GA/2.25g-fCh). The formation of coacervates was seamlessly achieved at pH 3.4 where attractive interactions between GA and fCh were maximised. This result has been even more evident with coacervates forming around an individual oil droplet as the walls of a microcapsule, which will be extensively discussed in Chapter 5. Thus, pH 3.4 has been adopted as the optimum completion pH_{CC} for the fCh-GA system. These findings were found to be in very good agreement with former literature suggesting that the highest cationic charges of chitosan, and hence the strongest protonation of the amine groups along its chains, occur at pH 3.6 [169], which is also reflected on the variation of its total conductivity [381]. Further studies

conducted by Butstraen and Salaün [169] have also shown that pH 3.6 was required for triggering CC between chitosan and GA at the maximum of their electrostatic interaction (*i.e.* zero-charge equivalence point). Overall, it could be inferred that the amounts of biopolymers to react *via* CC need to be adjusted in order to neutralise the oppositely charged ammonium and carboxylate functional groups carried by Ch/fCh and GA, respectively [47].

4.3.7 CC Effectiveness

As shown Figure 4.3, independent fCh-GA coacervates first separated out at pH~2.5. Subsequently, the effectiveness of CC was assessed by characterising the physical, structural and mechanical properties of the formed fCh-GA complexes *via* several analytical techniques, including particle sizing, SEM and micromanipulation.

4.3.7.1 Size and Size Distribution of Coacervate Beads

The size distribution of coacervate beads (CBs) was measured by LDPSA (Figure 4.5). The curve shows that the size of CBs ranged between 8 µm and 79 µm. The mean Sauter diameter $D_{[3,2]}$ was determined to be 21.3±3.1 µm. A single-peak size distribution was determined, (SPAN~1.4), which could be fitted to a log-normal distribution with 95% confidence.

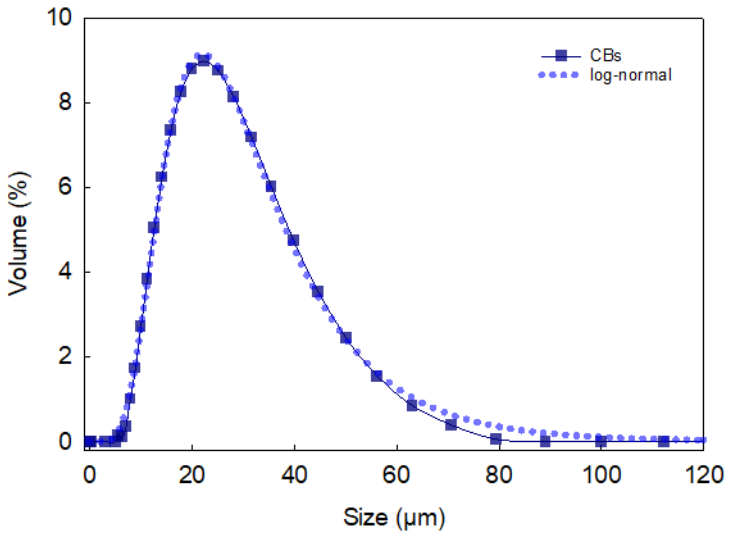

Figure 4.5– Size distribution of suspended coacervate beads (CBs) fitted to a log-normal distribution (95% confidence). The general form of a three-parameter (a, b, x_0) log-normal distribution function is $f(x) = \frac{a}{x}\exp\left(-\frac{1}{2}\left(\frac{\ln(x/x_0)}{b}\right)^2\right)$. Non-linear regression and performance parameters: a=2.3·10^2; b=0.5; x_0=28.5; coefficient of determination R^2= 0.998.

4.3.7.2 Morphology of CBs

SEM micrographs of CBs are displayed in Figure 4.6. Dry CBs may aggregate altogether, yet their outline is still visible. It was noticed that CBs could be easily separated out from each other when suspended in water (§4.3.7.1). A self-isolated CB was observed (Figure 4.6A), which was spherical with a smooth surface. Mechanical characterisation using micromanipulation was thus possible on individual CBs, as detailed later. Additionally, the internal structure (cross-sectional areas) of CBs was examined (Figure 4.6B). CBs (~60µm) exhibited a porous structure (honeycomb) with a significant number of heterogeneous inner voids with random sizes. This phenomenon was likely ascribable to the presence of former water molecules which had been caught within the biopolymeric networks of the coacervates, thereby resulting in minute structural vacuoles [382]. As described by Burgess [199],

bound/unbound water molecules may be conducive to forming water-swollen coacervate structures. In contrast, no porosity could be observed on smaller CBs (~10µm). Similar results were also reported by Espinosa-Andrews *et al.* (2010) on non-vegetable chitosan coacervates. The researchers observed sponge-like microstructures with a high density of inner vacuoles, without any in-depth mechanical characterisation.

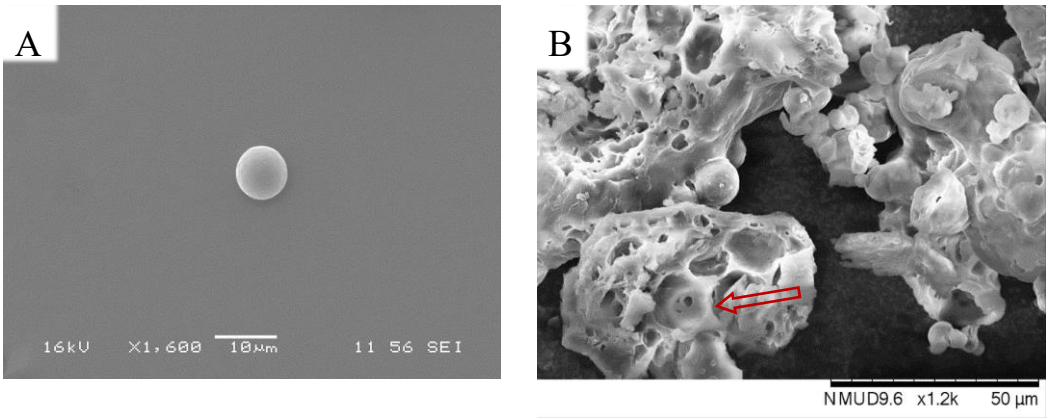

Figure 4.6– SEM micrographs of CBs; (A) self-isolated CB (~10µm) and (B) cross-section area of large CBs with a honeycomb-like structure.

4.3.7.3 Mechanical Properties of CBs

Since inner structural features of CBs can be reflected on their mechanical properties, they were characterised using a micromanipulation technique, and the data of the rupture force, displacement at rupture, nominal rupture stress, and elastic modulus [266] were obtained.

4.3.7.3.1 Compression of Single CBs

Figure 4.7 displays the interrelationship between the force gradually exerted onto a single CB (20 µm) and the displacement. There appeared to be an increasing force generated by the probe

compressing the CB, yet no dramatic force drop was registered. This behaviour is typically observed when no bursting point occurs on solid microparticles, as reported by Pan *et al.* [31]. However, only a slightly flattened segment of the curve was recorded between ~10µm and ~12µm of displacement, which seems to suggest the solid CB to have transitioned from an elastic into a plastic behaviour. Although no clear rupture point occurred possibly due to the solid nature of CBs, the force-displacement curves are helpful to estimate the elastic moduli of CBs, which was done by fitting the experimental data in the linear-like region (0-8 µm) to the Hertz model. However, there appears that the linearity of the force-displacement curve of the CB is not continued until its yield point. Some bending effect may occur prior to reaching the actual yield point, which tentatively suggests incipient pre-yield plasticity. Overall, the data shows that the transition region of CBs from the elastic into the plastic deformation can be identified effectively [18].

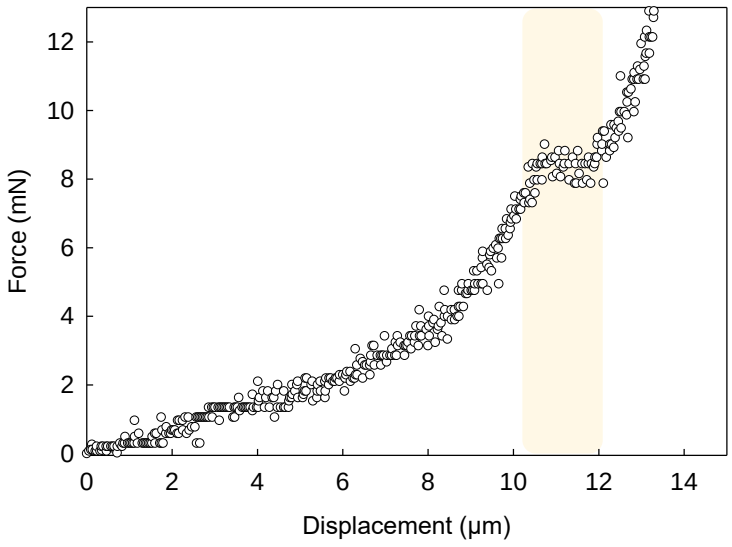

Figure 4.7– Typical Force-displacement curve of a single 20-µm CB.

4.3.7.3.2 Key Mechanical Property Parameters

In order to obtain statistically representative results (§3.4.8.3), thirty individual CBs were randomly selected, and compressed. Figure 4.8 shows that the compression force required by CBs between two parallel plates (*i.e.* flat-end glass probe and glass substrate) mildly increased with their diameter. Since no clear rupture was attained from solid CBs, the compression force value was intercepted at the flattening point of the curve, which may represent the onset of plastic deformation of CBs (Figure 4.7- highlighted region) and is therefore called "the compression force at the yield point". This finding seemed consistent with Figure 4.6A-B, as large CBs have shown a more porous inner structure, whereas small CBs appeared more solid. Interestingly, the compression force at the yield point of CBs fell into the range 2.5mN–17.8mN, corresponding to CBs of 8.1µm-21.5µm. The average compression force at the yield point was 7.4±0.7 mN, which is in agreement with other polymeric microparticles reported in literature [317]. In contrast, this result is around five to ten-fold larger than that associated with some core-shell microcapsules [25, 126]. For this reason, it is important to compare CBs with the microcapsules fabricated in this project, as detailed in Chapter 5.

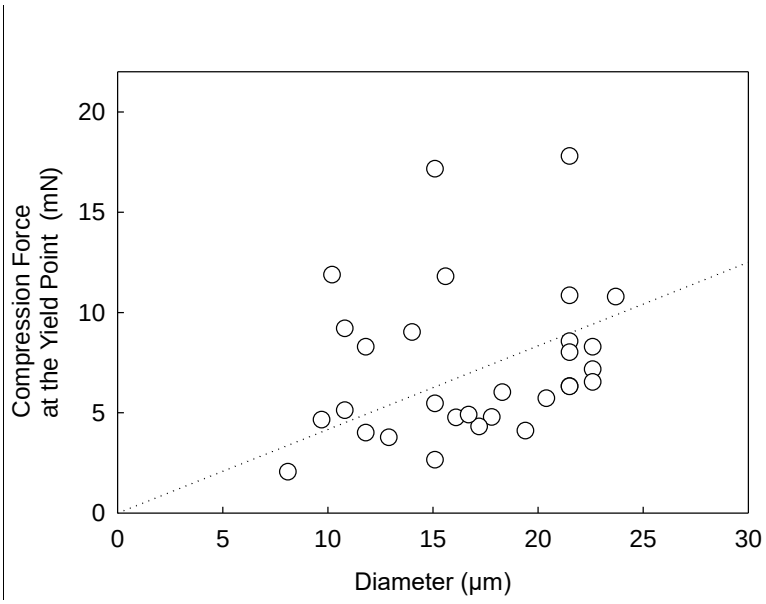

Figure 4.8– Compression force at the yield point *versus* diameter of CBs. The dotted line represents the trend only.

Figure 4.9A displays the displacement at the yield point of CBs which range between 4.2µm and 13.3µm, with the exception of one point (3.3µm). The trend suggested that the displacement at the yield point of CBs increased linearly with their diameter (average 8.3±0.5 µm), which may be due to the different inner structure and degree of porosity between small and large CBs. However, the beads have different sizes, therefore the displacement is not only force dependent but also size dependent. Accordingly, the nominal deformation (strain) at the yield point should be considered, which is evaluated as the ratio of the variation in the bead size to its original diameter (Figure 4.9B). Interestingly, the deformation at yield point was found to be independent of the bead size, with a mean value of 49.7±2.0%, which was obtained from the slope of displacement at the yield point-diameter linear fitting.

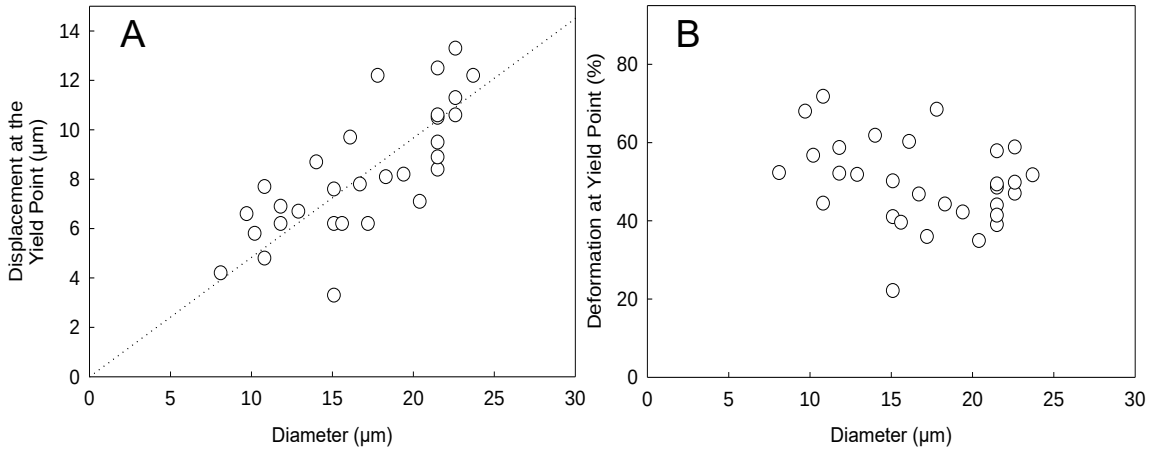

Figure 4.9– Displacement at the yield point (A) and nominal deformation (strain) at the yield point (B) *versus* diameter of CBs. The dotted line (A) represents the trend only.

The nominal stress of CBs (ratio of the compression force of CB at the yield point to its initial cross-sectional area) was found to decrease with their diameter (Figure 4.10), with a mean value of 39.5±5.8 MPa. This finding suggested that large CBs may be weaker and easier to be plastically deformed than small ones, as also reported in literature for calcium-shellac microspheres [383].

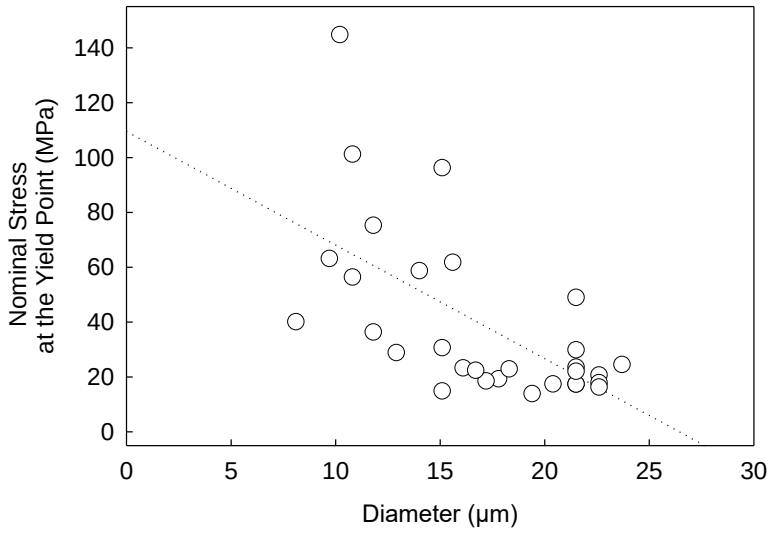

Figure 4.10– Nominal stress at the yield point *versus* diameter of CBs. The dotted line represents the trend only.

Figure 4.8-Figure 4.10 display some clear outliers which have long been observed from micromanipulation analysis when selecting a representative number of individual microcapsules [65]. These few points also provide information on the possible variability of the system. Unlike microfluidic devices, a minor number of microparticles might not form homogeneously possibly resulting in microparticles with different level of porosity and mechanical properties.

4.3.7.3.3 Elasticity of CBs

When dealing with spherical microparticles compressed between two parallel surfaces, the compression force (*F*) *versus* axial displacement (δ) can be classically described by the Hertz model:

$$F = \frac{\alpha}{1-\nu^2} E r^{1/2} \left(\frac{\delta}{2}\right)^{3/2} \quad (4.1)$$

where α=4/3 is the spherical shape factor, *E* is the Young's modulus (GPa), ν is the Poisson ratio, and *r* is the initial radius (μm). Under the assumptions of non-compressible (ν=0.5) material and small deformations (<10%), the Equation (4.1) was used to fit the experimental force-displacement data of CBs. Figure 4.11A shows the typical force *versus* displacement curve in comparison with the fitting generated *via* the Hertz model. The comparison between experimental and predicted data evidenced that a very good fitting was achieved, resulting in a coefficient of determination of 0.91. As shown in Figure 4.11B, *E* moderately decreased with diameter of CBs (average 0.61±0.07 GPa). The highest *E*-values were given by the smallest CBs. This behaviour can be associated with their porous nature of CBs, which is particularly significant in large particles (Figure 4.6B). This finding was in agreement with the observed microporous structure of coacervates by Espinosa-Andrews *et al.* [382].

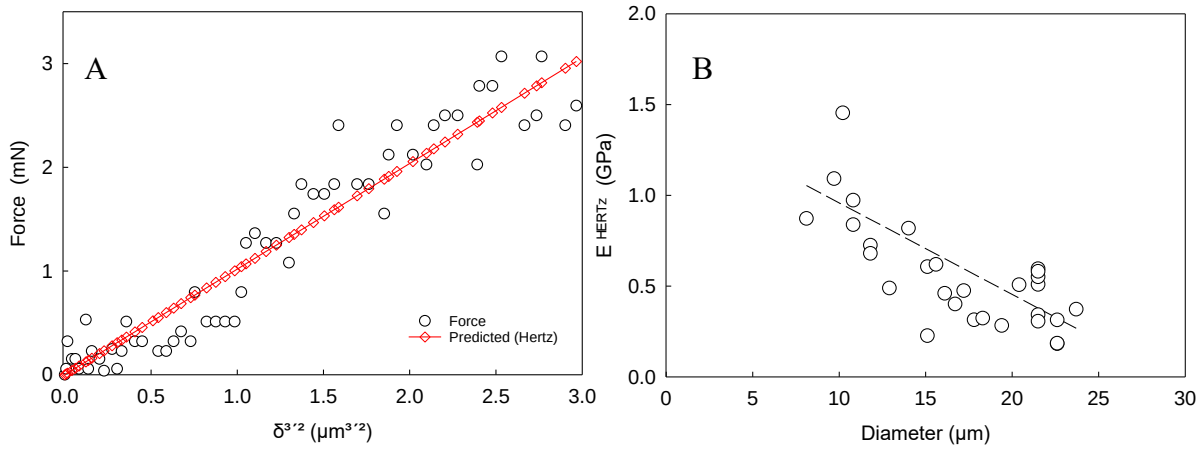

Figure 4.11–Typical force-displacement curve in comparison with the fitting (R^2=0.91) by the Hertz model (A); Young's modulus *versus* diameter of CBs *via* Hertz model. The dotted line represents the trend only (B).

4.3.8 Characterisation of Emulsion Stability

As a further step towards the microencapsulation of an active oil *via* CC, an o/w emulsion is required. The o/w emulsion was formed by inputting energy to a two-phase system being oil (disperse phase) into water (continuous phase). However, the emulsified droplets following homogenisation may be unstable due to coalescence phenomena. Therefore, kinetically stable emulsions are essential prior to inducing complex coacervation. The stability of emulsions is normally enhanced using emulsifiers. For this reason, a broad range of Span, Tween, and their matches were paired with the active oils in this project (HS, LC) to investigate the stability of the resulting o/w emulsions. Following optical density and interfacial tension (IFT) studies, the most suitable emulsifier was determined.

4.3.8.1 Hydrophilic Lipophilic Balance (HLB) of Emulsifiers

Stabilising an emulsion can be challenging. Thus, emulsifiers can ease this task. Depending on the required application, the suitability of emulsifiers can be investigated through their Hydrophilic-Lypophilic Balance (HLB), which represents the level to which an emulsifier is either hydrophilic or lipophilic. In other words, HLB is an expression of the balance between the polar (hydrophilic) and apolar (hydrophilic) sequences of an emulsifier. HLB values below 9.0 and above 11.0 are typically associated with a lipophilic and hydrophilic character of the emulsifier, respectively [384]. Emulsifiers falling into the transitional region (9.0<HLB<11.0) possess an intermediate character. Different factors, such as clarity, viscosity, and chemical type may influence the selection of the emulsifier, hence a blend of emulsifiers is often preferred. Although HLB schemes in literature may provide a theoretical guideline towards the 'right' emulsifier, experimental tests are still crucial to assess the stability of emulsions [384]. Overall, the factors that are mainly responsible for the stability of an emulsion include the nature (chemical type and HLB) and the strength of interfacial film forming between two immiscible phases, and the lowering of interfacial energy. Specifically, lowering the interfacial tension will lead to lowering the interfacial energy, hence increasing the chance to stabilise an emulsion [385]. This can be often achieved by emulsifiers, which may also increase surface elasticity of the droplets, thereby hampering droplet coalescence [386]. In this project, several o/w emulsions were created using emulsifiers of different HLB values (Table 4.1) in order to investigate the feasibility of lowering the IFT of the emulsions of interest (*i.e.* HS and LC in water) according to the methodology described in Section §3.4.10.

Table 4.1 – The IFT of o/w emulsions with emulsifiers (Spans, Tweens, and their matches) based on the resulting IFT and emulsifiers' HLB values. The mean IFT values (± St. Err) obtained after 6 hours at 20ºC are tabled (Krüss drop shape analyser DSA30, with a resolution unit ±0.1 $mN \cdot m^{-1}$). [(1)]Sample Identification (ID): 'OIL' refers to the oil used (*i.e.* HS/LC). Span concentration in oil 0.1%(w/w); Tween concentration in water 0.1%(w/w). For example, the ID for Hexylsalicylate (HS) with 0.1%(w/w) Span60 (SP60) within the continuous aqueous phase with 0.1%(w/w) Tween60 (TW60) is HS-SP60TW60.

Emulsifier type		Two-phase system		HLB	Average interfacial tension (IFT)		Sample ID[(1)]
		Oil (HS/LC)[1]	Water		IFT HS ($mN \cdot m^{-1}$)	IFT LC ($mN \cdot m^{-1}$)	
N/A				N/A	16.0±0.1	7.6±0.2	OIL-BLANK
SPAN	20	✓		8.7	4.8±0.1	1.5±0.5	OIL-SP20
	60	✓		4.8	4.0±0.3	0.8±0.6	OIL-SP60
	65	✓		2.1	4.7±0.1	0.9±0.5	OIL-SP65
	80	✓		4.3	7.0±0.3	1.2±0.5	OIL-SP80
	85	✓		1.9	3.8±0.1	4.1±0.8	OIL-SP85
TWEEN	20		✓	16.7	4.1±0.2	2.2±0.5	OIL-TW20
	60		✓	14.9	7.2±0.7	1.9±0.4	OIL-TW60
	65		✓	10.5	6.6±0.2	2.4±0.3	OIL-TW65
	80		✓	15.0	8.8±0.1	2.5±1.0	OIL-TW80
	85		✓	11.0	4.4±0.1	2.5±0.9	OIL-TW85
PAIRED MATCH (SPAN-TWEEN)	20-20	✓	✓	12.7	3.9±0.1	1.1±0.5	OIL-SP20TW20
	60-60	✓	✓	9.8	5.1±0.4	1.6±0.4	OIL-SP60TW60
	65-65	✓	✓	6.3	5.0±0.6	2.1±0.9	OIL-SP65TW65
	80-80	✓	✓	9.7	4.5±0.3	0.8±0.5	OIL-SP80TW80
	85-85	✓	✓	6.5	6.8±0.1	1.0±0.4	OIL-SP85TW85

4.3.8.2 Interfacial Tension Analysis

IFT studies were performed to investigate the interfacial character of o/w emulsions in the presence of emulsifiers, and a potential relationship between IFT and HLB. Effective emulsifiers should swiftly adsorb at the interface of emulsion droplets, hence depleting their IFT and interfacial energy. This phenomenon may thus promote the occurrence of the disperse phase into more stable droplets [385]. Moreover, the emulsifiers form an interfacial boundary layer onto the droplets, which inhibits coalescence phenomena [216]. All IFT curves were graphed as a function of time. Data was filtered *via* Matlab (Appendix B), which enabled to cancel random noise due to the high frequency of data collection, and to smooth data using Savitzy-Golay moving-average filter (Figure 4.12).

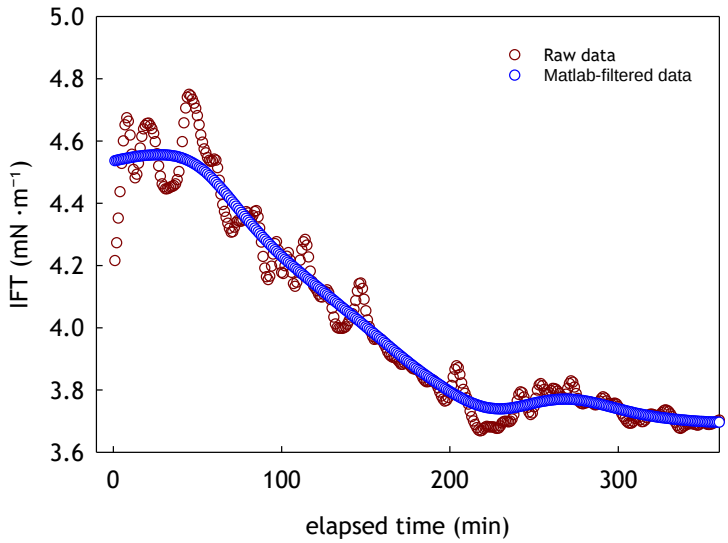

Figure 4.12– Comparison between raw and Matlab-filtered IFT data (HS-SP60).

4.3.8.2.1 Hexylsalicylate

Figure 4.13 displays the IFT values from all HS-emulsifier systems investigated as a function of their HLB. When compared to their reference (*i.e.* no emulsifier) IFT_{HS} (16.0±0.1 $mN \cdot m^{-1}$), all the emulsifiers had proven effective at lowering the IFT. After 6 hours, all IFT values fell into the region 3.9-8.8 $mN \cdot m^{-1}$, which is significantly lower than IFT_{HS}. Although former literature has tentatively suggested a link between IFT and HLB of surfactant-assisted petroleum hydrocarbons [387], there appeared to be no clear interrelationship between the average IFT values and the HLB of the HS-emulsifier system presented herein. Notwithstanding, it was important to understand how rapidly (≤6h) the adsorption of each emulsifier onto the HS droplet interface occurred.

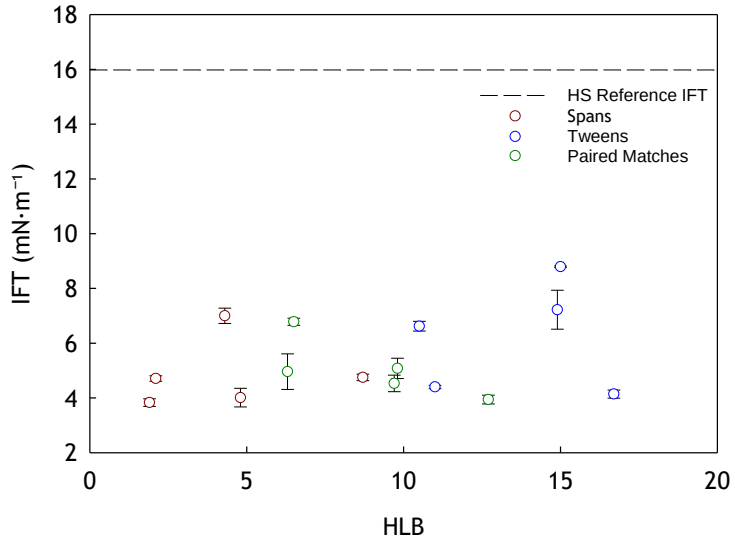

Figure 4.13– IFT after an elapsed time of 6 hours *versus* HLB of HS-emulsifier systems. Error bars may be smaller than the size of symbols.

IFT-time curves of HS-emulsifier systems are plotted in Figure 4.14. When compared to IFT_{HS}, Spans (Figure 4.14A) and Tweens (Figure 4.14B) seemed to adsorb rapidly at the interface of

HS, independently of their HLB. Most of HS-emulsifiers systems plateaued within 3h. No fluctuating trends were obvious, which may suggest good chemical affinity between HS and the emulsifier types [384]. Although paired Spans-Tweens seemed also effective, their trends appeared more unstable (Figure 4.14C), which led to no stable *plateau* after 6h. Based on the results, paired Spans-Tween may be naturally less suitable for the purpose, or insufficiently concentrated resulting in their slower adsorption. Besides, there appeared that some emulsifier combinations (*e.g.* SP80 and SP60TW60) surprisingly led to a mild increase of the IFT after 6h. Although a very small amount of emulsifier adsorbed at the droplet surface may contribute to reducing the IFT, hence promoting the stability of emulsions and hampering coalescence, the emulsifier's chemical type should also be considered. Specifically, increasingly high IFT trends over time seem to suggest that certain combinations of emulsifiers might be hardly compatible with the selected oil (HS) in water due to their nature and chemo-physical properties. Accordingly, this might probably lead to reducing the surface elasticity of the droplets, hence destabilising and possibly increasing their IFT. Having said that, the typical development of an emulsifier-assisted oil droplet over time is presented in Figure 4.15A-G.

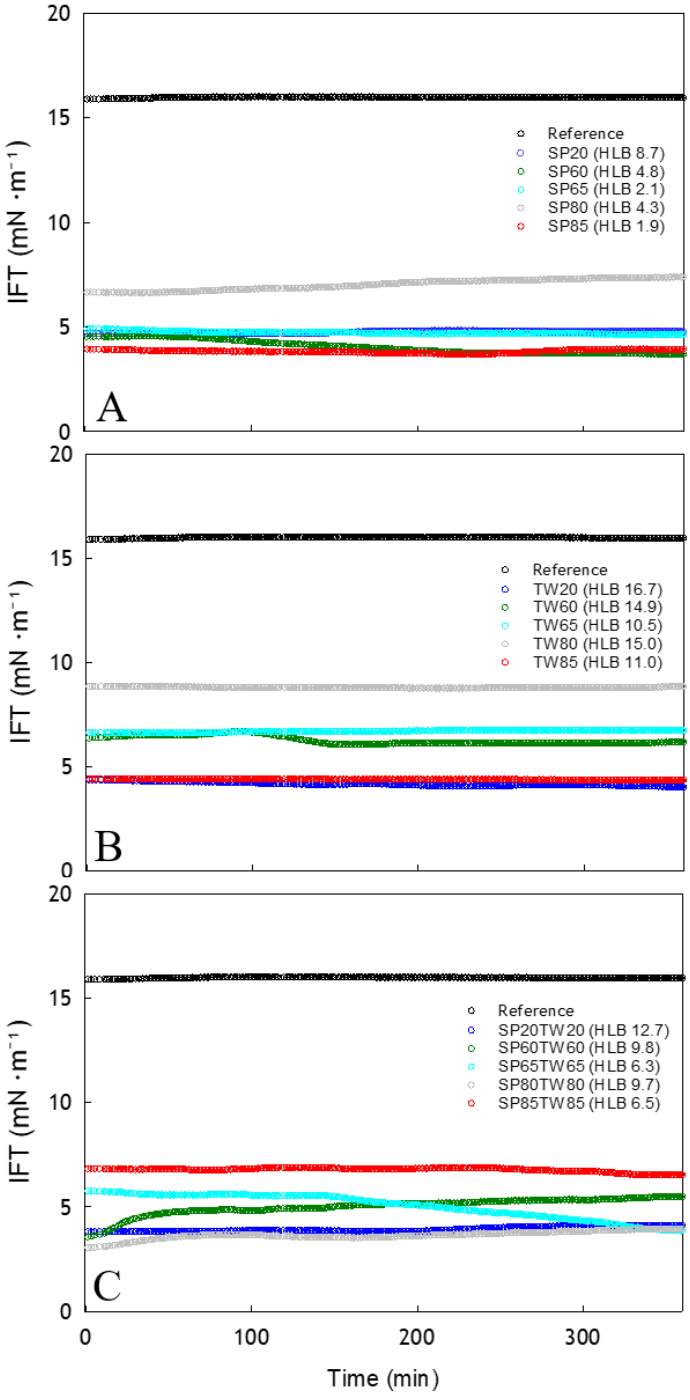

Figure 4.14– Effect of different (A) lipophilic (Span20,60,65,80,85), (B) hydrophilic (Tween20,60,65,80,85), and (C) hydro-lipophilic (Tween-Span20,60,65,80,85) emulsifiers (0.1% w/w) on the dynamic interfacial tension (IFT) of HS-water systems. IFT_{HS} is displayed for comparison.

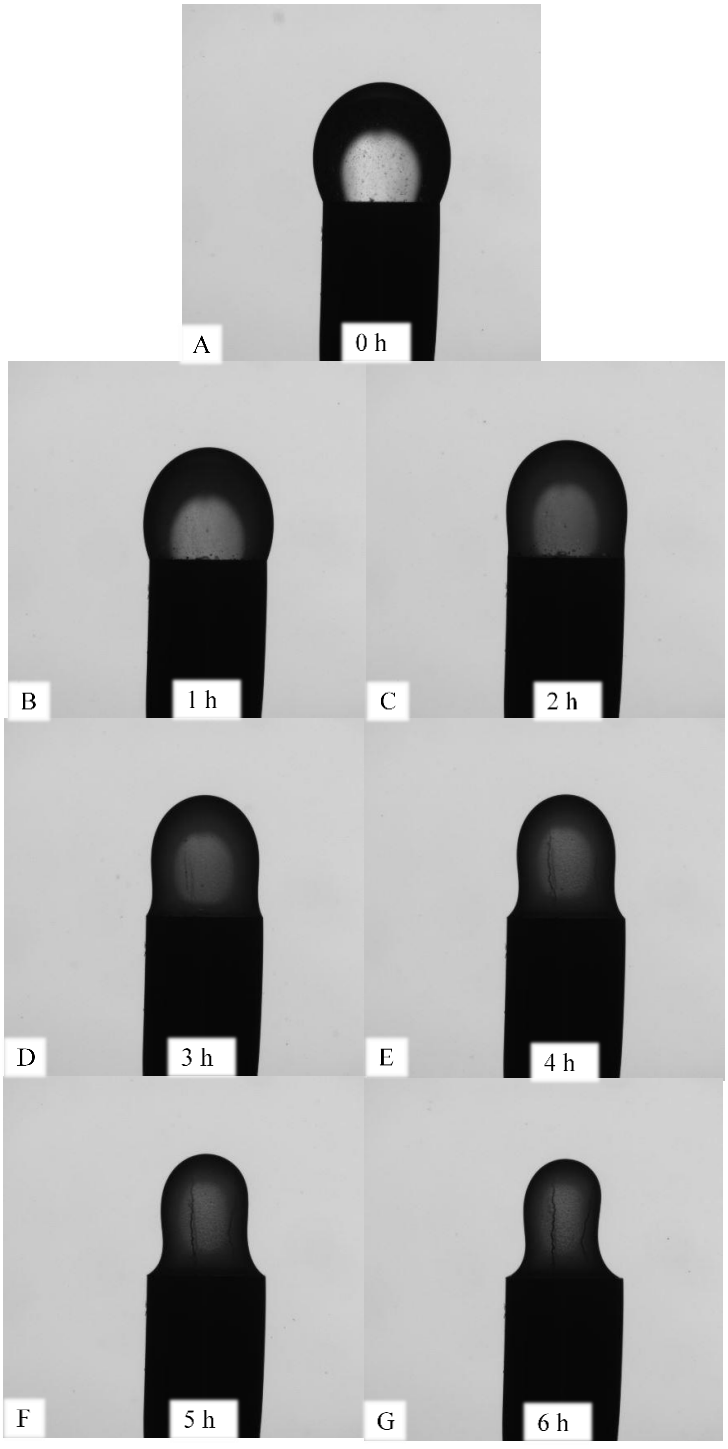

Figure 4.15– Real-time IFT adsorption of the emulsifier (Span) at 0h (A), 1h (B), 2h (C), 3h (D), 4h (E), 5h (F), and 6h (G).

4.3.8.2.2 L-Carvone

Figure 4.16 displays the IFT values from all LC-emulsifier systems investigated after 6 hours *versus* their HLB. As for HS, all the emulsifiers enabled IFT values significantly lower than IFT_{LC} (7.6±0.2 $mN \cdot m^{-1}$). The IFT values fell into the region 0.9-4.0 $mN \cdot m^{-1}$ and showed no direct dependency between IFT and their HLB values. Specifically, SP85 (HLB 1.8) and TW85 (HLB 11.0) reduced the IFT least significantly, whereas TW80 (HLB 15) showed higher affinity at lowering IFT_{LC}, as well as SP80TW80 (HLB 9.7; IFT=0.8±0.5 $mN \cdot m^{-1}$) and SP85TW85 (HLB 6.5; IFT=1.0±0.4 $mN \cdot m^{-1}$).

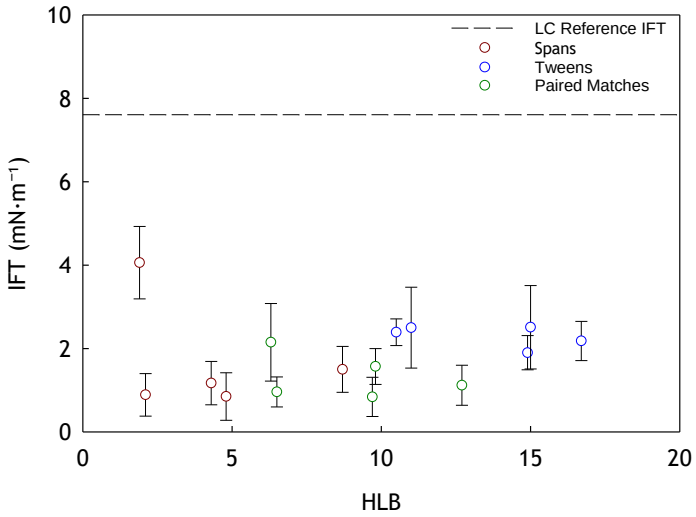

Figure 4.16– IFT after an elapsed time of 6 hours *versus* HLB of LC-emulsifier systems.

As can be seen in Figure 4.17, the dynamic adsorption of the emulsifiers at the LC-water interface was moderately slow, and a clear *plateau* was difficult to achieve. As for HS, this suggests that higher amounts of emulsifiers may be needed to accelerate the adsorption of the emulsifiers. Although HLB is primarily important to investigate the effect of emulsifiers on o/w systems, it may not be exhaustive. Additional parameters, such as the chemical nature of emulsifiers, should be considered to form stable and clear emulsions. As reported in literature, the clarity of emulsions can be evaluated *via* an optical density ratio technique, which was proven relatively accurate to investigate the emulsion stability as well [354]. Accordingly, investigation on the optical density of o/w emulsions was conducted.

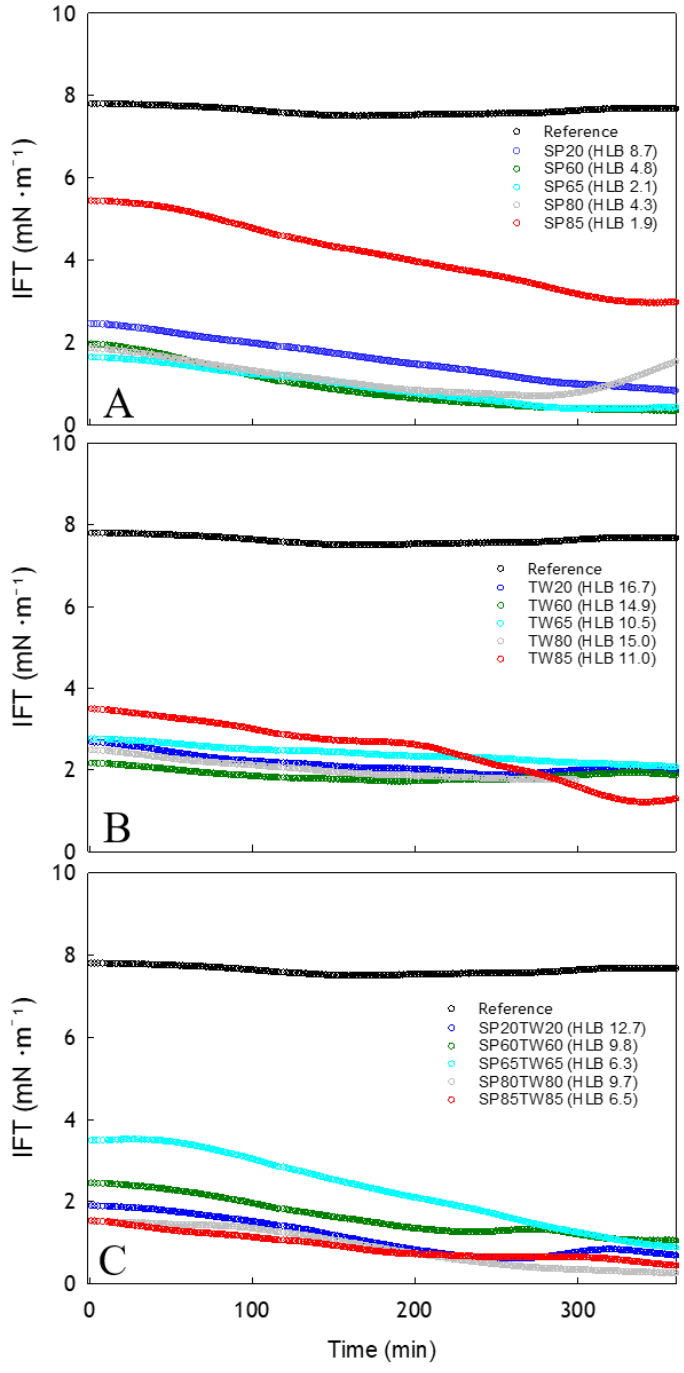

Figure 4.17– Effect of different (A) lipophilic (Span20,60,65,80,85), (B) hydrophilic (Tween20,60,65,80,85), and (C) hydro-lipophilic (Tween-Span20,60,65,80,85) emulsifiers (0.1% w/w) on the dynamic interfacial tension (IFT) of LC-water systems. IFT_{LC} is displayed for comparison.

4.3.8.3 Optical Density

Kinetically stable emulsions are desirable for microencapsulation. Therefore, coalescence phenomena should be inhibited [354]. Unstable emulsified oil droplets tend to coalesce into larger and larger droplets. This phenomenon leads to increase optical density, whose absorbance (Abs) can be measured *via* UV-Vis at specific wavelengths at given intervals. Song *et al.* [354] have used two different wavelengths, namely λ^* and λ_{Ref}, which represent the wavelength of maximum absorbance of the oil of interest and a reference wavelength, respectively. In this study, λ_{Ref} was 650nm, which has been widely used for turbidity and microbiological studies in wines and bacterial cultures [355]. Therefore, the λ_{Ref}-to-λ^* ratio was used to evaluate the increase in turbidity over time of fresh emulsions (*i.e.* HS, LC; oil-to-water fraction 4% w/w) with or without emulsifiers. Previous literature has elucidated that the turbidity at longer wavelengths (λ_{Ref}) should change much faster than at shorter wavelengths (λ^*_{HS}=306nm; λ^*_{LC}=320nm) since the larger droplets tend to coalesce and cream out at a much faster rate than the smaller ones [354, 388]. In other words, the more unstable the emulsion is, the faster the turbidity ratio changes. Therefore, the establishment of a normalised ratio between the absorbance recorded at λ_{Ref} and λ^* ($Abs_{\lambda ref}/Abs_{\lambda^*}$) may be beneficial to investigate the stability of emulsions. Although former literature has evidenced the effectiveness of this methodology [389], no study has arisen on the dynamic stability of emulsion so far. This piece of work originally focused on the emulsion dynamic stability (EDS) and the resulting EDS constants (ς_{EDS}) of the o/w systems of interest, based on the increase in optical density of emulsions over time. Figure 4.21 elucidates the procedure to determine ς_{EDS}, which is obtained from the normalised optical density (NOD) of o/w systems in the presence of emulsifiers (Table 4.2).

4.3.8.3.1 Determination of the Emulsion Dynamic Stability Constants

As shown in Figure 4.18, the normalised optical density of HS-SPAN85 was found to increase progressively with time. Specifically, the normalised optical density (NOD) exhibits a linear increase with time, which is likely due to coalescence and creaming-out processes [354]. A rapid increase in NOD suggests that freshly formed emulsions may be unstable. Although emulsifier-assisted emulsions are more likely to be stabilised, the nature of the o/w system along with the emulsifier's chemical type plays a synergistic role. Having said that, kinetically unstable emulsions may be also ascribable to a tentative/poor emulsifier-driven interfacial stabilisation of oil droplets resulting in their impaired surface elasticity, which in turn may lead to a weakened interfacial film forming between two immiscible phases [384]. Overall, the dynamic emulsion stability constant is a key indicator to assess the stability of oil droplets prior to microencapsulation processes. It was found that the experimental data could be fitted to a linear regression model. Specifically, a zero-order kinetics model best describes the emulsions' NOD:

$$\frac{d\,NOD}{dt} = \varsigma_{EKS} \tag{4.2}$$

with the integral boundary condition $NOD(t=0)=0$. Weak R^2 values (<0.5) observed from HS-TW60, HS-SP80TW80, LC-SP60, and LC-SP85 evidenced that no good fitting of the experimental data could be obtained. Thus, no statistically significant linear relationship could be identified in the above mentioned cases. This was due to the presence of outlying/scattered points, resulting in undefined trends. Besides, this finding seemed to highlight the behaviour of certain emulsions when combined with unsuitable emulsifiers, hence leading to their instability (*e.g.* creaming-out and coalescence phenomena).

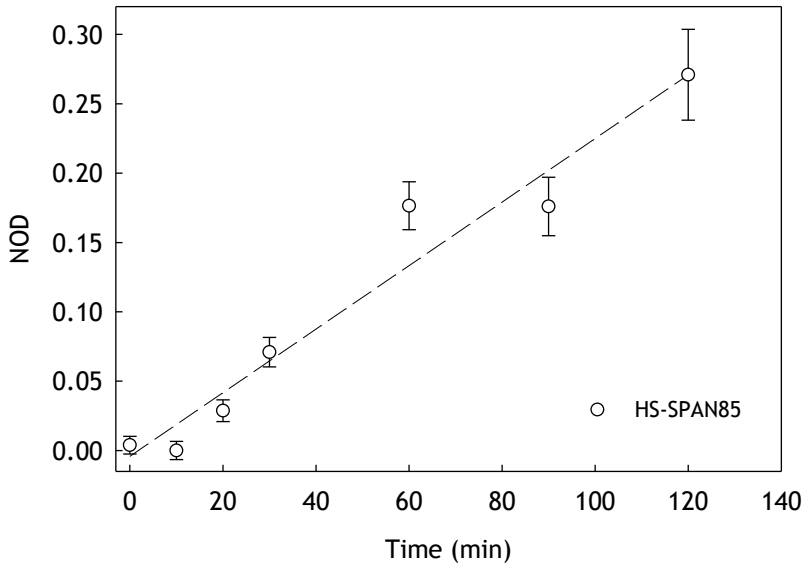

Figure 4.18– Determination of ς_{EDS} *via* linear regression (NOD=$\varsigma_{EDS\text{-}HS}$·t) of NOD ratio *versus* time. The slope (ς_{EDS}) is expressed as min^{-1}. The case herein shown (HS-Span85) provides $\varsigma_{EDS\text{-}HS}=2.24\cdot10^{-3}$ min^{-1}; $R^2=0.95$.

Table 4.2 displays all ς_{EDS} obtained together with their coefficients of determination. Span 85 was determined to be the most effective in stabilising the o-w systems, as its increase in NOD was the lowest. The lowest ς_{EDS} was $2.24\cdot10^{-3}$ min^{-1} attained with Span 85-assisted HS, which was around 20% lower than that determined in absence of any emulsifier ($2.68\cdot10^{-3}$ min^{-1}). When dealing with LC, food industry has long focused on polysorbates (Tweens) for emulsion preparations. Among all, Tween80 (often labelled as E433), has been preferred in food-grade formulations [390]. E433 has proven effective in facilitating aqueous ingredients and oils to blend together, such as ice creams, vitamins, and dietary supplements [391]. Accordingly, the extensive use of Tween80 in industry seems to confirm the versatility and suitability of its chemical type to many formulations. Based on the EDS results, Tween80 has also proven relatively effective in decreasing its reference $\varsigma_{EDS\text{-}LC}$ ($2.08\cdot10^{-2}$ min^{-1}) by around 58%

($8.56 \cdot 10^{-3}$ min^{-1}), which may suggest a stabilising effect of Tween80 on the LC emulsion in water.

Overall, these results seem to confirm a beneficial effect of Span 85 and Tween 80 on HS and LC, respectively. However, the stabilisation of an emulsion should be validated by the droplet size distribution (DSD) data, and how it this varies with time. The EDS analysis could be used as a methodology to quickly preselect the emulsifiers which may possess an emulsion stabilisation effect on the required o/w system. The DSD data for Span 85-assisted HS and Tween 80-assisted LC emulsions are presented as follows.

Table 4.2 – Determination of the dynamic emulsion stability (EDS) constants (ς_{EDS}) of o/w emulsions using emulsifiers. The optical density measurements are referred to λ^* and λ_{ref}. [(1)]Sample Identification (ID): 'OIL' refers to HS/LC. Span concentration in oil 0.1%(w/w); Tween concentration in water 0.1%(w/w). For example, the EDS constant (ς_{EDS}) for Hexyl Salicylate (HS) at 0.1% (w/w) Span60 (SP60) and 0.1%(w/w) Tween60 (TW60) is $\varsigma_{EDS\text{-}HS(SP60TW60)}$.

Emulsifier type		Two-phase system		HLB	Dynamic Emulsion Stability (EDS) constant (ς_{EDS})				Reference ID[1]
		Oil (HS/LC)[1]	Water		ς_{EDS-HS} (min^{-1})	R^2	ς_{EDS-LC} (min^{-1})	R^2	
N/A				N/A	$2.68 \cdot 10^{-3}$	0.91	$2.08 \cdot 10^{-2}$	0.68	OIL-BLANK
SPAN	20	✓		8.7	$2.29 \cdot 10^{-3}$	0.96	$6.62 \cdot 10^{-3}$	0.85	OIL-SP20
	60	✓		4.8	$3.08 \cdot 10^{-3}$	0.91	$5.72 \cdot 10^{-3}$	0.17	OIL-SP60
	65	✓		2.1	$2.36 \cdot 10^{-3}$	0.81	$6.11 \cdot 10^{-3}$	0.58	OIL-SP65
	80	✓		4.3	$2.26 \cdot 10^{-3}$	0.76	$5.04 \cdot 10^{-3}$	0.53	OIL-SP80
	85	✓		1.9	$2.24 \cdot 10^{-3}$	0.95	$2.45 \cdot 10^{-3}$	0.18	OIL-SP85
TWEEN	20		✓	16.7	$8.7 \cdot 10^{-3}$	0.98	$7.5 \cdot 10^{-3}$	0.72	OIL-TW20
	60		✓	14.9	$5.36 \cdot 10^{-3}$	0.26	$1.05 \cdot 10^{-2}$	0.93	OIL-TW60
	65		✓	10.5	$5.14 \cdot 10^{-3}$	0.89	$7.4 \cdot 10^{-3}$	0.80	OIL-TW65
	80		✓	15.0	$9.19 \cdot 10^{-3}$	0.84	$8.56 \cdot 10^{-3}$	0.64	OIL-TW80
	85		✓	11.0	$1.15 \cdot 10^{-2}$	0.86	$8.45 \cdot 10^{-3}$	0.93	OIL-TW85
PAIRED MATCH (SPAN-TWEEN)	20-20	✓	✓	12.7	$5.37 \cdot 10^{-3}$	0.69	$7.82 \cdot 10^{-3}$	0.86	OIL-SP20TW20
	60-60	✓	✓	9.8	$9.52 \cdot 10^{-3}$	0.59	$7.67 \cdot 10^{-3}$	0.76	OIL-SP60TW60
	65-65	✓	✓	6.3	$6.8 \cdot 10^{-3}$	0.96	$5.27 \cdot 10^{-3}$	0.70	OIL-SP65TW65
	80-80	✓	✓	9.7	$8.8 \cdot 10^{-3}$	0.20	$9.46 \cdot 10^{-3}$	0.89	OIL-SP80TW80
	85-85	✓	✓	6.5	$8.87 \cdot 10^{-3}$	0.78	$6.73 \cdot 10^{-3}$	0.88	OIL-SP85TW85

4.3.8.4 Droplet Size Distribution (DSD)

The size distributions (DSD) of the oil droplets of Span 85-assisted HS and Tween 80-assisted LC following o/w emulsification (1000 rpm (HS) and 8000 rpm (LC) for 30 min) are shown in Figure 4.19A and Figure 4.19B, respectively. Their variation with time is also displayed. From the analysis of DSD of HS, there appeared to be no significant variation or broadening of the DSD with time. This suggests that only a single population of droplets stayed relatively stable during the investigated timeframe (0-45 min). This timeframe was found to be compatible to perform all the physical operations required for microencapsulation, hence inducing complex coacervation safely without any significant variation of the droplet size. At t=0, a minor submicronic population with a broad peak was also detected. However, this peak was found to flatten down rapidly, confirming that very small droplets may tend to coalesce more quickly than larger ones. The Sauter mean diameter of HS droplets was found to be 27.9±0.2 μm at time 0 h (upon emulsification), which increased slightly to 35.4±0.7 μm after 45 min, as shown in Figure 4.19A (built-in graph). When dealing with Tween 80-assisted LC droplets, the DSD was found to shift towards a higher mean size much more rapidly than that of HS (Figure 4.19B). Therefore, the homogenisation of LC required much higher stirring speed in order to obtain sufficiently small droplets (27.4±1.3 μm) after 45 min. The built-in graph shows that only marginal increase of the Sauter diameter was thus detected. Overall, it seemed that the pre-selected emulsifiers, namely Span 85 and Tween 80 for HS and LC respectively, helped to stabilise the emulsified droplets, at least during the required timeframe prior to microencapsulation.

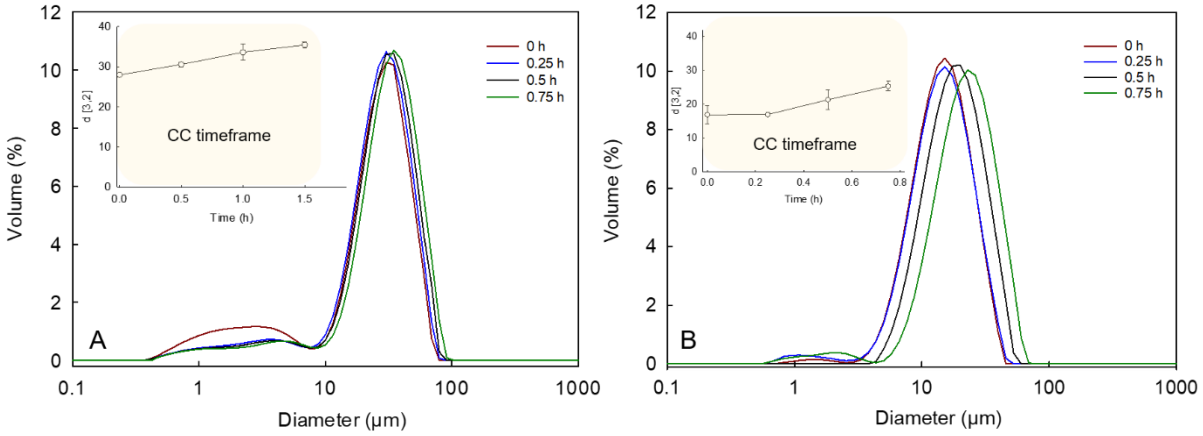

Figure 4.19– Droplet size distribution with time of Span 85-assisted HS (A) and Tween 80-assisted LC (B) emulsions in water. The o/w droplets of Span 85-assisted HS and Tween 80-assisted LC were generated into thermostated vessels at 30 ºC using a homogeniser (Model L4RT, Silverson Ltd, UK) operated at 1000 rpm and 8000 rpm for HS and LC, respectively. The investigated timeframe (0.75h) is based on the maximum operational timeframe required to carry out all the operations required prior to microencapsulation *via* complex coacervation.

4.3.8.5 Interrelationship among IFT, EDS, and DSD

Generally, NOD increases with time because emulsified oil droplets may coalesce. The more unstable the emulsion, the faster the increase in NOD [354, 390], and the higher the ς_{EDS}. As such, measurement of NOD is a relatively simple approach for evaluating EDS. However, it gives no information on IFT directly. For this reason, any potential interrelationship between IFT and EDS should be further investigated. Four aspects are crucial: (i) rapid adsorption of the emulsifier at the o-w interface resulting in an effective IFT and interfacial energy reduction; (ii) generation of non-fluctuating IFT trends, which helps identify the ideal emulsifying chemical types and their stabilising strength; (iii) low EDS values, which are associated with

potentially stable emulsions; and (iv) slowly/non-increasing droplet size with time, which is essential to identify the timeframe within which droplets do not coalesce, prior to any microencapsulation process.

For HS, the lowest $\varsigma_{EDS\text{-}HS}$ ($2.24 \cdot 10^{-3}$ min^{-1}) was obtained with SP85 (HLB 1.9) with R^2=0.95. Moreover, the $IFT_{HS\text{-}SP85}$ trend showed no fluctuation, which confirmed that SPAN85 reduced its IFT by ~75% ($IFT_{HS\text{-}SP85}$=3.8±0.2 $mN \cdot m^{-1}$), when compared to its reference (IFT_{HS}=16.0±0.1 $mN \cdot m^{-1}$). Additionally, the DSD of Span 85-assisted HS showed no significant variation or shifting with time up to 0.75h, with a very marginal increase of the droplet size. Overall, these findings seem consistent, thereby confirming that the emulsifier (Span85) preselected by EDS method can stabilise HS effectively, at least throughout the required timeframe prior to microencapsulation.

When dealing with LC, the dynamic adsorption of the emulsifiers at the LC-water interface seemed slow. A clear *plateau* was difficult to achieve in the presence of Spans for the time period investigated. Alternatively, Tweens were relatively effective at lowering IFT, with the exception of Tween85. LC-TW20 (HLB 16.7), LC-TW60 (HLB 14.9), LC-TW65 (HLB 10.5), and LC-TW80 (HLB 15.0) exhibited relatively stable trends and lowered the IFT_{LC} (7.6±0.2 $mN \cdot m^{-1}$) down to 2.2±0.5 $mN \cdot m^{-1}$, 2.0±0.4 $mN \cdot m^{-1}$, 2.4±0.3 $mN \cdot m^{-1}$, and 2.5±1.0 $mN \cdot m^{-1}$, respectively, after ~2h. Their mean IFT values did not differ significantly from each other, which confirms that the stabilising effect of these emulsifiers may not be directly related to their HLB. Based on the EDS analysis, LC-TW65 ($\varsigma_{EDS\text{-}LC\text{-}TW65}=7.4 \cdot 10^{-3} min^{-1}$) and LC-TW80 ($\varsigma_{EDS\text{-}LC\text{-}TW80}=8.6 \cdot 10^{-3} min^{-1}$) seemed to trigger the best dynamically stable systems. Although the coefficient of determination of the latter was weaker (R^2=0.64) than the former (R^2=0.8), Tween80 has been preferred to be used in food formulations, as extensively documented in literature [390]. Furthermore, the DSD analysis of Tween 80-assisted LC shows that relatively stable oil droplets were achieved without dramatic size variations during the investigated timeframe. However, the DSD tended to shift towards a higher mean size more rapidly than HS (Figure 4.19), which might be probably ascribable to the nature of LC being a terpene, whereas HS is an ester. Overall, the emulsifier (Tween80) preselected by the EDS method

seemed to provide relative oil (LC) droplet stabilisation, thereby hampering major coalescence throughout the required timeframe prior to microencapsulation.

4.4 Conclusions

The feasibility of pH-driven complex coacervation (CC) on a novel plant-based biopolymer system (*i.e.* fCh and GA) was investigated. The process based on the electrostatic-turbidimetric analysis of the biopolymers in order to determine the optimum processing conditions (pH_{CC} and biopolymer mixing ratio). The interrelationship between electrostatic and turbidimetric studies enabled to establish a theoretical-experimental complex coacervation comfort zone (CCCZ) according to the net electrokinetic charge/zeta-potential (ζ-CCCZ) and critical turbidity zone (CTZ) of both biopolymers. CCCZ was applied, which allowed to identify pH_{CC}=3.4 corresponding to a GA-to-fCh weight ratio of 6.7. These conditions led to formation of coacervate beads (CBs), with relatively smooth surface and a mean size of 21.3±3.1μm. Further characterisation included using a micromanipulation technique to determine the mechanical properties of CBs. Specifically, the rupture force and Young's modulus were 7.4±0.7 mN and 0.61±0.07 GPa, respectively. As a step forward towards microencapsulation *via* CC, oil-in-water emulsions were generated *via* homogenisation using oils with a potential application in detergent (HS) and food (LC) industry. Moreover, the emulsions were stabilised using emulsifiers (Spans, Tweens, and their blends), which allowed to investigate their dynamic stability. It was found that the effectiveness of emulsifiers to lower the IFT of oil droplets was not related to their HLB value. Span 85 was proven highly effective on HS ($IFT_{HS\text{-}SP85}$=3.8±0.1 $mN{\cdot}m^{-1}$) when compared to its reference IFT_{HS}=16.0±0.1 $mN{\cdot}m^{-1}$. This finding was also endorsed by the determination of EDS constants (ς_{EDS}), which were the lowest with Span85 ($\varsigma_{EDS\text{-}HS\text{-}SP85}$=$2.24{\cdot}10^{-3}min^{-1}$). Similarly, Tween 80 seemed to perform effectively with LC by decreasing its IFT_{LC} by 303±18% within 2h. Furthermore, the DSD analysis of both Span 85-assisted HS and Tween 80-assisted LC showed that relatively stable oil droplets were achieved without dramatic size variations during the timeframe prior to their microencapsulation.

Overall, it could be inferred that CCCZ may be beneficially envisioned as an *a-priori* route for predicting suitable biopolyelectrolyte pairs to chemically react *via* CC. The employment of plant-based materials to produce the coacervates may provide a novel approach towards the microencapsulation of value-added oils with a potential application in industry. Therefore, this may pave the avenue towards replacing the current products on the market, which is relying on animal derivatives or non-biodegradable polymers.

The next chapters address the microencapsulation of HS and LC guided by the established CCCZ and the EDS-DSD analysis.

Chapter 5 Fabrication of Perfume Oil Microcapsules using a Fungal Chitosan-based Shell Material with Potential Applications in Detergents †

5.1 Introduction

5.1.1 Overview

Microencapsulation in detergent industry is a very high-demanding area where sustained release is driven to the extreme. Specifically, detergent formulations are often produced with encapsulated perfumes to be released onto fabrics at a controlled rate for weeks after their last washing-impregnation cycle. Therefore, microcapsules need to be tested under the harshest conditions to assure that they can stay intact after washing and drying cycles, hence delivering their active perfume to fabrics sustainably and effectively [6]. Thus, it is essential to identify and optimise those properties of microcapsules responsible for assuring their prolonged stability, sustained release, and effective adhesion to fabrics. In other words, the mechanical, barrier, and adhesion properties are crucial for microcapsules with potential applications in detergents. The work presented in this chapter first focused towards encapsulating a model perfume oil within safe biopolymers, and then characterising the resulting microcapsules with a potential application in detergent industry accordingly. Specifically, the encapsulation of HS within a plant-based shell of fungal chitosan and gum Arabic *via* complex coacervation was investigated herein. The fabrication of microcapsules relied upon the CCCZ and EDS analysis, as presented in Chapter IV. A comprehensive characterisation of perfume oil microcapsules is

† Part published at Baiocco, D., Preece, J. A., & Zhang, Z. (2021), *Colloids and Surfaces A: Physicochemical and Engineering Aspects*, 126861.

herein provided, with particular emphasis on their mechanical, barrier, and adhesion properties. Three states of microcapsules (moist, air-dried and spray-dried) were characterised using several analytical techniques, namely SEM, TEM, FT-IR, and UV-Vis spectrophotometry. Moreover, the microcapsules were assayed for their mechanical properties, namely rupture force, nominal rupture stress, and nominal deformation at rupture. Both payload and encapsulation efficiency of HS were also quantified. Their oil leakage rate in aqueous environments was determined. The morphology, and structure including shell thickness of microcapsules were investigated by SEM and TEM respectively. Furthermore, the adhesion properties of the resulting plant-based perfume microcapsules onto fabric surface were characterised by using a flow chamber technique equipped with smooth polyethylene terephthalate (PET) film as a model. The interaction between the microcapsules and the PET film was investigated *via* image analysis (ImageJ), and their retention performance (RP) at increasing shear stress and different environmental pH was quantified.

5.1.2 Fragrance Encapsulation in Industry

Fragrances are currently added to many consumer products, such as detergent and personal care products, to aid the consumer perception of cleanliness and freshness to encourage consumer to repeat purchase [4, 7]. Fragrances are volatile organic compounds (VOCs) which may be chemically reactive and prone to evaporating during storage and/or react with other formulated ingredients, if incorporated directly into a product formulation [8, 9]. Therefore, strategies to inhibit fragrance evaporation and chemical degradation in formulated products are desirable, as they allow minimising the fragrance required in the final product. This dramatically reduces the cost of manufacturing, but still contributes to enhancing consumers' experience, subsequently leading to an increasing revenue. To this end microencapsulation, first pioneered by Bungenberg de Jong in 1929 [12], has been used to encapsulate VOCs leading to (i) reduced oil volatility in formulated products, and (ii) partitioning from the rest of formulation reducing cross-reactivity with other actives. Microencapsulation has successfully enabled a reduction in the amount of fragrance required without impacting consumers'

experience [16]. Furthermore, microcapsules containing the fragrance act as delivery vehicles by physically attaching themselves onto clothes or fibres during a washing cycle. They are designed not to release their fragrance until mechanical action breaks the capsule, such as caressing or wearing a garment, resulting in a prolonged customer experience of freshness [18]. Several techniques have been developed to encapsulate value-added actives against adverse environmental conditions [3]. Among all, complex coacervation has proven effective, leading to high-payload microcapsules with potentially tuneable mechanical properties [58]. Well established in fine decorative cosmetics, personal care toiletries, and household cleaning products, hexylsalicylate can provide an appealing hazard-free floral scent. Moreover, it is a single-molecule chemical, hence can be used as a model oil in microencapsulation [119].

5.2 Materials & Methods

5.2.1 Materials

Details on all materials can be found at Section §3.2.

5.2.2 Preparation of HS-Microcapsules

The microcapsules were fabricated *via* one-step complex coacervation extensively detailed by Baiocco *et al.* [238], as well as in §3.3.4.

5.3 Results & Discussion

5.3.1 Formation of HS-Microcapsules: Real-Time Monitoring

As discussed in Chapter 4, pH_{ψ} has been experimentally validated as the starting point of CC, at which insoluble GA-fCh complexes began forming. In the presence of oil droplets (oil-to-water fraction 4.5% w/w), GA-fCh complexes were observed to form at pH_{ψ}, which migrated towards the surface of oil droplets, subsequently encircling them (Figure 5.1A). The upper bound pH of CC has been associated with its pKa_{fCh} (~6.0) where no clear formation of the intact shells *via* CC around single oil droplets was observed (Figure 5.1C). Hindered CC phenomena were probably due to the cationic charge drop of fCh at pH~pKa_{fCh}. Importantly, it was found that GA-fCh shells could be seamlessly formed around each individual oil droplet at pH_{CC} 3.4 (Figure 5.1B), where the attractive interaction between GA and fCh was maximised, as discussed for coacervate beads (§4.3.7).

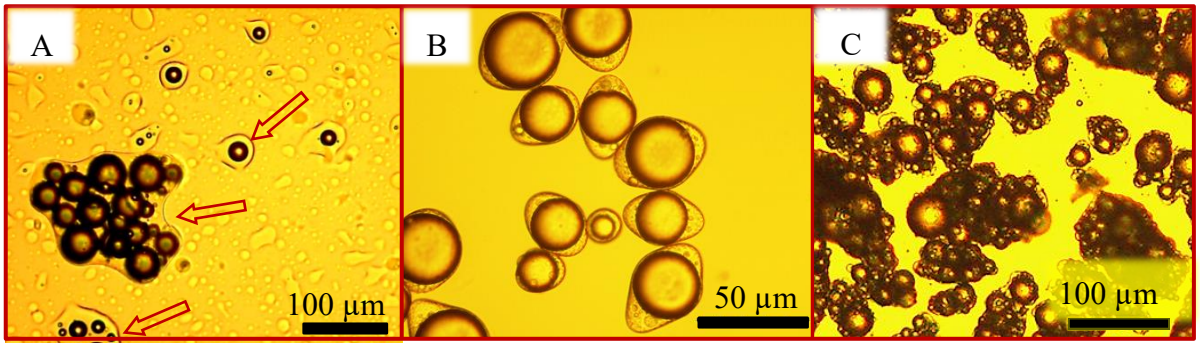

Figure 5.1– Optical microscopy imaging of: (A) incipient formation of shells entrapping single/multiple oil droplets *via* CC (pH_{ψ} 2.5, T=25°C); (B) eye-shaped microcapsules with a core of HS (pH 3.4, T=25.0°C); (C) no clear formation of the intact shell *via* CC around single/multiple oil droplets (pH 6.0, T=25.0°C). The arrows in (A) indicate the formation of coacervate network around the oil droplets.

5.3.2 Morphology

SEM images of dried HS-entrapping microcapsules are presented in Figure 5.2. An overview of the microcapsules is displayed in Figure 5.2A. It can be observed that the microcapsules were relatively spherical with a moderately rough surface (Figure 5.2B). The presence of significant surface pores might have been due to the extreme vacuum conditions resulting in the typical liquid-puffing phenomenon (Figure 5.2H), which had been extensively investigated by Farshchi *et al.* [392]. The microcapsules were found to be sensitive to high vacuum as well as prolonged electron beam exposure due to which structural damage of microcapsules with the resulting oil leakage were observed (Figure 5.2C-D). Interestingly, eye-shaped microcapsules were obtained by moderate stirring (400 rpm) (Figure 5.2E); alternatively, more spherical microcapsules were obtained at 1000 rpm (Figure 5.2F). At the lower stirring speed, the oil droplets/microcapsules were larger on average (Figure 5.3), which means their corresponding specific surface area (surface area per volume) was smaller. Consequently, there would be more shell materials available for coating each oil droplet. Therefore, the excess amount of the shell materials could be deformed around the oil droplets by the agitation during the solidification, thereby generating eye-shapes shells. Similarly, elongated shapes were also reported by Leclercq *et al.* [173] for gelatine-based microcapsules by CC. At the higher speed, the oil droplets were expected to be smaller, and the effect of their interfacial tension with the continuous phase was more significant to minimise their surface area, resulting in more spherical droplets, then microcapsules. The shell of a randomly selected cryo-damaged microcapsule is also presented in Figure 5.2G. Interestingly, there appeared that the shell of such HS-entrapping microcapsules may be several hundred nanometers thick.

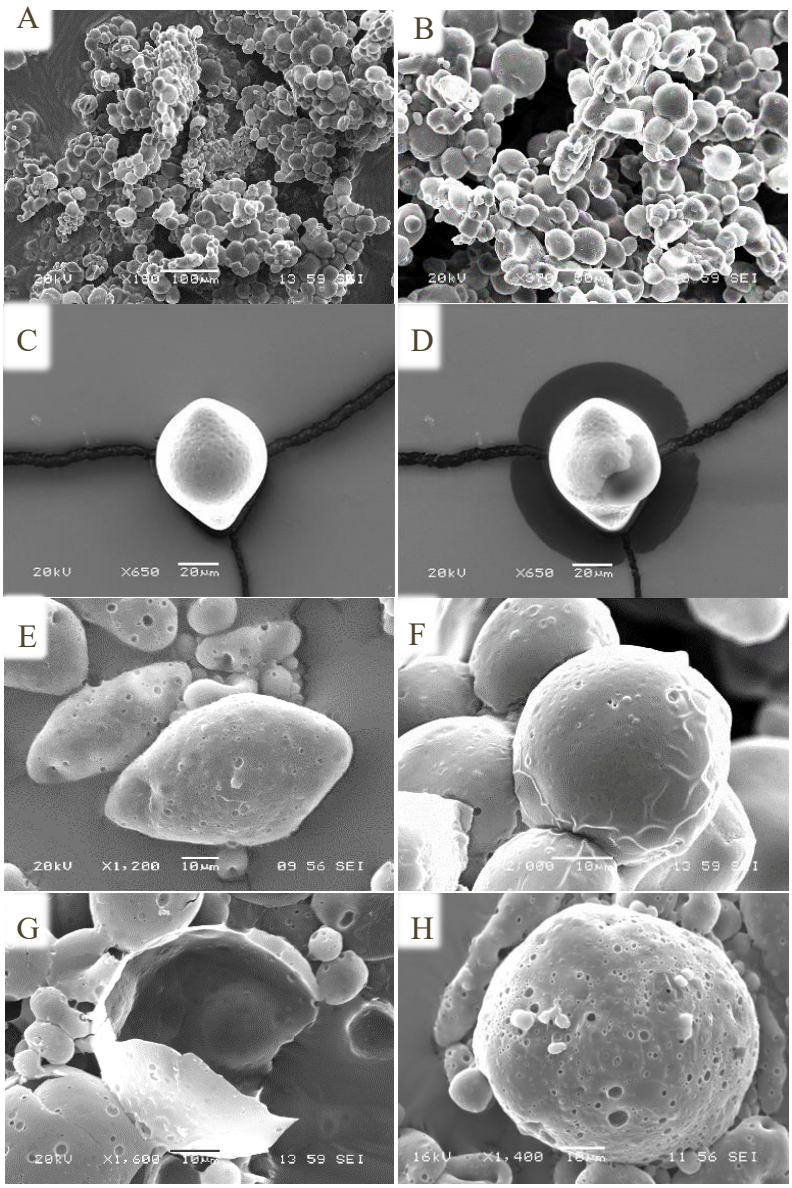

Figure 5.2– SEM images of dried HS-entrapping microcapsules with different magnifications being ×100 (A) and ×370 (B); foreground images of a dried microcapsule exposed to high vacuum conditions before (C) and after leaking (D); effect of the stirring rate on microcapsules obtained at 400 rpm (E) and 1000 rpm (F); highlight of a cryo-damaged microcapsule (G) and multiple surface pores possibly due to liquid puffing from microcapsules (H).

5.3.3 Size Distribution

The size distribution of HS-entrapping microcapsules obtained at 400 rpm , ranged between 20 and 117 µm (SPAN=1.23) together with a mean Sauter diameter of 50±2 µm (Figure 5.3). As expected, microcapsules obtained at a higher stirring speed (1000 rpm) exhibited a narrower particle size distribution (SPAN=0.94), between 15 to 78 µm with a mean diameter $D_{[3,2]}$ of 35±1 µm. In addition, statistical analysis highlights that a Gaussian distribution can be plausibly fitted to the microcapsule size distribution with 95% confidence. Both size and size distribution of moist microcapsules were proven consistent with their SEM micrographs (Figure 5.2).

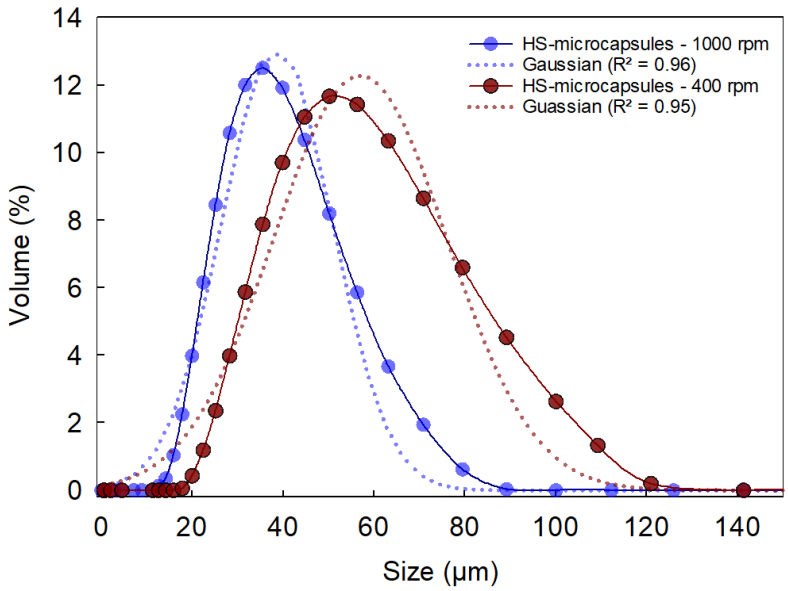

Figure 5.3– Size distribution of moist HS-microcapsules obtained at 400 rpm (red) and 1000 rpm (blue) fitted to a Gaussian distribution with 95% confidence. The general form of a three-parameter (a, b, x_0) Gaussian distribution function is $f(x) = a \cdot \exp\left(-\frac{1}{2}\left(\frac{x-x_0}{b}\right)^2\right)$. Non-linear regression and performance parameters: $a_{HS,400}$=12.3±0.53; $b_{HS,400}$=19.1±0.88; $x_{0HS,400}$=56.9±0.97; coefficient of determination $R^2_{HS,400}$=0.95; $a_{HS,1000}$=13.0±0.40; $b_{HS,400}$=12.5±0.42; $x_{0HS,400}$=38.7±0.45; coefficient of determination $R^2_{HS,400}$= 0.96.

5.3.4 Functional Groups Interrelationship (FT-IR)

GA and fCh powders, HS as well as HS-entrapping microcapsules were all assayed for their FTIR spectra. An observation of fCh's spectrum (spectrum α Figure 5.4) highlights a broad vibrational band occurring at 3383 cm^{-1}, which is related to the amino-hydroxyl ($–NH_2$ –OH) moieties. A characteristic band found at 2893 cm^{-1} was obvious and ascribable to the vibration of C–H bond [171, 382]. A few more bands peaking at 1681, 1595, 1303 cm^{-1} were detected and tentatively associated with the stretching vibration of the double-bounded C=O segment occurring in the acetylated groups ($–CONH_2$), the amide III units ($–NH_3^+$) [34], and the synergic effect due to –CH and –OH, respectively [393]. Furthermore, the symmetrical stretching vibration of C–O–C and the stretch absorption of C–O could be read at 1159 and 1036 cm^{-1}, respectively. The typical absorption bands of GA are displayed in the spectrum β Figure 5.4. Specifically, the –OH-related stretching vibrations could be identified at 3340 cm^{-1}. Another absorption band was evident at 1610 cm^{-1}, which was attributable to the conjugated C=C units. Furthermore, the non-symmetrical as well as symmetrical vibration of the carboxylated ions ($–COO^–$) was detected in the region of 1290 cm^{-1}. Similarly to fCh, a 1033cm^{-1} peak was found to be corresponding to C–O-unit stretching [394]. The spectrum γ in Figure 5.4 displays the FTIR spectrum of HS. Specifically, the strong band appearing at 1720-1630 cm^{-1} was assigned to the typical stretching vibration of the double-bounded C=O segment of aromatic carboxylic esters [395]. Similarly, the bands located at 1230-1140 cm^{-1} and 1120-1020 cm^{-1} were related to the stretching of C–C–O and O–C–C groups of the saturated ester [396]. Moreover, the peaks at 2954 cm^{-1} and 2864 cm^{-1} were ascribable to the aromatic and alkyl C-H stretching, respectively. The FTIR spectrum of tableted HS-microcapsules is shown in the spectrum δ in Figure 5.4. The band visible around 3280cm^{-1} was ascribable to the stretching vibration of amine ($–NH_2$) and hydroxyl (–OH) groups. When comparing the spectra α and β in Figure 5.4 with the spectrum δ in Figure 5.4, it could be deduced that a significant modification of the FTIR spectrum occurred in HS-microcapsules due to the presence of the fCh-GA shells. This phenomenon was also reflected in the presence of broader peaks assigned to the carbonyl-amide region (1650-1300cm^{-1}), possibly suggesting the successful electrostatic interplays between the $–NH_3^+$ segments of fCh and the $–COO^–$ of GA [382]. Besides, Kildeeva

et al. [397] have also reported the formation of azomethine groups (Schiff base) in the region of 1680–1620 cm^{-1}, which cannot be excluded following CC. Other peaks were also obvious at 3315 cm^{-1} as well as 3159 cm^{-1}, 1406 cm^{-1}, and 1033 cm^{-1}, which were cautiously associated with the stretching vibrations of amino(–NH_2)-hydroxyl(–OH) groups, alcoholic segments (–OH), amino-acid zwitterions exhibiting a C=O group, and C–O units, respectively. Furthermore, a narrow peak possibly indicating the development as well as the stretching of vinyl groups (–CH=CH_2) was also detected at 920 cm^{-1}. The absorbance peak occurring at 611 cm^{-1} may suggest the stretching vibration of N–H. However, it may also indicate the establishment of a new chemical segment attributable to the side formation of chloro-alkanes, since HCl had been employed to adjust the pH in the process. In addition, a moderately broad absorbance peak detected at 1033 cm^{-1} may be due to the major vibrational stretching of alcoholic segments. Overall, these peaks were found to be in agreement with what was reported by Espinosa-Andrews *et al.* [382]. Additionally, the comparison between spectra γ and δ highlighted that no strong signal associated with HS was detectable in the tableted HS-microcapsules. This phenomenon may be due to HS being screened out by the encapsulating polymeric matrix made of fCh and GA. Therefore, the spectra of fCh (Figure 5.4 spectrum α) and GA (Figure 5.4 spectrum β) seemed much similar to that of HS-microcapsules (Figure 5.4 spectrum δ). However, Figure 5.4δ also exhibited two relatively broad bands with sharp peaks at 1400-1200 cm^{-1} and 750-600 cm^{-1}. Since these peaks were not observed from the spectra α and β, they could be likely attributed to some weak interference due to presence of sub-shell oil (HS) in the HS-microcapsules. In addition, this finding may also provide indirect information on the shell thickness of HS-microcapsules, given that the depth of penetration of FTIR measurements is typically in the micron range. The shell thickness should be in the range of several hundreds of nanometres and the FTIR penetration depth itself, following the very weak signal attributable to HS in the FTIR spectrum of HS-microcapsules. This observation was consistent with the SEM micrograph presented in Figure 5.2G.

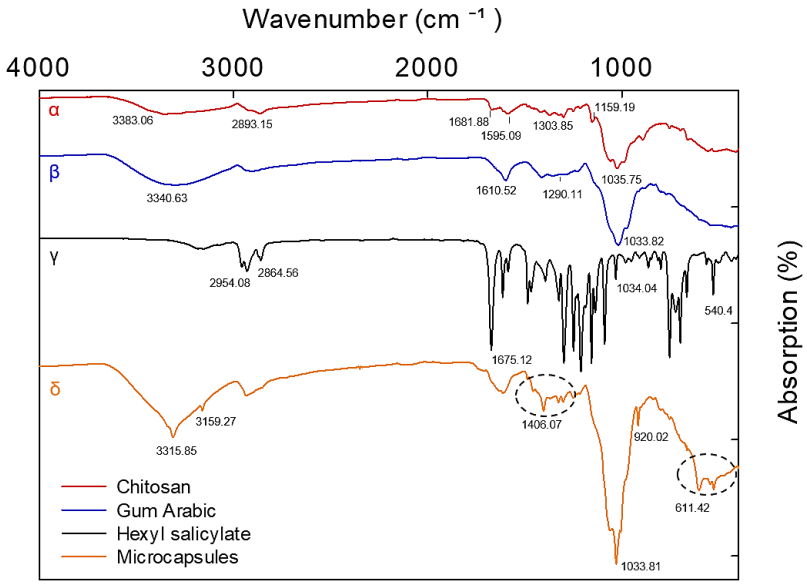

Figure 5.4– FT-IR spectra of solid fCh (α), GA (β), HS (γ), and tableted microcapsules (δ).

5.3.5 Encapsulation Efficiency (EE)

The EE and payload tests were directly carried out on freshly spray-dried HS-entrapping microcapsules with a spherical shape obtained following the procedure at 1000 rpm. The EE and payload values were determined to be 47±11% and 40±7%, respectively. With regards to the results obtained, it could be inferred that an aliquot of the HS dispensed in the formulation stage was either lost or unable to get encapsulated during the encapsulation process. This phenomenon might be due to naturally occurring oil encapsulation limitations, possible interactions between the chemicals, surface oil residues, oil leakage, and environmental, hydrodynamic and mechanical stress. However, similar values of EE (30-80%) for microcapsules achieved via CC were also reported in former literature [6, 7, 169, 173].

5.3.6 Barrier Properties

Oil release profile of microcapsules is primarily conditional upon the nature of the retained active ingredient interacting with the reticular shell complex. The composition of the dispersing medium also plays a key role. Water-based (cosolvent-free) medium is the most typically used, but also cosolvent-enriched media can be employed if accelerated tests are required [16].

5.3.6.1 Solubility Experiments

The solubility HS in water at ambient temperature ($c_{s,HS} \simeq 10^{-6} g \cdot mL^{-1} \simeq 4.5$ μM) is very low [264]. Therefore, a different HS-receptor system should be identified to increase c_s to adequate values ($\sim 10^{-2} g \cdot mL^{-1}$) above the limit of detection of the UV-Vis setup. This system should be hazard-free, fully miscible with HS, not highly viscous to assure well-mixed conditions. Importantly, it should trigger no structural damage of the capsule shells. Previous literature suggested that ethanol and 1-propanol may fulfil these requirements [16]. HS was assayed for its solubility in 1-propanol by UV-Vis (§3.4.4.2), which is less volatile (1.9 kPa) than ethanol (5.4 kPa) at 20ºC. Figure 5.5 displays the saturation concentration of HS in 1-propanol ($c_{s,HS}$) in different hydro-propanolic environments (0-50%w/w). It was found that 36%(w/w) aqueous propanol solution increased the solubility of HS to $\sim 9 \cdot 10^{-3} g \cdot mL^{-1}$ effectively, as reported by Mercade-Prieto *et al.* [16]. For this reason, 36% (w/w) hydro-propanol was adopted as a model receptor medium for HS released from microcapsules.

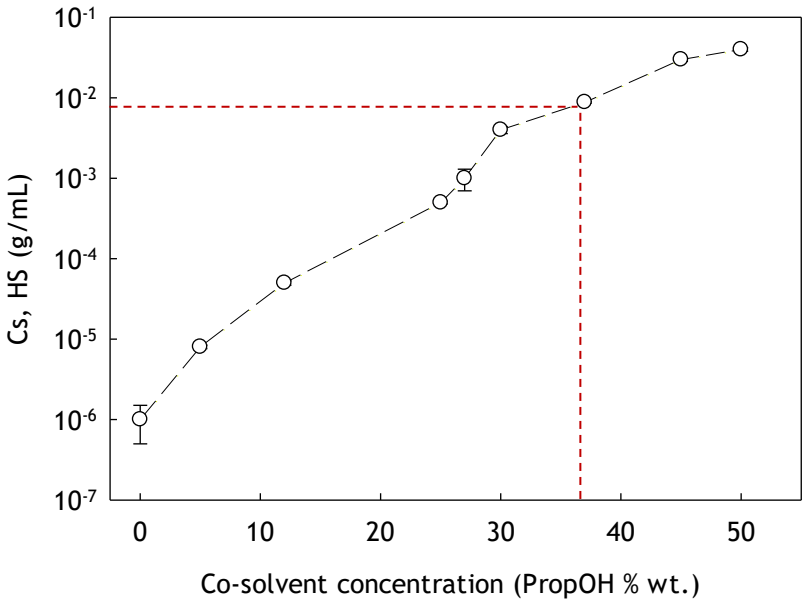

Figure 5.5– Saturation concentration of HS ($c_{s,HS}$) in hydro-propanolic media (0-50 w/w). The Error bars that represent the standard error may be smaller than the size of the symbols.

5.3.7 Release Profile

As shown in Figure 5.6, a different time-dependent release of HS occurred from fCh-GA microcapsules when exposed to chemically different environments. In water for a month, only <10% HS leakage was observed, which is very encouraging, and might result from the good barrier properties of solid coacervate shells being polymer-rich and, thus water-insoluble complexes [398]. Alternatively, the evaluations in the presence of 36%(w/w) aqueous propanol have found that ~60% of the oil load leaked out from the microcapsules after 1 month. This suggested that the coacervate shells may be sensitive to slightly alkaline solutions [399] which might act as a leakage aid to microcapsules to release oil faster. Alternatively, the effect of the higher solubility of HS in aqueous propanol on its release may be significant. Accordingly, the increased solubility of the oil in aqueous propanol can thus accelerate the mass (HS) transfer from the microcapsules into the receptor medium significantly, when compared to absolute

water. When dealing with the long-term release, a typical exponential trend was identified for both cases over the investigated timeframe (>500h). This was more obvious for the propanol-driven test, which curve flattened after ~250h. Overall, it could be deduced that suitable co-solvents may proactively contribute to determining the oil leakage rate of oil-entrapping microcapsules, thereby assessing their barrier properties.

Since the release tests were designed such that no saturation of HS can be reached in water/aqueous propanol, it is important to understand why 100% release of HS did not occur. Although oils might be lost by evaporation, the vapour pressure of HS at ambient temperature is extremely low (0.07 Pa), which does not explain why ~40% of the total oil could not be detected. A more likely hypothesis deals with the nature of the coacervate shells. Since the shells are fabricated by coacervation from organic materials, the solubility and absorbability of HS in the coacervate matter can be significant. Therefore, the coacervate shells might get saturated with HS before the oil (HS) can be transferred into the receptor medium.

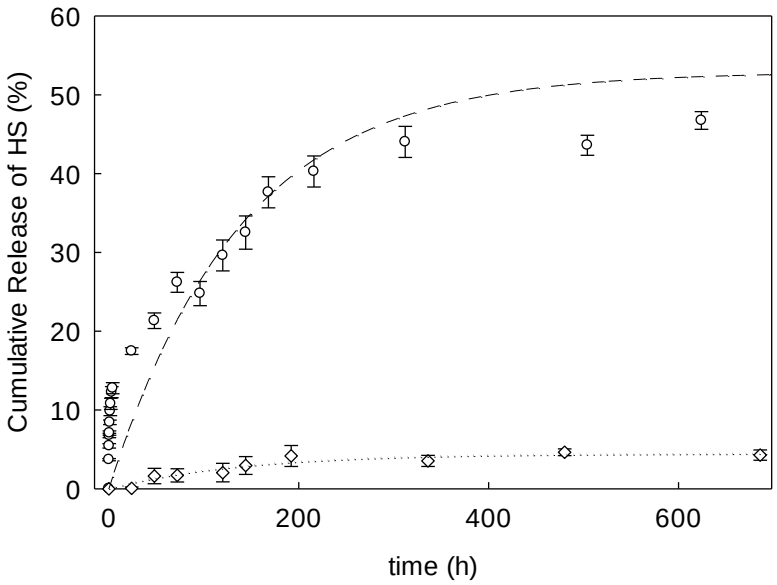

Figure 5.6– Leakage profile of HS-microcapsules in cosolvent-free water (◊) cosolvent-enriched (○) water (36%(w/w) propanol). Dashed and dotted curves display the trend of the release profile fitted to a non-linear regression model $y = \xi(1-e^{-ßt})$ based on the least squares analysis, with the corresponding evaluation of the coefficient of variation (CV(%) = St. Deviation/mean·10^2) using SigmaPlot 14.0 (SystatSoftware Inc.). Performance parameters (± St. errors): cosolvent-free (◊) $\xi_{◊}$=5.5±0.5, $CV_{\xi◊}$=9.0%, $ß_{◊}$=5.7·10^{-3}±1.2·10^{-3} h^{-1}, $CV_{ß◊}$=21.9%, R^2=0.93; cosolvent-enriched (○) $\xi_{○}$=54.1±3.0, $CV_{\xi○}$=5.7%, $ß_{○}$=7.1·10^{-3}±1.3·10^{-3} h^{-1}, $CV_{ß○}$=18.3%, R^2=0.87. Further analysis of the release data is presented in Chapter VII (§7.2.2).

5.3.8 Mechanical Properties

5.3.8.1 Compression of Single Microcapsules

A typical force-displacement curve from compression of a single randomly chosen microcapsule is shown in Figure 5.7. Points *α* to *β* correspond to the progressive compression of a microcapsule (built-in picture*s α-β*). Specifically, the *α-β* sequence shows an intact capsule before (*α*) being squashed out following the increasing force exerted by a descending probe onto the surface of the microcapsule itself. This results in a flattened-up coacervate structure

from which the oil leaked out. Oil residues are also shown (β). In addition, a clear depletion of the force applied is evident at point β, which is due to the sudden burst of the microcapsule. Accordingly, the rupture force (F_r) of the selected microsphere can be determined. The nominal rupture stress (σ, defined as the ratio of the rupture force to its initial cross-sectional area) and the nominal strain at rupture (%, defined as the ratio of the displacement at rupture to original diameter) of microcapsules [400] have been calculated.

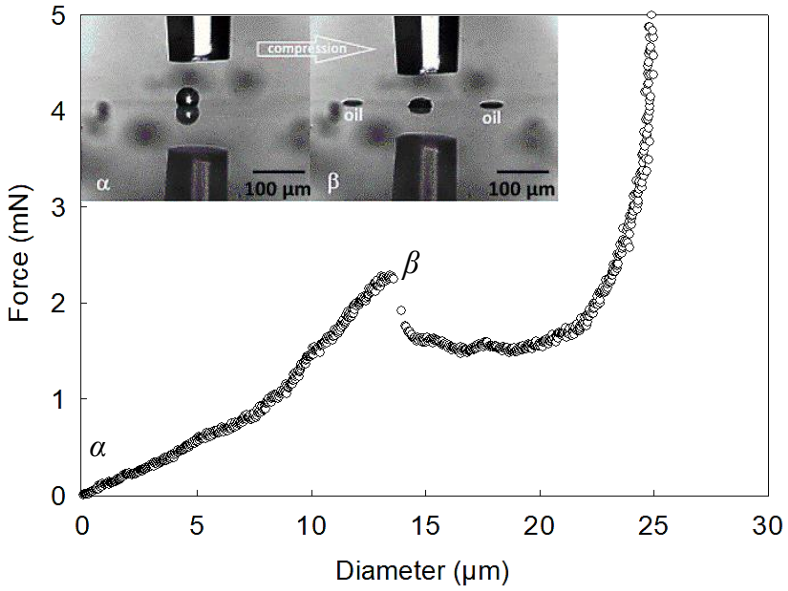

Figure 5.7– Typical force-displacement curve from compression of an air-dried 40µm microcapsule (fabricated at 1000rpm according to the procedure detailed in §3.3.4.3) with real-time pictures of its onset of compression (α) to its rupture (β).

5.3.8.2 Rupture Force, Nominal Rupture Stress, and Displacement at rupture of Single Microcapsules

The rupture force of HS-microcapsules was found to be averagely increasing with diameter (Figure 5.8A), which is in good agreement with melamine-formaldehyde microcapsules [25, 400, 401]. As displayed in Figure 5.8B, the nominal rupture stress was found to be decreasing with diameter, highlighting that greater microcapsules may be weaker and more likely to be broken than the smaller ones [14, 383]. Interestingly, the displacement at rupture increased with the size of the microcapsule. This may suggest that large microcapsules tend to deform for longer before getting ruptured. The nominal deformation (strain) at rupture did not change with the diameter significantly Figure 5.8D, and the mean value (22.7±1.5%) was obtained from the slope of the trendline in Figure 5.8C. This value is very similar to that obtained by Long *et al.* [14] from MF-microcapsules (24.8±1.5%), as shown in Table 5.1.

Table 5.1 – Key mechanical property parameters of HS microcapsules in comparison with MF-based microcapsules (Mean ± St. Error)

	HS-microcapsules	**MF-based**
Mean Diameter (μm)	27.5±1.5	4.0–24.0±1.0
Rupture Force (mN)	2.0±0.1	0.7±0.1– 2.1±0.2
Nominal Rupture stress (MPa)	3.6±0.3	4.2±0.4
Displacement at Rupture (μm)	6.3±3.1	3.5±0.2
Rupture Deformation (%)	22.7±1.5	24.8±1.5
Number of particles compressed	30	-
Reference		[14, 21]

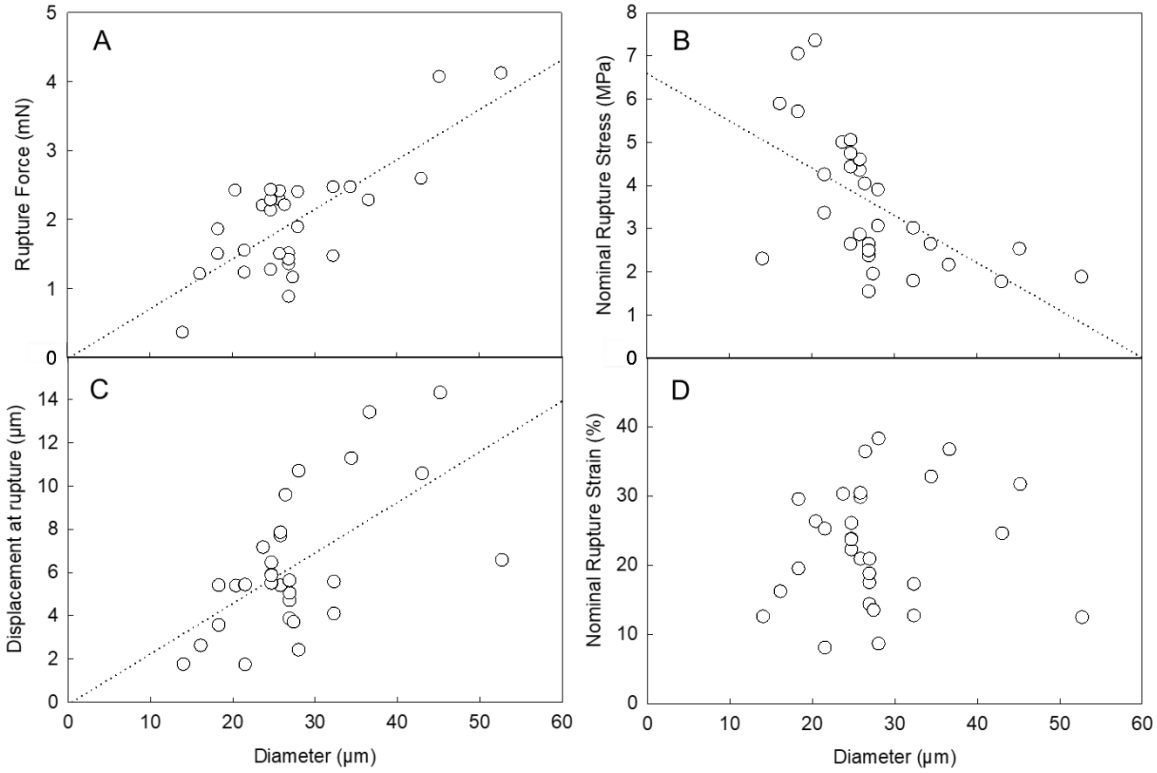

Figure 5.8– Mechanical properties of HS-microcapsules *vs* diameter (*d*): rupture force (A), nominal rupture stress (B), displacement at rupture (C), and deformation (strain) at rupture (D). The dotted lines represent the trend only.

As for the coacervate beads (§4.3.7.3), some outliers were clear in Figure 5.8. Unlike microfluidic devices, a minor number of microcapsules might not form homogeneously during coacervation possibly leading to shells with variable thickness. Therefore, the mechanical properties may be affected depending on the surface of the microcapsule exposed to the compressing parallel plate, which may correspond to the thinnest or the thickest side of the shell (Figure 5.1B).

5.3.9 Shell Thickness

Figure 5.9 shows the TEM micrograph of an ultrathin cross-section of a 20μm HS-microcapsule. The shell thickness appeared reasonably homogeneous. Specifically, the shell thickness at point A and B was 1.78 μm and 1.74 μm, respectively, which is very similar. By contrast, point C evidenced a slightly thinner thickness (1.4 μm). This discrepancy may be due to shells being non-uniform locally. Most likely, this could be ascribable to artifacts during TEM preparation [18, 266]. Thirty cross-sections of HS-microcapsules from thirty randomly selected microcapsules were examined. The shell topography of each microcapsule was investigated. Subsequently, the shell thickness was measured at three different regions of the shell itself *via* ImageJ analysis, hence an average was calculated. Following image analysis, a relationship between the shell thickness (h) and the diameter (d) of microcapsules was obtained (Figure 5.10). It was found that h increased linearly with d (R^2=0.86), which suggests that the larger the oil droplet, the thicker the shell. The apparent mean shell thickness (h_{app}) was determined to be 0.78±0.06 μm. However, the effect of random slicing should be considered, hence the effective thickness (h_{eff}) can be estimated by modelling, as described later in Chapter 7.

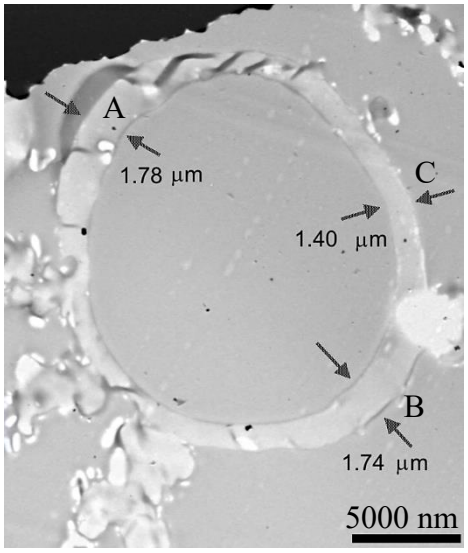

Figure 5.9– Cross-section of a HS-microcapsule (20µm) with its shell thickness measured at three different points: h_A=1.78±0.01 µm (A), h_B=1.74±0.02 µm (B), and h_C=1.40±0.02 µm (C).

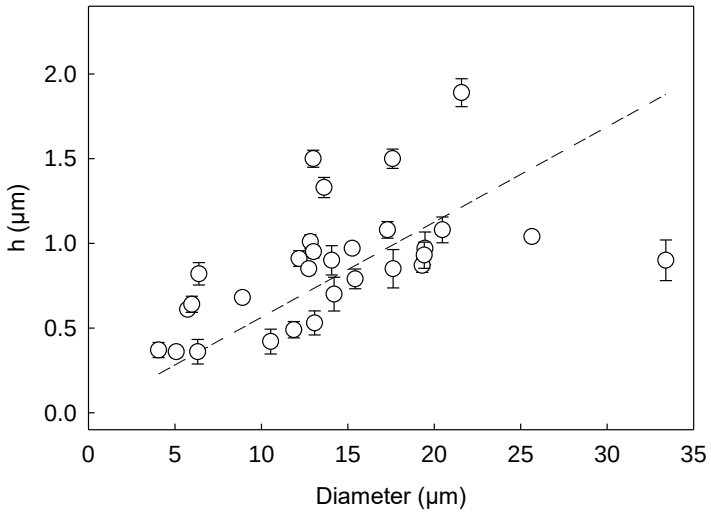

Figure 5.10– Apparent shell thickness *versus* diameter from 30 randomly selected cross-sections of HS-microcapsules. The linear fitting has R^2=0.86. The shell thickness was measured at three different regions of the shell itself *via* ImageJ analysis, and the resulting average ± St. error was calculated.

5.3.10 Adhesion Properties

5.3.10.1 Overview

Effective cleaning of fabrics has always been crucial to the entire global community [402]. Modern laundry has been actively present in human life since the introduction of life-easing amenities, such as synthetic detergents and electric household washing machines in the early years of the twentieth century [403]. To date, the fundamentals of domestic/industrial laundry processes still remain unchanged, which include a cycle of physico-chemical steps occurring within a washing machine at the interface between textiles and the washing medium [403, 404]. Specifically, three leading factors are involved to achieve high standards of laundering: (i) the nature of fabrics (natural/synthetic) and the type of dirt (soil, food residues, and grease); (ii) the chemistry and concentration of chemicals (detergents, bleach, and softeners); and (iii) the processing conditions (mechanical action, temperature, and time) operated during the laundry process [6, 405]. Although all these factors have a synergetic effect on the laundry process, the chemicals used, and their concentration play a special role. Chemicals penetrate through the interface between the dirt attached to textiles and the washing medium, thereby enabling mechanical action to lift and release the loosened particles of dirt [406]. Moreover, high temperatures, operated for the required time, enhance washing by decreasing water viscosity and the surface energy at the interfaces, as well as promoting the mass transfer of chemicals employed in the laundry process [407]. Although the basics of laundry processes have not changed much during the years, there has been a rising demand to deliver perfume molecules to fabric surfaces during laundry processes in order to impregnate clothes with pleasant scents, and thus enhance the end-use consumer's experience [6, 403, 408]. Detergent formulations typically comprise of many ingredients, which trigger specific pHs and ionic gradients when combined to aqueous environments in order to optimise washing conditions [26, 28]. Detergents and softeners contribute to washing off dirt/grease from textile surfaces, onto which also promote the adhesion/impregnation of certain substances contained in the formulations, such as perfumes, during the washing cycle [6]. However, perfumes contain highly volatile

organic compounds (VOCs), hence they have long been delivered by microencapsulation for assuring their preservation and controlled release onto the fabric surfaces [6, 408, 409]. Readily available fabrics are typically made of natural cotton fibres and synthetic fibres. The former are the most popular at a large scale but are coarse, whereas the latter are much smoother. Thus, smooth textiles should be preferred for experiments. Interestingly, polyethylene terephthalate (PET) films are smooth, hence can be utilised as model substrates to mimic the adhesion of PMCs during washing. Moreover, perfume microcapsules (PMCs) onto smooth PET films are not involved in any physical entrapment and/or steric effect, which is frequently observed on coarse surfaces. Thin PET films can be fitted into microfluidic devices, such as flow chambers, to mimic real washing conditions by exposing PMCs to different shear stresses and/or environmental pHs. Accordingly, suspensions of PMCs can be fed to a flow chamber in order to examine the interaction and adhesion of PMCs onto PET films. Previous literature has elucidated that a parallel plate flow chamber can be successfully employed to investigate the adhesion phenomena of cells and particles onto different substrates/surfaces [341, 342]. Moreover, the degree of particle removal from a solid surface has proven to be conditional upon flow velocity/shear stress [358]. Particles facing shear stress and torque may experience lifting, sliding, dragging, and rolling phenomena due to which their adhesion may be impaired. In addition, a flow chamber technique offers statistically significant data on a population of particles within a reasonably brief period of time. Based on the above, the studies herein presented were aimed at (*i*) mimicking the adhesion of plant-based HS-microcapsules to fabric surface in real washing by using a flow chamber technique equipped with smooth PET film as a model; and (*ii*) understanding the interactions of microcapsules with the PET film, hence their retention at increasing shear stress and different environmental pHs.

5.3.10.2 Retention Performance (RP) of HS-microcapsules

A flow chamber technique was utilised to quantify the adhesion of HS-microcapsules onto thin PET model films, as well as understanding their mutual interactions. The data (*i.e.* real-time

pictures captured at different shear stress and pH) generated from the flow chamber experiments were processed *via* ImageJ in order to quantify the adhesion of the microcapsules to PET films. Figure 5.11 displays the retention performance (RP) of HS-microcapsules onto PET films as a function of the shear stress/Reynolds, respectively. pH-dependent curves were obtained. As can be seen in Figure 5.11, HS-microcapsules exhibited the best retention performance onto PET films at pH 3.2. At such pH and low shear stress (<50 mPa), the RP was more than 70%. It was also found that the RP of HS-microcapsules at the same pH (3.2) was no less than ~60% under high shear stress (0.9 Pa). In addition, no significant difference in RP at 0.35 Pa (Re≃12) and 0.9 Pa (Re≃30) was observed, which suggests that an equilibrium between the two contact surfaces (*i.e.* microcapsules and PET films) may have been reached. Similarly, HS microcapsules at pH 4.1 showed a high RP (~70%) below 50 mPa, as for pH 3.2. However, lower RP of ~50% and ~45% were observed at 0.7 Pa (Re≃25) and 0.9 Pa (Re≃30), respectively. These values were determined to be around ~15% lower than those at pH 3.2, which tentatively suggested a possible effect of environmental pH on the RP of microcapsules onto PET films. This phenomenon was more evident at high shear stress. Accordingly, lower microcapsules RP values were determined at increasingly high environmental pHs, particularly at weakly acidic (5.1-6.2) and near neutral (7.2) pHs. The curves obtained at pH 5.1, 6.2, and 7.2 showed a dramatic drop in the RP of HS microcapsules onto PET films, which was obvious from 0.1 Pa (Re≃5). Specifically, the microcapsule RP was found to be less than 45% at 0.15 Pa, which was much lower than that observed at pH 3.2 (73%) and pH 4.1 (70%). The lowest RP values for HS-microcapsules were 25%, 21%, and 19% at pH 5.1, 6.2, and 7.2, respectively, when facing a shear stress of 0.9 Pa (Re≃30). An example of real-time removal of HS PB-PMCs under increasingly high shear stress (5 mPa-0.9 Pa) is presented in Figure 5.12.

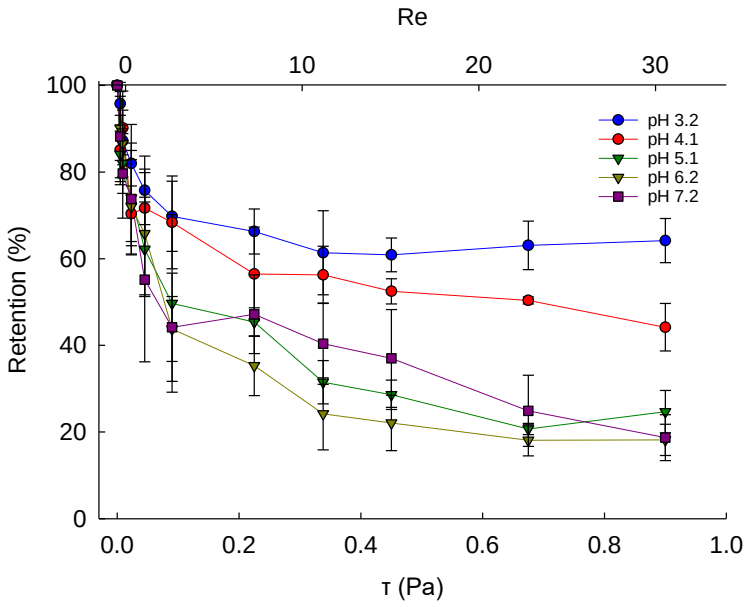

Figure 5.11– Retention performance of HS-microcapsules onto thin PET model film as a function of shear stress (τ) and Reynolds (Re; secondary *x*-axis) at different pHs.

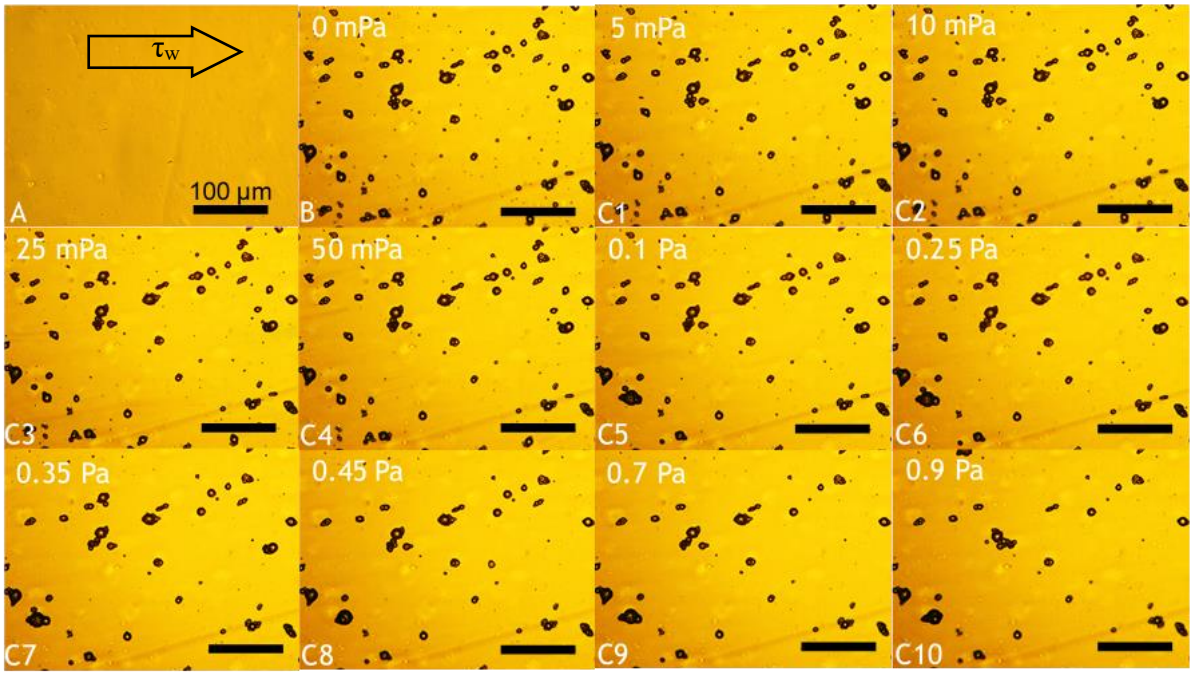

Figure 5.12– Example of real-time removal of microcapsules adhering to a fully flat PET film at pH 3.2. Background obtained from a blank PET film (baseline) prior to microcapsule inoculation (A); deposition of microcapsules following their inoculation and cleaning (B); and flushing of microcapsules exposed to increasing shear stress, as follows: 5 mPa (C1), 10 mPa (C2), 25 mPa (C3), 50 mPa (C4), 0.1 Pa (C5), 0.25 Pa (C6), 0.35 Pa (C7), 0.45 Pa (C8), 0.7 Pa (C9), 0.9 Pa (C10). The scale bar displayed in (A) is applicable to all images.

5.3.10.3 Influence of the pH on the Retention Performance of HS-microcapsules

As shown in Figure 5.11, the highest RP of HS-microcapsules onto PET films was obtained at the lowest acidic pH investigated (pH 3.2). In contrast, the RP of microcapsules was reduced at increasingly higher environmental pHs ($4.1<pH\leq7.2$). Since the microcapsules were fabricated *via* pH-driven complex coacervation (CC), an effect of the environmental pH on

their adhesion/hydrodynamic properties may not be surprising. Butstraen and Salaün [169] have reported that chitosan-GA microcapsules *via* CC are highly stable when the electrostatic interaction between the two biopolymers is maximised at pH 3.6. Therefore, an effect of the pH on the adhesion properties of pH-sensitive fCh-GA microcapsules cannot be excluded. When exposed to weakly acidic (pH 5.1-6.2) as well as near-neutral (pH 7.2) environments, the RP of microcapsules was low. This suggests that the microcapsules may not be capable of adhering firmly to the PET films at $5.1 \leq pH \leq 7.2$, even under low shear stress ($Re \simeq 2$). This phenomenon resulted in microcapsules rolling out along the chamber, without reaching any equilibrium with the PET films. When compared to pH 3.2 and pH 4.1, the RP of microcapsules onto PET films at pHs ≥ 5.1 was much worse. This finding suggested that the environmental pH may play a crucial role on the hydrophobic interaction between microcapsules and PET films. Generally, the hydrophobic interaction is responsible for hydrophobic substrates to cluster, aggregate, or bond together [410]. There appeared to be a much stronger hydrophobic interaction between microcapsules and PET films at low acidic pHs (particularly around $pH_{CC} \simeq 3.4$), hence leading to a higher RP. Previous literature has shown that hydrophobic interactions play a leading role in bioadhesion phenomena [411]. Specifically, the adhesion of certain bacteria to glass, such as *Staphylococcus aureus*, may be highly affected by the environmental pH [412]. Hamadi *et al.* have reported that the quantitative adhesion of bacteria to a glass substrate was promoted in the pH range 3.5-5.0, whereas their adhesion performance dropped at near-neutral (pH 6.0) and alkaline pHs. Similarly, He *et al.* [28] have highlighted that the adhesion between MF-based microcapsules and a cellulose film was reduced when the pH was increased. Specifically, both cellulose as well as PET film and MF-based microcapsules are negatively charged, hence their surfaces became more and more negative by increasing the pH. Therefore, the adhesion between MF-based microcapsules and cellulose was impaired at increasing pHs. This resulted in a reduced pull-off force between microcapsules and the cellulose film, leading microcapsules to roll off the film more easily. When dealing with chitosan, Liu *et al.* [27] have suggested that the presence of fully and partially protonated amines at pH 3 and 5, respectively, may generate enhanced electrostatic interactions between the microcapsules and the cellulose substrate. Thus, both amines (fCh) and carboxyl groups

(GA) were not only responsible for coacervation but also contributed to generating hydrogen bonding [413], which may promote the adhesion phenomena. These results seemed to support the hypothesis that enhanced hydrophobic interactions between HS-microcapsules and PET films were more likely at low acidic pHs [414], thereby leading to a much more effective RP. High RP of microcapsules has also been associated with the high level of free surface energy of PET films, which may be conducive to its hydrophobic nature [415]. By contrast, the low RPs of HS-microcapsules at weakly acidic (pH 5.1-6.2) and near-neutral pHs (7.2) can be related to the increased repulsive interaction between the coacervate shells and the PET films possibly occurring at such pHs, which may inhibit both surfaces (microcapsules and PET films) to come into close contact with each other [28].

5.3.10.4 Retention Performance at the Highest Hydrodynamic Shear Stress

Figure 5.13 displays the RP of HS-microcapsules onto PET films at different pHs under the highest hydrodynamic shear stress investigated (τ^{max}=0.9 Pa). As can be seen, there appeared to be an exponentially decreasing trend with the pH. The highest RP was observed at the most acidic pH (3.2). Therefore, this finding seems to confirm that the effect of the environmental pH on the RP of HS-microcapsules may not be negligible. As formerly mentioned, HS-microcapsules fabricated *via* pH-driven CC are likely pH-sensitive, which can influence the hydrophobic as well as electrostatic interaction between the microcapsules and PET films at different pHs, hence their RP. Based on the results, the highest RPs were achieved at pH 3.2 and pH 4.1, confirming that the strongest hydrophobic interaction between HS-microcapsules and PET films was at low acidic pHs (3.2-4.1). This finding seemed consistent since pH 3.2 and pH 4.1 are close to pH_{CC} (~3.4), at which the coacervate shells of microcapsules benefit from the highest electrostatic interaction between the biopolymers forming the shell [169]. Thus, pH~pH_{CC} may be conducive to more solid shells, and then more robust contact surfaces to the PET films, hence a higher RP. Overall, it could be inferred that the environmental pH may play a role in determining the RP of microcapsules fabricated *via* CC. In addition, the

results have proven ImageJ highly effective at quantifying the RP of microcapsules onto PET films.

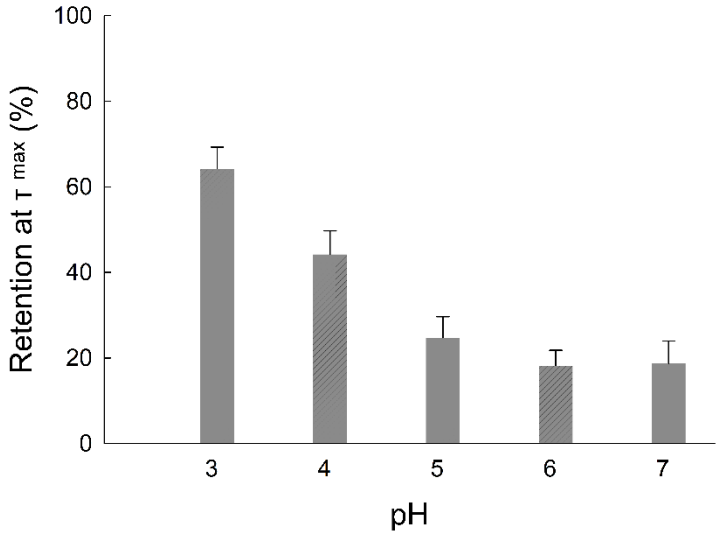

Figure 5.13– Comparison of the retention performance of HS-microcapsules onto PET films at $\tau = \tau^{max}$ (≃0.9 Pa) and different environmental pHs.

5.4 Conclusions

The fabrication of perfume oil microcapsules within a fungal fCh-GA shell *via* complex coacervation was investigated. HS perfume oil was successfully encapsulated. The highest EE of HS-microcapsules was ~60%, which is similar to what is reported in literature for microcapsules *via* CC from animal-derived Ch and other biopolymers. It was found that the stirring rate during CC affected the morphology of microcapsules which appeared elongated and spherical at 400 and 1000 rpm, respectively. The micromanipulation results highlighted that the rupture force of HS-entrapping microcapsules increased with the diameter, whereas the nominal rupture stress decreased with the size on average, as expected. The average rupture force of HS-microcapsules was determined to be 2.0±0.1 mN, which is also very similar to that

of MF-based microcapsules (2.1±0.2 mN) [14]. The average nominal rupture stress of HS-microcapsules (3.6±0.3 MPa) was also similar to that of MF-based microcapsules (4.2±0.4 MPa). Besides, HS-microcapsules exhibited an average deformation at rupture of 22.7±1.5%, which is also similar to that of MF-based microcapsules (24.8±1.5%), as reported in literature [14]. In other words, HS-microcapsules may not be structurally brittler than MF-based microcapsules, which is promising. In addition, the shell thickness of HS-microcapsules was found to increase linearly with their diameter, hence the larger the oil droplet, the thicker the shell. The average shell thickness value was 0.87±0.1 μm for HS-microcapsules. The adhesion properties of HS-microcapsules onto fabric surfaces in real washing were mimicked using a microfluidic flow chamber equipped with a smooth PET film as model. The interaction between HS-microcapsules and PET films was investigated, and their retention performance (RP) was quantified at increasing hydrodynamic shear stress and different environmental pHs. Applying ImageJ analysis, it was found that the RP of HS-microcapsules was promoted at low acidic pHs (<5.1) leading to ~85% and ~60% at low (≤50 mPa) and high shear stress (0.9 Pa), respectively. In contrast, the RP was severely impaired at weakly acidic (pH 5.1-6.2) as well as near-neutral pHs (7.2). This phenomenon was probably attributable to the nature of the biopolymeric shells of microcapsules obtained *via* CC, which may be pH sensitive. The results also suggested that both pH and shear stress influenced the RP. Specifically, the pH might affect the hydrophobic interaction between the microcapsule shells and PET films, hence their mutual adhesion. Stronger hydrophobic interactions between HS-microcapsules and PET films appeared more likely at a pH close to the coacervation pH_{CC} (3.4), possibly due to the stronger electrostatic interaction between the shell-forming biopolymers, which might thus result in more solid shells. Accordingly, the highest retention of HS-microcapsules onto PET films was observed at pH 3.2.

The first driving force for this work was to manufacture perfume oil entrapping microcapsules with a potential for fabric care. However, the typical pH of detergents is 10-11.5 [416], which is much higher than that of fCh-GA microcapsules (pH_{CC} 3.4). Although the pH is reduced to ~7-8 during a washing cycle due to the high amount of water [417], the related pH window may still be incompatible. However, some other laundry products, such as heavy-duty cleaning liquids, sprays, and disinfectant are formulated at a more acidic pH e.g. ethanol-phosphoric

acid (pH 2.8) and ethanol-citric acid (pH 4.1) [418]. Therefore, the microcapsules herein fabricated may still be relevant for the cleaning, disinfectant, and detergent manufacturing industry.

Overall, the feasibility of fabricating microcapsules with a core of HS based on the concept of CCCZ-CTZ was demonstrated. Such promising results suggest the fCh-GA system to be a potential carrier for the encapsulation of fragrance ingredients, offering a potential for more sustainable and consumer-friendly applications in detergent formulations, as well as an opportunity to globally overcome cultural and religious beliefs associated with animal-derived products. Besides, a flow chamber technique alongside with ImageJ analysis software can be employed as a powerful microfluidic platform to quantify the retention performance of microcapsules onto model fabrics (PET films) at different environmental pH conditions and hydrodynamic shear stress.

Chapter 6 Fabrication of Microcapsules with a Fungal Chitosan-Gum Arabic-Maltodextrin Shell to Encapsulate Health-Beneficial Peppermint Oil †

6.1 Introduction

6.1.1 Overview

Fast-growing food industry has long included many appealing essential oils (EOs) in food products to meet consumers' needs, taste, and expectation for quality, thereby encouraging them to repeat product purchase [9]. Among all, the demand for peppermint oil (PO) has recently surged due to its multiple health-beneficial properties at end-use applications against heartburn, digestive problems, irritable bowel syndrome (IBS) [134-136], and to treat the common cold, sinus infections, and headaches [419], which have been formerly assessed by the joint panel comprising of Food and Agriculture Organization (FAO) of the United Nations and the World Health Organization (WHO) [273, 274]. Moreover, PO is used topically as a spasmolytic agent to ease muscle aches, joint pain, and itching [420]. Notwithstanding, PO is extremely volatile, may not be used as such in food manufacturing. Therefore, PO has often been encapsulated for a longer shelf-life. To date, animal-derived ingredients have been extensively employed but there is a rising demand from consumers for solely plant-based ingredients. In this chapter, PO-entrapping microcapsules were fabricated *via* complex coacervation using gum Arabic (GA) and fungal chitosan (fCh) as shell precursors followed by maltodextrin-assisted spray drying. The microcapsules were crosslinked using vegan transglutaminase. The encapsulation efficiency (EE) of the oil, and its static/dynamic leakage

† Published at Baiocco, D., Preece, J. A., & Zhang, Z. (2021), *Food Hydrocolloids For Health*, 100016.

profile of the microcapsules in several hydroalcoholic environments were quantified by UV-Vis spectroscopy. The morphology of PO-entrapping microcapsules was investigated *via* bright-field/fluorescent optical microscopy and scanning/transmission electron microscopy, and the mechanical properties of the shell were characterised using a micromanipulation technique.

6.1.2 The Encapsulation of Essential Oils (EOs) in Industry

In recent years, natural EOs and oleoresins as well as synthetic flavourings have played an important role in many readily available products worldwide [11]. However, natural plant extracted ingredients have lately gained increasing attention over synthetic and/or animal derived ingredients, since their production is easier and more cost-effective, and have sustainability, eco-friendly and ethical benefits [421]. Moreover, synthetic ingredients are shrouded in controversy due to their negative health effects [273, 274]. Accordingly, increasing regulatory pressures on food/healthcare product formulations are urging for replacing synthetic flavourings with natural EOs [9, 273]. Many nutraceuticals, pharmaceuticals, and cosmetic products are being enriched with bioactive EOs, due to their outstanding health-beneficial properties, including therapeutic, antioxidant and antimicrobial activities [129, 422, 423]. As for peppermint oil, a broad range of EOs have proven health-promoting properties, such as oregano (bactericidal activity, asthma/diarrhoea relief) [78, 424], rosemary (antioxidant and hepatoprotective activity) [131, 425], ginger (anti-inflammatory and antiemetic activity) [132, 426], lemon (anti-depressant, digestion-aid, and skin-healing activity) [133, 427], orange (digestion-aid, antimicrobial and anti-inflammatory activity) [71], cinnamon (antimycotic and antimicrobial activity) [123, 428]. EOs are chemical substances consisting of terpenes, alcohols, esters, aldehydes, and ketones, which are naturally prone to evaporating [423], and may also undergo structural changes triggered by atmospheric factors (light, oxygen, and temperature) [120]. For this reason, EOs may not be used directly in product manufacturing. Therefore, they are often encapsulated for a longer product shelf-life [3]. Among all

microencapsulation methods [3, 88], spray drying (SD) has long been a preferred technique to achieve dry powders of microcapsules, especially when dealing with food and pharmaceutical formulations [9, 135, 429]. Although microcapsules with different EOs have been effectively fabricated by SD only, the process requires high temperatures, which may still thermally degrade/oxidise EOs [430], causing them to evaporate [431], hence leading to reduced oil-loading efficiency [279]. Therefore, alternative encapsulation solutions are being sought. Complex coacervation (CC presented in Chapter V for fabricating HS-microcapsules) typically leads to payloads higher than SD [3, 154]. However, free-flowing powders of microcapsules are difficult to achieve *via* CC only, especially at a large scale. Since industrial food products often require dry ingredients, intense endeavours have been undertaken towards achieving free-flowing powders of microcapsules. Thus, a two-step microencapsulation process consisting of CC followed by SD for the encapsulation of peppermint oil (L-Carvone) is herein presented. To the best of the author's knowledge, little is known on the two-step food-grade microencapsulation processes, other than the encapsulation of garlic extract [432], fish [63] anchovy [48] and orange oils [9, 433].

Microencapsulation in food and healthcare industry is a very high-demanding area where the preservation of flavours and bioactives, as well as their controlled release, is driven to the extreme. Unlike laundry applications which also aim for excellent textile-adhesion properties of microcapsules, this is not relevant for food-grade microcapsules at end-use applications (*e.g.* dry food formulations, oral care products, chewing gum, ointments). In contrast, food microcapsules should segregate and preserve the active cores which can then be released on demand. Therefore, an insightful characterisation of microcapsules for food and healthcare applications should be based on their mechanical, structural, and barrier properties.

6.2 Materials & Methods

6.2.1 Materials

Fungal chitosan (fCh) used as the microcapsule shell-precursor was purchased from Kitozyme (Herstal, Belgium, EU). More details on all the materials used can be found at Section §3.2.

6.2.2 Preparation of LC-Microcapsules

The microcapsules were fabricated *via* two-step microcapsulation processes being complex coacervation followed by spray drying detailed by Baiocco *et al.* [353], as well as in §3.3.5.3.

6.3 Results & Discussion

6.3.1 Limitations of One-Step Encapsulation Process

As presented in Chapter 5, HS-microcapsules were successfully fabricated *via* one-step microencapsulation process (complex coacervation). A similar procedure was attempted for the microencapsulation of LC. Single oil droplets were encircled by a coacervate shell at pH 3.4, at the highest electrostatic interaction between fCh and GA. Morphological analysis highlighted spherically shaped microcapsules with a core-shell structure. Additional smaller oil droplets were also visible within the fCh-GA shells (Figure 6.1A-B). Accordingly, fCh-GA networks by coacervation seemed capable of entrapping small oil droplets, other than the key oil core, thereby creating multinuclear networks [434]. Similar networks are also reported in former literature, with emphasis on the bioencapsulation of cells [435], pharmaceuticals [436], and essential oils for biomedical applications [437]. Furthermore, previous research work has focused on microcapsules exhibiting multiple cores of terpenic oils within chitosan-gelatine based networks in suspension [47], rather than fungal chitosan-gum Arabic microcapsules.

However, no detail on dried microcapsules has been provided. Although LC-entrapping microcapsules could be formed *via* CC only (Figure 6.1A), they were found unable to survive air drying (Figure 6.1B).

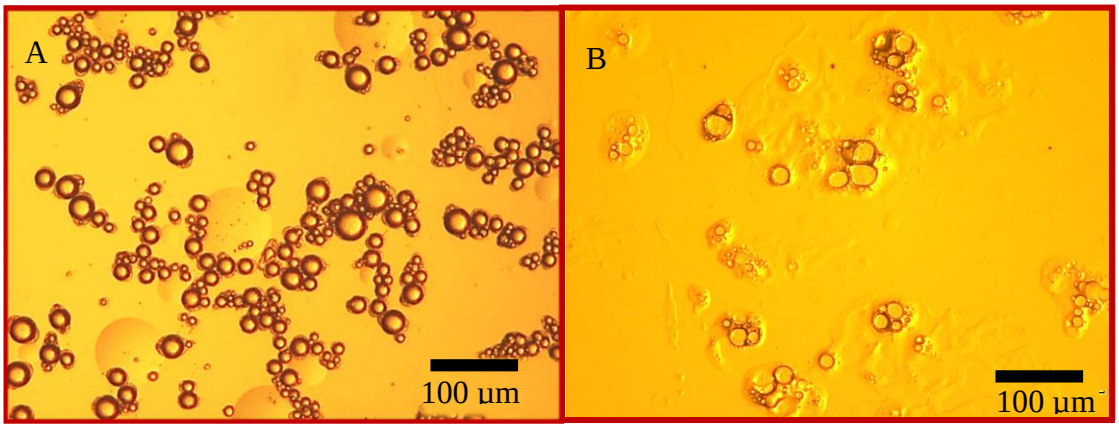

Figure 6.1– Optical microscopy images of suspended (A) and collapsed LC-microcapsules upon air drying (B).

SEM micrographs displayed in Figure 6.2 highlight the different morphological features between intact HS-microcapsules (Figure 6.2A) and collapsed LC-microcapsules in a dry form (Figure 6.2B). No intact LC-microcapsules after the drying were found. The only presence of polymeric debris suggested that LC-microcapsules had ruptured before being exposed to the high vacuum conditions of SEM, as shown in Figure 6.1. This finding evidenced that LC-microcapsules by CC only were much weaker than HS-microcapsules. This was likely due to the enzymatic crosslinker employed (transglutaminase), which was probably not as effective as glutaraldehye to reticulate microparticles/microcapsules *via* CC [288]. Moreover, a direct effect of LC on impairing the structural stability of fCh-GA shells cannot be excluded. Most likely, this phenomenon may be due to the chemistry of LC, as well as the interfacial interaction

between LC and fCh-GA shells. Based on the above, two-step microencapsulation processes consisting of CC followed by spray-drying were performed to encapsulate LC. Maltodextrin was used to further strengthen the shells of LC-microcapsules during spray drying.

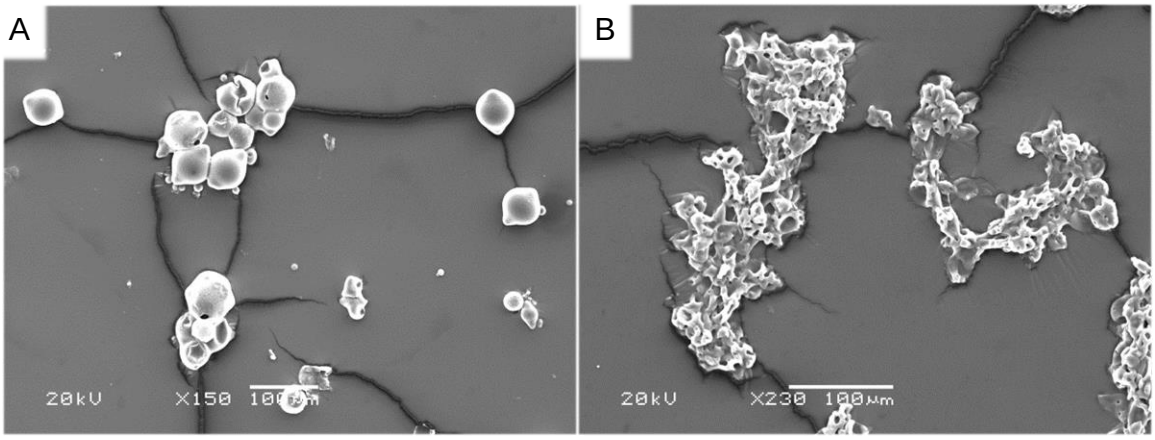

Figure 6.2– SEM micrographs of HS-microcapsules (A) and debris from LC-microcapsules (B).

6.3.2 Two-Step Encapsulation Processes

6.3.2.1 SEM Observation

LC-microcapsules were also investigated by SEM. Figure 6.3A provides an overview of microcapsules following spray drying (atomisation). Microcapsules were found to have spherical shapes and relatively smooth surfaces. However, the surface topography of microcapsules also revealed the presence of dents, creases, and depressions at their surfaces, which might be an effect of the high vacuum inside the SEM [392]. Alternatively, crease-rich surfaces might also be related to the loss of water following spray drying [270], or to the remaining coacervate matter and MD having deposited irregularly onto the surface of

microcapsules during spray drying [286]. Similar results were reported by Jafari *et al.* [438] where microcapsules made of whey protein had exhibited round shapes and rough surfaces. No incomplete microcapsules nor surface cracks were found. Generally, hole-free microcapsules were achieved, which suggests that LC might be entrapped within the polymeric shell. Figure 6.3B displays a self-isolated microcapsule in the foreground with a dark round area through the shell, which was tentatively related to the presence of sub-shell oil. Former works have elucidated that only hole-free structures are capable of entrapping the active oil effectively [9]. To this end, the addition of an extra strengthening agent, such as maltodextrin and sucrose, has proven beneficial for filling possible surface vacuoles that were observed on microcapsules obtained *via* spray drying only [439]. As shown in Figure 6.3A-B-C, complete microcapsules were attained following spray drying. This suggests that the addition of maltodextrin might be conducive to generating more solid and compact microcapsules. Similar results were reported by Jun-xia *et al.* [9] for the encapsulation of orange oil by sucrose-assisted spray drying. Although mostly spherical microcapsules with a relatively smooth surface were achieved, multiple tiny crusts were also observed at the surface of microcapsules (Figure 6.3C). These crusts might result from some extra polymeric fragments having adhered to the surface of microcapsules during spray drying. Similarly, additional minute coacervates (1~2 μm) with a smooth surface occurred at the surface of individual microcapsules as well (Figure 6.3D). As for surface crusts, they were likely to attach to the surface of relatively large microcapsules during spray drying. However, their inner structure is unknown, and the presence of oil within cannot be excluded. Partly incomplete microcapsules were also observed, with particular emphasis on those with unsealed shells (Figure 6.3E-F), which helped to understand the morphology and inner structure of microcapsules. Oil-hosting cavities of microcapsules were obvious, thereby suggesting a core-shell structure (Figure 6.3E). As shown in Figure 6.3E-F, the analysis of incomplete microcapsules also revealed the presence of solid and non-porous shells, which were in the order of 0.5~2 μm, approximately.

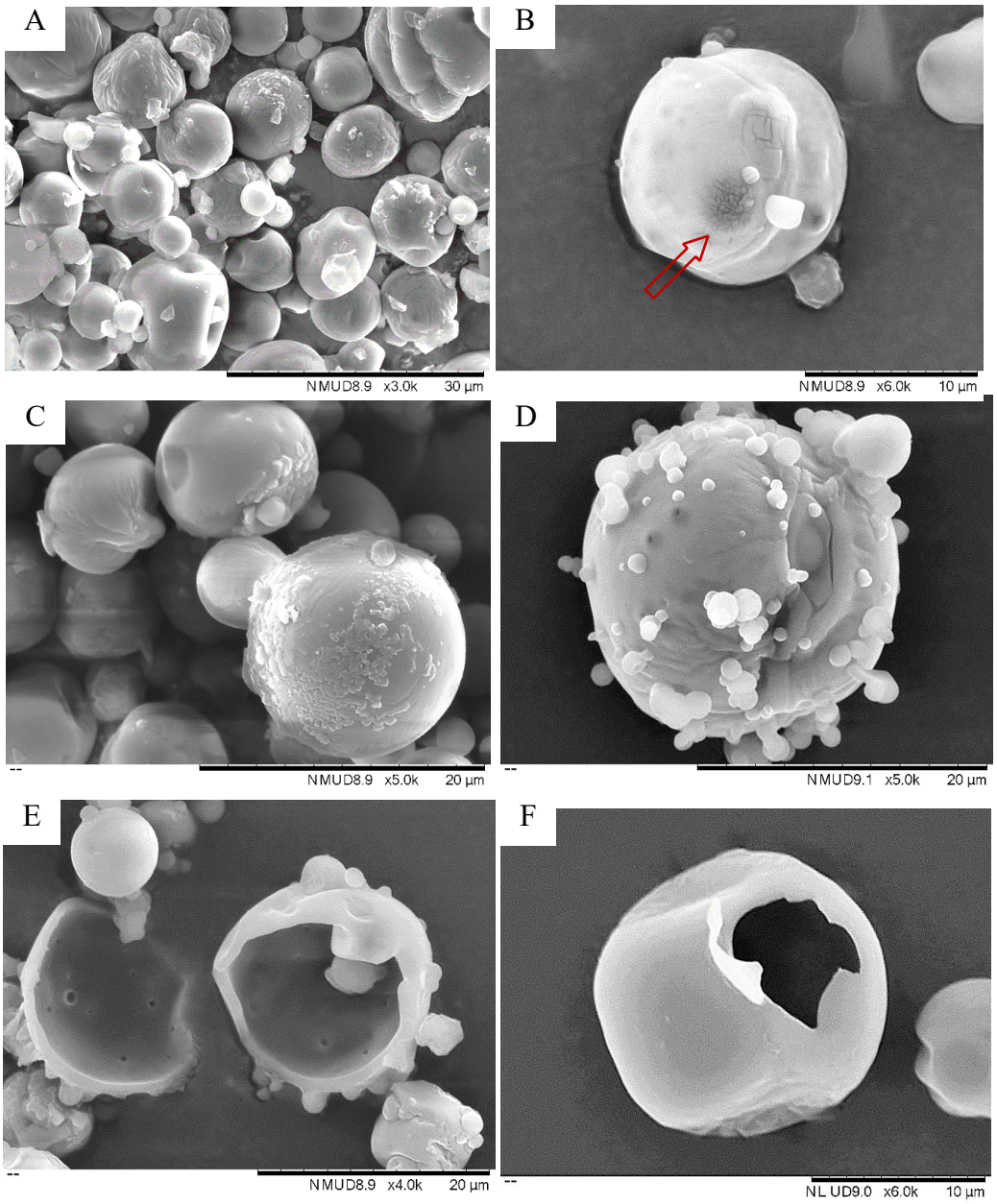

Figure 6.3– SEM micrographs of: (A) spray-dried microcapsules with relatively smooth surfaces; (B) a single microcapsule exhibiting a dark shade (subshell oil); (C) complete microcapsules displaying surface crusts; (D) a single microcapsule with extra coacervate formations adhered to its surface; (E) partly incomplete microcapsules with solid shells; (F) a single microcapsule with core-shell structure.

6.3.2.2 Fluorescence Microscopy

The effective retention of LC within spray-dried microcapsules was assessed by fluorescence microscopy. The same sample of spray-dried microcapsules was imaged twice, first *via* OM (Figure 6.4A) and then *via* FM (Figure 6.4B). Interestingly, different colours were exhibited by the microcapsules under fluorescence. Figure 6.4B shows a large prismatic-like structure of around 50 μm turning red under fluorescence, whilst most of smaller microcapsules emit a green light. Previous literature has shown that fluorescent dyes, such as Nile red, are useful for assessing the presence of actives inside the capsules quickly and effectively [126]. The fluorescence sensing technique with Nile red relies on the solvatochromism phenomenon. Accordingly, the position of the emission bands of Nile red depends on the nature of its environment. Thus, filled and hollow capsules should exhibit different emission bands under fluorescent excitation, conditionally upon what material Nile red is exposed to. When unsolvated, Nile red hits the bathochromic emission band, whereas a spectral hypsochromic shift (blue shift) occurs when it is exposed to non-polar solvents. In other words, high-polarity solvents provide bluer spectral emission, whereas less polar solvents produce redder emission. Polarity of a solvent depends upon the charge of its moieties. LC is a relatively polar molecule owing to its functional groups. Specifically, its ketonic branch confers a certain degree of polarity due to the carbon-oxygen double bond, whereas the alkenes are non-polar. For this reason, LC is expected to produce intermediate emission bands, as shown in Figure 6.4B. When LC is effectively entrapped within the polymeric shell, the photonic emission of Nile red is affected by its relatively polar environment, hence leading to the green visible spectrum [126]. In contrast, the red emission band corresponds to the loss of LC, since Nile red is no longer solvated in LC, thereby emitting its natural colour [125]. In addition, the top-sitting capsule in Figure 6.4B exhibited a yellow band, which suggests that some of the oil initially present might have leaked out, resulting in microcapsules with a partial oil retention. Relying on the fundamentals, these results suggest that a ternary fluorescence sensing technique could be employed, where green, yellow, and red emission bands correspond to successful oil entrapment, partial oil retention/leakage, and complete oil loss, respectively [125].

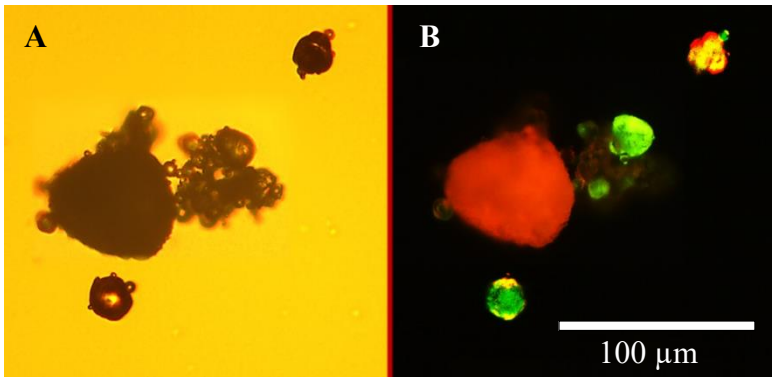

Figure 6.4– Spray-dried microcapsules by bright-field (A) and fluorescence (B) microscopy.

6.3.2.3 Size Distribution

Both size and size distribution of LC-entrapping microcapsules were evaluated. There was no significant variation of the size between pre- and post-crosslinking stage. As displayed in Figure 6.5, the PSD of microcapsules (SPAN 1.376) varied between 10 µm and 125 µm. The Sauter mean diameter was determined to be 37.8±1.4 µm. Statistical analysis spotlighted that such PSD could be fitted to a log-normal distribution function with 95% confidence. In addition, the mean size of moist microcapsules determined by light scattering was in good agreement with the SEM micrographs of dry microcapsules (Figure 6.3A-F).

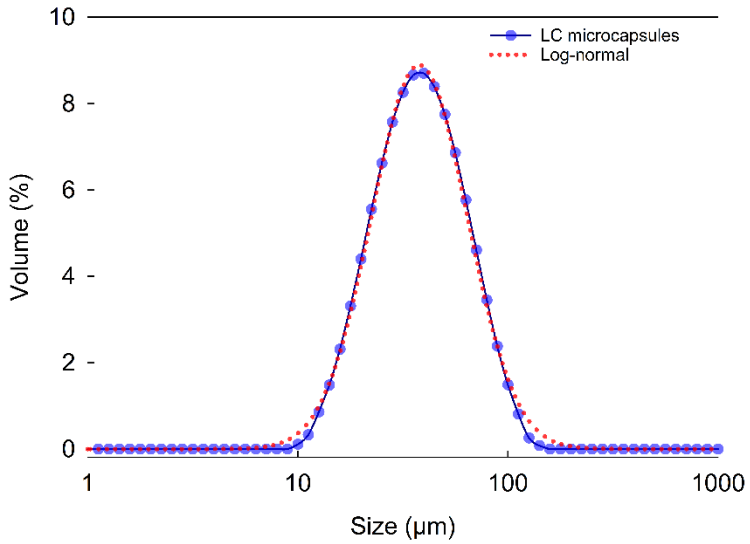

Figure 6.5– Log-scale particle size distribution of moist LC-entrapping microcapsules fitted to a log-normal distribution with 95% confidence. The general form of a three-parameter (a, b, x_0) log-normal distribution function is $f(x) = \frac{a}{x}\exp\left(-\frac{1}{2}\left(\frac{\ln(x/x_0)}{b}\right)^2\right)$. Non-linear regression and performance parameters: a=3.88·10^2; b=0.53; x_0=50; coefficient of determination R^2= 0.998.

6.3.2.4 Encapsulation Efficiency

The encapsulation efficiency and payload attained from LC-microcapsules were 29±4% and 19±3%, respectively. Similar values have been reported in literature, with particular attention to the EE of peppermint oil (27%) of pectin-based microcapsules fabricated by a coaxial electrospray system [270]. In addition, animal chitosan microcapsules entrapping different EOs yielded slightly higher EEs, such as orange (43-56%) and vanillin oil (50%), reported by Li *et al.* [440] and Yang *et al.* [7], respectively. Generally, these values were much lower than the EE (89%) of gelatine-chitosan microcapsules with a load of limonene [47]. These results suggest that gelatine may still be the best performing ingredient to form microcapsules with remarkable structural properties, thereby yielding the highest EE [6]. Although the chemical nature of the shell precursors plays a very important role in microencapsulation, decreased EE

may also be due to the oil being partially lost during processing (homogenisation and spray drying at high temperatures). Moreover, chemical interactions between the active oil and the shell materials cannot be excluded.

6.3.2.5 Static Leakage

Figure 6.6 displays the payload of LC-microcapsules, which was quantified by UV-Vis (§3.4.4.1). There appeared to be no significant variation of the payload after storage for 50 days, hence no static leakage. These results suggest a promising shelf life of microcapsules when stored in airtight vials (Figure 6.6-i). Therefore, the two-stage fabricated microcapsules may not only be capable of entrapping LC effectively, but also able to secure the oil within the shell for an extended period of time. This finding is important since many essential oils may promptly evaporate and undergo oxidisation when exposed to atmospheric conditions, leading to their depletion/degradation [441]. LC is not an exception, hence its storage conditions (temperature, environmental pH, atmospheric oxygen) are crucial [442]. Furthermore, the chemical inertness between oils and the polymeric shell is essential. Oil degradation has often been associated with the physiochemical variation of the encapsulating materials during storage [443]. As reported in literature, maltodextrin may have a positive effect on LC-microcapsules providing them with a stronger coating to act as an oxidation-delaying barrier, thereby preserving the oil for longer.

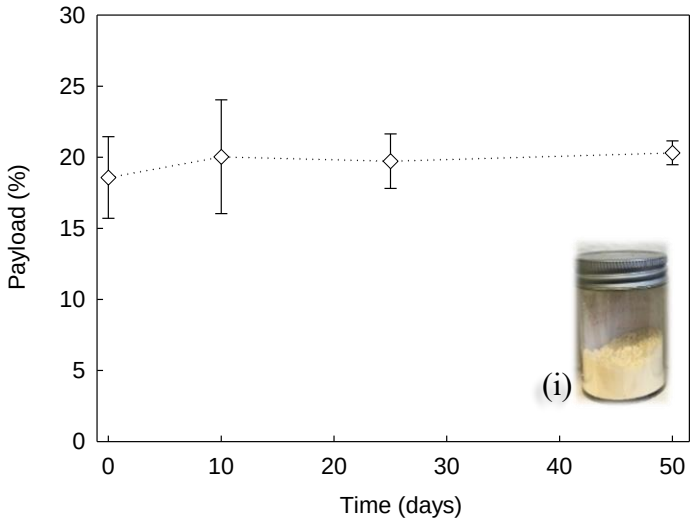

Figure 6.6– Payload of LC-microcapsules obtained from fungal chitosan and gum Arabic *via* complex coacervation followed by spray drying. The payload ($P_{\%}$) is evaluated according to Equation (3.6). The symbol (i) refers to the airtight vials in which free-flowing powders of microcapsules were stored.

6.3.2.6 Mechanical Properties

The mechanical properties of LC-microcapsules (diameter based on thirty microcapsules $d_{n\text{-}b}$=18.0±1.4 μm) characterised *via* a micromanipulation technique are presented in Figure 6.7. The rupture force of LC-microcapsules was found to be averagely increasing with diameter (Figure 6.7A). The mean rupture force was 0.6±0.1 mN. Similar results were also obtained by other researchers for melamine-formaldehyde [25], and calcium-shellac microspheres [99]. The nominal rupture stress (*i.e.* ratio of the rupture force of a single capsule to its original cross-sectional area) averagely decreased with diameter (Figure 6.7B), which seems to suggest that larger microcapsules may be weaker when compared to smaller ones [14, 31]. This behaviour is often desirable at end-use applications, when microcapsules are required to rupture promptly, thereby releasing their active on-demand, particularly for chewing gum and dental care products. The mean nominal rupture stress was 2.1±0.3 MPa, which is in line with the gelatine-

gum Arabic microcapsules with double shells and similar size (13.9±0.3 μm – 21.5±0.8 μm) presented by Yu *et al.* [63]. Figure 6.7C shows the displacement at rupture increasing with the diameter of microcapsules. Its average nominal deformation at rupture (*i.e.* the slope of the displacement at rupture *vs* diameter) was 8.0±0.9%, which suggests a much earlier rupture of LC-microcapsules under compression when compared to the data reported by Yu *et al.* [63] for similar systems obtained by coacervation (14.2±2.0% – 22.4±3.4%). This phenomenon may be due to the more brittle nature of the outermost coating of fCh-GA-MD-based LC-microcapsules, which is non-gelatine based. Xue and Zhang [383] also found a relationship between the displacement at rupture and diameter of calcium-shellac microspheres.

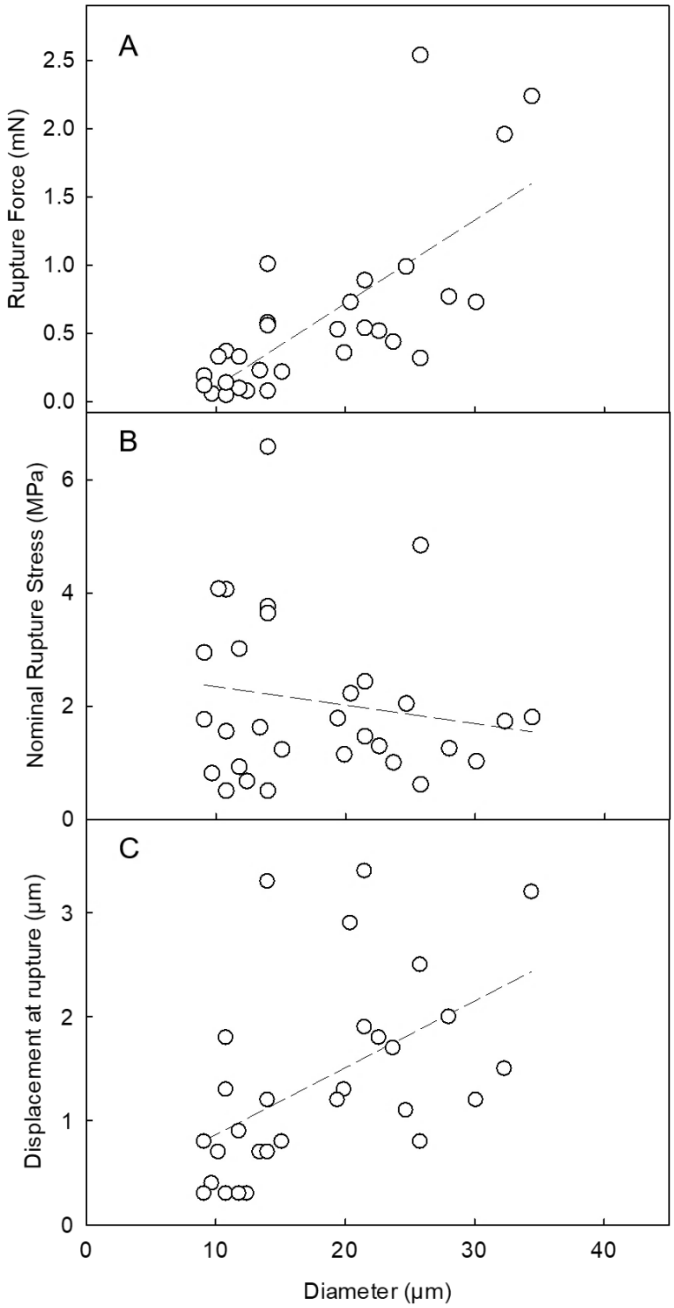

Figure 6.7– Mechanical properties of single LC- microcapsules fabricated *via* two-stage encapsulation (complex coacervation followed by spray drying): rupture force (A), nominal rupture stress (B), and displacement at rupture *versus* diameter of LC-microcapsules (C). The dashed lines only represent the trend.

6.3.2.7 Shell Thickness

TEM imaging was used to investigate the shell thickness of LC-microcapsules, which had been ultracut with a sectioning microtome. The procedure was applied to thirty randomly selected LC-microcapsules in order to obtain statistically representative results [17, 18, 266]. Solid shells with a relatively spherical shape were identified (Figure 6.8A-B). The shell topography of each microcapsule was investigated, and shell thickness was measured at three different regions of the shell itself *via* image analysis, hence an average was calculated. Several extra intra-shell cavities were also discernible, which may be the result of TEM artifacts probably occurring during TEM sample preparation. Alternatively, such cavities (Figure 6.8C) may endorse our previous OM observations, where multinuclear structures had been seen (Figure 6.1). In addition, these cavities could also be associated with the presence of residual surface oil droplets following coacervation, which might have been entrapped during spray drying. Figure 6.9 displays the relationship between the shell thickness (h) and the microcapsule diameter (d). It was found that h increased linearly with d (R^2=0.9), which suggests that the larger the oil droplet, the thicker the shell forming around the oil droplet during coacervation. There findings are in very good agreement with HS-microcapsules, as presented in Chapter V. The corresponding average shell thickness attained from 30 TEM-imaged microcapsules was 0.91±0.15 μm. In addition, TEM micrographs of the shell were consistent with the observations of microcapsule shells *via* SEM (Figure 6.3E-F). In addition, the average shell thickness was comparable with that observed from HS-microcapsules (0.78±0.06 μm). Overall, it could be deduced that relatively thick shells can form around LC-oil droplets successfully, leading to a core-shell structure (Figure 6.8A-C).

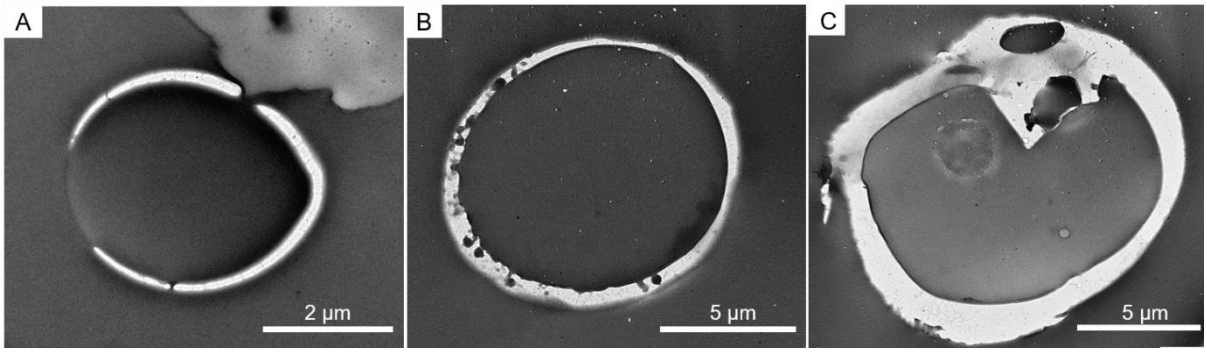

Figure 6.8– Cross-sectional TEM imaging of spherical microcapsules with a diameter and average shell thickness of (A) ~5 µm and 0.4 µm, respectively; (B) ~10 µm and ~0.5 µm, respectively, and exhibiting multiple intra-shell voids; (C) ~15µm and 0.85 µm, respectively, and displaying intra-shell pockets.

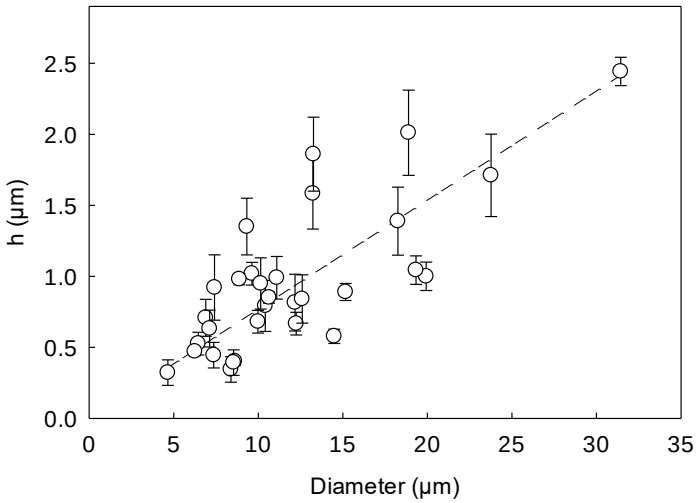

Figure 6.9– Shell thickness *versus* diameter of 30 randomly selected TEM-imaged microcapsules. Some error bars are smaller than the size of the symbols. Linear fitting performance: coefficient of determination (R^2=0.9).

6.3.2.8 Solubility of LC in different Aqueous Ethanol Media with Commercial Interest

In personal care and cosmetic products, ethanol is often used in the formulation [444]. The solubility of LC ($c_{s,LC}$) in aqueous ethanol media are presented in Figure 6.10. When compared to pure water, 5%(w/w) ethanol as the co-solvent was found to increase the solubility of LC by 97±7% leading to $c_{s,5\%}$=1.4·10^{-4}±1.5·10^{-5} g·mL^{-1}. As expected, the solubility improved even more at higher alcoholic concentrations, with particular emphasis on 20% (w/w) where it was higher ($c_{s,20\%}$=2.4·10^{-3}±3.7·10^{-4} g·mL^{-1}) than that at 5%(w/w) aqueous ethanol by approximately one order of magnitude. This suggests that the increase in solubility with the co-solvent concentration may not be linear. Accordingly, the solubility appeared to have plateaued ($c_{s,50\%}$=0.13±0.02 g·mL^{-1}) between 50%(w/w) and 60%(w/w) aqueous ethanol.

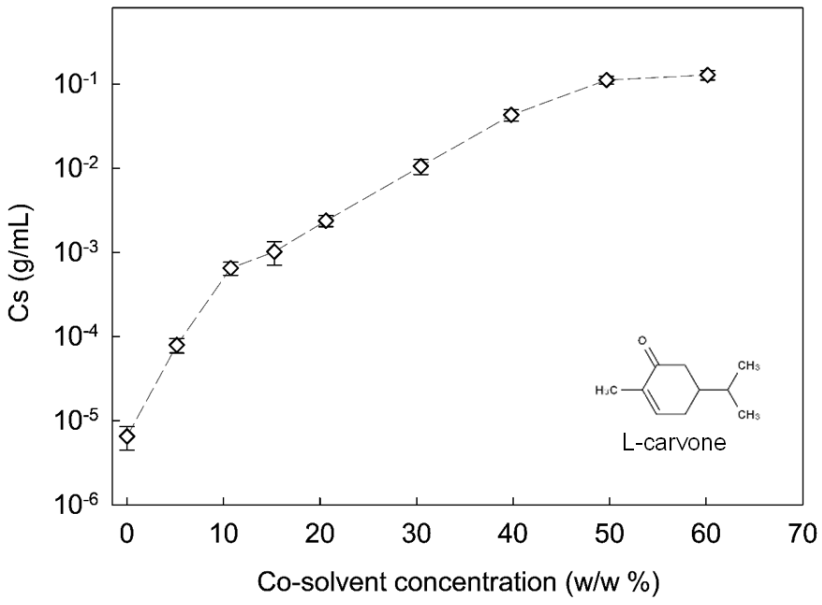

Figure 6.10– Saturation concentration ($c_{s,LC}$) in different aqueous ethanol environments at 22±1 °C.

6.3.2.9 Oil Release

Figure 6.11 displays the oil release profiles in all aqueous ethanol media investigated. As can be seen, the experimental cumulative release ($R(t)$) data were also fitted to a non-linear regression model ($R(t)=\xi(1-e^{-ßt}$) with physical significance (Eq.(7.5C)) in order to best describe the exponential release of the oil (LC) within the whole timeframe investigated (~1.5h). Oil release from microcapsules depends upon the nature of active ingredient contacting the reticular shell complex. In addition, the composition of the dispersing medium also plays a key role. As shown in Figure 6.11, different time-dependent release profiles of LC were observed from fCh-GA microcapsules when exposed to environments with different aqueous ethanol concentrations. In water (0% EtOH) for 1.5h, less than 40% LC leakage was observed, which was significantly less than ~85% in 20% aqueous ethanol. Oil leakage in pure water was the slowest. Accordingly, the cumulative release of LC in 5%, 10%, and 15% (w/w) aqueous EtOH after 1.5h was increasingly higher, *i.e.* 49%, 52%, and 60%, respectively. Thus, there appeared to be a clear effect of EtOH as the co-solvent to drive the leakage of LC. Similar results were also reported by Mercade-Prieto *et al.* [16] utilising a hydro-propanolic system. This finding is not surprising since the solubility of LC in aqueous ethanol environments is much greater than in water ($c_{s,LC-w}$). Thus, the co-solvent accelerated the mass (oil) transfer from the microcapsules into the receptor medium.

Interestingly, the curve at 10%, 15%, 20% aqueous ethanol in Figure 6.11 clearly display some oil detected at time zero. This is likely ascribable to damaged microcapsules which can release the oil core partly/completely when contacting a high-driving force solvent. Alternatively, surface oil may also be present, which can be solubilised into the aqueous solvent receptor medium instantaneously. This does not contribute to a sustained release, which has been referred to as the waste oil parameter (w_{oil}) by Mercade-Prieto *et al.* [16].

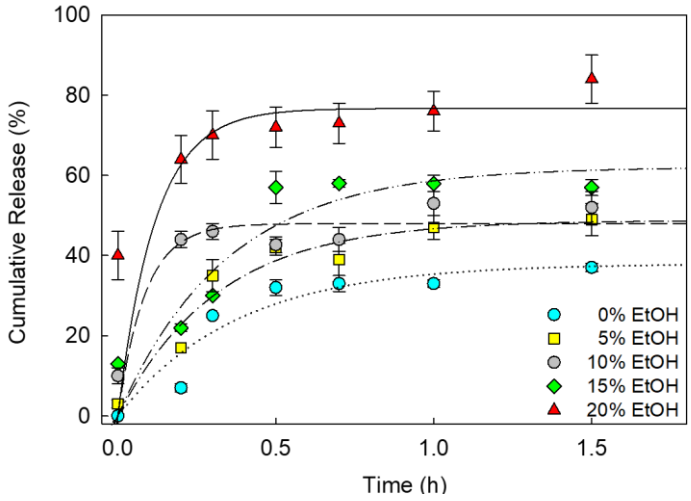

Figure 6.11– Release profiles of LC in aqueous ethanol media with different co-solvent concentration (w/w), which are represented by the following graphical symbols: 0% (·····), 5% (—·—), 10% (— — —), 15% (—··—), 20% (——).

6.3.2.10 Potential Applications of LC-microcapsules in Aqueous Ethanol based Formulations

When dealing with end-use applications, the dry microcapsules herein fabricated may have a potential for personal care and cosmetics products, with particularly emphasis on chemical depilatory creams for topical hair removal [269]. Depilatory formulations rely on thioglycolates as the penetration enhancers through the hair shaft, which are as such harmful skin-sensitisers due to their alkaline pH (10~12.5) [445]. Interestingly, Moghimi et al. (2013) have demonstrated that the synergetic action between peppermint oil and aqueous ethanol may help to promote a quicker depilation by enhancing the activity of thioglycolates, [269] hence reducing the risk of skin sensory irritation due to extended exposure. To this end, peppermint oil microcapsules directly attached to the hair shaft may be particularly helpful since they can rupture and thus release their peppermint oil load directly onto the hair follicle, when exposed to aqueous ethanol (Figure 6.12). Therefore, the penetration activity of thioglycolates may

improve significantly, thereby possibly leading to a much lower concentration of thioglycolates required in formulation, hence to a lower pH on the skin. Moreover, microcapsules may contribute to better controlling the overall time required for depilation, since the oil from microcapsules may be readily available onto the hair shaft, thus reducing mass (oil) transfer losses from the bulk (depilatory formulation) towards the follicles (active depilation site). A diagram of the potential mechanism of oil delivery to the active depilation site is displayed below.

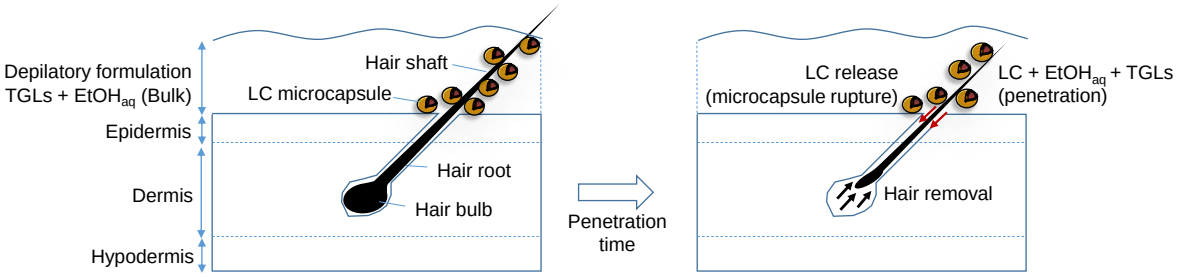

Figure 6.12– Potential mechanism of oil (LC) delivery from microcapsules towards the active depilation site (follicle) to facilitate depilation with a depilatory formulation containing a reduced concentration of thioglycolates (TGLs), and aqueous ethanol ($EtOH_{aq}$).

6.4 Conclusions

The results herein presented showed that fungal chitosan-based microcapsules with a core of peppermint oil (LC) can be fabricated *via* two-stage encapsulation processes including complex coacervation followed by spray drying. A size distribution in the range of 10-125 µm and a Sauter diameter of 37.8±1.4 µm were obtained. Encapsulation efficiency and payload of microcapsules were 29±4 % and 19±3%, respectively, which are in line with other microcapsules with different essential oils reported in literature [6]. Moreover, dry

microcapsules did not show any significant oil leakage over 50 days. SEM micrographs displayed spherically shaped microcapsules with a core-shell structure. Microcapsule surface topography evidenced relatively smooth surfaces, with several dent- as well as crease-rich regions. Effective oil entrapment was assessed via fluorescence microscopy using Nile red as a solvatochromic dye. In addition, the shell thickness of LC-microcapsules was investigated by TEM imaging, and its resulting average value was 0.91±0.15 μm, which was similar to that observed from HS-microcapsules. Micromanipulation showed that the rupture force of LC-microcapsules averagely increased with diameter, with an average value of 0.6±0.1 mN. The mean nominal rupture stress was 2.1±0.3 MPa, which is close to that of the gelatine-gum Arabic microcapsules with double shells presented by Yu *et al.* [63]. In addition to functional food and oral care, a potential end-use application of such LC-microcapsules in depilatory formulations has been outlined.

Chapter 7 In-depth Analysis of the Micromanipulation and Release Data Using Numerical and Mathematical Modelling †

7.1 Introduction

Previous chapters have focused on the preparation and characterisation of microcapsules with a core of fragrance oil and a flavour oil. Specifically, it has been demonstrated that micromanipulation is a powerful platform to measure the mechanical properties of microcapsules. However, determination of the intrinsic material property parameters of microcapsule shells, such as the Young's modulus, need a more sophisticated analysis. In this chapter, the Young's modulus of microcapsule shells was determined by combining the experimental micromanipulation data with numerical modelling results. Specifically, the results from Finite Element Analysis (FEA) [18, 331] were utilised to fit the micromanipulation data of single core-shell microcapsules, enabling to determine the shell thickness and the shell Young's modulus. The shell Young's modulus obtained was also compared with the Young's modulus value of the whole microcapsule treated as a solid spherical particle, determined by the classical Hertz model. These results led to establish a theoretical relationship between the two Young's modulus values, which is reported herein. In addition, the shell thickness of the microcapsules obtained by the FEA modelling was also validated *via* TEM. Furthermore, the release behaviour of fragrance and flavour oil from microcapsules was examined to quantify their barrier properties. This was fulfilled by

† Part Published at Baiocco, D., Preece, J. A., & Zhang, Z. (2021), *Food Hydrocolloids For Health*, 100016.

combining the experimental release data with mathematical modelling in order to determine the shell permeability of microcapsules.

7.2 Methodology

The methodology is based on the Finite Element Analysis (FEA) and a solute-diffusion model, which have been previously introduced by Mercade-Prieto *et al.* [16], [18]. Subsequently, the modelling has been combined with the micromanipulation and release data of HS and LC-microcapsules, which are explained herein.

7.2.1 Core-Shell FEA Model

7.2.1.1 Introduction to the Core-Shell FEA Model

As extensively discussed in Chapter 5 and Chapter 6, both HS and LC-microcapsules exhibited a core-shell structure. This information was beneficial since it enabled to identify the correct model (*i.e.* core-shell) to be fitted to the experimental data. Besides, this model also enables to predict the shell thickness to the microcapsule radius ratio (h/r) of single microcapsules simultaneously [18], which should be then compared with that obtained experimentally by TEM imaging. Interestingly, the FEA model includes the bending of the shell in the numerical calculations, which is not considered in the Hertz model [101]. Therefore, the shell Young's modulus can be determined by applying the micromanipulation data combined with the results of FEA of core-shell microcapsules [16], which is presented as follows:

$$E_{FEA} = \frac{F}{\frac{h}{r}\left(f_1\left(\frac{\delta}{2}\right)^2 + f_2\left(\frac{\delta}{2}\right)r + f_3\, r^2\right)} \tag{7.1}$$

where E_{FEA} is the predicted Young's modulus of the shell, F is the experimental compression force obtained *via* micromanipulation, δ is the compressive axial displacement during compression, h/r is the ratio of the shell thickness to the microcapsule initial radius, and f_1, f_2, and f_3 (Model applicability domain $0.03<h/r<0.14$) are polynomial functions (Table 7.1) of h/r first presented by Mercadé-Prieto *et al.* [18]. Practically, the Young's modulus value of each microcapsule shell was determined by fitting the experimental force (F) versus displacement (δ) data up to a nominal deformation of 10% to (7.1) using the least squares method with E_{FEA} and (h/r) as adjustable parameters, which was implemented based on a function of Solver in Excel.

Table 7.1 – Polynomial functions of h/r by Mercadé-Prieto *et al.* [18]. More details are available at Appendix C.

Coefficient	Polynomial
f_1	$95071.891\,(h/r)^5 - 28426.030\,(h/r)^4 + 2411.056\,(h/r)^3 - 7.476\,(h/r)^2 - 10.829\,(h/r) + 1.52882$
f_2	$-318.702\,(h/r)^4 + 120.784\,(h/r)^3 - 11.380\,(h/r)^2 + 2.518\,(h/r) - 0.05792$
f_3	$-0.004242\,(h/r) + 0.00107$

7.2.1.2 Mathematical Interrelationship between Core-Shell and Hertz Models for Microcapsules: an Original Approach

As presented in Chapter 4 for coacervate beads, the Hertz model can be applied to solid particles. Over the years, the classic Hertz model has also proven effective to describe the relationship between the compression force and axial displacement for small deformations of an elastic particle (nominal strain ≤10%) assuming frictionless contact [63]. Under these

conditions, it has been successfully applied to determine Young's modulus (E_H) of whole microcapsules treated as solid spheres, as described by the following Equation (7.2):

$$E_H = \frac{\psi}{\vartheta}(1-\nu^2)Fr^{-1/2}\left(\frac{\delta}{2}\right)^{-3/2} \tag{7.2}$$

where ψ/ϑ is the spherical shape factor equal to 4/3, ν is the Poisson ratio that is assumed to be 1/2 for non-compressible materials. Since the compression force F is obtained experimentally, which is the same in both Eq. (7.1) and (7.2), the two equations can be combined into:

$$\frac{\psi}{\vartheta}\frac{r^{1/2}\left(\frac{\delta}{2}\right)^{3/2}}{(1-\nu^2)}E_H = \frac{h}{r}\left(f_1\left(\frac{\delta}{2}\right)^2 + f_2\left(\frac{\delta}{2}\right)r + f_3 r^2\right)E_{FEA} \tag{7.3}$$

Let $\varepsilon = \delta/2r$ be the fractional deformation of a single microcapsule [31], thus E_H can be expressed as:

$$E_H = \frac{\vartheta}{\psi}(1-\nu^2)\cdot\frac{h}{r}\cdot(f_1\varepsilon^{1/2} + f_2\varepsilon^{-1/2} + f_3\varepsilon^{-3/2})E_{FEA} \tag{7.4}$$

which results in a theoretical correlation between E_H and E_{FEA}. If the correlation could be validated, the equation may be utilised to predict one of the two parameters provided that the other one is known. Therefore, it is crucial to compare the Young's modulus values of E_H and E_{FEA} in order to validate the relationship.

7.2.2 Introduction to the Solute-Diffusion Model

7.2.2.1 Oil Release from Microcapsules

In past years, a slurry of perfume microcapsules was typically immersed in an aqueous solution, and subsequently an organic solvent, such as hexane, was added in order to release the active oil into the organic phase [14]. However, the presence of two phases created a resistance of perfume transfer [16]. Given that, the release rate based on the change in perfume concentration in the organic phase was the result of several perfume transfer steps, leading to apparently slower release rate than from the microcapsules to the aqueous phase. For this reason, the shell permeability could not be quantified easily, since it was conditional upon the mass transfer coefficient between the two phases. This shortcoming was recently overcome by Mercade-Prieto *et al.* [16] by employing a two-component miscible receptor medium. Accordingly, a co-solvent was introduced to enhance the solubility of the oil in the medium, without damaging the microcapsule shells. Overall, the co-solvent can assist the oil release from microcapsules facilitating the mass transfer into the receptor medium, hence ruling out any partition coefficient between immiscible phases. Accordingly, the release would be only linked to the oil concentration gradient (driving force) between the inside of microcapsules and the outside (receptor medium).

7.2.2.2 Solute-Diffusion Model

Noteworthy efforts to quantify the shell permeability (P) of perfume oil microcapsules *via* a linear diffusion model have been recently made by Mercade-Prieto *et al.* [16]. The mathematical modelling (Appendix D) was developed for thin-shell microcapsules, where h and r are the shell thickness and the radius of the microcapsules, respectively. The model relies on a simple solute-diffusion mechanism (Fick's first law) of the oil present in the microcapsule into a suitable receptor medium [16]. The time-dependent cumulative release $R(t)$, evaluated

experimentally, was used to determine P/h by the following generalised set of equations (7.5A,B,C):

$$R(t) = \begin{cases} \dfrac{\vartheta}{r\left(1-\dfrac{h}{r}\right)^3}\dfrac{c_{s,oil}-c_{out}(t)}{\rho_{oil}}\left(\dfrac{P}{h}\right)t & t < t^* \quad (7.5A) \\ 1-\dfrac{c_{s,oil}}{\rho_{oil}} & t = t^* \quad (7.5B) \\ \dfrac{\vartheta}{\psi}\dfrac{V_s}{\pi(r-h)^3}\dfrac{c_{s,oil}}{\rho_{oil}}\left(1-e^{-N_{tot}\frac{\psi\pi r^2}{V_s}\left(\frac{P}{h}\right)t}\right) & t > t^* \quad (7.5C) \end{cases}$$

where $R(t)$ is the cumulative released oil in weight percentage (dimensionless) at time t (s), h/r the shell thickness to microcapsule radius ratio, ρ_{oil} (ρ_{HS}, ρ_{LC}) the oil density (kg·m^{-3}), (P) the permeability (m^2·s^{-1}), and $\vartheta = 3$ and $\psi = 4$ are the volume and surface factors for spherical microcapsules, respectively; $c_{s,oil} - c_{out}(t)$ represents the concentration driving force (kg·m^{-3}), namely the difference between the oil saturation concentration $c_{s,oil}$ (kg·m^{-3}) in a given aqueous propanol (HS 36% w/w) or ethanol (LC 0-20% w/w) receptor medium and the concentration of the oil solubilised in a well-mixed aqueous ethanol receptor medium. Equation (7.5A) refers to the linear regime (the oil core is still present inside the shell of the microcapsule) from which P/h can be evaluated, under the following assumptions: (*i*) the oil concentration in the solvent outside the shell ($\boldsymbol{c_{out}}$) is much lower than that inside ($\boldsymbol{c_{in}}$) the shell ($\boldsymbol{c_{out} \ll c_{in}}$); (*ii*) the concentration of solubilised oil inside the capsule equals the saturation concentration ($\boldsymbol{c_{in} = c_{s,oil}}$) of the oil in the receptor medium ($\boldsymbol{c_{s,oil}}$); (*iii*) the linear regime does

not depend upon extrinsic parameters, such as V_s (m^3) [16]. In contrast, Equation (7.5C) depends on V_s, and refers to exponential regime when the solubilised oil inside the microcapsule is progressively released, hence the oil core gradually disappears, under the following assumption: the concentration of solubilised oil inside the capsule shell ($\boldsymbol{c_{in}}$) is much lower than that oil saturation concentration in the receptor medium ($\boldsymbol{c_{in} \ll c_{s,oil}}$). When the total volume inside the microcapsule is at concentration $\boldsymbol{c_{s,oil}}$, the linear regime will transition into the exponential regime at $t = t^*$ (Equation ((7.5B)), as previously described by Antipov *et al.* [446] and shown in Figure D2 (Appendix D.1) . Accordingly, Equation (7.5C) should refer to the total surface area of microcapsules, hence the total number of microcapsules (N_{tot}), which can be simply evaluated based on the bulk density (ρ_b) of dry microcapsules resulting from the weighted average of the individual ρ_b of the shell precursors.

When dealing with HS, $c_{s,HS\text{-}H2O} = 6.0 \cdot 10^{-6}\ g \cdot mL^{-1}$ and $c_{s,HS\text{-}PropOH} = 6.7 \cdot 10^{-3}\ g \cdot mL^{-1}$ (36% w/w) for pure water and aqueous propanol at 22±1°C, respectively [264]. The concentration of HS was assumed homogeneous in the total receptor medium, thereby fulfilling two crucial criteria, namely well-mixed conditions and thin boundary layer outside the microcapsule.

7.3 Results & Discussion

7.3.1 Investigation of the Young's Modulus of Microcapsules

7.3.1.1 Determination of the Young's Modulus of Microcapsule Shell via FEA Modelling

Figure 7.1 displays the typical fitting of the force-displacement and force-fractional deformation data ($\varepsilon \leq 0.1$) fitted by the Hertz model and FEA simulation results for individual microcapsules.

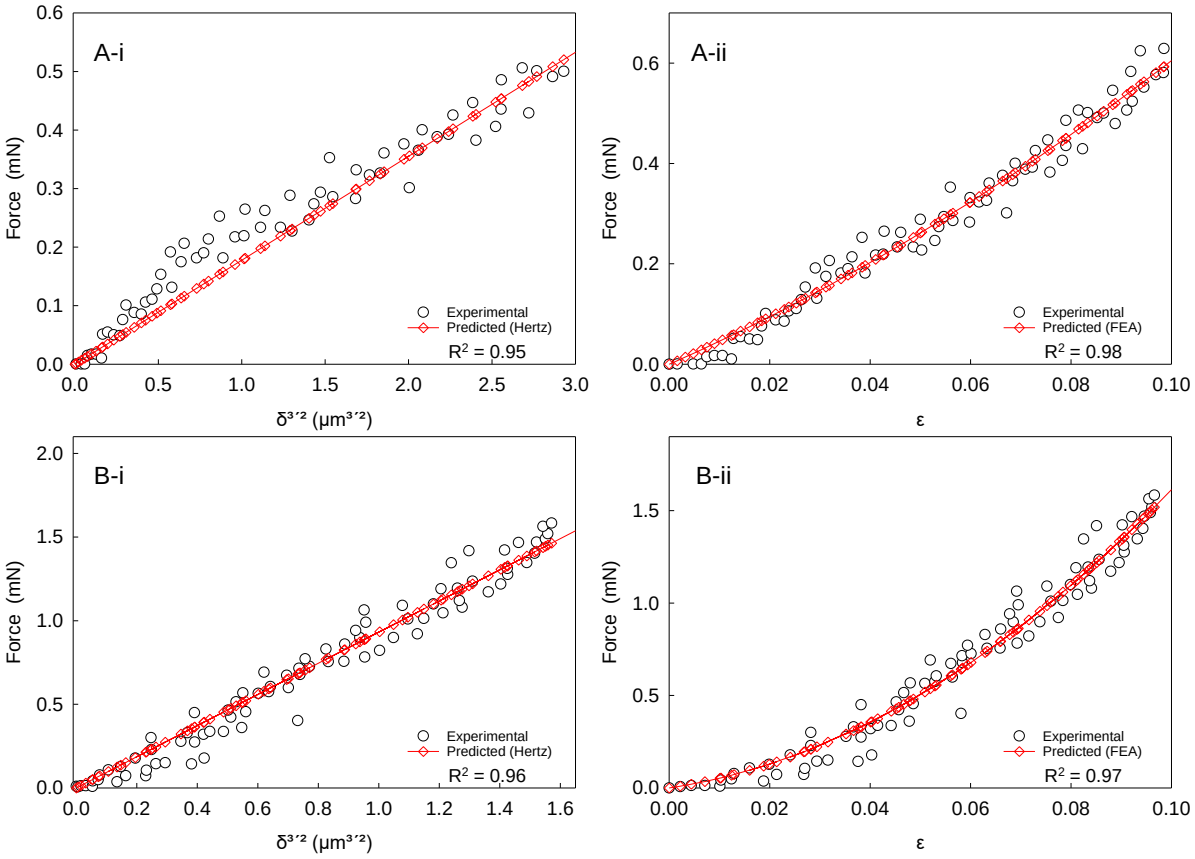

Figure 7.1– Typical fitting of the force-displacement and force-fractional deformation data ($\varepsilon \leq 0.1$) fitted by the Hertz model and FEA simulation results for a single HS-microcapsule (d=23.7 μm) (A-i: Hertz; A-ii: FEA) and LC-microcapsule (d=14.0 μm) (B-i: Hertz; B-ii: FEA).

For the two samples, as displayed in Figure 7.2– , the Young's modulus of HS and LC-microcapsule shells seemed to slightly decrease with diameter. The corresponding Young's moduli obtained from thirty microcapsules were 1.0±0.1 GPa and 1.3±0.3 GPa for HS- and LC-microcapsule shells, respectively. Interestingly, these values were found close to the Young's modulus evaluated *via* FEA by Mercadé-Prieto *et al.* [18] for MF-based microcapsules (1.6±0.3 GPa). A statistical analysis (*t*-test) indicates that the mean difference

in E_{FEA} between HS and LC-microcapsule shells is not significant with 95% confidence [447]. This also suggested that both HS-microcapsules formed with fCh and GA by complex coacervation only and LC-microcapsules additionally processed by maltodextrin-assisted spray drying, which has probably created an additional component in coating, resulted in a similar Young's modulus.

Furthermore, the Young's moduli observed from HS and LC-microcapsule shells were also close to those from other polymeric microspheres for pharmaceutical applications (1.6±0.2 GPa) documented by Yap *et al.* [317]. In addition, similar Young's moduli were also reported in literature based on AFM, which is a different technique from micromanipulation. Specifically, core-shell microcapsules formulated with aminoplast [448], poly(styrene sulfonate)/poly(allylamine) [312], and poly(D,L-lactide-co-glycolide) [449] exhibited a Young's modulus of 1.7 GPa, 1.3±0.15-1.9±0.2 GPa, and 0.1–3.0 GPa, respectively. In contrast, Tan *et al.* [450] conducted AFM measurements on oil-laden microcapsules made of thiolated chitosan surprisingly showing a Young's modulus of 1.44 MPa, which is around three order of magnitude lower than what is reported earlier. This major discrepancy was probably due to the combination of several effects, including the processing conditions (*i.e.* ultrasonic synthesis), and the chemistry of chitosan used, which had been grafted with thiol groups using DL-N-acetylhomocysteine thiolactone [450]. Moreover, a crucial role may also be played by the size of the spheres (<10 μm) and the extremely thin shells (<180 nm). Having said that, the determination of the shell thickness as well as the h/r of the HS- and LC-microcapsules have been extensively studied *via* TEM imaging and FEA, as detailed later in this chapter.

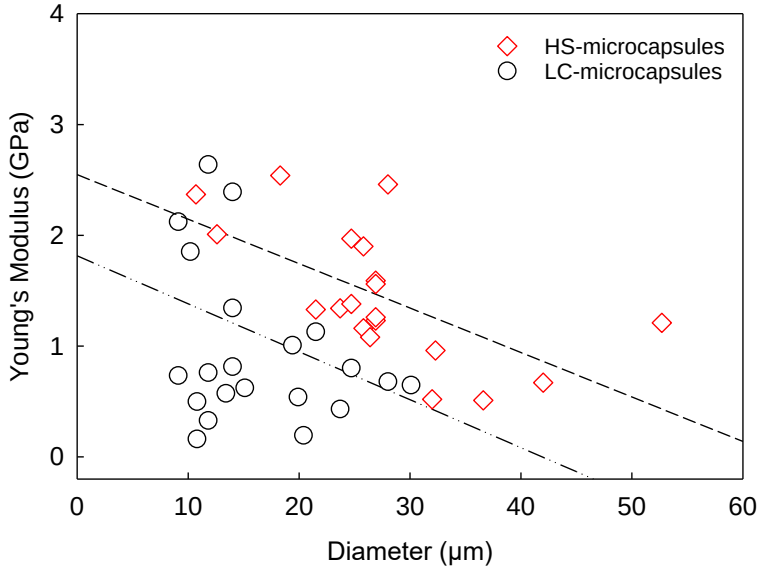

Figure 7.2– Young's modulus of HS (◊) and LC-microcapsule shells (○) obtained using the micromanipulation data combined with FEA as described in Equation (7.1). The dashed lines represent the trend only.

7.3.1.2 Comparison between the Young's Moduli of Microcapsules obtained via Hertz Model and FEA

The Hertz model has proven relatively accurate to determine the Young's modulus (E_H) of whole and smooth particles. [18]. On average, the Young's modulus of whole HS microcapsules determined by the Hertz model was $E_{H,HS}$=0.095±0.014 GPa. This value is much lower than E_{FEA}, which is expected since the microcapsules contained liquid HS that has zero Young's modulus. E_H versus E_{FEA} is thus plotted for HS and L-carvone microcapsules. There appears to be a strong linear correlation between E_H and E_{FEA} (R^2=0.88), as shown in Figure 7.3– A. Similar results were observed from the analysis of the Young's moduli (determined by the Hertz model and FEA) of LC-microcapsules. It was found that the Young's modulus determined by the Hertz model based on thirty LC-microcapsules was $E_{H,LC}$=0.118±0.023 GPa,

whereas $E_{FEA,LC}$=1.3±0.3 GPa. A strong linear correlation between E_H and E_{FEA} (R^2=0.96) was also obvious in this case (Figure 7.3B). Overall, the slope ($\Lambda_{H\cdot FEA}$) of the trendline represents a factor of proportionality between the two corresponding Young's moduli:

$$E_H = \Lambda_{H\cdot FEA}\, E_{FEA} \tag{7.6}$$

where $\Lambda_{H\cdot FEA}$ were determined to be 0.0932±4.7·10^{-3} and 0.0895±4.4·10^{-3} from HS- and LC-microcapsules, respectively. As can be seen, the two values appeared in very good agreement with each other, which seems to confirm that a linear correlation between E_H and E_{FEA} occurs.

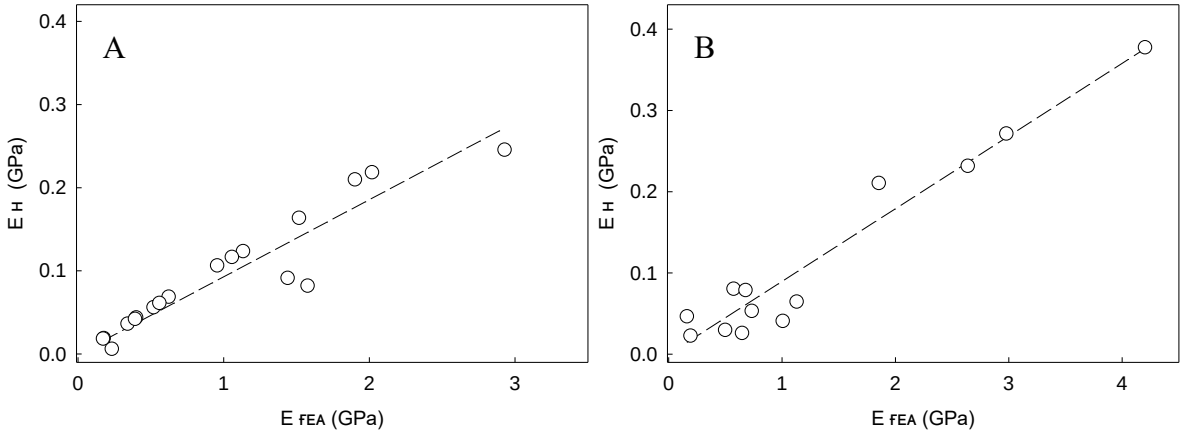

Figure 7.3– Linear relationship between the Young's modulus values determined by the Hertz model and FEA for (A) HS-microcapsules (R^2=0.88) and (B) LC-microcapsules (R^2=0.96).

However, $\Lambda_{H\cdot FEA}$ is a complex function of several parameters (*i.e.* r, ν, h/r) theoretically, as clearly displayed by Equation (7.4). For the two samples, they had similar sizes, ν=0.5, and h/r values (see Table 7.2), which led to a similar value of $\Lambda_{H\cdot FEA}$.

Table 7.2 –Shell thickness and Young's moduli (Mean ± St. err) of HS- and LC-microcapsules obtained *via* FEA and the Hertz model. The results were based on thirty microcapsules in each sample.

	HS-microcapsules	**LC-microcapsules**
Number-based Diameter (μm)	27.5 ± 1.5	17.8 ± 1.4
$(h/r)_{FEA}$	0.132 ± 0.009	0.141 ± 0.008
$\Lambda_{H\cdot FEA}$	$0.0932 \pm 4.7\cdot10^{-3}$	$0.0895 \pm 4.4\cdot10^{-3}$
E_{FEA} (GPa)	1.0 ± 0.1	1.3 ± 0.3
E_H (GPa)	0.095 ± 0.014	0.118±0.023

7.3.1.3 Comparison of $(h/r)_{FEA}$ with $(h/r)_{TEM}$

As presented in Chapters V (§5.3.9) and VI (§6.3.2.7) for HS- and LC-microcapsules respectively, TEM imaging was performed on thirty randomly selected microcapsules to measure the shell thickness and the resulting average $(h/r)_{TEM}$ of microcapsules experimentally. Furthermore, $(h/r)_{TEM}$ was compared with the FEA-predicted $(h/r)_{FEA}$ to assess whether the two parameters would be mutually consistent. In Section 5.4.8, a linear relationship between the shell thickness of HS-microcapsules and their diameter was found. The apparent shell thickness of HS-microcapsules was h_{app}=0.78±0.06 μm on average resulting in $(h/r)_{TEM}$=0.138±0.009. The FEA-predicted $(h/r)_{FEA}$ of HS-microcapsules was 0.132±0.009, which was found to be in good agreement with $(h/r)_{TEM}$. Although artifacts due to ultracutting during the preparation of TEM-samples were likely, they were carefully minimised by measuring the thickest as well as thinnest shell at three locations for each microcapsule. However, cross-sectional ultracutting typically occurs at random planes other than the equator, thus $(h/r)_{TEM}$ should be corrected using a correction parameter of 0.86 according to Mercadé-Prieto *et al.* [18]. The correction provided $(h/r)_{TEM*}$=0.119±0.008. A *t*-test was performed, which showed there is no statistically

significant difference between the means of $(h/r)_{FEA}$ and $(h/r)_{TEM}$ with 95% confidence. Figure 7.4A displays both FEA-predicted $(h/r)_{FEA}$ and TEM-derived $(h/r)_{TEM}$ of HS-microcapsules as a function of their diameter, together with their average values. As can be seen, h/r did not change significantly with the microcapsule diameter. Similar studies were reported for other microcapsules with a shell of MF [18, 62, 451]. However, the microcapsules with a shell of MF revealed much lower h/r values on average by FEA and TEM imaging, hence much thinner shells (~0.2 μm) [18] than that of HS-microcapsules (0.78±0.06 μm).

Similar findings were obtained for LC-microcapsules as well. Specifically, it was found that the apparent shell thickness was 0.91±0.15 μm on average, resulting in $(h/r)_{TEM}$=0.157±0.009. This value was in agreement with the FEA-predicted $(h/r)_{FEA}$=0.141±0.008. Notwithstanding, the corrected $(h/r)_{TEM*}$ according to Mercadé-Prieto *et al.* [18] provided $(h/r)_{TEM*}$=0.135±0.008, which is closer to the FEA-predicted value. Again, the *t*-test revealed no statistically significant difference between $(h/r)_{FEA}$ and $(h/r)_{TEM}$ for LC-microcapsules. As for HS-microcapsules, Figure 7.4B displays both FEA-predicted $(h/r)_{FEA}$ and TEM-derived $(h/r)_{TEM}$ of LC-microcapsules as a function of their diameter, together with their average values. As observed from HS-microcapsules, h/r did not seem to change significantly with the microcapsule diameter. This result also appears to be consistent with the trend of shell thickness *versus* diameter presented for HS- and LC-microcapsules in Chapter V and VI, respectively. Overall, it could be inferred that the h/r values obtained from different methodologies were in good agreement, and this finding may open up an avenue towards predicting the actual h/r of microcapsules, and their shell thickness, directly from the micromanipulation data when TEM analysis is not available.

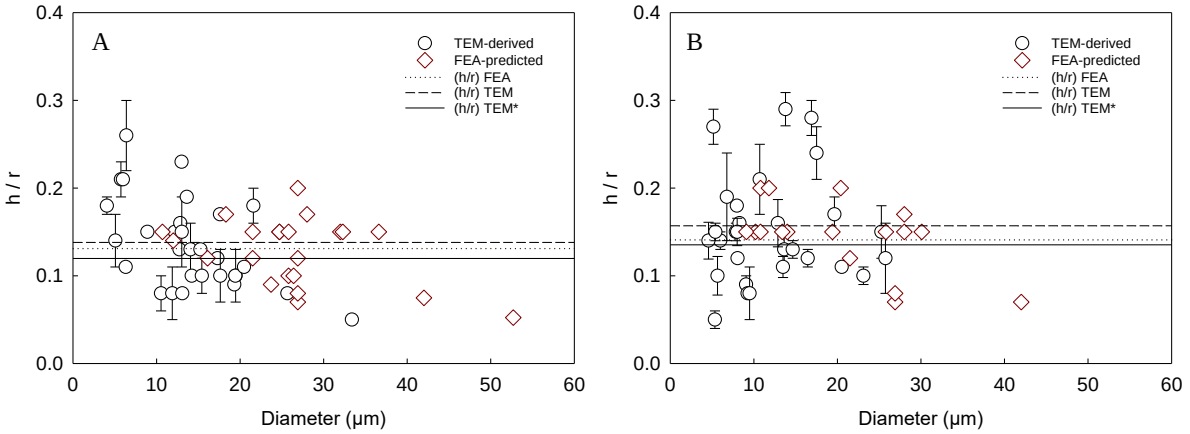

Figure 7.4– TEM-derived (○) and FEA-predicted (◊) h/r of single HS-microcapsules (A) and LC-microcapsules (B). The dashed, dotted, and straight lines represent the average TEM-derived $(h/r)_{TEM}$ (— — —), FEA-predicted $(h/r)_{FEA}$ (···), and TEM-corrected $(h/r)_{TEM^*}$ (—), respectively. The mean values are presented in Table 7.5.

7.3.2 Oil Release Rate

7.3.2.1 Shell Permeability of HS

Oil leakage from microcapsules may occur in different ways. Specifically, static leakage occurs naturally if the oil molecules are small enough to diffuse through the shell. By contrast, burst release of the oil occurs when the shells are ruptured due to an external mechanical action. Alternatively, gradual release of the oil can be driven by cosolvent-enriched receptor media, which substantially increase the solubility of the oil, thereby promoting the mass transfer [16]. The natural release of the oil during storage is undesirable yet not unusual, whereas the accelerated release is used to investigate the barrier properties of microcapsules and quantify the shell permeability. The rate of oil release also depends on the nature of the oil, the polymeric

shell, and the composition of the receptor medium. The linear model developed by Mercade-Prieto *et al.* [16] enables to estimate P/h using the experimental data in the linear regime of $R(t)$, when the oil is present inside the capsule (Appendix D). As shown in Figure 7.5, the experimental data was fitted to Equation (7.5A), under the assumption of a homogeneous concentration of the oil (HS) in the receptor medium (well-mixed conditions). The values of shell permeability to shell thickness ratio from cosolvent-free (water) and cosolvent-driven (36% w/w aqueous propanol) experiments were determined to be $(P/h)_{0\%}=2.3\cdot10^{-8}\ m\cdot s^{-1}$ ($R^2_A=0.75$) and $(P/h)_{36\%}=1.7\cdot10^{-8}\ m\cdot s^{-1}$ ($R^2_B=0.84$), respectively. Interestingly, the order of magnitude between $(P/h)_{0\%}$ and $(P/h)_{36\%}$ was the same, yet slightly different coefficients were determined. Although they appeared not to be statistically different, this minor discrepancy may be ascribable to the different viscosity of the two receptor media, with aqueous propanol (2.21 mPa·s) being more viscous than water (0.99 mPa·s) [452]. Similar results were provided by Mercade-Prieto *et al.* [16] on a different alcoholic system (aqueous 1-3-butanediol). Accordingly, the researchers have reported slightly lower values of the permeability at increased concentrations of the co-solvent, resulting from an increased viscosity in the receptor media [16, 453]. Overall, consistent P/h values (same order of magnitude) between cosolvent-free and cosolvent-enriched media suggest that the co-solvent may promote the release of the oil without damaging the polymeric shell of microcapsules significantly. Therefore, the accelerated oil release rate was likely due to the increased solubility of the oil in the selected medium [16]. Appropriate co-solvents may thus help to conduct accelerated oil release tests in order to estimate the shell permeability by a linear model quickly and effectively.

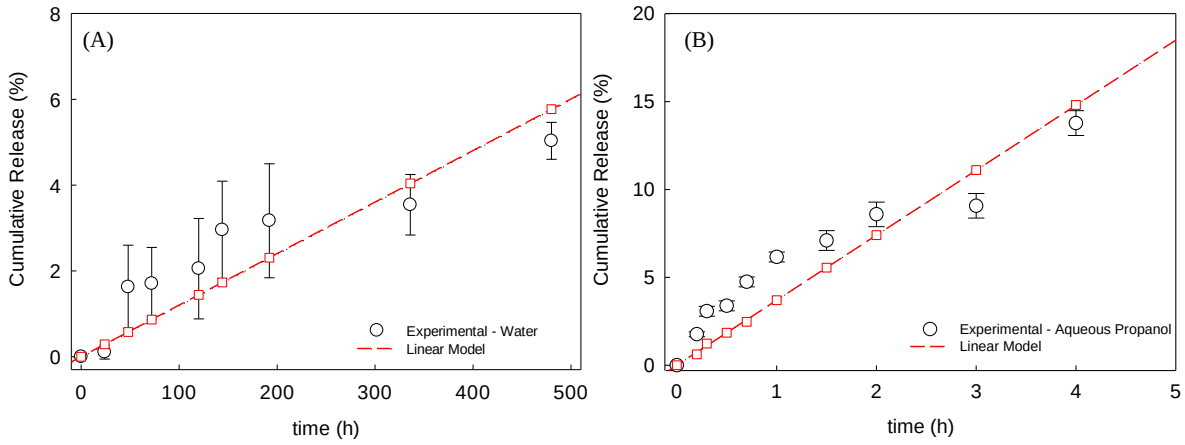

Figure 7.5– Cumulative release R(t) of HS-microcapsules (linear regime) exposed to water (cosolvent-free) (A) and 36%(w/w) aqueous propanol (cosolvent-enriched) (B); Experimental points (o), and the linear model (—□—). Model Performance coefficients: R^2_A=0.75; R^2_B=0.84.

The post-linear region of the oil release curve is typically followed by the exponential regime when the solubilised oil inside the microcapsule is gradually released, thus the oil core progressively disappears. The regressions of experimental data for HS in absolute water and aqueous propanol (36% w/w) are presented in Chapter V (§5.3.7; Figure 5.6). The regression coefficients of the non-linear regime ($R(t) = \xi(1 - e^{-ßt})$) are tabled below.

Table 7.3 – Non-linear regression coefficients for HS release from microcapsules to absolute water and aqueous propanol (36% w/w) as the receptor media.

Aqueous Propanol (w/w (%))	ξ (%)	ß (h^{-1})	R^2
0	5.5	$5.7 \cdot 10^{-3}$	0.93
36	54.1	$7.1 \cdot 10^{-3}$	0.87

7.3.2.2 Shell Permeability to shell thickness ratio (*P/h*) of LC

Following the experimental leakage data, *P/h* was calculated according to the generalised equations (Equation (7.5A) of the solute-diffusion model introduced by Mercade-Prieto *et al.* [16]. As shown in Figure 7.6, it was found that *P*/*h* ($1.8 \cdot 10^{-6}$ m·s^{-1}) was independent of the co-solvent concentration at 5%, 10%, 15%, and 20% aqueous EtOH, where the solubility of LC in such media was of the order of 10^{-4}-10^{-3} g·mL^{-1}. In contrast, a higher value of permeability to shell thickness ratio equal to $2.2 \cdot 10^{-5}$ m·s^{-1} was observed without EtOH as the co-solvent. One important factor to affect the permeability may be the viscosity of the aqueous ethanol environments. As reported in literature, the viscosity of 5% (w/w) aqueous ethanol is double that of absolute water [454]. Similar results were also reported by Mercade-Prieto *et al.* [16] for a different alcoholic system consisting of water and 1-3 butanediol. The authors have found that lower permeability values at higher co-solvent concentrations may be associated with the increase in viscosity of the receptor media [16, 453]. In addition, the shell chemical composition of LC-microcapsules may play a crucial role. As reported previously, maltodextrin is highly water-soluble [455, 456]. In contrast, the solubility of maltodextrin in aqueous ethanol solution can be significantly lower than in water [457]. Therefore, the effect of maltodextrin on increasing the shell permeability in pure water cannot be excluded. Overall, similar *P*/*h* values at different aqueous ethanol concentrations suggest that such environments may not trigger any significant damage to the polymeric shell of microcapsules, hence the different oil leakage rate may be ascribable to the different solubility values [16].

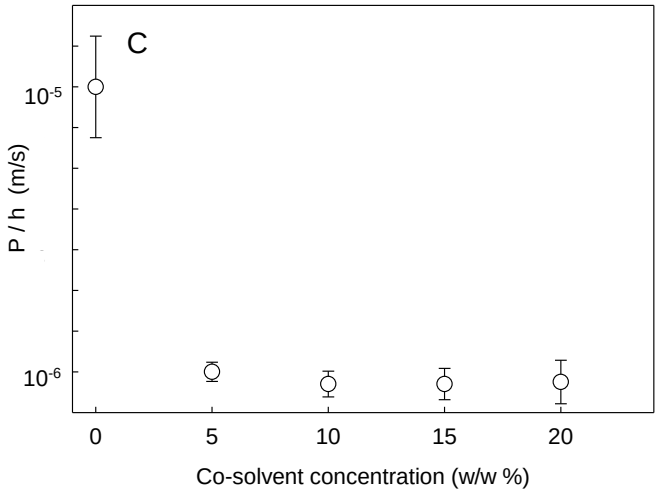

Figure 7.6– Permeability to shell thickness ratio (*P*/*h)* evaluated according to the model (7.5A). Some error bars are smaller than the size of the symbols.

As for HS, an exponential oil (LC) release regime was observed. The non-linear regression of the experimental data has been presented in Chapter VI (§6.3.2.9). The non-linear regression ($y=\xi(1 - e^{-\beta t})$) as well as the performance parameters (coefficient of determination R^2) which best describe the trend are tabled below. The physical significance of the performance parameters is detailed in Eq. (7.5A).

Table 7.4 – Non-linear model coefficients associated with the oil (LC) release of microcapsules exposed to aqueous ethanol receptor media at different co-solvent concentration (w/w).

Aqueous Ethanol (w/w (%))	ξ (%)	ß (h^{-1})	R^2
0	37.8	2.6	0.91
5	48.8	3.2	0.94
10	48.0	11.6	0.86
15	62.1	2.9	0.85
20	76.8	8.5	0.89

7.3.2.3 Determination of the Effective Oil Permeability

Following the studies on *P/h* by solute-diffusion model and shell thickness by FEA and TEM, the permeability (*P*) was calculated based on the $(h/r)_{TEM*}$ of microcapsules and their resulting number-based diameter. Specifically, it was found that the average permeability of HS in water and 36% (w/w) aqueous propanol were $P_{eff,HS\text{-}w}=(3.5\pm0.3)\cdot10^{-14}\ m^2\cdot s^{-1}$ and $P_{eff,HS\text{-}Pr}=(2.6\pm0.2)\cdot10^{-14}\ m^2\cdot s^{-1}$, respectively, which are of the same order of magnitude, as expected. Previous literature shows that the permeability of HS from the microcapsules with a shell of MF into 36%(w/w) aqueous propanol was around two order of magnitude higher [16] than that obtained from fungal chitosan-gum Arabic microcapsules fabricated for this project. This finding suggests that fCh-GA microcapsules might provide promising barrier properties when exposed to absolute water and aqueous propanol environments. In contrast, the effective diffusivity ($\mathbb{D}_{eff}$) of HS from fCh-GA microcapsules was approximately two order of magnitude greater than that reported by Long *et al.* [21] for MF microcapsules embedded in shellac ($\mathbb{D}_{eff}=1.4\cdot10^{-16}\ m^2\cdot s^{-1}$). This difference is plausible since the shellac-based matrix around MF microcapsules provides an additional coating, which thus delays the diffusion of oil through the shell [232, 458]. When dealing with LC-microcapsules, the effective permeability of LC through fCh-GA-MD microcapsules in the aqueous ethanol solutions (5-20% w/w) was determined to be $P_{eff,LC}=(4.2\pm0.3)\cdot10^{-12}\ m^2\cdot s^{-1}$, whereas in absolute water was

$P_{eff,LC}$=(5.1±0.2)·10^{-11} $m^2 \cdot s^{-1}$. These results were two and three orders of magnitude higher than what was determined from HS-microcapsules made with fCh-GA only. Most likely, the different permeability values may be associated with the different nature of the oils, hence their mechanism of dissolution and diffusion into the given receptor media.

Specifically, HS is an ester oil with a relatively extended linear structure, consisting of a carbon ring functionalised with oxygen and combined with a six-carbon alkyl chain. By contrast, LC is a terpene with a more compact structure with a lower molecular mass (150 $g \cdot mol^{-1}$) than that of HS (223 $g \cdot mol^{-1}$).

As formerly discussed, the presence of a co-solvent was proven to accelerate the solubility of the oil thereby accelerating its mass transfer into an aqueous medium significantly.

In presence of a co-solvent, the solubility (c_s) of HS in 36% (w/w) aqueous propanol and LC in 20% (w/w) aqueous ethanol were of the order of 10^{-2} $g \cdot mL^{-1}$ and 10^{-3} $g \cdot mL^{-1}$, respectively. Overall, $P_{eff,LC}$ was determined to be of around two orders of magnitude greater than $P_{eff,HS}$, which suggests that LC may naturally diffuse through the polymeric shell more rapidly than HS.

In other words, the mechanism of diffusion of HS through the microcapsule shell into the receptor medium (*i.e.* water or aqueous propanol) was probably partly inhibited due to the presence of its alkyl chain. This has probably led to the lower permeability of HS when compared to LC which possesses a more compact structure. Therefore, the lower permeability value may be ascribable to a relative steric effect of the alkyl chain of HS through the microcapsule shell. Alternatively, the conformation of LC having no alkyl chain seems to naturally facilitate its diffusion through the shell thereby leading to a higher permeability in aqueous ethanol.

Table 7.5 – Structural and diffusion key parameters of HS-microcapsules by modelling (Mean ± St. err).

	HS-microcapsules	**LC-microcapsules**
Number-based Diameter (μm)	27.5±1.5	17.8±1.4
Average Shell Thickness, h (μm)	0.78±0.06	0.91±0.15
$(P/h)_{water}$ $(m \cdot s^{-1})$	$2.3 \cdot 10^{-8}$	$2.2 \cdot 10^{-5}$
$(P/h)_{co\text{-}solvent}$ $(m \cdot s^{-1})$	$1.7 \cdot 10^{-8}$	$1.8 \cdot 10^{-6}$
$P_{eff,water}$ $(m^2 \cdot s^{-1})$	$(3.5\pm0.3) \cdot 10^{-14}$	$(5.1\pm0.2) \cdot 10^{-11}$
$P_{eff,co\text{-}solvent}$ $(m^2 \cdot s^{-1})$	$(2.6\pm0.2) \cdot 10^{-14}$	$(4.2\pm0.3) \cdot 10^{-12}$
$(h/r)_{FEA}$	0.132±0.009	0.141±0.008
$(h/r)_{TEM}$	0.138±0.009	0.157±0.009
$(h/r)_{TEM^*}$	0.119±0.008	0.135±0.008

7.4 Conclusions

In this chapter, the intrinsic material property parameter (Young's modulus) of HS and LC microcapsules was first investigated using the micromanipulation data combined with FEA. The FEA-predicted Young's modulus of HS and LC-microcapsules were determined to be 1.0±0.1 GPa and 1.3±0.3 GPa, respectively, which have no significant difference. Although the fabrication of LC-microcapsules included maltodextrin-assisted spray-drying following CC unlike HS-microcapsules (CC only), the Young's modulus of their shell was determined to be statistically equal. Interestingly, the values obtained were also in good agreement with the Young's modulus evaluated *via* FEA by Mercadé-Prieto *et al.* [18] for microcapsules with a shell of MF (1.6±0.3 GPa), and also similar to the Young's modulus of other polymeric microcapsules in literature which had been estimated by AFM [312, 448]. FEA-predicted Young's modulus values (E_{FEA}) of HS and LC microcapsules were further compared with their corresponding Young's modulus value (E_H) determined by the Hertz model. Although the E_H values of HS ($E_{H,HS}$=0.095±0.014 GPa) and LC-microcapsules ($E_{H,LC}$=0.118±0.023 GPa) were

much lower than their corresponding E_{FEA} as expected, there existed a strong linear correlation ($R^2 \geq 0.88$) between E_H and E_{FEA}. The factor of proportionality between the two corresponding Young's moduli was estimated from the correlation in both cases ($\Lambda_{H \cdot FEA}$). Moreover, the theoretical expression of $\Lambda_{H \cdot FEA}$ was developed in order to assess its validity to predict the Young's modulus ($E_{H,p}$) based on the other one (E_{FEA}). Alongside with the Young's modulus, FEA also enables to predict the shell thickness to microcapsule radius ratio $(h/r)_{FEA}$ based on the micromanipulation data of core-shell microcapsules. Moreover, TEM imaging was performed on the microcapsules to measure the shell thickness and the resulting average $(h/r)_{TEM}$ of microcapsules accordingly. The consistency between the experimental $(h/r)_{TEM}$ and the FEA-predicted $(h/r)_{FEA}$ was verified.

In addition, a solute-diffusion model based on the experimental oil release data from HS and LC-microcapsules was employed to investigate their barrier properties. The model enabled to estimate the shell permeability to shell thickness ratio (P/h) of HS and LC microcapsules in aqueous propanol ($1.7 \cdot 10^{-8}$ $m \cdot s^{-1}$) and aqueous ethanol ($1.8 \cdot 10^{-6}$ $m \cdot s^{-1}$). Therefore, the effective permeability of the oil through the microcapsule shell could be determined following the shell thickness analysis. Overall, fungal chitosan based shells were proven thicker (0.78±0.06 µm - 0.91±0.15 µm) than those of commercially available MF based microcapsules (~0.2 µm) [18]. These are probably conducive to the promising barrier properties of the vegetable microcapsules in object.

Chapter 8 Overall Conclusions & Future Work

8.1 Conclusions

8.1.1 Electrokinetic and Turbidimetric Analysis towards Coacervation

The key goal of this project was to encapsulate value-added perfume/flavour oils with potential applications for detergent and food industry sectors within a novel plant-based biopolymer pair (*i.e.* fungal chitosan and gum Arabic) to form the shells by pH-driven complex coacervation. Significant endeavours were undertaken towards understanding the process conditions for the encapsulation of single-molecule model oils (*i.e.* hexylsalicylate and L-carvone for detergent and food industry, respectively) and characterising the resulting microcapsules comprehensively. To achieve this goal, systematic studies were aimed at investigating the physico-chemical properties of the shell-precursor biopolymers at different pHs in order to determine the optimal conditions for developing fungal chitosan-gum Arabic based complexes effectively. Specifically, the fabrication conditions of complexes were investigated, with particular emphasis on the optimal mixing ratio between gum Arabic and fungal chitosan based on the electrokinetic as well as turbidimetric analysis of the biopolymeric solution/suspensions. The interrelationship between electrokinetic and turbidimetric results was identified, which enabled to establish a theoretical complex coacervation comfort zone (CCCZ) according to the net electrokinetic charge/zeta-potential (ζ-CCCZ) and critical turbidity zone (CTZ) of both biopolymers.

8.1.2 Effectiveness of Coacervation

Applying CCCZ, the optimal complex coacervation pH_{CC}=3.4 was determined, which corresponded to a GA-to-fCh weight ratio of 6.7. Complex coacervation between fungal

chitosan and gum Arabic was found to be highly affected by the medium pH as well as the biopolymer mixing ratio. Complexes could be developed only within a relatively narrow pH-window where fungal chitosan and gum Arabic carried opposite charges, hence electrostatic attractions. Under the above mentioned conditions, the effectiveness of complex coacervation was verified. Coacervate beads were successfully fabricated, with a relatively smooth surface and a mean size of 21.3±3.1 μm. In addition, the key physico-chemical properties of the resulting coacervate beads were comprehensively characterised. A micromanipulation technique enabled to evaluate their main mechanical and material property parameters, such as rupture force (7.4±0.7 mN) and Young's modulus using the Hertz model to fit the micromanipulation data (0.61±0.07 GPa).

8.1.3 Towards Microencapsulation: Stabilising oil-in-water Emulsions

As a further step towards microencapsulation *via* CC, oil-in-water emulsions were produced *via* one-step homogenisation. Added-value oils with potential applications in detergent (hexylsalicylate) and food industry (L-Carvone) were selected. The emulsions were added with emulsifying agents (Spans, Tweens, and their blends) to improve their dynamic stability that was extensively studied. It was found that the capability of these emulsifiers to reduce the interfacial tension (IFT) of oil droplets was not directly linked to their hydrophilic-lipophylic balance (HLB). Interestingly, Span85 was proven highly effective on HS ($IFT_{HS\text{-}SP85}$=3.8±0.1 $mN{\cdot}m^{-1}$) lowering its IFT by ~320% (IFT_{HS}=16.0±0.1 $mN{\cdot}m^{-1}$). These findings were also endorsed by additional EDS studies, in which the EDS constants (ς_{EDS}) were determined. It was found that the lowest EDS constant value for HS was with Span85 ($\varsigma_{EDS\text{-}HS\text{-}SP85}$=$2.24{\cdot}10^{-3}min^{-1}$). Similarly, Tween80 seemed to perform efficiently with LC by lowering its IFT_{LC} by around 300% within 2h. Furthermore, the analysis of the droplet size distribution (DSD) on both Span85-assisted HS and Tween80-assisted LC revealed that relatively stable oil droplets were obtained with a very marginal increase of their mean size during the timeframe prior to their microencapsulation.

8.1.4 Fabrication and Characterisation of Perfume Oil Microcapsules by pH-driven coacervation

The development of perfume oil (*i.e.* HS) microcapsules with a potential application for detergent industry relied on the novel concepts of CCCZ and the EDS. Since microcapsules in detergent must be designed to assure prolonged storage stability, no significant release of the active, their effective adhesion to fabrics, and quick release by external mechanical forces after laundry, their specific properties should be examined. Particular emphasis was placed towards investigating the mechanical, barrier, and adhesion properties of HS-microcapsules with a potential application for detergent industry. Their highest encapsulation efficiency was in the range 50-60%, which was in agreement with other microcapsules fabricated *via* CC from animal-derived chitosan and other biopolymers [6]. It was found that the stirring rate during CC influenced the morphology of HS-microcapsules which exhibited elongated and spherical shapes at 400 and 1000 rpm, respectively. The micromanipulation studies revealed that the rupture force of HS-microcapsules increased with the diameter, whereas the nominal rupture stress decreased with the size on average, as also reported in literature [63]. The rupture force of HS-microcapsules was 2.0±0.1 mN on average, which is also similar to that of MF based microcapsules (2.1±0.2 mN) [14]. Accordingly, the average nominal rupture stress of HS-microcapsules was 3.6±0.3 MPa, which is also similar to that MF based microcapsules (4.2±0.4 MPa). Besides, the average deformation at rupture of HS-microcapsules was 22.7±1.5%, which is similar to that of MF based microcapsules (24.8±1.5%) [14]. The shell thickness of HS-microcapsules (average 0.87±0.1 μm) increased linearly with their diameter, thus the larger the oil droplet, the thicker the shell.

The adhesion properties of HS-microcapsules onto fabric surfaces in real washing were mimicked using a microfluidic flow chamber equipped with a smooth model PET film. The interaction between HS-microcapsules and the PET film was studied. Their retention performance (RP) was quantified at different hydrodynamic shear stresses and different environmental pHs. Applying ImageJ analysis, it was found that the RP of HS-microcapsules was promoted at low acidic pHs (<5.1) leading to ~85% and ~60% at low (≤50 mPa) and high shear stress (0.9 Pa), respectively. By contrast, the RP was dramatically impaired at weakly

acidic (pH 5.1-6.2) as well as near neutral pHs (7.2). This phenomenon was probably ascribable to the nature of the biopolymeric shell of microcapsules developed *via* CC, which was pH sensitive. Moreover, the results suggest that both pH and shear stress had an effect on the RP. Specifically, the pH might influence the hydrophobic interaction between the microcapsule shell and PET film, hence their mutual adhesion. In other words, a role of the pH on promoting a hydrophobic effect between the microcapsule shells and the PET film cannot be underestimated, which may be conducive to their mutual interaction. As reported in literature, the hydrophobicity of proteins may influence their adhesion on hydrophobic substrates [459]. Accordingly, the shell of HS-microcapsules is protein-based, whose scaffolding relies on the glucosamine segments along the backbone of fungal chitosan. As mentioned in Chapter IV, the glucosamine segments are affected at weakly acidic and near neutral pHs, resulting in non-extended or folded conformation of chitosan, hence a reduction of microcapsule shell surface hydrophobicity. Based on the results, stronger interaction between the HS-microcapsules and PET film appeared more likely at a pH close to the coacervation pH_{CC}=3.4, which is indeed highly acidic and CTZ-free. Alternatively, this phenomenon was possibly due to the stronger electrostatically binding interaction between the shell-forming biopolymers, thus leading to more solid shells. Accordingly, the highest RP of the HS-microcapsules onto PET film was observed at pH 3.2.

8.1.5 Fabrication and Characterisation of Food-grade Flavour Oil Microcapsules *via* Two-stage Encapsulation

The studies went further by encapsulating a favour oil with a potential application in food industry. The food-grade microcapsules should segregate and preserve the active core that can be then released on demand. Therefore, an insightful characterisation of food-grade microcapsules should target their mechanical, structural, and barrier properties. Fungal chitosan-based microcapsules with a core of peppermint oil (LC) were fabricated *via* two-stage encapsulation processes being complex coacervation followed by spray drying. A size distribution ranging 10-125 μm and a Sauter diameter of 37.8±1.4 μm were determined. The

encapsulation efficiency and payload of LC-microcapsules were 29±4 % and 19±3%, respectively, which are in agreement with other microcapsules encapsulating different essential oils via coacervation [6]. Additionally, LC-microcapsules in a dry state did not show any significant oil leakage over 50 days. SEM micrographs revealed spherically shaped microcapsules with a core-shell structure. Microcapsule surface topography evidenced relatively smooth surfaces, with dent- and crease-rich regions. Effective oil entrapment was assessed *via* fluorescence microscopy using Nile red as a solvatochromic dye. In addition, the shell thickness (average 0.91±0.15 μm) of LC-microcapsules was investigated by TEM imaging, which was consistent with what was observed from HS-microcapsules. Micromanipulation showed that the rupture force of LC-microcapsules increased with diameter, with an average value of 0.6±0.1 mN. The nominal rupture stress was 2.1±0.3 MPa on average, which is also consistent with gelatine-gum Arabic based microcapsules with double shells reported by Yu *et al.* [63]. Moreover, potential end-use applications of such LC-microcapsules in aqueous ethanol based formulations have been outlined, with particular emphasis on depilatory applications.

8.1.6 Application of Numerical and Mathematical Modelling

Chapter 4, Chapter 5, and Chapter 6 have focused on the preparation and characterisation of microcapsules with a core of fragrance, flavour oil, and in-depth analysis of their material and barrier properties. Specifically, it has been confirmed that micromanipulation is a powerful technique to measure the mechanical properties of microcapsules. However, determination of the intrinsic material property parameters of microcapsules, such as the Young's modulus, requires further data analysis. The intrinsic material property parameter (Young's modulus) values of HS and LC-microcapsules were studied using the micromanipulation combined with numerical and mathematical modelling. The numerical model based on the simulation results of FEA was successfully utilised to quantify the Young's modulus of microcapsule shells. The FEA-predicted Young's modulus values of HS and LC-microcapsules were 1.0±0.1 GPa and 1.3±0.3 GPa, respectively, between which no statistically significant difference was found with

95% confidence ($p > 0.05$). Interestingly, the values obtained are in good agreement with the Young's modulus evaluated *via* FEA by Mercadé-Prieto *et al.* [18] for MF-based microcapsules (1.6±0.3 GPa). Moreover, these values are also similar to the Young's modulus of other polymeric microcapsules reported in literature, which had been determined by AFM [312, 448]. FEA-predicted Young's moduli (E_{FEA}) of HS and LC microcapsules were also compared with their corresponding Young's modulus (E_H) of the whole microcapsules, which were determined by the Hertz model. Although the E_H values of HS ($E_{H,HS}$=0.095±0.014 GPa) and LC-microcapsules ($E_{H,LC}$=0.118±0.023 GPa) were much lower than their corresponding E_{FEA} as expected since the liquid core does not exhibit any elastic property, there existed a linear correlation ($R^2 \geq 0.88$) between E_H and E_{FEA}. The factor of proportionality between the two corresponding Young's moduli was determined in both cases ($\Lambda_{H \cdot FEA}$). Furthermore, the theoretical expression of $\Lambda_{H \cdot FEA}$ was developed in order to ascertain its validity to predict the Young's modulus ($E_{H,p}$) based on the other one (E_{FEA}). Along with the Young's modulus, the FEA also enabled to predict the shell thickness to microcapsule ratio $(h/r)_{FEA}$ based on micromanipulation data of the microcapsules. Moreover, TEM imaging was performed on microcapsules to measure the shell thickness and the resulting average $(h/r)_{TEM}$ of microcapsules experimentally. The consistency between the experimental $(h/r)_{TEM}$ and the FEA-predicted $(h/r)_{FEA}$ was verified.

Additionally, a solute-diffusion model based on experimental oil release data from HS and LC-microcapsules was employed to investigate their barrier properties. The model enabled to estimate the shell permeability to shell thickness ratio (P/h) of HS and LC microcapsules in aqueous propanol ($1.7 \cdot 10^{-8}$ m·s^{-1}) and aqueous ethanol ($1.8 \cdot 10^{-6}$ m·s^{-1}) respectively, hence their effective permeability following the microcapsule shell thickness analysis. Overall, fungal chitosan based shells were proven thicker (0.78±0.06 µm - 0.91±0.15 µm) than those of commercially available MF-based microcapsules (~0.2 µm) [18]. These are probably conducive to the promising barrier properties of the vegetable microcapsules in object, hence their reduced oil (HS, LC) permeability through the shells.

8.1.7 Conclusions: a Brief Overview

Overall, such promising results suggest that:

(i) microcapsules with a core of fragrance or flavour oil (HS or LC) can be fabricated by complex coacervation relying on the novel concept of CCCZ-CTZ;

(ii) fCh-GA system may be a suitable carrier for the encapsulation of fragrance and flavour oils, for more sustainable and consumer-friendly applications in commercial detergent and food formulations, offering an opportunity to globally overcome cultural and religious beliefs associated with animal-derived products;

(iii) in-depth analysis of the experimental data (mechanical properties and release) using appropriate numerical and mathematical modelling has led to beneficial determination of intrinsic material property parameter (Young's modulus) and the barrier properties (effective permeability), which are important parameters to be related to their performance for end-use applications.

8.2 Future Work

8.2.1 The Implications of Biopolymers

The experimental conditions towards developing fungal chitosan-gum Arabic based complexes were intensively examined herein. However, the interaction between the biopolymers as well as the mechanism of formation of the complexes themselves is still not well understood. In the present research, the significance of the electrostatic interaction between the oppositely charged biopolymers to bind into complexes was revealed, yet no other interaction was known.

Since multiple interplays other than electrostatics may influence the stability of complexes, it is vital to investigate the nature of any potential interaction involved in the process of formation of complexes, as well as the presence of CC-promoting/inhibiting salts, and the resulting ionic strength. Moreover, since the key materials for this research were sourced from biological materials, it would be interesting to investigate their chemical composition which may change from batch to batch. Specifically, in-depth studies on the nature of the ingredients may be desirable, with particular emphasis on the degree of deacetylation of fungal chitosan, which may strongly affect the performance of the microcapsule shell. Moreover, insightful analysis on the conformational changes of chitosan at different pHs and temperatures may provide useful information on the resulting inner structure of the coacervates. This may also contribute to better understanding the different functionalities of the resulting microcapsules, which can help to tune the structural and mechanical properties more effectively, hence fabricating bespoke microcapsules for the desired end-use applications.

8.2.2 Towards new characterisation horizons

Additional studies may also address the encapsulation of different oil-based active ingredients, guided by the established CCCZ, as well as understanding the influence of the core oil onto the structural stability and mechanical properties of the microcapsule. Besides, it would be very interesting to conduct more specific performance and release tests of the microcapsules under highly controlled conditions, for example, by using a micromanipulation rig equipped with a closed chamber to control both temperature and relative humidity or under friction force by a tribometer in order to mimic the conditions under which the fragrance oil should be released.

In addition, a deeper insight towards enhancing the adhesion of biodegradable perfume microcapsules to fabrics could be offered by modifying their surface chemically. Interestingly, preliminarily work conducted by Liu *et al.* [27] *via* AFM on surface modified MF-based microcapsules provided by Procter & Gamble (P&G) was proven conducive to their adhesion onto PET and cellulose films. However, the research mainly focused on MF-based microcapsules that urge for more sustainable and versatile alternatives. Accordingly, AFM

force measurements could be performed on the vegetable chitosan-based microcapsules developed in this PhD project following their surface modification.

In addition, specific surface areas on the microcapsules may be targeted in order to enhance their adhesion onto fabrics, which can be explored by grafting specific chemical branches directly to their surface. So far, there has been lack of understanding of the effect of the size and shape of the microcapsules on their adhesion properties in real washing. Although the adhesion properties were investigated by a microfluidic flow chamber technique, it is not clear whether larger microparticles would tend to be pulled off from the adhering substrate more easily than the smaller ones. Theoretically speaking, larger microparticles should allow a greater shear force due to their larger cross-sectional area when compared to smaller ones under the same hydrodynamic shear stress, which may thus facilitate their removal. However, this should be investigated experimentally.

In this project, microcapsules with a spherical and elongated shape were obtained. When compared to smaller microcapsules, the elongated ones occurred with a pair of polymeric 'wings' hence a greater surface area available to expose to potential model substrates, such as PET or cellulose films. This may then result in a much more effective adhesion onto model substrates in real washing. However, this should be explored experimentally.

8.2.3 Towards Novel Applications of Microcapsules

As the research presented has focused on formulating and characterising fragrance and flavour oil microcapsules with potential applications in detergent manufacturing and food industry sectors, plenty of other potential application sectors remain unexplored, which may provide great opportunities for future projects. A new possible approach may imply the fabrication of nutra-/pharmaceutical plant-based microcapsules, for which specific *in-vivo* characterisation is required. Specifically, novel plant-based microcapsules should be designed to survive the harshest environmental conditions throughout the whole digestive tract, where the intraluminal pH changes from low acidic in the stomach (pH~1.5) to nearly neutral (pH~6) in the duodenum.

In other words, another big challenge would be to design zero-leakage plant-based microcapsules to release their drug load only when exposed to certain pHs.

8.2.4 The zero-leakage Challenge

Besides, extra research opportunities may include the development of double-coated microcapsules in order to create an extra protective shell against undesirable leakage of the active ingredient. Although some evidence in literature has recently arisen, there appears to still be important gaps to be addressed. For example, although double coatings were formed around primary MF-shelled microcapsules, some oil leakage was still evident [451]. Moreover, very little is known on safe biopolymers or inorganic materials to act as potential secondary shells. For this reason, Sui *et al.* [460] have recently filed a patent on fabricating leakage-free microcapsules *via* two-step *in-situ* polymerisation employing a superhydrophobic copolymer precursor (octadecyltrichlorosilane), which was skilfully utilised as an interlayer to prevent the water-based active from leaking out undesirably. Although this has proven effective, there is still much research to be undertaken, especially when dealing with oil-based actives forming highly kinetically unstable o/w emulsions. Theoretically, superhydrophilic nanocomposites, such as SiO_2 and $CaCO_3$, may play a crucial role to generate and stabilise o/w Pickering emulsions, which could be then interlayered using a superhydrophilic agent, such as tetraethylorthosilicate (TEOS) and polydimethylsiloxane (PDMS). However, TEOS and PDMS have shown relatively low toxicity to human beings, which makes them suitable for non-food products only. Although both double coatings and interlayers may improve the barrier properties of microcapsules, this would lead to a significantly reduced payload. Having said that, more experimental work is required to shed new light on this outstanding task.

Overall, both continuous improvement of the current technologies and the development of less energy-intensive processes, as well as the search for more and more sustainable shell precursor

alternatives, have become imperative for shifting towards the next generation of microcapsules, which must be highly performant, consumer-friendly, and environment caring.

8.2.5 Technoeconomic Analysis & Industrial Scale-up

Although industrial-scale coacervation-driven microencapsulation processes (*e.g.* ink-loaded microcapsules for carbonless copy paper) have long been known, their scale-up is not trivial as morphology and size of microcapsules are severely affected by the turbulence level within the stirred tank reactor. Turbulent kinetic energy and the local energy dissipation rate are the key scale-up criteria, which are imperative to control in order to avoid aggregation/clustering among microcapsules [60]. Industrial manufacturing criteria face high capital and production costs, hence scale-up may be extremely challenging. Therefore, a technoeconomic process analysis of industrial scale microencapsulation should be conducted attentively [61]. Specifically, a cost analysis should be based on the understanding of the whole process (materials, technology, sales, revenue), which is crucial towards determining the overall input-to-output manufacturing cost ratio effectively. This is vital to assess the potential benefits of a new product *versus* its cost, which then dictates its market price. Sometimes additional costs associated with the quality control, safety, and performance of the product at end-use applications might restrain its applicability. Overall, weighing the economic costs to pursue the production of a good is critical to make the whole manufacturing process viable and highly profitable.

Appendix

Appendix A

A.1 ImageJ code for investigating the adhesion properties *via* image analysis – Flow Chamber technique

Acknowledgement: The code herein presented was conceptualised and developed by Juan Carlos Alvarez Fernandez and Dan Baiocco in August 2020.

```
run("Clear Results");
setBatchMode(true);
inputDirectory = getDirectory("Choose a Directory of Images");
fileList = getFileList(inputDirectory);

    print(inputDirectory);
    splitDir= inputDirectory + "/ImageJ/";
    print(splitDir);
    File.makeDirectory(splitDir);

for (i = 0; i < fileList.length; i++)
{
    processImage(fileList[i]);

}

setBatchMode(false);
updateResults();
```

```
selectWindow("Summary");
saveAs("text", splitDir + "/summary.txt");
selectWindow("Results");
saveAs("text", splitDir + "/results.txt");

close("Threshold");
close("Results");
close("Log");

function processImage(imageFile)
{
    prevNumResults = nResults;
    open(imageFile);

    // PART 1 - SET THE SCALE HERE

    // run("Set Scale...", "distance=224.0000 known=100 unit=Âµm global");
//for Zoom 5x1.6
    // run("Set Scale...", "distance=285.0000 known=100 unit=Âµm global");
//for Zoom 10x1.0
    // run("Set Scale...", "distance=354.0000 known=100 unit=Âµm global");
//for Zoom 10x1.25
    run("Set Scale...", "distance=453.0000 known=100 unit=Âµm global"); //for
Zoom 10x1.6

    filename = getTitle();
    run("8-bit");
    setAutoThreshold("Default");
    run("Threshold...");

    // PART 2 - MANUAL OR AUTOMATIC THRESHOLD? Activate the command below for
a manual threshold
    //setThreshold(0, 65);

    getThreshold(lower, upper);
```

```
    setOption("BlackBackground", true);
    run("Convert to Mask");



    //PART 3 - CUSTOMIZE
    //run("Dilate"); //Only for PAC Capsules
    run("Fill Holes");
    run("Watershed");
    run("Analyze Particles...", "size=20-2000 circularity=0.2-1.00 show=Masks
display summarize");


    saveAs("Tiff", splitDir+filename);


    for (row = prevNumResults; row < nResults; row++)
    {
        setResult("Filename", row, filename);
        setResult("Threshold", row, upper);
    }
        close("*");
}
```

Appendix B

B.1 MATLAB® code for smoothing Interfacial Tension (IFT)

Acknowledgement: The code herein presented was conceptualised and developed by Erick A. León-Henneberg and Dan Baiocco in August 2020.

```
%Smoothing of experimental data by removing random noise
clc
clear all

% Input variables:
disp('Input data :')
SampleName=input('Input name of sample :','s');

% X_s --> time in seconds
% Y_mNm --> sft in mN/m.

%Copy % paste data in respective variable

X_s=input('Input time data vector, between brackets :');
Y_mNm=input('Input SFT data vector, between brackets :');

%Check if there are any relevant outliers
Fig1=figure('Name','Are there outliers in the data? -- Respond in command
window');
plot(X_s,Y_mNm,'b*--','MarkerSize',5) %If necessary, change size of markers for
better visibility of plot
xlabel("t (s)")
ylabel("SFT (mN/m)")
title(strcat("SFT vs. t. Sample =",SampleName))
```

```
legend("Raw Data")

Decision1=input('Are there outliers in the data? (Y/N):','s');

if Decision1=='Y'

    %Removal of Outliers (Random noise)
    disp('Removal of Outliers (Random noise) :')

    % Select a critical value of SFT in order to
    % remove outlier data (YUpper_mNm & YLower_mNm)

    YLower_mNm=input('Input lower critical value of SFT (mN/m) :');
    YUpper_mNm=input('Input upper critical value of SFT (mN/m) :');

%     if Ycritical_mNm>=max(Y_mNm)
%         disp('Error_2=critical value is greater than or equal to maximum value
of SFT in raw data set -- Restart script.')
%         return
%     end

    MatrixData=[X_s,Y_mNm]; %Generate Matrix data for removal.
    MatrixDataTreated=MatrixData; %Dummy variable of treated data

    IndexVector1=find(MatrixData(:,2)<=YLower_mNm); %Locate the rows (index) of
the random noise data points
    lengthIndexVector1=length(IndexVector1); %Size of index vector.
    %Set outlier points to zero with for loop
    for i=1:lengthIndexVector1
       MatrixDataTreated(IndexVector1(i),1)=0;
       MatrixDataTreated(IndexVector1(i),2)=0;
    end

    IndexVector2=find(MatrixData(:,2)>=YUpper_mNm); %Locate the rows (index) of
the random noise data points
    lengthIndexVector2=length(IndexVector2); %Size of index vector.
    %Set outlier points to zero with for loop
    for i=1:lengthIndexVector2
```

```
        MatrixDataTreated(IndexVector2(i),1)=0;
        MatrixDataTreated(IndexVector2(i),2)=0;
    end

    %Separate time and SFT vector and remove zeros from them.
    XTreated_s=MatrixDataTreated(:,1);
    YTreated_mNm=MatrixDataTreated(:,2);

    XTreated_s(XTreated_s==0)=[];
    YTreated_mNm(YTreated_mNm==0)=[];

    Fig2=figure('Name','Comparison of raw data and treated data (without
outliers)');
    plot(X_s,Y_mNm,'b*--',XTreated_s,YTreated_mNm,'k*-','MarkerSize',5) %If
necessary, change size of markers for better visibility of plot
    xlabel("t (s)")
    ylabel("SFT (mN/m)")
    title(strcat("SFT vs. t. Sample =",SampleName))
    legend("Raw Data",strcat("Treated Data - Ycritical lower
limit=",string(YLower_mNm)," mN/m, Ycritical upper limit=",string(YUpper_mNm)."
mN/m"))
    savefig(strcat('Figure_RawAndOutlierData_Of_',SampleName,'.fig'));

    %Smoothing of data
    disp('Smoothing of data :')

    % Smoothing of the data is done using a gaussian-weighted moving average.To
test the effect of different methods and span's widths,
    % use the script 'ComparisonBetweenDifferentSmoothingmethods', located
    % in the same path as this script.

    SmoothingMethod="Gaussian-weighted moving average";
    MovingSpan=input('Input length of moving span (number of points) :');

    YSmoothed_mNm=smoothdata(YTreated_mNm,'gaussian',MovingSpan);

    Fig3=figure('Name','Comparison of treated data and smoothed data');
```

```
    plot(XTreated_s,YTreated_mNm,'b*--',XTreated_s,YSmoothed_mNm,'k*-
','MarkerSize',5) %If necessary, change size of markers for better visibility of
plot
    xlabel("t (s)")
    ylabel("SFT (mN/m)")
    title(strcat("SFT vs. t. Sample =",SampleName))
    legend(strcat("Treated Data - Ycritical lower limit=",string(YLower_mNm),"
mN/m, Ycritical upper time=",string(YUpper_mNm)," mN/m"),strcat("Smoothed Data -
Gaussian-weighted Moving Average - Moving Span=",string(MovingSpan)," points"))
    savefig(strcat('Figure_RawAndSmoothedData_Of_',SampleName,'.fig'));


    % Saving smoothed data


    %Smoothed data will be saved on the same path as the script is located


    FilenameTable=strcat('SmoothedData_Of_',SampleName); %Name of the text file.
Assign name according to characteristics of sample studied.
    FilenameStruct=strcat('TotalData_Of_',SampleName);



SmoothedData=struct('t_s',XTreated_s,'SFT_mNm',YSmoothed_mNm,'SFTUpper_mNm',YUpper
_mNm,'SFTLower_mNm',YLower_mNm,'Smoothing_Method',SmoothingMethod,'Moving_Span',Mo
vingSpan);
    SmoothedDataTable=table(XTreated_s,YSmoothed_mNm,'VariableNames',('t (s)','SFT
(mN/m)');% Smoothed data is restructured as a table variable for saving data as
text file


    writetable(SmoothedDataTable,FilenameTable);
    save(FilenameStruct,'SmoothedData')


    elseif Decision1=='N'


    %Removal of Outliers (Random noise)


    % Select a critical value of SFT in order to
    % remove outlier data (YUpper_mNm & YLower_mNm)


    YLower_mNm=0;
    YUpper_mNm=Inf;
```

```
 %Smoothing of data
disp('Smoothing of data :')

% Smoothing of the data is done using a gaussian-weighted moving
% average. To test the effect of different methods and span's widths,
% use the script 'ComparisonBetweenDifferentSmoothingmethods', located
% in the same path as this script.

SmoothingMethod="Gaussian-weighted moving average";
MovingSpan=input('Input length of moving span (number of points) :');

YSmoothed_mNm=smoothdata(Y_mNm,'gaussian',MovingSpan);

Fig3=figure('Name','Comparison of raw data and smoothed data');
plot(X_s,Y_mNm,'b*--',X_s,YSmoothed_mNm,'k*-','MarkerSize',5) %If necessary,
change size of markers for better visibility of plot
xlabel("t (s)")
ylabel("SFT (mN/m)")
title(strcat("SFT vs. t. Sample =",SampleName))
legend("Raw Data",strcat("Smoothed Data - Gaussian-weighted Moving Average -
Moving Span=",string(MovingSpan)," points"))
savefig(strcat('Figure_RawAndSmoothedData_Of_',SampleName,'.fig'));

% Saving smoothed data

%Smoothed data will be saved on the same path as the script is located

FilenameTable=strcat('SmoothedData_Of_',SampleName); %Name of the text file.
Assign name according to characteristics of sample studied.
FilenameStruct=strcat('TotalData_Of_',SampleName);


SmoothedData=struct('t_s',X_s,'SFT_mNm',YSmoothed_mNm,'SFTUpper_mNm',YUpper_mNm,'S
FTLower_mNm',YLower_mNm,'Smoothing_Method',SmoothingMethod,'Moving_Span',MovingSpa
n);
SmoothedDataTable=table(X_s,YSmoothed_mNm,'VariableNames',('t (s)','SFT
(mN/m)'); % Smoothed data is restructured as a table variable for saving data as
text file

writetable(SmoothedDataTable,FilenameTable);
```

```
    save(FilenameStruct,'SmoothedData')

else
    disp('Error_1=Wrong input -- Input Y or N (response is case sensitive). Restart script')
    return
end
disp('Process Finished')
```

B.2 MATLAB® code for smoothing Interfacial Tension (IFT) – Comparison among different smoothing methods

```
MovingSpan=10; %Set the number of data points used in the sliding window
Y_movmean=smoothdata(Y_mNm,'movmean',MovingSpan); %Smoothing method = moving average
Y_gaussian=smoothdata(Y_mNm,'gaussian',MovingSpan);% Smoothing method = gaussian-weighted moving average
Y_sgolay=smoothdata(Y_mNm,'sgolay',MovingSpan);% Smoothing method = Savitzky-Golay with quadratic polynomial
Y_rloess=smoothdata(Y_mNm,'loess',MovingSpan);% Smoothing method = Quadratic regression

figure
plot(X_s,Y_mNm,'b*--',X_s,Y_movmean,'k-',X_s,Y_gaussian,'-',X_s,Y_sgolay,'r-',X_s,Y_rloess,'c-','MarkerSize',5) %If necessary, change size of markers for better visibility of plot
xlabel("t (s)")
ylabel("SFT (mN/m)")
title(strcat("SFT vs. t. Sample =",SampleName))
legend("Raw Data",strcat("Smoothed Data - Moving Average - Moving Span=",string(MovingSpan)," points"),strcat("Smoothed Data - Gaussian-weighted moving average - Moving Span=",string(MovingSpan)," points"),strcat("Smoothed Data - Savitzky golay using quadratic polynomial - Moving Span=",string(MovingSpan)," points"),strcat("Smoothed Data - Quadratic regression - Moving Span=",string(MovingSpan)," points"))
```

Appendix C

C.1 Finite Element Analysis (FEA) of Compression of Core-Shell Microcapsules

The elastic properties of the shell of core-shell microcapsules were investigated using micromanipulation data and finite element analysis (FEA) introduced by Mercadé-Prieto *et al.* [18]. A rigid parallel plate system was employed for the frictionless compression of microcapsules, namely between a compressing probe and the outer shell of a single microcapsule (Figure C.1). As for the Hertz model, the microcapsule shell was assumed incompressible (Poisson ratio ν=0.5) and elastic. Only small fractional deformations were considered ($\varepsilon \leq 0.1$), hence the liquid core had no effect on the compression [309]. Thus, liquid was not accounted for in FEA. The model was implemented using a software recently developed in our group by Dr Zhihua Zhang (2020). Previous literature has suggested that the fractional deformation (ε) of microcapsules should be sufficiently large to provide reliable compression data, yet not too large to involve the liquid core [66]. Accordingly, a deformation of 10% was assumed. The model was based on several simulations conducted at different h/r values, in which h and r are the shell thickness and radius of a single capsule, respectively [18]. Thus, the normalised force can be expressed as a second-order polynomial function of the fractional deformation (Figure C.2):

$$\frac{F}{Erh} = f_1\varepsilon^2 + f_2\varepsilon + f_3 \tag{C.1}$$

where F is the compression force, E the Young's modulus, and $\varepsilon = \delta/2r$ the fractional deformation as the ratio between the displacement (δ) to the initial diameter of the microcapsule ($2r$). Applying high order polynomials, three modelling coefficients f_1, f_2 and f_3 were expressed as a function of h/r (Table 7.1).

Substituting the coefficients into Equation (C.1), the compression force F can be expressed as follows

$$F = Er\left(\frac{h}{r}\right)^2 (f_1+f_2+f_3) \quad \text{(C.2)}$$

For a given dataset of F *vs* ε of microcapsules with known radii (r), E and h/r can be evaluated by the least squares method (Solver function). The model is predictive at $0.03 \leq \varepsilon \leq 0.1$ only (Figure C.3).

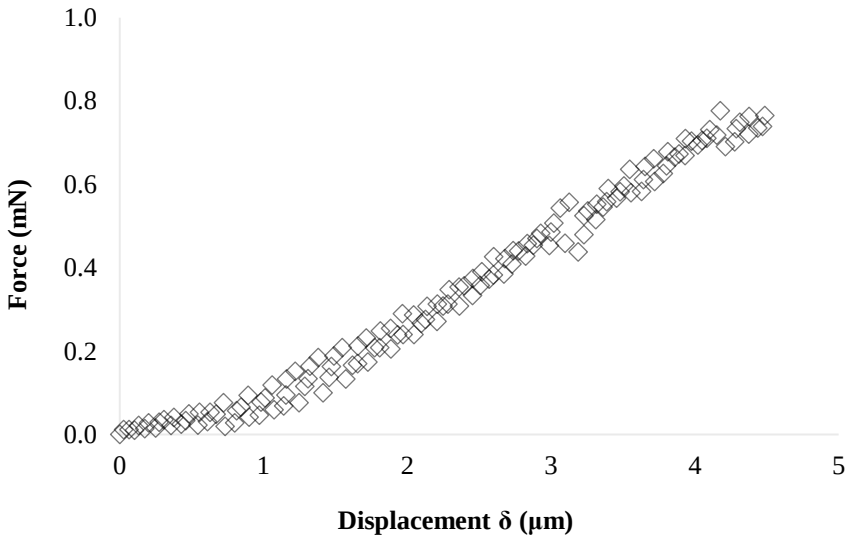

Figure C.1 – Typical Force-Displacement curve obtained from a micromanipulation technique at early deformation (<10%).

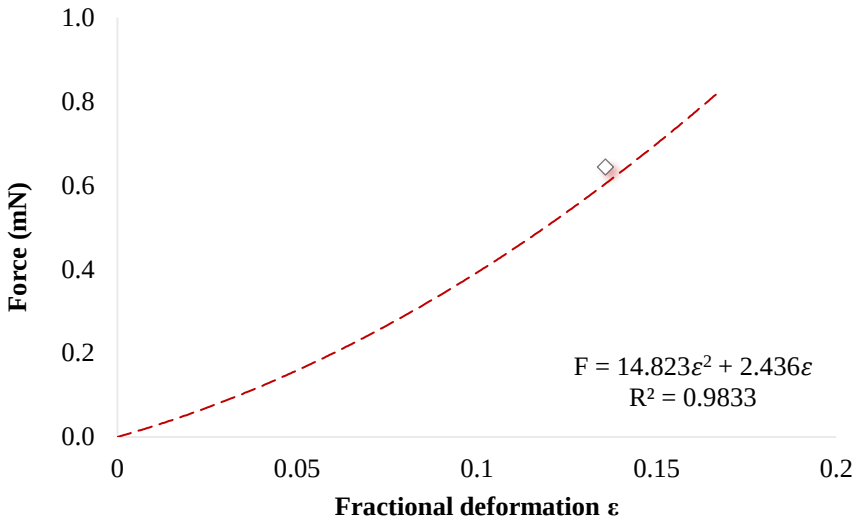

Figure C.2 – Typical FEA results of parallel compression of core-shell microcapsules with a second-order polynomial regression.

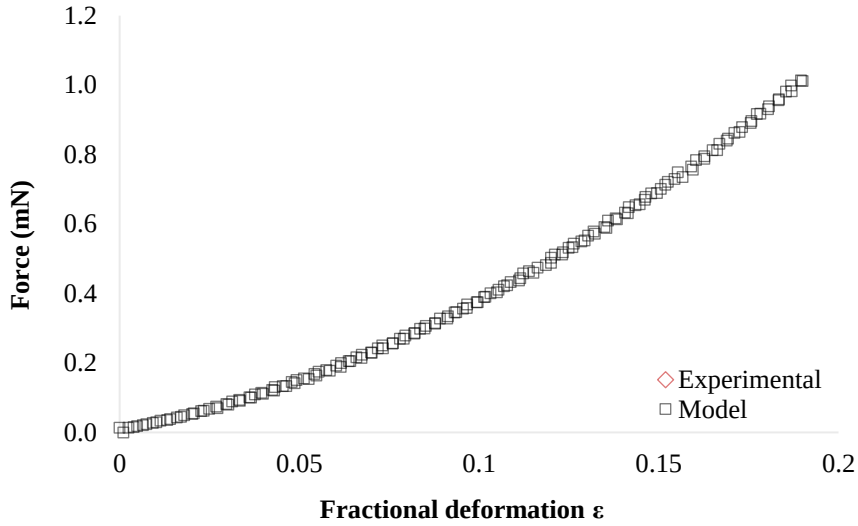

Figure C.3 – Comparison between model-predictive analysis (FEA) and experimental data obtained from the parallel plate compression of a core-shell microcapsule.

Appendix D

D.1 Solute-Diffusion Model

The calculation of shell permeability for the microcapsules presented in this thesis was based on the solution-diffusion model for intramembranous mass transfer [461]. In recent years, noteworthy endeavours have been undertaken by Mercade-Prieto *et al.* [16], which has applied this theory to core-shell microcapsules. Figure D1 schematically represents the mass transfer of oil out of a thin shell. As displayed, the oil diffusing through the shell of a single microcapsules generates a flux (J) defined using Fick's first law:

$$J = \frac{D_{o,s}}{h}\left(c_{in,i} - c_{out,i}\right) \tag{D.3}$$

where $\mathbb{D}_{o,s}$ $[m^2 \cdot s^{-1}]$ is the diffusivity of the oil within the shell, and $c_{in,i}$ and $c_{out,i}$ are the oil concentrations $[mol \cdot l^{-1}]$ at the inner and outer shell-fluid interface, respectively. The concentration difference ($c_{in,i} - c_{out,i}$) generates the concentration driving force.

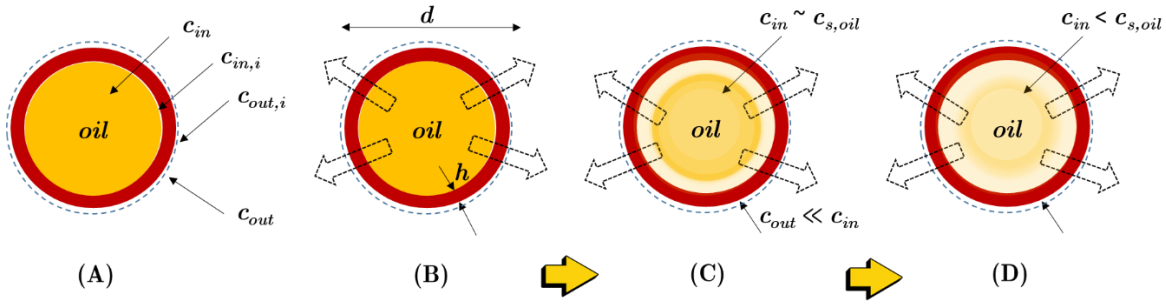

Fig. D.1 A Schematics of encapsulated oil leaking out through the polymeric shell. Thin-shell microcapsules fully loaded with oil **(A)**; oil-entrapping microcapsule having a shell thickness *h* releasing the core oil into the receptor medium outside (early stage) **(B)**; linear regime with a core of oil still present inside the shell of the microcapsule. Assumptions: (*i*) the oil concentration in the solvent outside the shell (c_{out}) is much lower than that inside (c_{in}) the shell ($c_{out} \ll c_{in}$); (*ii*) the concentration of solubilised oil inside the capsule equals the saturation concentration ($c_{in} \sim c_{s,oil}$) of the oil in the receptor medium ($c_{s,oil}$) **(C)**; exponential regime: release of the solubilised oil, hence the oil core progressively disappears. Assumption: the concentration of solubilised oil inside the capsule shell (c_{in}) is much lower than that oil saturation concentration in the receptor medium ($c_{in} \ll c_{s,oil}$) **(D)**.

Considering the partition coefficient $k = c_{in,i} / c_{in} = c_{out,i} / c_{out}$, the equation (A1) can be rearranged into:

$$J = k\frac{D_{o,s}}{h}(c_{in} - c_{out}) \tag{D.4}$$

where $k\mathbb{D}_{o,s} / h$ is the shell permeability to shell thickness ratio (P/h), c_{in} and c_{out} are the concentration of the oil solubilised (in the solvent) inside and outside the microcapsule. The model relies on the following assumptions:

(i) Rapid mass transfer between the oil core towards the inner shell interface, leading to $c_{in} \sim c_{s,oil}$. This assumption is consistent if $P/h \ll \mathbb{D}_{water}/d$, where $\mathbb{D}_{water}$ is the diffusivity of the oil in pure water and d the diameter of the microcapsule;

(ii) The oil concentration in the receptor medium is much lower than the saturation concentration of the oil ($c_{out} \ll c_{s,oil}$), resulting in $J = \left(\frac{P}{h}\right)c_{s,oil}$;

(iii) No concentration gradient is experienced in the cosolvent-enriched receptor medium, hence well-mixed conditions apply at all times;

(iv) No significant variation in the volume of the receptor medium occurs [d]

Considering the above-listed assumptions, the mass balance associated with Equation (D.4) can be written as follows:

$$V_s \frac{dc_{out}}{dt} = JA_{caps} = \frac{P}{h} c_{s,oil} \pi d^2 \tag{D.5}$$

with the boundary condition $c_{out}(t = 0) = 0$. Therefore, the concentration profile of the oil outside a single microcapsule is predicted to increase linearly with the release time t:

[d]The oil is soluble in the solvent ($c_{out} \ll c_s$). No volume variation of the receptor medium occurred. The non-steady state mass balance is: $\frac{dm}{dt} = \frac{d(V_s c_{out})}{dt} = V_s \frac{dc_{out}}{dt} + c_{out}(t)\frac{dVs}{dt}$ where $dV_s/dt = 0$.

$$c_{out}(t) = \frac{\pi d^2}{V_s}\frac{P}{h}c_{s,oil}t \quad \text{(D.6)}$$

where $A_{caps}=\pi d^2$ is the surface area of a spherically shaped microcapsule and V_s the volume of the receptor medium with the co-solvent. Therefore, this equation enables to estimate P/h from the slope (dR/dt) of the release profile ($R(t)$) [446], as shown in Figure D2.

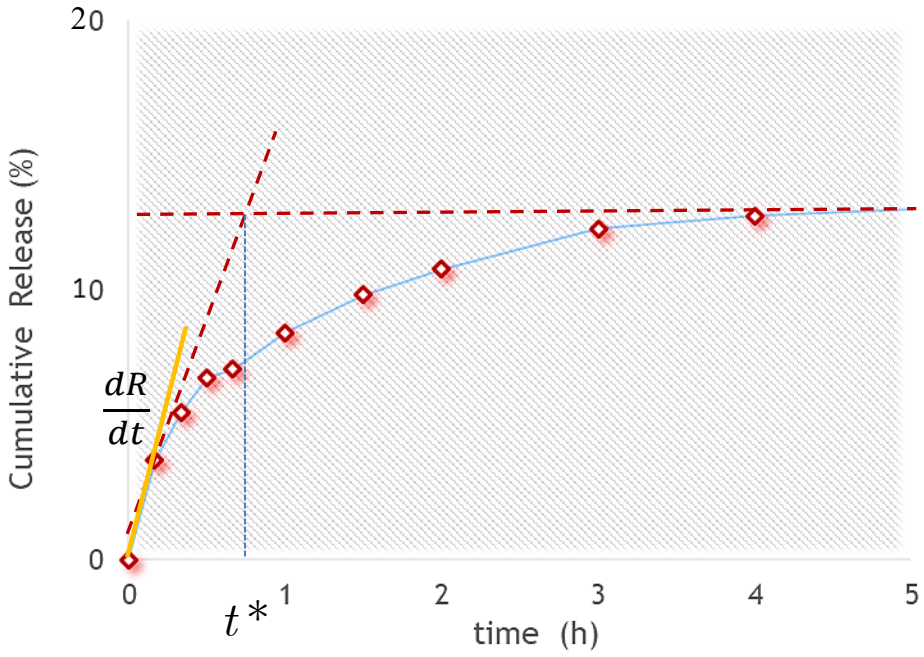

Fig. D.2 – Typical release profile of thin-shell microcapsules with two regimes: linear ($t < t^*$) and ($t > t^*$), where t^* is the oil-release regime transition point **(A)**; adapted from Antipov *et al.* [446].

Following extensive release of the solubilised oil, the point at which the oil concentration inside is no longer equal to its saturation concentration ($\boldsymbol{c_{in} \neq c_{s,oil}}$). After the oil-release regime transition point ($t > t^*$), the late stage of oil release begins ($\boldsymbol{c_{in} < c_{s,oil}}$), as displayed in Figure

D1**(D)**. Therefore, the release with time is no linear anymore, yet follows an exponential trend (*i.e.* rise to maximum), as shown in Figure D.2 [446]:

$$\frac{c_{out}(t)}{c_{s,oil}} = 1 - \exp\left(-\frac{\pi d^2}{V_s}\frac{P}{h}t\right) \tag{D.7}$$

Overall, the concentration of the solubilised oil gradually released over time can be summarised as follows:

$$c_{out}(t) = \begin{cases} \frac{\pi d^2}{V_s}\frac{P}{h}c_{s,oil}t & t < t_{c_{in}<c_{s,oil}} \\ c_{s,oil}\left(1 - \exp\left(-\frac{\pi d^2}{V_s}\frac{P}{h}t\right)\right) & t \geq t_{c_{in}<c_{s,oil}} \end{cases} \tag{D.8}$$

The relative oil release by weight as a function of time is given by:

$$R(t) = \frac{V_s}{\frac{\pi}{6}(d-2h)^3}\frac{c_{out}(t)}{\rho_{oil}} \tag{D.9}$$

where ρ_{oil} is the density of the pure core oil. Based on the above mentioned assumptions at late stage of release ($c_{in} < c_{s,oil}$), the relative oil release at the oil-release regime transition point ($t > t^*$) is defined as:

$$R(t_*) = 1 - \frac{c_{out}(t_*)}{\rho_{oil}} = 1 - \frac{c_{s,oil}}{\rho_{oil}} \tag{D.10}$$

Overall, the relative oil release can be summarised as follows:

$$R(t) = \begin{cases} \dfrac{d^2}{\frac{1}{6}(d-2h)^3\rho_{oil}}\dfrac{P}{h}c_{s,oil}t & t < t_* \\ 1 - \dfrac{c_{s,oil}}{\rho_{oil}} & t = t_* \\ \dfrac{V_s}{\frac{\pi}{6}(d-2h)^3\rho_{oil}}\, c_{s,oil}\left(1 - \exp\left(-N_{caps}\dfrac{\pi d^2}{V_s}\dfrac{P}{h}t\right)\right) & t > t_* \end{cases} \quad \text{(D.11)}$$

which could be further simplified under the assumption of thin–shell microcapsules ($h \ll d$). This model is effective at predicting for a single microcapsule as well as a monodisperse population of microcapsules with non-soluble active oils. As formerly discussed by Mercade-Prieto *et al.* [16], a convenient experimental oil release timeframe should be between 10^2 *s* and 10^4 *s*. Based on the linear regime, the resulting permeability $P/h|_*$ is calculated as follows:

$$\left(\frac{P}{h}\right)_* = \frac{\left(\frac{dR}{dt}\right)_*}{1 - w_{oil}}\frac{\frac{1}{6}(d-2h)^3}{d^2}\frac{\rho_{oil}}{c_{s,oil}} \quad \text{(D.12)}$$

where w_{oil} is the waste oil parameter to be graphically estimated as the 'hop' release due to those damaged microcapsules releasing their whole oil load immediately after contacting the receptor medium. Moreover, the relative release profile may not be fully linear at $R(t) \geq 60\%$, thereby resulting in a certain degree of uncertainty associated with $P/h|_*$. For this reason, an average linear slope $(dR/dt)_*$ is recommended, which can be evaluated from the slopes at

maximum $(dR/dt)_{max}$ and minimum $(dR/dt)_{min}$ concavity of the release curve. Both $(dR/dt)_{max}$ and $(dR/dt)_{min}$ were calculated as shown in the following table:

Table D.1 – Model coefficients

	Low R value	**High R value**
$(dR/dt)_{max}$	w_{oil}	$\frac{1}{2}\left(w_{oil}+\frac{3}{5}\right)$
$(dR/dt)_{min}$	$\frac{1}{2}\left(w_{oil}+\frac{3}{5}\right)$	$\frac{3}{5}$

If $h \ll d$, further simplification may apply

$$\left(\frac{P}{h}\right)_* = \frac{\frac{d}{6}\left(\frac{dR}{dt}\right)_*}{1-w_{oil}}\frac{\rho_{oil}}{c_{s,oil}} \tag{D.13}$$

References

1. Hu, J., Z.-B. Xiao, R.-J. Zhou, S.-S. Ma, Z. Li, and M.-X. Wang, *Comparison of compounded fragrance and chitosan nanoparticles loaded with fragrance applied in cotton fabrics.* Textile Research Journal, 2011. **81**(19): p. 2056-2064.
2. Teixeira, M.A., O. Rodríguez, S. Rodrigues, I. Martins, and A.E. Rodrigues, *A case study of product engineering: Performance of microencapsulated perfumes on textile applications.* AIChE Journal, 2012. **58**(6): p. 1939-1950.
3. Madene, A., M. Jacquot, J. Scher, and S. Desobry, *Flavour encapsulation and controlled release - a review.* International Journal of Food Science and Technology, 2006. **41**(1): p. 1-21.
4. Brain, J., S.W. Bennett, Y. Zhen, J.G.L. Pluyter, L.M. Popplewell, and K.D. Lee, *Encapsulated Fragrance Chemicals.* US 7632789, 2009. **B2**.
5. Rodrigues, S.N., I.M. Martins, I.P. Fernandes, P.B. Gomes, V.G. Mata, M.F. Barreiro, and A.E. Rodrigues, *Scentfashion®: Microencapsulated perfumes for textile application.* Chemical Engineering Journal, 2009. **149**(1): p. 463-472.
6. Bruyninckx, K. and M. Dusselier, *Sustainable Chemistry Considerations for the Encapsulation of Volatile Compounds in Laundry-Type Applications.* ACS Sustainable Chemistry & Engineering, 2019. **7**(9): p. 8041-8054.
7. Yang, Z., Z. Peng, J. Li, S. Li, L. Kong, P. Li, and Q. Wang, *Development and evaluation of novel flavour microcapsules containing vanilla oil using complex coacervation approach.* Food Chem, 2014. **145**: p. 272-7.
8. Tekin, R., N. Bac, and H. Erdogmus, *Microencapsulation of Fragrance and Natural Volatile Oils for Application in Cosmetics, and Household Cleaning Products.* Macromolecular Symposia, 2013. **333**(1): p. 35-40.
9. Jun-xia, X., Y. Hai-yan, and Y. Jian, *Microencapsulation of sweet orange oil by complex coacervation with soybean protein isolate/gum Arabic.* Food Chemistry, 2011. **125**(4): p. 1267-1272.

10. Hsieh, W.-C., C.-P. Chang, and Y.-L. Gao, *Controlled release properties of Chitosan encapsulated volatile Citronella Oil microcapsules by thermal treatments.* Colloids and Surfaces B: Biointerfaces, 2006. **53**(2): p. 209-214.

11. Botrel, D.A., R.V.d.B. Fernandes, and S.V. Borges, *Chapter 12 - Microencapsulation of Essential Oils Using Spray Drying Technology*, in *Microencapsulation and Microspheres for Food Applications*, L.M.C. Sagis, Editor. 2015, Academic Press: San Diego. p. 235-251.

12. Bungenberg de Jong, H.G.K., H. R. , *Coacervation (partial miscibility in colloid systems).* Proceedings of the Koninklijke Nederlandse Akademie der Wetenschappen, 1929. **32**: p. 849–856.

13. Ghosh, S.K., *Functional Coatings by Polymer Microencapsulation: A General Perspective.* Functional Coatings by Polymer Microencapsulation, 2006. **WILEY-VCH**: p. 1-28.

14. Long, Y., D. York, Z. Zhang, and J.A. Preece, *Microcapsules with low content of formaldehyde: preparation and characterization.* J. Mater. Chem., 2009. **19**(6882-6887).

15. Dong, Z., Y. Ma, K. Hayat, C. Jia, S. Xia, and X. Zhang, *Morphology and release profile of microcapsules encapsulating peppermint oil by complex coacervation.* Journal of Food Engineering, 2011. **104**(3): p. 455-460.

16. Mercade-Prieto, R., R. Allen, D. York, J.A. Preece, T.E. Goodwin, and Z. Zhang, *Determination of the shell permeability of microcapsules with a core of oil-based active ingredient.* J Microencapsul, 2012. **29**(5): p. 463-74.

17. Mercadé-Prieto, R., R. Allen, D. York, J.A. Preece, T.E. Goodwin, and Z. Zhang, *Determination of the Failure Stresses for Fluid-filled Microcapsules that Rupture Near the Elastic Regime.* Experimental Mechanics, 2012. **52**(9): p. 1435-1445.

18. Mercadé-Prieto, R., B. Nguyen, R. Allen, D. York, J.A. Preece, T.E. Goodwin, and Z. Zhang, *Determination of the elastic properties of single microcapsules using micromanipulation and finite element modeling.* Chemical Engineering Science, 2011. **66**(10): p. 2042-2049.

19. Thies, C., *A survey of microencapsulation processes.* In S. Benita (Ed.) . Microencapsulation Methods and Industrial Application, 2005. **Marcel Dekker, Inc.:** (New York, NY.): p. 1-20.

20. Rodrigues do Amaral, P.H., P. Lopes Andrade, and L. Costa de Conto, *Microencapsulation and Its Uses in Food Science and Technology: A Review.* Processes, Technologies and Industrial Applications, 2018.

21. Long, Y., K. Song, D. York, Z. Zhang, and J.A. Preece, *Composite microcapsules with enhanced mechanical stability and reduced active ingredient leakage.* Particuology, 2016. **26**: p. 40-46.

22. Pan, X., D. York, J.A. Preece, and Z. Zhang, *Size and strength distributions of melamine-formaldehyde microcapsules prepared by membrane emulsification.* Powder Technology, 2012. **227**: p. 43-50.

23. Brown, E.N., M.R. Kessler, N.R. Sottos, and S.R. White, *In situ poly(urea-formaldehyde) microencapsulation of dicyclopentadiene.* Journal of Microencapsulation, 2003. **20**(6): p. 719-730.

24. Ghorbanzadeh Ahangari, M., A. Fereidoon, M. Jahanshahi, and N. Sharifi, *Effect of nanoparticles on the micromechanical and surface properties of poly(urea–formaldehyde) composite microcapsules.* Composites Part B: Engineering, 2014. **56**: p. 450-455.

25. Sun, G. and Z. Zhang, *Mechanical properties of melamine-formaldehyde microcapsules.* Journal of Microencapsulation, 2001. **18**(5): p. 593-602.

26. Guinebretiere, S.J.S., Johan; Sands, Peggy Dorothy; Pintens, An; Dihora, Jiten Oghavij;, *Benefit agent-containing delivery particle*, Procter&Gamble, Editor. 2007: Belgium.

27. Liu, K.M., J.A. Preece, D. York, J. Bowen, and Z. Zhang, *Measurement of the adhesion between single melamine-formaldehyde resin microparticles and a flat fabric surface using AFM.* Journal of Adhesion Science and Technology, 2013. **27**(9): p. 973-987.

28. He, Y., J. Bowen, J.W. Andrews, M. Liu, J. Smets, and Z. Zhang, *Adhesion of perfume-filled microcapsules to model fabric surfaces.* Journal of Microencapsulation, 2014. **31**(5): p. 430-439.

29. Hu, J., X. Zhang, and J. Qu, *Investigation on the mechanical properties of polyurea (PU)/melamine formaldehyde (MF) microcapsules prepared with different chain extenders.* Journal of Microencapsulation, 2018. **35**(3): p. 219-228.

30. Walter, A., H. Rehage, and H. Leonhard, *Shear-induced deformations of polyamide microcapsules.* Colloid and Polymer Science, 2000. **278**(2): p. 169-175.

31. Pan, X., R. Mercadé-Prieto, D. York, J.A. Preece, and Z. Zhang, *Structure and Mechanical Properties of Consumer-Friendly PMMA Microcapsules.* Industrial & Engineering Chemistry Research, 2013. **52**(33): p. 11253-11265.

32. Ganza-Gonzalez, A., S. Anguiano-Igea, F.J. Otero-Espinar, J.B. Mendez, and P. Buri, *Polyacrylate-based microparticles for sustained release of metoclopramide.* Stp Pharma Sciences, 2002. **12**: p. 103-107.

33. Hwang, J.-S., J.-N. Kim, Y.-J. Wee, H.-G. Jang, S.-H. Kim, and H.-W. Ryu, *Factors affecting the characteristics of melamine resin microcapsules containing fragrant oils.* Biotechnology and Bioprocess Engineering, 2006. **11**(5): p. 391.

34. Hwang, J.-S., J.-N. Kim, Y.-J. Wee, J.-S. Yun, H.-G. Jang, S.-H. Kim, and H.-W. Ryu, *Preparation and characterization of melamine-formaldehyde resin microcapsules containing fragrant oil.* Biotechnology and Bioprocess Engineering, 2006. **11**(4): p. 332-336.

35. Miró Specos, M.M., G. Escobar, P. Marino, C. Puggia, M.V. Defain Tesoriero, and L. Hermida, *Aroma Finishing of Cotton Fabrics by Means of Microencapsulation Techniques.* Journal of Industrial Textiles, 2010. **40**(1): p. 13-32.

36. Cole, P., H.-O. Adami, D. Trichopoulos, and J. Mandel, *Formaldehyde and lymphohematopoietic cancers: A review of two recent studies.* Regulatory Toxicology and Pharmacology, 2010. **58**(2): p. 161-166.

37. Lazenby, V., A. Hinwood, A. Callan, and P. Franklin, *Formaldehyde personal exposure measurements and time weighted exposure estimates in children.* Chemosphere, 2012. **88**(8): p. 966-973.

38. Kelly, T.J., D.L. Smith, and J. Satola, *Emission Rates of Formaldehyde from Materials and Consumer Products Found in California Homes.* Environmental Science & Technology, 1999. **33**(1): p. 81-88.

39. Tang, X., Y. Bai, A. Duong, M.T. Smith, L. Li, and L. Zhang, *Formaldehyde in China: Production, consumption, exposure levels, and health effects.* Environment International, 2009. **35**(8): p. 1210-1224.

40. Peña, B., C. Panisello, G. Aresté, R. Garcia-Valls, and T. Gumí, *Preparation and characterization of polysulfone microcapsules for perfume release.* Chemical Engineering Journal, 2012. **179**: p. 394-403.

41. Park, S.-J., Y.-J. Yang, and H.-B. Lee, *Effect of acid–base interaction between silica and fragrant oil in the PCL/PEG microcapsules.* Colloids and Surfaces B: Biointerfaces, 2004. **38**(1): p. 35-40.

42. Alongi, J., M. Ciobanu, J. Tata, F. Carosio, and G. Malucelli, *Thermal stability and flame retardancy of polyester, cotton, and relative blend textile fabrics subjected to sol–gel treatments.* Journal of Applied Polymer Science, 2011. **119**(4): p. 1961-1969.

43. Li, S., *Degradation of Biodegradable Aliphatic Polyesters.* 2006.

44. Karlsson, L.E. and P. Jannasch, *Polysulfone ionomers for proton-conducting fuel cell membranes: sulfoalkylated polysulfones.* Journal of Membrane Science, 2004. **230**(1): p. 61-70.

45. Piirilä, P.L., A. Meuronen, M.L. Majuri, R. Luukkonen, T. Mäntylä, H.J. Wolff, H. Nordman, H. Alenius, and A. Laitinen, *Inflammation and functional outcome in diisocyanate-induced asthma after cessation of exposure.* Allergy, 2008. **63**(5): p. 583-591.

46. Piacentini, E., L. Giorno, M.M. Dragosavac, G.T. Vladisavljević, and R.G. Holdich, *Microencapsulation of oil droplets using cold water fish gelatine/gum arabic complex coacervation by membrane emulsification.* Food Research International, 2013. **53**(1): p. 362-372.

47. Prata, A.S. and C.R.F. Grosso, *Production of microparticles with gelatin and chitosan.* Carbohydrate Polymers, 2015. **116**: p. 292-299.

48. Wang, B., B. Adhikari, M. Mathesh, W. Yang, and C.J. Barrow, *Anchovy oil microcapsule powders prepared using two-step complex coacervation between gelatin and sodium hexametaphosphate followed by spray drying.* Powder Technology, 2019. **358**: p. 68-78.

49. Silva, D.F., C.S. Favaro-Trindade, G.A. Rocha, and M. Thomazini, *Microencapsulation of Lycopene by Gelatin-Pectin Complex Coacervation.* Journal of Food Processing and Preservation, 2012. **36**(2): p. 185-190.

50. Irma, K.K., A. Qurrota, M. Hanina, and M.R.A. Marsasi, *Encapsulation of Peppermint Oil withCarboxymethyl kappa Carrageenan-Gelatine-Chitosan.* Mater. Sci. Eng., 2019. **012096**.

51. Chourpa, I., V. Ducel, J. Richard, P. Dubois, and F. Boury, *Conformational Modifications of α Gliadin and Globulin Proteins upon Complex Coacervates Formation with Gum Arabic as Studied by Raman Microspectroscopy.* Biomacromolecules, 2006. **7**(9): p. 2616-2623.

52. Weinbreck, F., R. de Vries, P. Schrooyen, and C.G. De Kruif, *Complex Coacervation of Whey Proteins and Gum Arabic.* Biomacromolecules, 2003. **4**: p. 293-303.

53. De Kruif, C., F. Weinbreck, and R. de Vries, *Complex coacervation of proteins and anionic polysaccharides.* Current Opinion in Colloid & Interface Science, 2004. **9**: p. 340-349.

54. Mendanha, D.V., S.E. Molina Ortiz, C.S. Favaro-Trindade, A. Mauri, E.S. Monterrey-Quintero, and M. Thomazini, *Microencapsulation of casein hydrolysate by complex coacervation with SPI/pectin.* Food Research International, 2009. **42**(8): p. 1099-1104.

55. Eriksson, A., J. Burcharth, and J. Rosenberg, *Animal derived products may conflict with religious patients' beliefs.* BMC Medical Ethics, 2013. **14**(1): p. 48.

56. Imran, M. and S. Mahmood, *An overview of animal prion diseases.* Virology Journal, 2011. **8**(1): p. 493.

57. Ach, D., S. Briançon, G. Broze, F. Puel, A. Rivoire, J.M. Galvan, and Y. Chevalier, *Formation of Microcapsules by Complex Coacervation.* Can. J. Chem. Eng. , 2015. **93**: p. 183–191

58. Gouin, S., *Microencapsulation: industrial appraisal of existing technologies and trends.* Trends in Food Science & Technology, 2004. **15**(7): p. 330-347.

59. Maalouf, G.E., *Microcapsules useful in carbonless copying systems and process for their preparation* Moore Business Forms Inc., 1976. **US4000087A**.

60. Lemetter, C.Y.G., F.M. Meeuse, and N.J. Zuidam, *Control of the morphology and the size of complex coacervate microcapsules during scale-up.* AIChE Journal, 2009. **55**(6): p. 1487-1496.

61. Strobel, S.A., L. Knowles, N. Nitin, H.B. Scher, and T. Jeoh, *Comparative technoeconomic process analysis of industrial-scale microencapsulation of bioactives in cross-linked alginate.* Journal of Food Engineering, 2020. **266**: p. 109695.

62. Hu, J., H.-Q. Chen, and Z. Zhang, *Mechanical properties of melamine formaldehyde microcapsules for self-healing materials.* Materials Chemistry and Physics, 2009. **118**(1): p. 63-70.

63. Yu, F., C. Xue, and Z. Zhang, *Mechanical characterization of fish oil microcapsules by a micromanipulation technique.* LWT, 2021. **144**: p. 111194.

64. Thomas, C.R., Z. Zhang, and C. Cowen, *Micromanipulation measurements of biological materials.* Biotechnology Letters, 2000. **22**(7): p. 531-537.

65. Sun, G. and Z. Zhang, *Mechanical strength of microcapsules made of different wall materials.* International Journal of Pharmaceutics, 2002. **242**(1): p. 307-311.

66. Mercadé-Prieto, R., R. Allen, D. York, J.A. Preece, T.E. Goodwin, and Z. Zhang, *Compression of elastic–perfectly plastic microcapsules using micromanipulation and finite element modelling: Determination of the yield stress.* Chemical Engineering Science, 2011. **66**(9): p. 1835-1843.

67. Kleinschmidt, E.J. and R.G. Cooper, *The impact of product innovativeness on performance.* Journal of Product Innovation Management, 1991. **8**(4): p. 240-251.

68. Bansode, S.S., S.K. Banarjee, D.D. Gaikwad, S.L. Jadhav, and R.M. Thorat, *Microencapsulation : A review.* 2010. **1**(2).

69. Frascareli, E.C., V.M. Silva, R.V. Tonon, and M.D. Hubinger, *Effect of process conditions on the microencapsulation of coffee oil by spray drying.* Food and Bioproducts Processing, 2012. **90**(3): p. 413-424.

70. Abbaspourrad, A., W.J. Duncanson, N. Lebedeva, S.-H. Kim, A.P. Zhushma, S.S. Datta, P.A. Dayton, S.S. Sheiko, M. Rubinstein, and D.A. Weitz, *Microfluidic Fabrication of Stable Gas-Filled Microcapsules for Acoustic Contrast Enhancement.* Langmuir, 2013. **29**(40): p. 12352-12357.

71. de Melo Ramos, F., V. Silveira Júnior, and A.S. Prata, *Assessing the Vacuum Spray Drying Effects on the Properties of Orange Essential Oil Microparticles.* Food and Bioprocess Technology, 2019. **12**(11): p. 1917-1927.

72. Lensen, D., D.M. Vriezema, and J.C.M. van Hest, *Polymeric Microcapsules for Synthetic Applications.* Macromolecular Bioscience, 2008. **8**(11): p. 991-1005.

73. Dubey, R., T.C. Shami, and K.U. Bhasker Rao, *Microencapsulation Technology and Applications.* Defence Science Journal 2009. **59**: p. 82-95.

74. Gasperini, L., J.F. Mano, and R.L. Reis, *Natural polymers for the microencapsulation of cells.* Journal of The Royal Society Interface, 2014. **11**(100): p. 20140817.

75. Bernheim-Grosswasser, A., S. Ugazio, F. Gauffre, O. Viratelle, P. Mahy, and D. Roux, *Spherulites: A new vesicular system with promising applications. An example: Enzyme microencapsulation.* The Journal of Chemical Physics, 2000. **112**(7): p. 3424-3430.

76. Nixon, J.R., *Preparation of microcapsules with possible pharmaceutical use.* Endeavour, 1985. **9**(3): p. 123-128.

77. Augustin, M.A., L. Sanguansri, C. Margetts, and B. Young, *Microencapsulation of Food Ingredients.* Food Australia, 2001. **53**(6): p. 220-223.

78. Asensio, C.M., A.J. Paredes, M.P. Martin, D.A. Allemandi, V. Nepote, and N.R. Grosso, *Antioxidant Stability Study of Oregano Essential Oil Microcapsules Prepared by Spray-Drying.* Journal of Food Science, 2017. **82**(12): p. 2864-2872.

79. Wilson, N. and N.P. Shah, *Microencapsulation of Vitamins.* ASEAN Food Journal, 2007. **14**(1): p. 1-14.

80. Charcosset, C., *Preparation of emulsions and particles by membrane emulsification for the food processing industry.* Journal of Food Engineering, 2009. **92**(3): p. 241-249.

81. Khor, C.M., W.K. Ng, P. Kanaujia, K.P. Chan, and Y. Dong, *Hot-melt extrusion microencapsulation of quercetin for taste-masking.* Journal of Microencapsulation, 2017. **34**(1): p. 29-37.

82. Huang, D., M. Sun, Y. Bu, F. Luo, C. Lin, Z. Lin, Z. Weng, F. Yang, and D. Wu, *Microcapsule-embedded hydrogel patches for ultrasound responsive and enhanced transdermal delivery of diclofenac sodium.* Journal of Materials Chemistry B, 2019. **7**(14): p. 2330-2337.

83. Luppi, B., F. Bigucci, V. Zecchi, and T. Cerchiara, *Gastroresistant microcapsules: new approaches for site-specific delivery of ketoprofen.* Drug Delivery, 2009. **16**(1): p. 24-29.

84. Rodrigues, S.N., I. Fernandes, I.M. Martins, V.G. Mata, F. Barreiro, and A.E. Rodrigues, *Microencapsulation of Limonene for Textile Application.* Industrial & Engineering Chemistry Research, 2008. **47**(12): p. 4142-4147.

85. Liu, F., L.-X. Wen, Z.-Z. Li, W. Yu, H.-Y. Sun, and J.-F. Chen, *Porous hollow silica nanoparticles as controlled delivery system for water-soluble pesticide.* Materials Research Bulletin, 2006. **41**(12): p. 2268-2275.

86. Wang, Z., C. Li, J. Xu, K. Wang, X. Lu, H. Zhang, S. Qu, G. Zhen, and F. Ren, *Bioadhesive Microporous Architectures by Self-Assembling Polydopamine Microcapsules for Biomedical Applications.* Chemistry of Materials, 2015. **27**(3): p. 848-856.

87. Bustos C., R.O., F.V. Alberti R., and S.B. Matiacevich, *Edible antimicrobial films based on microencapsulated lemongrass oil.* Journal of Food Science and Technology, 2016. **53**(1): p. 832-839.

88. Saifullah, M., M.R.I. Shishir, R. Ferdowsi, M.R. Tanver Rahman, and Q. Van Vuong, *Micro and nano encapsulation, retention and controlled release of flavor and aroma compounds: A critical review.* Trends in Food Science & Technology, 2019. **86**: p. 230-251.

89. Jyothi Sri., S., A. Seethadevi, K. Suria prabha, P. .Muthuprasanna, and P. Pavitra, *Microencapsulation: A review.* International Journal of Pharma and Bio Sciences, 2012. **3**(1): p. 509-531.

90. Parthasarathi, S. and C. Anandharamakrishnan, *Enhancement of oral bioavailability of vitamin E by spray-freeze drying of whey protein microcapsules.* Food and Bioproducts Processing, 2016. **100**: p. 469-476.

91. Reineccius, G.A., *The Spray Drying of Food Flavors.* Drying Technology, 2004. **22**(6): p. 1289-1324.

92. Teixeira, M.I., L.R. Andrade, M. Farina, and M.H.M. Rocha-Leão, *Characterization of short chain fatty acid microcapsules produced by spray drying.* Materials Science and Engineering: C, 2004. **24**(5): p. 653-658.

93. Bakry, A.M., S. Abbas, B. Ali, H. Majeed, M.Y. Abouelwafa, A. Mousa, and L. Liang, *Microencapsulation of Oils: A Comprehensive Review of Benefits, Techniques, and Applications.* Comprehensive Reviews in Food Science and Food Safety, 2016. **15**(1): p. 143-182.

94. Raybaudi-Massilia, R. and J. Mosqueda-Melgar, *Polysaccharides as carriers and protectors of additives and bioactive compounds in foods.* The complex word of polysaccharides, 2012. **16**: p. 429–53.

95. Atkin, R., P. Davies, J. Hardy, and B. Vincent, *Preparation of Aqueous Core/Polymer Shell Microcapsules by Internal Phase Separation.* Macromolecules, 2004. **37**(21): p. 7979-7985.

96. Kim, C., S. Chung, Y.E. Kim, K.S. Lee, S.H. Lee, K.W. Oh, and J.Y. Kang, *Generation of core-shell microcapsules with three-dimensional focusing device for efficient formation of cell spheroid.* Lab on a Chip, 2011. **11**(2): p. 246-252.

97. Fang, Z. and B. Bhandari, *Encapsulation of polyphenols – a review.* Trends in Food Science & Technology, 2010. **21**(10): p. 510-523.

98. Brandau, T., *Preparation of monodisperse controlled release microcapsules.* International Journal of Pharmaceutics, 2002. **242**(1): p. 179-184.

99. Xue, J. and Z. Zhang, *Physical, structural, and mechanical characterization of calcium–shellac microspheres as a carrier of carbamide peroxide.* Journal of Applied Polymer Science, 2009. **113**(3): p. 1619-1625.

100. Dziezak, J.D., *Microencapsulation and encapsulated food ingredients.* Food Technology, 1988. **42**: p. 136-151.

101. Mercadé-Prieto, R. and Z. Zhang, *Mechanical characterization of microspheres – capsules, cells and beads: a review.* Journal of Microencapsulation, 2012. **29**(3): p. 277-285.

102. Schrooyen, P.M.M., R.v.d. Meer, and C.G.D. Kruif, *Microencapsulation: its application in nutrition.* Proceedings of the Nutrition Society, 2001. **60**(4): p. 475-479.

103. Trojanowska, A., A. Nogalska, R.G. Valls, M. Giamberini, and B. Tylkowski, *Technological solutions for encapsulation.* Physical Sciences Reviews, 2017. **2**(9): p. 20170020.

104. Jurkowska, M. and I. Szczygieł, *Review on properties of microencapsulated phase change materials slurries (mPCMS).* Applied Thermal Engineering, 2016. **98**: p. 365-373.

105. Shishir, M.R.I., L. Xie, C. Sun, X. Zheng, and W. Chen, *Advances in micro and nano-encapsulation of bioactive compounds using biopolymer and lipid-based transporters.* Trends in Food Science & Technology, 2018. **78**: p. 34-60.

106. White, M.A., *The Chemistry behind Carbonless Copy Paper.* Journal of Chemical Education, 1998. **75**(9): p. 1119.

107. Boyes, R.N., T.R. Tice, R.M. Gilley, and K.L. Pledger, *Pharmaceutical formulations comprising microcapsules* U.S. Patent, 1987. **US5384133A**

108. Jin, Y., Q. Zhou, Z. Li, Z. Yang, and H.-J.S. Fan, *Calcium-cross linked polysaccharide microcapsules for controlled release and antimicrobial applications.* Colloids and Surfaces A: Physicochemical and Engineering Aspects, 2020. **600**: p. 125025.

109. Mooranian, A., N. Zamani, M. Mikov, S. Goločorbin-Kon, G. Stojanovic, F. Arfuso, and H. Al-Salami, *Stability and biological testing of taurine-conjugated bile acid antioxidant microcapsules for diabetes treatment.* Therapeutic Delivery, 2019. **10**(2): p. 99-106.

110. Selina, O.E., S. Belov, N.N. Vlasova, V.I. Balysheva, A.I. Churin, A. Bartkoviak, G.B. Sukhorukov, and E.A. Markvicheva, *Biodegradable microcapsules containing DNA for the new DNA vaccine design.* Bioorganicheskaia khimiia, 2009. **35**(1): p. 113-121.

111. Kulkarni, A.R., K.S. Soppimath, T.M. Aminabhavi, A.M. Dave, and M.H. Mehta, *Glutaraldehyde crosslinked sodium alginate beads containing liquid pesticide for soil application.* Journal of Controlled Release, 2000. **63**(1): p. 97-105.

112. Liu, B., Y. Wang, F. Yang, X. Wang, H. Shen, H. Cui, and D. Wu, *Construction of a controlled-release delivery system for pesticides using biodegradable PLA-based microcapsules.* Colloids and Surfaces B: Biointerfaces, 2016. **144**: p. 38-45.

113. Habibi, A., J. Keramat, M. Hojjatoleslamy, and F. Tamjidi, *Preparation of Fish Oil Microcapsules by Complex Coacervation of Gelatin–Gum Arabic and their Utilization for Fortification of Pomegranate Juice.* Journal of Food Process Engineering, 2017. **40**(2): p. e12385.

114. Carvalho, I.T., B.N. Estevinho, and L. Santos, *Application of microencapsulated essential oils in cosmetic and personal healthcare products – a review.* International Journal of Cosmetic Science, 2016. **38**(2): p. 109-119.

115. Patchan, M.W., B.W. Fuller, L.M. Baird, P.K. Gong, E.C. Walter, B.J. Vidmar, I. Kyei, Z. Xia, and J.J. Benkoski, *Robust Composite-Shell Microcapsules via Pickering Emulsification.* ACS Applied Materials & Interfaces, 2015. **7**(13): p. 7315-7323.

116. Koh, E., N.-K. Kim, J. Shin, and Y.-W. Kim, *Polyurethane microcapsules for self-healing paint coatings.* RSC Advances, 2014. **4**(31): p. 16214-16223.

117. Song, Y., K.-F. Chen, J.-J. Wang, Y. Liu, T. Qi, and G.L. Li, *Synthesis of Polyurethane/Poly(urea-formaldehyde) Double-shelled Microcapsules for Self-healing Anticorrosion Coatings.* Chinese Journal of Polymer Science, 2020. **38**(1): p. 45-52.

118. Kralovec, J.A., S. Zhang, W. Zhang, and C.J. Barrow, *A review of the progress in enzymatic concentration and microencapsulation of omega-3 rich oil from fish and microbial sources.* Food Chemistry, 2012. **131**(2): p. 639-644.

119. Surburg, H. and J. Panten, *Common fragrance and flavor materials: Preparation, properties and uses.* 2006. **5th ed. Weinheim, Germany: Wiley-VCH**.

120. Calo, J.R., P.G. Crandall, C.A. O'Bryan, and S.C. Ricke, *Essential oils as antimicrobials in food systems – A review.* Food Control, 2015. **54**: p. 111-119.

121. Abdul Aziz, F.R., J. Jai, R. Raslan, and I. Subuki, *Microencapsulation of Essential Oils Application in Textile: A Review.* Advanced Materials Research, 2015. **1113**: p. 346-351.

122. Lomascolo, A., C. Stentelaire, M. Asther, and L. Lesage-Meessen, *Basidiomycetes as new biotechnological tools to generate natural aromatic flavours for the food industry.* Trends in Biotechnology, 1999. **17**(7): p. 282-289.

123. Felix, P.H.C., V.S. Birchal, D.A. Botrel, G.R. Marques, and S.V. Borges, *Physicochemical and Thermal Stability of Microcapsules of Cinnamon Essential Oil by Spray Drying.* Journal of Food Processing and Preservation, 2017. **41**(3): p. e12919.

124. Jang, I.B., J.H. Sung, and H.J. Choi, *Synthesis of microcapsule containing oil phase via in-situ polymerization.* Journal of Materials Science, 2005. **40**(4): p. 1031-1033.

125. Zhang, Y., A.N. Mustapha, X. Zhang, D. Baiocco, G. Wellio, T. Davies, Z. Zhang, and Y. Li, *Improved volatile cargo retention and mechanical properties of capsules via sediment-free in situ polymerization with cross-linked poly(vinyl alcohol) as an emulsifier.* Journal of Colloid and Interface Science, 2020. **568**: p. 155-164.

126. Zhang, Y., D. Baiocco, A.N. Mustapha, X. Zhang, Q. Yu, G. Wellio, Z. Zhang, and Y. Li, *Hydrocolloids: Nova materials assisting encapsulation of volatile phase change materials for cryogenic energy transport and storage.* Chemical Engineering Journal, 2020. **382**: p. 123028.

127. Urala, N. and L. Lähteenmäki, *Attitudes behind consumers' willingness to use functional foods.* Food Quality and Preference, 2004. **15**(7): p. 793-803.

128. Albert Christine, M., K. Oh, W. Whang, E. Manson JoAnn, U. Chae Claudia, J. Stampfer Meir, C. Willett Walter, and B. Hu Frank, *Dietary α-Linolenic Acid Intake and Risk of Sudden Cardiac Death and Coronary Heart Disease.* Circulation, 2005. **112**(21): p. 3232-3238.

129. Freitas, I.R. and M.G. Cattelan, *Chapter 15 - Antimicrobial and Antioxidant Properties of Essential Oils in Food Systems—An Overview*, in *Microbial Contamination and Food Degradation*, A.M. Holban and A.M. Grumezescu, Editors. 2018, Academic Press. p. 443-470.

130. Shams, R., E. Oldfield, J. Copare, and D. Johnson, *Peppermint Oil: Clinical Uses in the Treatment of Gastrointestinal Diseases.* JSM Gastroenterol Hepatol, 2015. **3**(1): p. 1036.

131. Fernandes, R.V., S.V. Borges, and D.A. Botrel, *Gum arabic/starch/maltodextrin/inulin as wall materials on the microencapsulation of rosemary essential oil.* Carbohydr Polym, 2014. **101**: p. 524-32.

132. Fernandes, R.V.d.B., S.V. Borges, E.K. Silva, Y.F. da Silva, H.J.B. de Souza, E.L. do Carmo, C.R. de Oliveira, M.I. Yoshida, and D.A. Botrel, *Study of ultrasound-assisted emulsions on microencapsulation of ginger essential oil by spray drying.* Industrial Crops and Products, 2016. **94**: p. 413-423.

133. Janiszewska, E., A. Jedlińska, and D. Witrowa-Rajchert, *Effect of homogenization parameters on selected physical properties of lemon aroma powder.* Food and Bioproducts Processing, 2015. **94**: p. 405-413.

134. Adamiec, J., *Moisture Sorption Characteristics of Peppermint Oil Microencapsulated by Spray Drying.* Drying Technology, 2009. **27**(12): p. 1363-1369.

135. Badee, A.Z.M., E. Amal, A. El-Kader, and M. Hanan, *Microencapsulation of Peppermint Oil by Spray-Drying.* Australian Journal of Basic and Applied, 2012. **6**(12): p. 499-504.

136. Sarkar, S., S. Gupta, P.S. Variyar, A. Sharma, and R.S. Singhal, *Hydrophobic derivatives of guar gum hydrolyzate and gum Arabic as matrices for microencapsulation of mint oil.* Carbohydrate Polymers, 2013. **95**(1): p. 177-182.

137. Karim, A.A. and R. Bhat, *Gelatin alternatives for the food industry: recent developments, challenges and prospects.* Trends in Food Science & Technology, 2008. **19**(12): p. 644-656.

138. Jafari, S.M., K. Mahdavi-Khazaei, and A. Hemmati-Kakhki, *Microencapsulation of saffron petal anthocyanins with cress seed gum compared with Arabic gum through freeze drying.* Carbohydr Polym, 2016. **140**: p. 20-5.

139. King, A.H., *Encapsulation and controlled release of food ingredients.* In S. J. Risch & G. Reineccius (Eds.) 1995. **American Chemical Society**(Washington, DC): p. 26-39.

140. Finch, C.A. and R. Bodmeier, *Microencapsulation.* Ullman's Encyclopedia of Industrial Chemistry, 2002. **Wiley-VCH**(Weinheim).

141. Petrusic, S. and V. Koncar, *5 - Controlled release of active agents from microcapsules embedded in textile structures*, in *Smart Textiles and their Applications*, V. Koncar, Editor. 2016, Woodhead Publishing: Oxford. p. 89-114.

142. Hassan, A., M. Shakeel Laghari, and Y. Rashid, *Micro-Encapsulated Phase Change Materials: A Review of Encapsulation, Safety and Thermal Characteristics.* Sustainability, 2016. **8**(10).

143. Zuidam, N.J. and E. Shimoni, *Overview of Microencapsulates for Use in Food Products or Processes and Methods to Make Them*, in *Encapsulation Technologies for Active Food Ingredients and Food Processing*, N.J. Zuidam and V. Nedovic, Editors. 2010, Springer New York: New York, NY. p. 3-29.

144. Whelehan, M. and I. Marison, *Microencapsulation using vibrating technology.* Journal of microencapsulation, 2011. **28**: p. 669-88.

145. Barbosa-Cánovas, G., E. Ortega-Rivas, P. Juliano, and H. Yan, *Food powders: physical properties, processing, and functionality.* Springer, 2005.

146. Lam, P.L. and R. Gambari, *Advanced progress of microencapsulation technologies: In vivo and in vitro models for studying oral and transdermal drug deliveries.* Journal of Controlled Release, 2014. **178**: p. 25-45.

147. Karim, F.T., K. Ghafoor, S. Ferdosh, F. Al-Juhaimi, E. Ali, K.B. Yunus, M.H. Hamed, A. Islam, M. Asif, and M.Z.I. Sarker, *Microencapsulation of fish oil using supercritical antisolvent process.* Journal of Food and Drug Analysis, 2017. **25**(3): p. 654-666.

148. Kaushik, P., K. Rawat, V.K. Aswal, J. Kohlbrecher, and H.B. Bohidar, *Mixing ratio dependent complex coacervation versus bicontinuous gelation of pectin with in situ formed zein nanoparticles.* Soft Matter, 2018. **14**(31): p. 6463-6475.

149. Henao, E., E. Delgado, H. Contreras, and G. Quintana, *Polyelectrolyte Complexation versus Ionotropic Gelation for Chitosan-Based Hydrogels with Carboxymethylcellulose, Carboxymethyl Starch, and Alginic Acid.* International Journal of Chemical Engineering, 2018. **2018**: p. 3137167.

150. Weinbreck, F., R. De Vries, P. Schrooyen, and C.G. de Kruif, *Complex Coacervation of Whey Proteins and Gum Arabic.* Biomacromolecules 2003. **4**: p. 293-303.

151. Loftsson, T. and T. Kristmundsdóttir, *Microcapsules Containing Water-Soluble Cyclodextrin Inclusion Complexes of Water-Insoluble Drugs*, in *Polymeric Delivery Systems*. 1993, American Chemical Society. p. 168-189.

152. Lévy, M.C. and M.C. Andry, *Microcapsules prepared through interfacial cross-linking of starch derivatives.* International Journal of Pharmaceutics, 1990. **62**(1): p. 27-35.

153. Soper, J.C., D.K. Young, and M.T. Thomas, *Method of encapsulating flavors and fragrances by controlled water transport into microcapsules.* US Patent, 2000. **6106875**.

154. Espinosa-Andrews, H., J.G. Baez-Gonzalez, F. Cruz-Sosa, and E.J. Vernon-Carter, *Gum Arabic-Chitosan Complex Coacervation.* Biomacromolecules 2007. **8**: p. 1313-1318.

155. Dardelle, G., P. Beaussoubre, and P. Erni, *Hybrid coacervate capsules*, in *Google Patents*. 2015.

156. Weinbreck, F., R.H. Tromp, and C.G. De Kruif, *Composition and Structure of Whey Protein/Gum Arabic Coacervates.* Biomacromolecules 2004. **5**: p. 1437-1445.

157. Piacentini, E., *Coacervation, Droli E. and Giorno L.* Encyclopaedia of Membranes, 2015. **Springer Berlin Heidelberg**: p. pp.1-3.

158. Dickinson, E., *Hydrocolloids at interfaces and the influence on the properties of dispersed systems.* Food Hydrocolloids, 2003. **17**(1): p. 25-39.

159. Bohidar, H.B., *Coacervates: A novel state of soft matter - an overview.* J. Surface Sci. Technol., 2008. **24**: p. 105-124.

160. Weiß, G., A. Knoch, A. Laicher, F. Stanislaus, and R. Daniels, *Simple coacervation of hydroxypropyl methylcellulose phthalate (HPMCP) II. Microencapsulation of ibuprofen* International Journal of Pharmaceutics 1995. **124**: p. 97-105.

161. Bungenberg de Jong, H.G., *Crystallisation- Coacervation- Flocculation. In Colloid Science.* In Colloid Science, 1949. **Kruyt H. R., Ed., Vol. II,**(Chapter VIII, Elsevier Publishing Company: Amsterdam, 1949a): p. p.232-258.

162. Mohanty, B. and H.B. Bohidar, *Systematic of Alcohol-Induced Simple Coacervation in Aqueous Gelatin Solutions* Biomacromolecules, 2003. **4**: p. 1080-1086.

163. Wu, K.-G. and Q. Xiao, *Microencapsulation of Fish Oil by Simple Coacervation of Hydroxypropyl Methylcellulose.* Chinese Journal of Chemistry, 2005. **23**(11): p. 1569-1572.

164. Ocak, B., G. Gülümser, and E. Baloğlu, *Microencapsulation of Melaleuca alternifolia (Tea Tree) Oil by Using Simple Coacervation Method.* Journal of Essential Oil Research, 2011. **23**(4): p. 58-65.

165. Shimokawa, K.-i., K. Saegusa, Y. Wada, and F. Ishii, *Physicochemical properties and controlled drug release of microcapsules prepared by simple coacervation.* Colloids and Surfaces B: Biointerfaces, 2013. **104**: p. 1-4.

166. Lazko, J., Y. Popineau, and J. Legrand, *Soy glycinin microcapsules by simple coacervation method.* Colloids Surf B Biointerfaces, 2004. **37**(1-2): p. 1-8.

167. Mauguet, M.C., J. Legrand, L. Brujes, G. Carnelle, C. Larre, and Y. Popineau, *Gliadin matrices for microencapsulation processes by simple coacervation method.* Journal of Microencapsulation, 2002. **19**(3): p. 377-384.

168. Xiao, J.-X., G.-Q. Huang, S.-Q. Wang, and Y.-T. Sun, *Microencapsulation of capsanthin by soybean protein isolate-chitosan coacervation and microcapsule stability evaluation.* Journal of Applied Polymer Science, 2014. **131**(1).

169. Butstraen, C. and F. Salaün, *Preparation of microcapsules by complex coacervation of gum Arabic and chitosan.* Carbohydr Polym, 2014. **99**: p. 608-616.

170. Argin-Soysal, S., P. Kofinas, and Y.M. Lo, *Effect of complexation conditions on xanthan–chitosan polyelectrolyte complex gels.* Food Hydrocolloids, 2009. **23**(1): p. 202-209.

171. Huang, G.Q., Y.T. Sun, J.X. Xiao, and J. Yang, *Complex coacervation of soybean protein isolate and chitosan.* Food Chem, 2012. **135**(2): p. 534-9.

172. Deveci, S.S. and G. Basal, *Preparation of PCM microcapsules by complex coacervation of silk fibroin and chitosan.* Colloid and Polymer Science, 2009. **287**(12): p. 1455-1467.

173. Leclercq, S., K.R. Harlander, and G.A. Reineccius, *Formation and characterization of microcapsules by complex coacervation with liquid or solid aroma cores.* Flavour and Fragrance Journal, 2009. **24**(1): p. 17-24.

174. Bakan, J.A., *Microencapsulation of foods and related products.* Food Technology, 1973. **27**(11): p. 34-44.

175. Kamaljit Singh, S., D. Gangacharyulu, and B. Vijaya Kumar, *Effect of Reynolds Number and Concentration of Biopolymer (Gum Arabic) on Drag Reduction of Turbulent Flow in Circular Pipe.* Journal of Mechanical and Materials Engineering

2019. **13**(2).

176. Weinbreck, F., *Theoretical description of CC.* 2004.

177. Kaushik, P., K. Dowling, C.J. Barrow, and B. Adhikari, *Complex coacervation between flaxseed protein isolate and flaxseed gum.* Food Research International, 2015. **72**: p. 91-97.

178. V.B.Tolstoguzov, *Functional properties of food proteins and role of protein-polysaccharide interaction.* Food Hydrocolloids, 1991. **4**(6): p. 429-468.

179. Timilsena, Y.P., T.O. Akanbi, N. Khalid, B. Adhikari, and C.J. Barrow, *Complex coacervation: Principles, mechanisms and applications in microencapsulation.* International Journal of Biological Macromolecules, 2019. **121**: p. 1276-1286.

180. Bungenberg De Jong, H.G., *Complex colloid systems.* Colloid science, 1949. **Elsevier Amsterdam**.

181. Bungenberg De Jong, H.G., *Morphology of Coacervates.* Colloid science, 1949. **Elsevier Amsterdam**.

182. Overbeek, J. and M.J. Voorn, *Phase separation in polyelectrolyte solutions. Theory of complex coacervation.* J. Cell. Comp. Physiol., 1957. **49**: p. 7-26.

183. Dubin, P.L., C.H. Chew, and L.M. Gan, *Complex formation between anionic polyelectrolytes and cationic/nonionic mixed micelles.* Journal of Colloid and Interface Science, 1989. **128**(2): p. 566-576.

184. Veis, A. and C. Arany, *Phase separation in polyelectrolyte systems. I. Complex coacervates of gelatin* J. Phys. Chem. , 1960. **64**(9): p. 1203-1210.

185. Veis, A., *Phase separation in polyelectrolyte solutions. II. Interaction effects.* Journal of Physical Chemistry, 1961. **65**: p. 1798-1803.

186. Veis, A., *Phase separation in polyelectrolyte systems. III. Effect of aggregation and molecular weight heterogeneity.* Journal of Physical Chemistry, 1963. **67**: p. 1960-1964.

187. Veis, A., *The macromolecular chemistry of gelatin.* 1964. **New York, Academic Press**.

188. Veis, A., E. Bodor, and S. Mussell, *Molecular weight fractionation and the self-suppression of complex coacervation.* Biopolymers, 1967. **5**(1): p. 37-59.

189. Nakajima, A. and H. Sato, *Phase relationships of an equivalent mixture of sulfated polyvinyl alcohol and aminoacetalyzed polyvinyl alcohol in microsalt aqueous solution.* Biopolymers, 1972. **11**(7): p. 1345-1355.

190. Tainaka, K., *Effect of Counterions on Complex Coacervation.* Biopolymers, 1980. **19**: p. 1289-1298.

191. Thies, C., *Microcapsules*, in *Encyclopedia of Food Sciences and Nutrition (Second Edition)*, B. Caballero, Editor. 2003, Academic Press: Oxford. p. 3892-3903.

192. Cho, Y.S., S.H. Lee, H.M. Seo, K. Shin, M.H. Kang, M. Lee, J. Park, and J.W. Kim, *Structuring Pickering Emulsion Interfaces with Bilayered Coacervates of Cellulose Nanofibers and Hectorite Nanoplatelets.* Langmuir, 2021. **37**(13): p. 3828-3835.

193. Kirkwood, J., D. Hargreaves, S. O'Keefe, and J. Wilson, *Using isoelectric point to determine the pH for initial protein crystallization trials.* Bioinformatics, 2015. **31**(9): p. 1444-51.

194. Luft, J.R., J.R. Wolfley, and E.H. Snella, *What's in a drop? Correlating observations and out- 100 comes to guide macromolecular crystallization experiments.* Cryst. Growth Des., 2011. **11**(3): p. 651-663.

195. Turgeon, S.L., C. Schmitt, and C. Sanchez, *Protein–polysaccharide complexes and coacervates.* Current Opinion in Colloid & Interface Science, 2007. **12**(4-5): p. 166-178.

196. Malay, O., O. Bayraktar, and A. Batigun, *Complex coacervation of silk fibroin and hyaluronic acid.* Int J Biol Macromol, 2007. **40**(4): p. 387-93.

197. Espinosa-Andrews, H., K.E. Enriquez-Ramirez, E. Garcia-Marquez, C. Ramirez-Santiago, C. Lobato-Calleros, and J. Vernon-Carter, *Interrelationship between the zeta potential and viscoelastic properties in coacervates complexes.* Carbohydr Polym, 2013. **95**(1): p. 161-6.

198. Ducel, V., J. Richard, P. Saulnier, Y. Popineau, and F. Boury, *Evidence and characterisation of complex coacervates containing plant proteins: application to the microencapsulation of oil droplets.* Colloids and Surfaces, Physicochemical and Engineering Aspects, 2004. **232**: p. 239-247.

199. Burgess, D.J., *Practical analysis of complex coacervate systems.* Journal of Colloid and Interface Science, 1990. **140**(1): p. 227-238.

200. Kayitmazer, A.B., A.F. Koksal, and E. Kilic Iyilik, *Complex coacervation of hyaluronic acid and chitosan: effects of pH, ionic strength, charge density, chain length and the charge ratio.* Soft Matter, 2015. **11**(44): p. 8605-12.

201. Kaibara, K., T. Okazaki, H.B. Bohidar, and P.L. Dubin, *pH-Induced Coacervation in Complexes of Bovine Serum Albumin and Cationic Polyelectrolytes.* Biomacromolecules, 2000. **1**(1): p. 100-107.

202. Schmitt, C., C. Sanchez, S. Desobry-Banon, and J. Hardy, *Structure and Technofunctional Properties of Protein-Polysaccharide Complexes: A Review.* Critical Reviews in Food Science and Nutrition, 1998. **38**(8): p. 689-753.

203. Agostini, F., M. Vendruscolo, and G.G. Tartaglia, *Sequence-Based Prediction of Protein Solubility.* Journal of Molecular Biology, 2012. **421**(2): p. 237-241.

204. Pelegrine, D.H.G. and C.A. Gasparetto, *Whey proteins solubility as function of temperature and pH.* LWT - Food Science and Technology, 2005. **38**(1): p. 77-80.

205. Schön, A., B.R. Clarkson, M. Jaime, and E. Freire, *Temperature stability of proteins: Analysis of irreversible denaturation using isothermal calorimetry.* Proteins: Structure, Function, and Bioinformatics, 2017. **85**(11): p. 2009-2016.

206. Water, J.J., M.M. Schack, A. Velazquez-Campoy, M.J. Maltesen, M. van de Weert, and L. Jorgensen, *Complex coacervates of hyaluronic acid and lysozyme: effect on protein structure and physical stability.* Eur J Pharm Biopharm, 2014. **88**(2): p. 325-31.

207. Xie, Y.R. and N.S. Hettiarachchy, *Xanthan Gum Effects on Solubility and Emulsification Properties of Soy Protein Isolate.* Journal of Food Science, 1997. **62**(6): p. 1101-1104.

208. Turchiuli, C., N. Lemarié, M.-E. Cuvelier, and E. Dumoulin, *Production of fine emulsions at pilot scale for oil compounds encapsulation.* Journal of Food Engineering, 2013. **115**(4): p. 452-458.

209. Shah, R.K., H.C. Shum, A.C. Rowat, D. Lee, J.J. Agresti, A.S. Utada, L.-Y. Chu, J.-W. Kim, A. Fernandez-Nieves, C.J. Martinez, and D.A. Weitz, *Designer emulsions using microfluidics.* Materials Today, 2008. **11**(4): p. 18-27.

210. Arkoumanis, P.G., I.T. Norton, and F. Spyropoulos, *Pickering particle and emulsifier co-stabilised emulsions produced via rotating membrane emulsification.* Colloids and Surfaces A: Physicochemical and Engineering Aspects, 2019. **568**: p. 481-492.

211. Goodarzi, F. and S. Zendehboudi, *A Comprehensive Review on Emulsions and Emulsion Stability in Chemical and Energy Industries.* The Canadian Journal of Chemical Engineering, 2019. **97**(1): p. 281-309.

212. Wang, Y., J. Yuan, Y. Zhao, L. Wang, L. Guo, L. Feng, J. Cui, S. Dong, S. Wan, W. Liu, H. Hoffmann, K. Tieu, and J. Hao, *Water-in-Water Emulsions, Ultralow Interfacial Tension, and Biolubrication.* CCS Chemistry. **0**(0).

213. Batta, Y.A., *Invert emulsion: Method of preparation and application as proper formulation of entomopathogenic fungi.* MethodsX, 2016. **3**: p. 119-127.

214. Liu, E.-H. and K.M. McGrath, *Emulsion microstructure and energy input, roles in emulsion stability.* Colloids and Surfaces A: Physicochemical and Engineering Aspects, 2005. **262**(1): p. 101-112.

215. Jafari, S.M., E. Assadpoor, Y. He, and B. Bhandari, *Re-coalescence of emulsion droplets during high-energy emulsification.* Food Hydrocolloids, 2008. **22**(7): p. 1191-1202.

216. McClements, D.J., *Critical Review of Techniques and Methodologies for Characterization of Emulsion Stability.* Critical Reviews in Food Science and Nutrition, 2007. **47**(7): p. 611-649.

217. Petrovic, L.B., V.J. Sovilj, J.M. Katona, and J.L. Milanovic, *Influence of polymer–surfactant interactions on o/w emulsion properties and microcapsule formation.* Journal of Colloid and Interface Science, 2010. **342**(2): p. 333-339.

218. Karaca, A.C., N. Low, and M. Nickerson, *Emulsifying properties of chickpea, faba bean, lentil and pea proteins produced by isoelectric precipitation and salt extraction.* Food Research International, 2011. **44**(9): p. 2742-2750.

219. Damodaran, S., *Protein Stabilization of Emulsions and Foams.* Journal of Food Science, 2005. **70**(3): p. R54-R66.

220. Atarian, M., A. Rajaei, M. Tabatabaei, A. Mohsenifar, and H. Bodaghi, *Formulation of Pickering sunflower oil-in-water emulsion stabilized by chitosan-stearic acid nanogel and studying its oxidative stability.* Carbohydrate Polymers, 2019. **210**: p. 47-55.

221. McClements, D.J., *Lipid-Based Emulsions and Emulsifiers.* Food Lipids: Chemistry, Nutrition, and Biotechnology. Food Science and Technology 2008. **In Akoh, Casimir C.; Min, David B.**

222. Zahi, M.R., P. Wan, H. Liang, and Q. Yuan, *Formation and Stability of d-Limonene Organogel-Based Nanoemulsion Prepared by a High-Pressure Homogenizer.* Journal of Agricultural and Food Chemistry, 2014. **62**(52): p. 12563-12569.

223. Rueger, P.E. and R.V. Calabrese, *Dispersion of water into oil in a rotor–stator mixer. Part 1: Drop breakup in dilute systems.* Chemical Engineering Research and Design, 2013. **91**(11): p. 2122-2133.

224. Calabrese, R.V., T.P.K. Chang, and P.T. Dang, *Drop breakup in turbulent stirred-tank contactors. Part I: Effect of dispersed-phase viscosity.* AIChE Journal, 1986. **32**(4): p. 657-666.

225. Alliod, O., J.-P. Valour, S. Urbaniak, H. Fessi, D. Dupin, and C. Charcosset, *Preparation of oil-in-water nanoemulsions at large-scale using premix membrane emulsification and Shirasu Porous Glass (SPG) membranes.* Colloids and Surfaces A: Physicochemical and Engineering Aspects, 2018. **557**: p. 76-84.

226. Vladisavljević, G.T., I. Kobayashi, and M. Nakajima, *Production of uniform droplets using membrane, microchannel and microfluidic emulsification devices.* Microfluidics and Nanofluidics, 2012. **13**(1): p. 151-178.

227. Kim, S.-H. and D.A. Weitz, *One-Step Emulsification of Multiple Concentric Shells with Capillary Microfluidic Devices*, ed. A. Chem. 2011: Wiley-VCH Verlag GmbH & Co. KGaA, Weinheim.

228. Nie, Z., M. Seo, S. Xu, P.C. Lewis, M. Mok, E. Kumacheva, G.M. Whitesides, P. Garstecki, and H.A. Stone, *Emulsification in a microfluidic flow-focusing device: effectof the viscosities of the liquids.* Microfluid Nanofluid, 2008. **5**: p. 585-594.

229. van der Graaf, S., M.L.J. Steegmans, R.G.M. van der Sman, C.G.P.H. Schroën, and R.M. Boom, *Droplet formation in a T-shaped microchannel junction: A model system for membrane emulsification.* Colloids and Surfaces A: Physicochemical and Engineering Aspects, 2005. **266**(1): p. 106-116.

230. Hogan, S.A., B.F. McNamee, E.D. O'Riordan, and M. O'Sullivan, *Microencapsulating Properties of Sodium Caseinate.* Journal of Agricultural and Food Chemistry, 2001. **49**(4): p. 1934-1938.

231. Junyaprasert, V.B., A. Mitrevej, N. Sinchaipanid, P. Boonme, and D.E. Wurster, *Effect of Process Variables on the Microencapsulation of Vitamin A Palmitate by Gelatin-Acacia Coacervation.* Drug Development and Industrial Pharmacy, 2001. **27**(6): p. 561-566.

232. Dong, Z.J., A. Touré, C.S. Jia, X.M. Zhang, and S.Y. Xu, *Effect of processing parameters on the formation of spherical multinuclear microcapsules encapsulating peppermint oil by coacervation.* Journal of Microencapsulation, 2007. **24**(7): p. 634-646.

233. Weinbreck, F., M. Minor, and C.G. de Kruif, *Microencapsulation of oils using whey protein/gum arabic coacervates.* Journal of Microencapsulation, 2004. **21**(6): p. 667-679.

234. Tang, C.-H., *Emulsifying properties of soy proteins: A critical review with emphasis on the role of conformational flexibility.* Critical Reviews in Food Science and Nutrition, 2017. **57**(12): p. 2636-2679.

235. Siow, L.-F. and C.-S. Ong, *Effect of pH on Garlic Oil Encapsulation by Complex Coacervation.* Journal of Food Processing & Technology, 2013. **4**(1).

236. Mint, A., J.R. Virgoe, D.V. Palmer, and A.R. Kerr, *N-acetylglucosamine/glucosamine copolymer capsules*, in *UK Patent Applications*, L. Limited, Editor. 2015: GB2542224-A.

237. Holzerny, P., B. Ajdini, W. Heusermann, K. Bruno, M. Schuleit, L. Meinel, and M. Keller, *Biophysical properties of chitosan/siRNA polyplexes: Profiling the polymer/siRNA interactions and bioactivity.* Journal of Controlled Release, 2012. **157**(2): p. 297-304.

238. Baiocco, D., J.A. Preece, and Z. Zhang, *Encapsulation of Hexylsalicylate in an Animal-Free Chitosan-Gum Arabic Shell by Complex Coacervation.* Colloids and Surfaces A: Physicochemical and Engineering Aspects, 2021: p. 126861.

239. Chattopadhyay, D.K. and D.C. Webster, *Thermal stability and flame retardancy of polyurethanes.* Progress in Polymer Science, 2009. **34**(10): p. 1068-1133.

240. Park, S.-J. and H.-C. Kim, *Thermal stability and toughening of epoxy resin with polysulfone resin.* Journal of Polymer Science Part B: Polymer Physics, 2001. **39**(1): p. 121-128.

241. Krone, C.A. and T.D. Klingner, *Isocyanates, polyurethane and childhood asthma.* Pediatric Allergy and Immunology, 2005. **16**(5): p. 368-379.

242. Anvari, M., C.H. Pan, W.B. Yoon, and D. Chung, *Characterization of fish gelatin-gum arabic complex coacervates as influenced by phase separation temperature.* Int J Biol Macromol, 2015. **79**: p. 894-902.

243. Konuklu, Y. and H.O. Paksoy, *The Preparation and Characterization of Chitosan-Gelatin Microcapsules and Microcomposites with Fatty Acids as Thermal Energy Storage Materials.* Energy Technology, 2015. **3**(5): p. 503-508.

244. Cunha, L. and A. Grenha, *Sulfated Seaweed Polysaccharides as Multifunctional Materials in Drug Delivery Applications* Mar. Drugs, 2016. **14**(3): p. 42.

245. McNamee, B.F., E.D. O'Riordan, and M. O'Sullivan, *Emulsification and Microencapsulation Properties of Gum Arabic* J. Agric. Food Chem., 1998. **46**: p. 4551-4555.

246. Kashappa, D.G.H. and H.J. Park, *Recent Developments in Microencapsulation of Food Ingredients.* Drying Technology, 2005. **23**(7): p. 1361-1394.

247. Methacanon, P., M. Prasitsilp, T. Pothsree, and J. Pattaraarchachai, *Heterogeneous N-deacetylation of squid chitin in alkaline solution.* Carbohydrate Polymers, 2003. **52**: p. 119-123.

248. Aye, K.N., R. Karuppuswamy, T. Ahamed, and W.F. Stevens, *Peripheral enzymatic deacetylation of chitin and reprecipitated chitin particles.* Bioresour Technol, 2006. **97**(4): p. 577-82.

249. Jiang, T., R. James, S.G. Kumbar, and C.T. Laurencin, *Chitosan as a Biomaterial*, in *Natural and Synthetic Biomedical Polymers*. 2014. p. 91-113.

250. Hussain, M.R., M. Iman, and T. K. Maji, *Determination of Degree of Deacetylation of Chitosan and Their effect on the Release Behavior of Essential Oil from Chitosan and Chitosan Gelatin Complex Microcapsules.* International Journal of Advanced Engineering Applications, 2013. **2**(4): p. 4-12.

251. Huang, G.-Q., L.-Y. Cheng, J.-X. Xiao, S.-Q. Wang, and X.-N. Han, *Genipin-crosslinked O-carboxymethyl chitosan–gum Arabic coacervate as a pH-sensitive delivery system and microstructure characterization.* Journal of Biomaterials Applications, 2016. **31**(2): p. 193-204.

252. Tolaimate, A., J. Desbrieres, M. Rhazi, and A. Alagui, *Contribution to the preparation of chitins and chitosans with controlled physico-chemical properties.* Polymer International, 2003. **44**(26): p. 7939-7952.

253. Lalani, J. and A. Misra, *Gene Delivery Using Chemical Methods in Challenges in Delivery of Therapeutic Genomics and Proteomics.* 2011.

254. Balázs, N. and P. Sipos, *Limitations of pH-potentiometric titration for the determination of the degree of deacetylation of chitosan.* Carbohydr Res, 2007. **342**(1): p. 124-30.

255. Manigandan, V., R. Karthik, S. Ramachandran, and S. Rajagopal, *Chapter 15 - Chitosan Applications in Food Industry*, in *Biopolymers for Food Design*, A.M. Grumezescu and A.M. Holban, Editors. 2018, Academic Press. p. 469-491.

256. Shariatinia, Z., *Pharmaceutical applications of chitosan.* Advances in Colloid and Interface Science, 2019. **263**: p. 131-194.

257. Muzzarelli, R.A.A., J. Boudrant, D. Meyer, N. Manno, M. DeMarchis, and M.G. Paoletti, *Current views on fungal chitin/chitosan, human chitinases, food preservation, glucans, pectins and inulin: A tribute to Henri Braconnot, precursor of the carbohydrate polymers science, on the chitin bicentennial.* Carbohydrate Polymers, 2012. **87**(2): p. 995-1012.

258. Hofman, D.L., V.J. van Buul, and F.J.P.H. Brouns, *Nutrition, Health, and Regulatory Aspects of Digestible Maltodextrins.* Critical Reviews in Food Science and Nutrition, 2016. **56**(12): p. 2091-2100.

259. Takeiti, C.Y., T.G. Kieckbusch, and F.P. Collares-Queiroz, *Morphological and Physicochemical Characterization of Commercial Maltodextrins with Different Degrees of Dextrose-Equivalent.* International Journal of Food Properties, 2010. **13**(2): p. 411-425.

260. Fetzer, W.R., E.K. Crosby, C.E. Engel, and l.C. Kirst, *Effect of acid and heaton dextrose and dextrose polymers. .* Ind. Eng. Chem., 1953. **45**: p. 1075–1083.

261. Mishra, P., S. Mishra, and C.L. Mahanta, *Effect of maltodextrin concentration and inlet temperature during spray drying on physicochemical and antioxidant properties of amla (Emblica officinalis) juice powder.* Food and Bioproducts Processing, 2014. **92**(3): p. 252-258.

262. Flores, R.J., M.D. Wall, D.W. Carnahan, and T.A. Orofino, *An investigation of internal phase losses during the microencapsulation of fragrances.* Journal of Micro-encapsulation, 1992. **3**: p. 287-307.

263. Lapczynski, A., L. Jones, D. McGinty, S. Bhatia, C.S. Letizia, and A.M. Api, *Fragrance material review on hexyl salicylate.* Food and Chemical Toxicology, 2007. **45**(1, Supplement 1): p. S410-S417.

264. Lapczynski, A., D. McGinty, L. Jones, C.S. Letizia, and A.M. Api, *Fragrance material review on ethyl hexyl salicylate.* Food Chem Toxicol, 2007. **45 Suppl 1**: p. S393-6.

265. Zhang, Z., J.D. Stenson, and C.R. Thomas, *Chapter 2 Micromanipulation in Mechanical Characterisation of Single Particles*, in *Advances in Chemical Engineering*, J. Li, Editor. 2009, Academic Press. p. 29-85.

266. Gray, A., S. Egan, S. Bakalis, and Z. Zhang, *Determination of microcapsule physicochemical, structural, and mechanical properties.* Particuology, 2016. **24**: p. 32-43.

267. de Carvalho, C.C.C.R. and M.M.R. da Fonseca, *Carvone: Why and how should one bother to produce this terpene.* Food Chemistry, 2006. **95**(3): p. 413-422.

268. Morcia, C., G. Tumino, R. Ghizzoni, and V. Terzi, *Chapter 35 - Carvone (Mentha spicata L.) Oils*, in *Essential Oils in Food Preservation, Flavor and Safety*, V.R. Preedy, Editor. 2016, Academic Press: San Diego. p. 309-316.

269. Moghimi, H.R., B. Jamali, S. Farahmand, and B. Shafaghi, *Effect of essential oils, hydrating agents, and ethanol on hair removal efficiency of thioglycolates.* Journal of Cosmetic Dermatology, 2013. **12**(1): p. 41-48.

270. Koo, S.Y., K.H. Cha, D.-G. Song, D. Chung, and C.-H. Pan, *Microencapsulation of peppermint oil in an alginate–pectin matrix using a coaxial electrospray system.* International Journal of Food Science & Technology, 2014. **49**(3): p. 733-739.

271. Alvim, I.D. and C.R.F. Grosso, *Microparticles obtained by complex coacervation: influence of the type of reticulation and the drying process on the release of the core material.* Ciênc. Tecnol. Aliment., Campinas, 2010. **30**(4): p. 1069-1076.

272. Burgess, D.J. and S. Ponsart, *β-Glucuronidase activity following complex coacervation and spray drying microencapsulation.* Journal of Microencapsulation, 1998. **15**(5): p. 569-579.

273. Carocho, M., M.F. Barreiro, P. Morales, and I.C.F.R. Ferreira, *Adding Molecules to Food, Pros and Cons: A Review on Synthetic and Natural Food Additives.* Comprehensive Reviews in Food Science and Food Safety, 2014. **13**(4): p. 377-399.

274. WHO, W.H.O., *Concise International Chemical Assessment Document.* https://apps.who.int/iris/bitstream/handle/10665/330612/9789241210294-eng.pdf, 2019. **Technical Report Series.**: p. Accessed 2020 April.

275. Zhang, Z.-Q., C.-H. Pan, and D. Chung, *Tannic acid cross-linked gelatin–gum arabic coacervate microspheres for sustained release of allyl isothiocyanate: Characterization and in vitro release study.* Food Research International, 2011. **44**(4): p. 1000-1007.

276. Prata, A.S., M.H.A. Zanin, M.I. Ré, and C.R.F. Grosso, *Release properties of chemical and enzymatic crosslinked gelatin-gum Arabic microparticles containing a fluorescent probe plus vetiver essential oil.* Colloids and Surfaces B: Biointerfaces, 2008. **67**(2): p. 171-178.

277. Takigawa, T. and Y. Endo, *Effects of Glutaraldehyde Exposure on Human Health.* Journal of Occupational Health, 2006. **48**(2): p. 75-87.

278. O'Donnell, A., *Chapter 11 - Endodontics in primary teeth*, in *Harty's Endodontics in Clinical Practice (Sixth Edition)*, B.S. Chong, Editor. 2010, Churchill Livingstone. p. 197-207.

279. Rojas-Moreno, S., F. Cárdenas-Bailón, G. Osorio-Revilla, T. Gallardo-Velázquez, and J. Proal-Nájera, *Effects of complex coacervation-spray drying and conventional spray drying on the quality of microencapsulated orange essential oil.* Journal of Food Measurement and Characterization, 2018. **12**(1): p. 650-660.

280. Yang, C.Q., W. Weishu, and D.B. McIlwaine, *Evaluating Glutaraldehyde as a Nonformaldehyde Durable Press Finishing Agent for Cotton Fabrics.* Textile Research Journal, 2000. **70**(3): p. 230-236.

281. Leung, H.-W., *Ecotoxicology of Glutaraldehyde: Review of Environmental Fate and Effects Studies.* Ecotoxicology and Environmental Safety, 2001. **49**(1): p. 26-39.

282. Vandelli, M.A., F. Rivasi, P. Guerra, F. Forni, and R. Arletti, *Gelatin microspheres crosslinked with D,L-glyceraldehyde as a potential drug delivery system: preparation, characterisation, in vitro and in vivo studies.* Int J Pharm, 2001. **215**(1-2): p. 175-84.

283. Bhumkar, D.R. and V.B. Pokharkar, *Studies on Effect of pH on Cross-linking of Chitosan With Sodium Tripolyphosphate: A Technical Not3.* AAPS PharmSciTech, 2006. **7**(2): p. E1-E6.

284. Strauss, G. and S.M. Gibson, *Plant phenolics as cross-linkers of gelatin gels and gelatin-based coacervates for use as food ingredients.* Food Hydrocolloids, 2004. **18**(1): p. 81-89.

285. Peng, C., S.-Q. Zhao, J. Zhang, G.-Y. Huang, L.-Y. Chen, and F.-Y. Zhao, *Chemical composition, antimicrobial property and microencapsulation of Mustard (Sinapis alba) seed essential oil by complex coacervation.* Food Chemistry, 2014. **165**: p. 560-568.

286. Dong, Z.J., S.Q. Xia, S. Hua, K. Hayat, X.M. Zhang, and S.Y. Xu, *Optimization of cross-linking parameters during production of transglutaminase-hardened spherical multinuclear microcapsules by complex coacervation.* Colloids Surf B Biointerfaces, 2008. **63**(1): p. 41-7.

287. Motoki, M. and K. Seguro, *Transglutaminase and its use for food processing.* Trends in Food Science & Technology, 1998. **9**(5): p. 204-210.

288. Grosso, C.R.F., M.H. Zanin, M.I. Ré, and A.S. Prata, *Effect of Glutaraldehyde or Tranglutaminase as Crosslinking Agent in the Release of Coacervated Microparticles.* 2008.

289. Lv, Y., F. Yang, X. Li, X. Zhang, and S. Abbas, *Formation of heat-resistant nanocapsules of jasmine essential oil via gelatin/gum arabic based complex coacervation.* Food Hydrocolloids, 2014. **35**: p. 305-314.

290. Aryanti, N., R. Hou, and R.A. Williams, *Performance of a rotating membrane emulsifier for production of coarse droplets.* Journal of Membrane Science, 2009. **326**(1): p. 9-18.

291. Jono, K., H. Ichikawa, M. Miyamoto, and Y. Fukumori, *A review of particulate design for pharmaceutical powders and their production by spouted bed coating.* Powder Technology, 2000. **113**(3): p. 269-277.

292. Sarkar, A., K.K.T. Goh, and H. Singh, *Colloidal stability and interactions of milk-protein-stabilized emulsions in an artificial saliva.* Food Hydrocolloids, 2009. **23**(5): p. 1270-1278.

293. Malvern Instruments, L., *A basic guide to particle characterization.* Inform White Paper, 2012. **Worcestershire: Malvern Instruments Worldwide.**

294. Nangrejo, M.R., X. Bao, and M.J. Edirisinghe, *Preparation of silicon carbide–silicon nitride composite foams from pre-ceramic polymers.* Journal of the European Ceramic Society, 2000. **20**(11): p. 1777-1785.

295. Ohtsubo, T., S. Tsuda, and K. Tsuji, *A study of the physical strength of fenitrothion microcapsules.* Polymer, 1991. **32**(13): p. 2395-2399.

296. Taguchi, Y., H. Yokoyama, H. Kado, and M. Tanaka, *Preparation of PCM microcapsules by using oil absorbable polymer particles.* Colloids and Surfaces A: Physicochemical and Engineering Aspects, 2007. **301**(1): p. 41-47.

297. Poncelet, D. and R.J. Neufeld, *Shear breakage of nylon membrane microcapsules in a turbine reactor.* Biotechnology and Bioengineering, 1989. **33**(1): p. 95-103.

298. Zhang, W., A. Abbaspourrad, D. Chen, E. Campbell, H. Zhao, Y. Li, Q. Li, and D.A. Weitz, *Osmotic Pressure Triggered Rapid Release of Encapsulated Enzymes with Enhanced Activity.* Advanced Functional Materials, 2017. **27**(29): p. 1700975.

299. Ahearne, M., Y. Yang, and K.-K. Liu, *Mechanical Characterisation of Hydrogels for Tissue Engineering Applications.* Topics in Tissue Engineering, 2008. **4**.

300. Tan, Y., D. Sun, W. Huang, and S.H. Cheng, *Mechanical Modeling of Biological Cells in Microinjection.* IEEE Transactions on NanoBioscience, 2008. **7**(4): p. 257-266.

301. Dols-Perez, A., V. Marin, G.J. Amador, R. Kieffer, D. Tam, and M.-E. Aubin-Tam, *Artificial Cell Membranes Interfaced with Optical Tweezers: A Versatile Microfluidics Platform for Nanomanipulation and Mechanical Characterization.* ACS Applied Materials & Interfaces, 2019. **11**(37): p. 33620-33627.

302. Lefebvre, Y., E. Leclerc, D. Barthès-Biesel, J. Walter, and F. Edwards-Lévy, *Flow of artificial microcapsules in microfluidic channels: A method for determining the elastic properties of the membrane.* Physics of Fluids, 2008. **20**(12): p. 123102.

303. Corbin , E.A., F. Kong, C. Teck Lim, W. P. King, and R. Bashir, *Biophysical properties of human breast cancercells measured using silicon MEMS resonatorsand atomic force microscopy.* Lab Chip, 2015. **15**(839).

304. Hochmuth, R.M., *Micropipette aspiration of living cells.* Journal of Biomechanics, 2000. **33**(1): p. 15-22.

305. Fiddes, L.K., H.K.C. Chan, K. Wyss, C.A. Simmons, E. Kumacheva, and A.R. Wheeler, *Augmenting microgel flowviareceptor-ligand binding in the constrainedgeometries of microchannels.* Lab Chip,, 2009. **9**: p. 286-290.

306. Gugerli, R., E. Cantana, C. Heinzen, U.v. Stockar, and I.W. Marison, *Quantitative study of the production and properties of alginate/poly-L-lysine microcapsules.* Journal of Microencapsulation, 2002. **19**(5): p. 571-590.

307. Rosiñski, S., G. Grigorescu, D. Lewiñska, L.G. Ritzén, H. Viernstein, E. Teunou, D. Poncelet, Z. Zhang, X. Fan, D. Serp, I. Marison, and D. Hunkeler, *Characterization of microcapsules: recommended methods based on round-robin testing.* Journal of Microencapsulation, 2002. **19**(5): p. 641-659.

308. Ducker, W.A., T.J. Senden, and R.M. Pashley, *Direct measurement of colloidal forces using an atomic force microscope.* Nature, 1991. **353**(6341): p. 239-241.

309. Fery, A. and R. Weinkamer, *Mechanical properties of micro- and nanocapsules: Single-capsule measurements.* Polymer, 2007. **48**(25): p. 7221-7235.

310. Nguyen, A.V., J. Nalaskowski, J.D. Miller, and H.-J. Butt, *Attraction between hydrophobic surfaces studied by atomic force microscopy.* International Journal of Mineral Processing, 2003. **72**(1): p. 215-225.

311. Lulevich, V.V., I.L. Radtchenko, G.B. Sukhorukov, and O.I. Vinogradova, *Mechanical Properties of Polyelectrolyte Microcapsules Filled with a Neutral Polymer.* Macromolecules, 2003. **36**(8): p. 2832-2837.

312. Dubreuil, F., N. Elsner, and A. Fery, *Elastic properties of polyelectrolyte capsules studied by atomic-force microscopy and RICM.* The European Physical Journal E, 2003. **12**(2): p. 215-221.

313. Rahmat, A., J. Meng, D.R. Emerson, C.-Y. Wu, M. Barigou, and A. Alexiadis, *A practical approach for extracting mechanical properties of microcapsules using a hybrid numerical model.* Microfluidics and Nanofluidics, 2020. **25**(1): p. 1.

314. Zhang, Z., R. Saunders, and C.R. Thomas, *Mechanical strength of single microcapsules determined by a novel micromanipulation technique.* Journal of microencapsulation, 1999. **16**(1): p. 117-124.

315. Liu, T. and Z. Zhang, *Mechanical properties of desiccated ragweed pollen grains determined by micromanipulation and theoretical modelling.* Biotechnology and Bioengineering, 2004. **85**(7): p. 770-775.

316. Chung, J.T., K.D.F. Vlugt-Wensink, W.E. Hennink, and Z. Zhang, *Effect of polymerization conditions on the network properties of dex-HEMA microspheres and macro-hydrogels.* International Journal of Pharmaceutics, 2005. **288**(1): p. 51-61.

317. Yap, S.F., M.J. Adams, J.P.K. Seville, and Z. Zhang, *Single and bulk compression of pharmaceutical excipients: Evaluation of mechanical properties.* Powder Technology, 2008. **185**(1): p. 1-10.

318. Zhang, Z., J.M. Blewett, and C.R. Thomas, *Modelling the effect of osmolality on the bursting strength of yeast cells.* Journal of Biotechnology, 1999. **71**(1): p. 17-24.

319. Zhang, Z., M.A. Ferenczi, A.C. Lush, and C.R. Thomas, *A novel micromanipulation technique for measuring the bursting strength of single mammalian cells.* Applied Microbiology and Biotechnology, 1991. **36**(2): p. 208-210.

320. Liao, Q., J. Huang, T. Zhu, C. Xiong, and J. Fang, *A hybrid model to determine mechanical properties of soft polymers by nanoindentation.* Mechanics of Materials, 2010. **42**(12): p. 1043-1047.

321. Liu, T., A.M. Donald, and Z. Zhang, *Novel manipulation in environmental scanning electron microscope for measuring mechanical properties of single nanoparticles.* Materials Science and Technology, 2005. **21**(3): p. 289-294.

322. Dintwa, E., E. Tijskens, and H. Ramon, *On the accuracy of the Hertz model to describe the normalcontact of soft elastic spheres.* Granular Matter, 2008. **10**: p. 209–221.

323. Hertz, H., Miscellaneous Papers, 1896. **92,156**.

324. Ding, P., I.T. Norton, Z. Zhang, and A.W. Pacek, *Mechanical properties of gelatin-rich micro-particles.* Journal of Food Engineering, 2008. **86**(3): p. 307-314.

325. Tatara, Y., *On Compression of Rubber Elastic Sphere Over a Large Range of Displacements—Part 1: Theoretical Study.* Journal of Engineering Materials and Technology, 1991. **113**(3): p. 285-291.

326. Liu, K.K., D.R. Williams, and B.J. Briscoe, *The large deformation of a single micro-elastomeric sphere.* Journal of Physics D: Applied Physics, 1998. **31**(3): p. 294-303.

327. Yan, Y., Z. Zhang, J.R. Stokes, Q.-Z. Zhou, G.-H. Ma, and M.J. Adams, *Mechanical characterization of agarose micro-particles with a narrow size distribution.* Powder Technology, 2009. **192**(1): p. 122-130.

328. Feng, W.W. and W.H. Yang, *On the Contact Problem of an Inflated Spherical Nonlinear Membrane.* Journal of Applied Mechanics, 1973. **40**(1): p. 209-214.

329. Lardner, T.J. and P. Pujara, *XII - Compression of Spherical Cells*, in *Mechanics Today*, S. Nemat-Nasser, Editor. 1980, Pergamon. p. 161-176.

330. Liu, K.K., D.R. Williams, and B.J. Briscoe, *Compressive deformation of a single microcapsule.* Physical Review E, 1996. **54**(6): p. 6673-6680.

331. Nguyen, V.B., C.X. Wang, C.R. Thomas, and Z. Zhang, *Mechanical properties of single alginate microspheres determined by microcompression and finite element modelling.* Chemical Engineering Science, 2009. **64**(5): p. 821-829.

332. Yuan, L., A. Gu, and G. Liang, *Preparation and properties of poly(urea–formaldehyde) microcapsules filled with epoxy resins.* Materials Chemistry and Physics, 2008. **110**(2): p. 417-425.

333. Torras, C., L. Pitol-Filho, and R. Garcia-Valls, *Two methods for morphological characterization of internal microcapsule structures.* Journal of Membrane Science, 2007. **305**(1): p. 1-4.

334. Sohail, T., T. Tang, and B. Nadler, *Adhesive contact of a fluid-filled membrane driven by electrostatic forces.* International Journal of Solids and Structures, 2013. **50**(16): p. 2678-2690.

335. Ungai-Salánki, R., B. Peter, T. Gerecsei, N. Orgovan, R. Horvath, and B. Szabó, *A practical review on the measurement tools for cellular adhesion force.* Advances in Colloid and Interface Science, 2019. **269**: p. 309-333.

336. Bradley, R.S., *LXXIX. The cohesive force between solid surfaces and the surface energy of solids.* The London, Edinburgh, and Dublin Philosophical Magazine and Journal of Science, 1932. **13**(86): p. 853-862.

337. Johnson, K.L., K. Kendall, A.D. Roberts, and D. Tabor, *Surface energy and the contact of elastic solids.* Proceedings of the Royal Society of London. A. Mathematical and Physical Sciences, 1971. **324**(1558): p. 301-313.

338. Derjaguin, B.V., V.M. Muller, and Y.P. Toporov, *Effect of contact deformations on the adhesion of particles.* Journal of Colloid and Interface Science, 1975. **53**(2): p. 314-326.

339. Tabor, D., *Surface Forces and Surface Interactions*, in *Plenary and Invited Lectures*, M. Kerker, A.C. Zettlemoyer, and R.L. Rowell, Editors. 1977, Academic Press. p. 3-14.

340. Maugis, D., *Adhesion of spheres: The JKR-DMT transition using a dugdale model.* Journal of Colloid and Interface Science, 1992. **150**(1): p. 243-269.

341. Guillemot, G., S. Lorthois, P. Schmitz, and M. Mercier-Bonin, *Evaluating the Adhesion Force Between Saccharomyces Cerevisiae Yeast Cells and Polystyrene From Shear-Flow Induced Detachment Experiments.* Chemical Engineering Research and Design, 2007. **85**(6): p. 800-807.

342. Pierres, A., A.-M. Benoliel, and P. Bongrand, *Studying Molecular Interactions at the Single Bond Level with a Laminar Flow Chamber.* Cellular and Molecular Bioengineering, 2008. **1**(4): p. 247-262.

343. Varun, T.K., S. Senani, N. Jayapal, J. Chikkerur, S. Roy, V.B. Tekulapally, M. Gautam, and N. Kumar, *Extraction of chitosan and its oligomers from shrimp shell waste, their characterization and antimicrobial effect.* Veterinary world, 2017. **10**(2): p. 170-175.

344. Chang, Q., *Colloid and interface Chemistry for water quality control. Emulsion, Foam, and Gel. .* Academic Press, Inc., 2016: p. 227-245.

345. Poon, W.C.K., E.R. Weeks, and C.P. Royall, *On measuring colloidal volume fractions.* Soft Matter, 2012. **8**(1): p. 21-30.

346. Maji, T.K., I. Baruah, S. Dube, and M.R. Hussain, *Microencapsulation of Zanthoxylum limonella oil (ZLO) in glutaraldehyde crosslinked gelatin for mosquito repellent application.* Bioresource Technology, 2007. **98**(4): p. 840-844.

347. Keasler, V., R.M. De Paula, G. Nilsen, L. Grunwald, and T.J. Tidwell, *23 - Biocides overview and applications in petroleum microbiology*, in *Trends in Oil and Gas Corrosion Research and Technologies*, A.M. El-Sherik, Editor. 2017, Woodhead Publishing: Boston. p. 539-562.

348. Kieliszek, M. and A. Misiewicz, *Microbial transglutaminase and its application in the food industry. A review.* Folia Microbiologica, 2014. **59**(3): p. 241-250.

349. Ho, M.L., S.Z. Leu, J.F. Hsieh, and S.T. Jiang, *Technical Approach to Simplify the Purification Method and Characterization of Microbial Transglutaminase Produced from Streptoverticillium ladakanum.* Journal of Food Science, 2000. **65**(1): p. 76-80.

350. Shi, Y.-G., L. Qian, N. Zhang, C.-R. Han, Y. Liu, Y.-F. Zhang, and Y.-Q. Ma, *Changes in morphology and activity of transglutaminase following cross-linking and immobilization on a polypropylene microporous membrane.* Molecules (Basel, Switzerland), 2011. **16**(12): p. 10046-10058.

351. Clogston, J.D. and A.K. Patri, *Zeta Potential Measurement*, in *Characterization of Nanoparticles Intended for Drug Delivery*, S.E. McNeil, Editor. 2011, Humana Press: Totowa, NJ. p. 63-70.

352. Miller, J.F., *Determination of Protein Charge in Aqueous Solution Using Electrophoretic Light Scattering: A Critical Investigation of the Theoretical Fundamentals and Experimental Methodologies.* Langmuir, 2020. **36**(29): p. 8641-8654.

353. Baiocco, D., J.A. Preece, and Z. Zhang, *Microcapsules with a Fungal Chitosan-gum Arabic-maltodextrin Shell to Encapsulate Health-Beneficial Peppermint Oil.* Food Hydrocolloids for Health, 2021: p. 100016.

354. Song, M.-G., S.-H. Cho, J.-Y. Kim, and J.-D. Kim, *Novel evaluation method for the water- in- oil (W/O) emulsion stability by Turbidity Ratio Measurements.* Korean Journal of Chemical Engineering, 2002. **19**(3): p. 425-430.

355. Hills, A.E., *Spectroscopy in Biotechnology Research and Development*, in *Encyclopedia of Spectroscopy and Spectrometry (Third Edition)*, J.C. Lindon, G.E. Tranter, and D.W. Koppenaal, Editors. 2017, Academic Press: Oxford. p. 198-202.

356. Ren, Y.L., A.M. Donald, and Z. Zhang, *Investigation of radiation damage to microcapsules in environmental SEM.* Materials Science and Technology, 2007. **23**(7): p. 857-864.

357. Kumar, C.S.S.R., *Transmission Electron Microscopy Characterization of Nanomaterials.* Springer, 2013. **New York**.

358. Lane, W.O., A.E. Jantzen, T.A. Carlon, R.M. Jamiolkowski, J.E. Grenet, Ley, M., , M. Haseltine, Galinat, l. l. J., f.-h., , J.D. Allen, g.A. Truskey, and E. Achneck, *Parallel-plate Flow Chamber and Continuous Flow Circuit to Evaluate Endothelial Progenitor Cells under Laminar Flow Shear Stress.* Journal of Visualised Experiment, 2012. **(59) 3349**.

359. Kim, H. and D.J. Burgess, *Prediction of Interfacial Tension between Oil Mixtures and Water.* Journal of Colloid and Interface Science, 2001. **241**(2): p. 509-513.

360. Bagalkot, N., A.A. Hamouda, and O.M. Isdahl, *Dynamic interfacial tension measurement method using axisymmetric drop shape analysis.* MethodsX, 2018. **5**: p. 676-683.

361. Semenova, M.G., *Thermodynamic analysis of the impact of molecular interactions on the functionality of food biopolymers in solution and in colloidal systems.* Food Hydrocolloids, 2007. **21**(1): p. 23-45.

362. Walstra, P., *Physical chemistry of food.* Polymers, 2004. **New York-Basel: Marcel Dekker, Inc.**: p. 179-187.

363. Luzzi, L.A. and R.J. Gerraughty, *Effects of selected variables on the extractability of oils from coacervate capsules.* Journal of Pharmaceutical Sciences, 1964. **53**(4): p. 429-431.

364. Lee, A.-C. and Y.-H. Hong, *Coacervate formation of α-lactalbumin–chitosan and β-lactoglobulin–chitosan complexes.* Food Research International, 2009. **42**(5): p. 733-738.

365. Gulão, E.d.S., C.J.F. de Souza, C.T. Andrade, and E.E. Garcia-Rojas, *Complex coacervates obtained from peptide leucine and gum arabic: Formation and characterization.* Food Chemistry, 2016. **194**: p. 680-686.

366. Mano, J.F., G. Hungerford, and J.L. Gómez Ribelles, *Bioactive poly(L-lactic acid)-chitosan hybrid scaffolds.* Materials Science and Engineering: C, 2008. **28**(8): p. 1356-1365.

367. Claesson, P.M. and B.W. Ninham, *pH-dependent interactions between adsorbed chitosan layers.* Langmuir, 1992. **8**(5): p. 1406-1412.

368. Padmanabhan, A. and L.S. Nair, *Chitosan hydrogels for regenerative engineering.* In: Dutta P. K, editor. Chitin and Chitosan for Regenerative Medicine, 2016. **New Delhi: Springers**: p. 3-40.

369. Matusiak, J., E. Grządka, and A. Bastrzyk, *Stability, adsorption and electrokinetic properties of the chitosan/silica system.* Colloids and Surfaces A: Physicochemical and Engineering Aspects, 2018. **554**: p. 245-252.

370. Atgié, M., O. Masbernat, and K. Roger, *Emulsions Stabilized by Gum Arabic: Composition and Packing within Interfacial Films.* Langmuir, 2019. **35**(4): p. 962-972.

371. Dong, D. and Y. Hua, *Glycinin-gum arabic complex formation: Turbidity measurement and charge neutralization analysis.* Food Research International, 2016. **89**: p. 709-715.

372. Jiménez-Alvarado, R.B., C. I.; Medina-Torres, L.; Román-Guerrero, A.; Vernon-Carter, E. J., *Ferrous bisglycinate content and release in W1/O/W2 multiple emulsions stabilized by protein–polysaccharide complexes.* Food Hydrocolloids, 2009. **23**(8): p. 2425-2433.

373. Vuillemin, M.E., F. Michaux, L. Muniglia, M. Linder, and J. Jasniewski, *Gum Arabic and chitosan self-assembly: Thermodynamic and mechanism aspects.* Food Hydrocolloids, 2019. **96**: p. 463-474.

374. Lechevallier, M.W., Evans T. M. , and J.S. Ramon, *Effect of Turbidity on Chlorination Efficiency and Bacterial Persistence in Drinking Water.* Applied and Environmental Microbiology, 1981. **42**(1): p. 159-167.

375. Davies-Colley, R.J. and D.G. Smith, *Turbidity Suspended Sediment and Water Clarity: a review.* Journal of the American Water Resources Association, 2001. **37**(5): p. 1085-1101.

376. Geng, X., O.-H. Kwon, and J. Jang, *Electrospinning of chitosan dissolved in concentrated acetic acid solution.* Biomaterials, 2005. **26**(27): p. 5427-5432.

377. Hudson, S.M. and D.W. Jenkins, *Chitin and Chitosan*. 2001, Encyclopedia of Polymer Science and Technology.

378. Sogias, I.A., V.V. Khutoryanskiy, and A.C. Williams, *Exploring the Factors Affecting the Solubility of Chitosan in Water.* Macromolecular Chemistry and Physics, 2010. **211**(4): p. 426-433.

379. Lee, D.W., C. Lim, J.N. Israelachvili, and D.S. Hwang, *Strong Adhesion and Cohesion of Chitosan in Aqueous Solutions.* Langmuir, 2013. **29**(46): p. 14222-14229.

380. Kuck, L.S. and C.P.Z. Noreña, *Microencapsulation of grape (Vitis labrusca var. Bordo) skin phenolic extract using gum Arabic, polydextrose, and partially hydrolyzed guar gum as encapsulating agents.* Food Chemistry, 2016. **194**: p. 569-576.

381. Li, Q.-x., B.-z. Song, Z.-q. Yang, and H.-l. Fan, *Electrolytic conductivity behaviors and solution conformations of chitosan in different acid solutions.* Carbohydrate Polymers, 2006. **63**(2): p. 272-282.

382. Espinosa-Andrews, H., O. Sandoval-Castilla, H. Vázquez-Torres, E.J. Vernon-Carter, and C. Lobato-Calleros, *Determination of the gum Arabic–chitosan interactions by Fourier Transform Infrared Spectroscopy and characterization of the microstructure and rheological features of their coacervates.* Carbohydrate Polymers, 2010. **79**(3): p. 541-546.

383. Xue, J. and Z. Zhang, *Preparation and characterization of calcium-shellac spheres as a carrier of carbamide peroxide.* Journal of Microencapsulation, 2008. **25**(8): p. 523-530.

384. HLB, M.o., *The HLB System: a time-saving guide to emulsifier selection.* ICI Americas Inc., 1980. **Anticipating Needs, 19897**.

385. Chang, Q., *Chapter 11 - Emulsion, Foam, and Gel*, in *Colloid and Interface Chemistry for Water Quality Control*, Q. Chang, Editor. 2016, Academic Press. p. 227-245.

386. Schroën, K., J. de Ruiter, and C. Berton-Carabin, *The Importance of Interfacial Tension in Emulsification: Connecting Scaling Relations Used in Large Scale Preparation with Microfluidic Measurement Methods.* ChemEngineering, 2020. **4**(4).

387. Ibrahim, V., *Phase Behavior of Some Nonionics: Interfacial Tension and HLB at Optimum Conditions.* Petroleum Science and Technology, 2008. **26**(16): p. 1963-1976.

388. Reddy, S.R. and H.S. Fogler, *Emulsion stability: Delineation of different particle loss mechanisms.* Journal of Colloid and Interface Science, 1981. **79**(1): p. 105-113.

389. Lee, M.-H., C.Y. Tai, and C.-H. Lu, *Synthesis of spherical zirconia by reverse emulsion precipitation.* Korean Journal of Chemical Engineering, 1999. **16**(6): p. 818-822.

390. Mehmood, T. and A. Ahmed, *Tween 80 and Soya-Lecithin-Based Food-Grade Nanoemulsions for the Effective Delivery of Vitamin D.* Langmuir, 2020. **36**(11): p. 2886-2892.

391. Goff, H.D.L., M.; Jordan, W. K.; and Kinsella, J. E. , *The Effects of Polysorbate 80 on the Fat Emulsion in Ice Cream Mix: Evidence from Transmission Electron Microscopy Studies.* Food Structure:, 1987. **6:2**: p. 193-198.

392. Farshchi, A., A. Hassanpour, and A.E. Bayly, *The structure of spray-dried detergent powders.* Powder Technology, 2019. **355**: p. 738-754.

393. Qian, F., F. Cui, J. Ding, C. Tang, and C. Yin, *Chitosan Graft Copolymer Nanoparticles for Oral Protein Drug Delivery: Preparation and Characterization.* Biomacromolecules, 2006. **7**(10): p. 2722-2727.

394. Colthup, N.B., L.H. Daly, and S.E. & Wiberley, *Introduction to infrared and Raman spectroscopy.* Academic Press, Inc., 1990. **3rd ed.** : p. 319.

395. Alvarez-Ros, M.C., S. Sánchez-Cortés, and J.V. García-Ramos, *Vibrational study of the salicylate interaction with metallic ions and surfaces.* Spectrochimica Acta Part A: Molecular and Biomolecular Spectroscopy, 2000. **56**(12): p. 2471-2477.

396. Smith, B.C., *The C=O bond, Part VII: Aromatic Esters, Organic Carbonates, and more of the rule of three,.* Spectroscopy, 2018. **33**(9): p. 24-28.

397. Kildeeva, N.R., P.A. Perminov, L.V. Vladimirov, V.V. Novikov, and S.N. Mikhailov, *About mechanism of chitosan cross-linking with glutaraldehyde.* Russian Journal of Bioorganic Chemistry, 2009. **35**(3): p. 360-369.

398. Dompé, M., F.J. Cedano-Serrano, M. Vahdati, L. van Westerveld, D. Hourdet, C. Creton, J. van der Gucht, T. Kodger, and M. Kamperman, *Underwater Adhesion of Multiresponsive Complex Coacervates.* Advanced Materials Interfaces, 2020. **7**(4): p. 1901785.

399. Overbeek, J.T.G. and M.J. Voorn, *Phase separation in polyelectrolyte solutions. Theory of complex coacervation.* Journal of Cellular and Comparative Physiology, 1957. **49**(S1): p. 7-26.

400. Yap, S.F., M. Adams, J. Seville, and Z. Zhang, *Understanding the Mechanical Properties of Single Micro-particles and their Compaction Behaviour.* China PARTICUOLOGY, 2006. **04**(01): p. 35-40.

401. Zhang, Z., *Mechanical strength of single microcapsules determined by a novel micromanipulation technique.* Journal of Microencapsulation, 1999. **16**(1): p. 117-124.

402. McNeil, I., *An Encyclopedia of the History of Technology.* Taylor & Francis., 2002.

403. Showell, M., *Powdered detergents.* CRC Press., 1997.

404. Bajpai, D., *Laundry detergents: an overview.* Journal of Oleo Science, 2007. **56**: p. 327-340.

405. Katayama, M. and R. Sugihara, *Which type of washing machine should you choose?* International Journal of Consumer Studies, 2011. **35**(2): p. 237-242.

406. Lee, A., M.H. Seo, S. Yang, J. Koh, and H. Kim, *The effects of mechanical actions on washing efficiency.* Fibers and Polymers, 2008. **9**(1): p. 101-106.

407. Kissa, E., *Kinetics of Oily Soil Release.* Textile Research Journal, 1971. **41**(9): p. 760-767.

408. Kaur, R., D. Kukkar, S.K. Bhardwaj, K.-H. Kim, and A. Deep, *Potential use of polymers and their complexes as media for storage and delivery of fragrances.* Journal of Controlled Release, 2018. **285**: p. 81-95.

409. Quellet, C., M. Schudel, and R. Ringgenberg, International Journal for Chemistry, 2001. **55**(5): p. 421-428.

410. Meyer, E.E., K.J. Rosenberg, and J. Israelachvili, *Recent progress in understanding hydrophobic interactions.* Proceedings of the National Academy of Sciences, 2006. **103**(43): p. 15739.

411. Pezzini, J., G. Joucla, R. Gantier, M. Toueille, A.-M. Lomenech, C. Le Sénéchal, B. Garbay, X. Santarelli, and C. Cabanne, *Antibody capture by mixed-mode chromatography: A comprehensive study from determination of optimal purification conditions to identification of contaminating host cell proteins.* Journal of Chromatography A, 2011. **1218**(45): p. 8197-8208.

412. Hamadi, F., H. Latrache, M. Mabrrouki, A. Elghmari, A. Outzourhit, M. Ellouali, and A. Chtaini, *Effect of pH on distribution and adhesion of Staphylococcus aureus to glass.* Journal of Adhesion Science and Technology, 2005. **19**(1): p. 73-85.

413. Giesbers, M., J.M. Kleijn, and M.A. Cohen Stuart, *Interactions between Acid- and Base-Functionalized Surfaces.* Journal of Colloid and Interface Science, 2002. **252**(1): p. 138-148.

414. Jasmee, S., G. Omar, A.B. Masripan, A.A. Kamarolzaman, A.S. Ashikin, and F.C. Ani, *Hydrophobicity performance of polyethylene terephthalate (PET) and thermoplastic polyurethane (TPU) with thermal effect.* Materials Research Express, 2018. **5**(9).

415. Silverstein, T.P., *The Real Reason Why Oil and Water Don't Mix.* Journal of Chemical Education, 1998. **75**(1): p. 116.

416. Kinner, J.A. and W.A. Moats, *Effect of Temperature, pH, and Detergent on Survival of Bacteria Associated with Shell Eggs.* Poultry Science, 1981. **60**(4): p. 761-767.

417. Liu, S., *Understanding Molecular Interactions to Enhance Deposition of Perfume Microcapsules on Fabric Surfaces*, in *School of Chemical Engineering*. 2018, University of Birmingham: Birmingham.

418. Harada, Y.U., P. Lekcharoensuk, T. Furuta, and T. Taniguchi, *Inactivation of Foot-and-Mouth Disease Virus by Commercially Available Disinfectants and Cleaners.* Biocontrol Science, 2015. **20**(3): p. 205-208.

419. Göbel, H., A. Heinze, K. Heinze-Kuhn, A. Göbel, and C. Göbel, *Peppermint oil in the acute treatment of tension-type headache.* Schmerz (Berlin, Germany), 2016. **30**(3): p. 295-310.

420. Papathanasopoulos, A., A. Rotondo, P. Janssen, W. Boesmans, R. Farré, P. Vanden Berghe, and J. Tack, *Effect of acute peppermint oil administration on gastric sensorimotor function and nutrient tolerance in health.* Neurogastroenterology & Motility, 2013. **25**(4): p. e263-e271.

421. Carocho, M., P. Morales, and I.C.F.R. Ferreira, *Natural food additives: Quo vadis?* Trends in Food Science & Technology, 2015. **45**(2): p. 284-295.

422. Campêlo, M.C.S., J.M.S. Medeiros, and J.B.A. Silva, *Natural products in food preservation.* International Food Research Journal, 2019. **26**(1): p. 41-46.

423. Bakkali, F., S. Averbeck, D. Averbeck, and M. Idaomar, *Biological effects of essential oils – A review.* Food and Chemical Toxicology, 2008. **46**(2): p. 446-475.

424. Alvarenga Botrel, D., S. Vilela Borges, R. Victória de Barros Fernandes, A. Dantas Viana, J. Maria Gomes da Costa, and G. Reginaldo Marques, *Evaluation of spray drying conditions on properties of microencapsulated oregano essential oil.* International Journal of Food Science & Technology, 2012. **47**(11): p. 2289-2296.

425. Fernandes, R.V.d.B., S.V. Borges, D.A. Botrel, E.K. Silva, J.M.G.d. Costa, and F. Queiroz, *Microencapsulation of Rosemary Essential Oil: Characterization of Particles.* Drying Technology, 2013. **31**(11): p. 1245-1254.

426. Geiger, J.L., *The essential oil of ginger, Zingiber officinale, and anaesthesia.* International Journal of Aromatherapy, 2005. **15**(1): p. 7-14.

427. Bertuzzi, G., B. Tirillini, P. Angelini, and R. Venanzoni, *Antioxidative Action of Citrus limonum Essential Oil on Skin.* European Journal of Medicinal Plants,, 2012. **3(1)**(1): p. 1-9.

428. Cui, H., W. Li, C. Li, S. Vittayapadung, and L. Lin, *Liposome containing cinnamon oil with antibacterial activity against methicillin-resistant Staphylococcus aureus biofilm.* Biofouling, 2016. **32**(2): p. 215-225.

429. Busso, C.C., C. Schebor, M.C. Zamora, and C. Jorgea, *Glass transition temperatures and some physical and sensory changes in stored spray-dried encapsulated flavors.* Swiss Society of Food Science and Technology, 2007. **40**(10): p. 1792-1797.

430. Gibbs, B.F., S. Kermasha, I. Alli, and C.N. Mulligan, *Encapsulation in the food industry: a review.* International Journal of Food Sciences and Nutrition, 1999. **50**(3): p. 213-224.

431. Hecht, J.P. and C.J. King, *Spray Drying: Influence of Developing Drop Morphology on Drying Rates and Retention of Volatile Substances. 2. Modeling.* Industrial & Engineering Chemistry Research, 2000. **39**(6): p. 1766-1774.

432. Tavares, L. and C.P. Zapata Noreña, *Encapsulation of garlic extract using complex coacervation with whey protein isolate and chitosan as wall materials followed by spray drying.* Food Hydrocolloids, 2019. **89**: p. 360-369.

433. Rojas-Moreno, S., F. Cárdenas-Bailón, G. Osorio-Revilla, T. Gallardo-Velazquez, and J. Proal-Nájera, *Effects of complex coacervation-spray drying and conventional spray drying on the quality of microencapsulated orange essential oil*. Vol. 12. 2017. 1-11.

434. Arrañeta, E., S. Stewart, M. Ervine, R. Al-Kasasbeh, and R.F. Donnelly, *Hydrogels for Hydrophobic Drug Delivery. Classification, Synthesis and Applications.* J. Funct. Biomater., 2018. **9**(13): p. 1-20.

435. Sarker, B., D.G. Papageorgiou, R. Silva, T. Zehnder, F. Gul-E-Noor, M. Bertmer, J. Kaschta, K. Chrissafis, R. Detsch, and A.R. Boccaccini, *Fabrication of alginate–gelatin crosslinked hydrogel microcapsules and evaluation of the microstructure and physico-chemical properties.* Journal of Materials Chemistry B, 2014. **2**(11): p. 1470-1482.

436. Ma, M., A. Chiu, G. Sahay, J.C. Doloff, N. Dholakia, R. Thakrar, J. Cohen, A. Vegas, D. Chen, K.M. Bratlie, T. Dang, R.L. York, J. Hollister-Lock, G.C. Weir, and D.G. Anderson, *Core–Shell Hydrogel Microcapsules for Improved Islets Encapsulation.* Advanced Healthcare Materials, 2013. **2**(5): p. 667-672.

437. Syed, I., S. Garg, and P. Sarkar, *5 - Entrapment of essential oils in hydrogels for biomedical applications*, in *Polymeric Gels*, K. Pal and I. Banerjee, Editors. 2018, Woodhead Publishing. p. 125-141.

438. Jafari, S.M., E. Assadpoor, B. Bhandari, and Y. He, *Nano-particle encapsulation of fish oil by spray drying.* Food Research International, 2008. **41**(2): p. 172-183.

439. Bylaitë, E., P. Rimantas Venskutonis, and R. Maþdþierienë, *Properties of caraway (Carum carvi L.) essential oil encapsulated into milk protein-based matrices.* European Food Research and Technology, 2001. **212**(6): p. 661-670.

440. Li, Y., L. Ai, W. Yokoyama, C.F. Shoemaker, D. Wei, J. Ma, and F. Zhong, *Properties of Chitosan-Microencapsulated Orange Oil Prepared by Spray-Drying and Its Stability to Detergents.* Journal of Agricultural and Food Chemistry, 2013. **61**(13): p. 3311-3319.

441. Reitsema, R.H. and F.J. Cramer, *OXIDATION OF PEPPERMINT OIL.* Industrial & Engineering Chemistry, 1952. **44**(1): p. 176-180.

442. Shen, Q. and S.Y. Quek, *Microencapsulation of astaxanthin with blends of milk protein and fiber by spray drying.* Journal of Food Engineering, 2014. **123**: p. 165-171.

443. Hategekimana, J., K.G. Masamba, J. Ma, and F. Zhong, *Encapsulation of vitamin E: Effect of physicochemical properties of wall material on retention and stability.* Carbohydrate Polymers, 2015. **124**: p. 172-179.

444. Klaschka, U., *Natural personal care products—analysis of ingredient lists and legal situation.* Environmental Sciences Europe, 2016. **28**(1): p. 8.

445. Hahn, G.S., *Strontium Is a Potent and Selective Inhibitor of Sensory Irritation.* Dermatologic Surgery, 1999. **25**(9): p. 689-694.

446. Antipov, A.A., G.B. Sukhorukov, and H. Möhwald, *Influence of the Ionic Strength on the Polyelectrolyte Multilayers' Permeability.* Langmuir, 2003. **19**(6): p. 2444-2448.

447. Mishra, P., U. Singh, C.M. Pandey, P. Mishra, and G. Pandey, *Application of student's t-test, analysis of variance, and covariance.* Annals of cardiac anaesthesia, 2019. **22**(4): p. 407-411.

448. Pretzl, M., M. Neubauer, M. Tekaat, C. Kunert, C. Kuttner, G. Leon, D. Berthier, P. Erni, L. Ouali, and A. Fery, *Formation and Mechanical Characterization of*

Aminoplast Core/Shell Microcapsules. ACS Applied Materials & Interfaces, 2012. **4**(6): p. 2940-2948.

449. Sarrazin, B., N. Tsapis, L. Mousnier, N. Taulier, W. Urbach, and P. Guenoun, *AFM Investigation of Liquid-Filled Polymer Microcapsules Elasticity.* Langmuir, 2016. **32**(18): p. 4610-4618.

450. Tan, S., S. Mettu, M.D. Biviano, M. Zhou, B. Babgi, J. White, R.R. Dagastine, and M. Ashokkumar, *Ultrasonic synthesis of stable oil filled microcapsules using thiolated chitosan and their characterization by AFM and numerical simulations.* Soft Matter, 2016. **12**: p. 7212-7222.

451. Long, Y., B. Vincent, D. York, Z. Zhang, and J.A. Preece, *Organic-inorganic double shell composite microcapsules.* Chem Commun (Camb), 2010. **46**(10): p. 1718-20.

452. Mokhtarani, B., A. Sharifi, H.R. Mortaheb, M. Mirzaei, M. Mafi, and F. Sadeghian, *Density and viscosity of 1-butyl-3-methylimidazolium nitrate with ethanol, 1-propanol, or 1-butanol at several temperatures.* The Journal of Chemical Thermodynamics, 2009. **41**(12): p. 1432-1438.

453. Sun, T., R.M. DiGullio, and A.S. Teja, *Densities and Viscosities of Four Butanediols between 293K and 463K.* J. Chem. Eng. Data, 1992. **37**: p. 246-248.

454. Mazurkiewicz, J., H.M. Baranowska, M. Wojtasik, and P. Tomasik, *Macrostructure of aqueous solutions of ethanol and its implications.* Electronic journal of polish agricultural universities 2007. **10**(2).

455. Loksuwan, J., *Characteristics of microencapsulated β-carotene formed by spray drying with modified tapioca starch, native tapioca starch and maltodextrin.* Food Hydrocolloids, 2007. **21**(5): p. 928-935.

456. Parikh, A., S. Agarwal, and K. Raut, *A Review on applications of maltodextrin in pharmaceutical industry.* International Journal of Pharmacy and Biological Sciences, 2014. **4**(4): p. 67-74.

457. Yan, X., *Short-Chain Polysaccharide Analysis in Ethanol-Water Solutions.* Journal of AOAC International, 2017. **100(4)**: p. 1134–1136.

458. Pothakamury, U.R. and G.V. Barbosa-Cánovas, *Fundamental aspects of controlled release in foods.* Trends in Food Science & Technology, 1995. **6**(12): p. 397-406.

459. Xia, F., D. Nagrath, and S.M. Cramer, *Effect of pH changes on water release values in hydrophobic interaction chromatographic systems.* Journal of Chromatography A, 2005. **1079**(1): p. 229-235.

460. Sui, C., J.A. Preece, Z. Zhang, and S.-H. Yu, *Efficient encapsulation of water soluble inorganic and organic actives in melamine formaldehyde based microcapsules for control release into an aqueous environment.* Chemical Engineering Science, 2021. **229**: p. 116103.

461. Wijmans, J.G. and R.W. Baker, *The solution-diffusion model: a review.* Journal of Membrane Science, 1995. **107**(1): p. 1-21.